CALIFORNIA INSTITUTE OF TECHNOLOGY

EARTHQUAKE ENGINEERING RESEARCH LABORATORY

NONLINEAR EARTHQUAKE RESPONSE OF CONCRETE GRAVITY DAM SYSTEMS

By

Bahaa El-Aidi

Report No. EERL 88-02

A Report on Research Supported by Grants
from the National Science Foundation
and by the Earthquake Research Affiliates
of the California Institute of Technology

Pasadena, California

1988

This investigation was sponsored by Grant Nos. CEE81-19962, CEE83-17257, and CES-8619908 from the National Science Foundation and by the Earthquake Research Affiliates of the California Institute of Technology under the supervision of John F. Hall. Any opinions, findings, conclusions or recommendations expressed in this publication are those of the author and do not necessarily reflect the views of the National Science Foundation.

NONLINEAR EARTHQUAKE RESPONSE
of
CONCRETE GRAVITY DAM SYSTEMS

Thesis by

BAHAA EL-AIDI

In Partial Fulfillment of the Requirements

for the Degree of

Doctor of Philosophy

California Institute of Technology

Pasadena, California

1989

(Submitted August 24, 1988)

To My Parents

Acknowledgements

I would like to express my deep appreciation and gratitude to my advisor, Professor J.F. Hall, for his guidance and invaluable assistance during may stay at Caltech. He was always available and has contributed generously during all phases of this investigation.

I would like to thank the members of my defense committee for their interest and very useful suggestions.

The financial aid provided by the California Institute of Technology is greatly appreciated.

I am also thankful to Mr. Bill Donlon for sharing his experience with the experimental work on small scale dams with me. The contour plots were developed using the Surfmap program; the assistance of Mr. Kristin Wood is appreciated in this regard. Crista Potter helped in formatting the text and Cecilia Lin helped in preparing some of the figures. I would also like to extend my thanks to everybody, particularly the members of Thomas Building, who contributed in one way or another.

Finally, I am deeply indebted to my parents in Cairo for their steadfast love, unfailing support and continuous encouragement.

Abstract

The earthquake response of concrete gravity dam systems is investigated with emphasis on the nonlinear behavior associated with tensile concrete cracking and water cavitation. A single dam-monolith is considered and is assumed to respond independently as a two-dimensional system under plane stress conditions. The two-dimensional assumption is also extended to model the compressible water body impounded upstream of the dam. Standard displacement-based finite element techniques are used to spatially discretize the field equations and produce a single symmetric matrix equation for the dam-water system. Energy dissipation in the reservoir, through radiation in the infinite upstream direction and absorption at the bottom, is approximately accounted for, and a set of numerical examples is presented to demonstrate the accuracy of the present formulation in modeling the linear earthquake response of infinite reservoirs. An approximate procedure to account for dam-foundation interaction is incorporated based on the response of a rigid plate attached to a three-dimensional viscoelastic half-space.

Water cavitation is modeled by a smeared approach which uses a bilinear pressure-strain relation. It is shown that the water response becomes dominated by spurious high frequency oscillations upon closure of cavitated regions, and improved results can be obtained by using some stiffness-proportional damping in the water reservoir. As demonstrated in an example analysis of Pine Flat Dam (linear dam), cavitation occurs in the upper part of the reservoir along the dam

face, unlike other investigations which show cavitated regions at considerable distances from the dam, and both the tensile pressure cutoffs and compressive impacts have a minor effect on the dam response.

Tensile cracks are incorporated using the smeared crack approach, and sliding along closed cracks is allowed. Coupling effects inherent in the finite element formulation are explained, and their influence on open and closed cracks is investigated. Propagation of cracks is monitored in an interactive environment which uses an equivalent strength criterion and allows for user input; remeshing is avoided. The algorithm adopted here produces narrow cracks, unlike many other investigations which show large zones of cracking. An extensive numerical study of Pine Flat Dam demonstrates some interesting features of the nonlinear response of the system, identifies potential failure mechanisms, and reveals a number of difficulties that the analysis encounters. Although no instability of the dam occurs, the numerical difficulties will have to be overcome before definite conclusions regarding stability can be made. It is shown that cracking reduces the hydrodynamic pressures in the reservoir and, hence, reduces water cavitation.

Table of Contents

Acknowledgements iii

Abstract iv

Chapter One

INTRODUCTION

1.1 Background 1

1.2 Scope and Organization 3

References 4

Chapter Two

DAM-WATER-FOUNDATION SYSTEM

2.1 Introduction 5

2.2 Scope and Organization 6

2.3 Mathematical Formulation 7

2.3.1 Concrete Gravity Dam 10

2.3.2 Rock Foundation 11

2.3.3 Water 15

2.4 Earthquake Response 23

References 30

Appendix 2.A 32

Appendix 2.B 35

Appendix 2.C 37

Chapter Three

WATER CAVITATION

3.1 Introduction 42
3.2 Scope and Organization 43
3.3 Previous Work 43
3.4 Mathematical Formulation 47
3.5 Numerical Studies 49
3.6 Cavitation Effects on Dam Response 65
References 86

Chapter Four

TENSILE CRACKS IN CONCRETE GRAVITY DAMS

4.1 Introduction 87
4.2 Scope and Organization 88
4.3 Previous Work 88
4.3.1 Field and Laboratory Experience 88
4.3.2 Mathematical Studies 92
4.4 Crack Modeling 99
4.4.1 Open Crack Representation 100
4.4.2 Closed Crack Representation 101
4.4.3 Crack Initiation 102
4.4.4 Crack Propagation 103
4.4.5 Planes of Weakness 107
4.5 Numerical Analyses 109
4.5.1 Problem 4.1 110
4.5.2 Problem 4.2 131
4.5.3 Problem 4.3 136
4.5.4 Problem 4.4 142
4.5.5 Problem 4.5 146
4.5.6 Problem 4.6 151

References 158
Appendix 4.A 160
Appendix 4.B 162

Chapter Five
SUMMARY AND CONCLUSIONS
5.1 Summary 164
5.2 Discussions and Conclusions 166

Chapter One

INTRODUCTION

1.1 Background

Dams retaining large reservoirs of water play an important role in human life. With respect to environmental and economical considerations, their safe performance is vital. Statistically, failures of dams have been much fewer than those of other types of structures; however, in many cases, their failure has led to disastrous consequences.

Recently, there has been an increase in concern about the safety of dams, especially in seismically active regions. However, much about the complex behavior of dam systems under dynamic excitations is still not understood. In safety evaluation studies, attention has to be directed, not only to newly proposed dams, but also to existing dams, and several important questions need to be addressed. For instance, would it be appropriate to assume that a given dam system responds linearly during a given earthquake ? What are the sources of potential nonlinear behavior in the system ? How do different nonlinear mechanisms influence the stability of the system ? To what extent would the integrity of a given dam suffer under a given strong motion earthquake ? Would the dam collapse ?

Experience has shown that typical concrete dam-water-foundation systems

behave nonlinearly when subjected to high levels of earthquake excitations. Experimental and analytical research together with available field observations have identified several types of nonlinear phenomena which include mainly concrete cracking under tension; opening, closing and sliding along existing cracks and joints within the dam; water cavitation in the reservoir; and sliding along weak planes running under the dam (see Sections 3.3 and 4.3). Concrete behavior under high compressive stresses and strain rate effects are also candidates for investigation.

The experience of the Koyna earthquake of 1967 in India and the resulting severe damage to Koyna Dam [1] has drawn attention to the likely occurrence of cracks during strong shaking. Although Koyna Dam suffered extensive cracking and water leakage was observed on its downstream face and inside the inspection galleries, the dam did not collapse and was later restored. However, the duration of strong shaking lasted only a few seconds, and an earthquake of long duration likely would have produced more severe consequences. Fortunately, the reservoir was not filled to capacity.

In the water reservoir, numerical analyses have shown that the static water compression can be completely relieved during strong earthquake shaking [2]. Therefore, the inclusion of water cavitation in an analysis is more appropriate than the often assumed linear behavior. The importance of water cavitation stems from a concern about possible large water impacts on the dam face associated with collapsing cavitated regions. Because cavitation would largely develop in the upper part of the reservoir, these impacts are expected to alter the dam response mostly in the region most susceptible to cracking.

With regard to the foundation, long practice has shown that its stable performance is crucial to the safety of the dam itself. Statistically, about one third of the failures of dams have been attributed to foundation failures [3]. Weak planes in the foundation may affect the dam in various ways [3,4] depending on their profile and stress-carrying capacity. Sliding along a weak plane in the rock foundation or unkeyed joint at the dam base presents a possible failure

mechanism that must be thoroughly scrutinized to insure safety during operation. The eminent threat posed by weak planes in the foundation may have been demonstrated by the failure of Malpasset Dam in France [3]. This was a thin double curvature arch dam 60 m high that collapsed in absence of seismic loading when its reservoir was almost full for the first time. Concrete gravity dams may not be better off in this regard, as could be thought because of their wide base and stabilizing own weight, and the case of Dworshak Dam in the U.S.A. can be cited as an example where weak planes were detected under the dam during excavation and measures were taken to strengthen the foundation to prevent downstream sliding [3].

1.2 Scope and Organization

The present study investigates effects of reservoir cavitation and concrete cracking on the response of concrete gravity dam-water-foundation systems under earthquake-induced ground motions. Foundation-related nonlinearity is only included at the dam-foundation interface. The feasibility of using simple smearing techniques to represent the nonlinear behavior through a time domain displacement-based finite element approach is explored.

Each chapter in this study is self-contained and is concluded by references and appendices. Firstly, Chapter 2 describes the dam-water-foundation system adopted throughout this study. The dam-water system is treated as an integral system in which the field equations are discretized following the standard displacement-based finite element techniques; a two-dimensional assumption is employed. Energy dissipation in the reservoir, due to absorption at the bottom and radiation in the infinite upstream direction, is approximately included. Dam-foundation interaction is idealized based on the theory of a rigid plate resting on top of a three-dimensional viscoelastic half-space. A linear analysis of the Pine Flat Dam-water-foundation system demonstrates the tendency toward water cavitation and concrete cracking.

In Chapter 3, reservoir cavitation is investigated. First, a bilinear material

model is incorporated in the water to simulate cavitation; the inertia forces are calculated assuming a continuous mass distribution. Numerical effects associated with closing of cavitated regions are investigated, and the chapter concludes with a numerical study demonstrating the effects of cavitation on the earthquake response of Pine Flat Dam.

In Chapter 4, the smeared crack model is implemented to simulate crack opening and closing in the dam, and the influence of some undesirable coupling inherent in the finite element method for open and closed cracks is explained in the appendices. Crack propagation is monitored through an interactive algorithm that incorporates the equivalent strength criterion. A series of numerical studies is presented to demonstrate the earthquake response of the Pine Flat Dam-water-foundation system under different cracking conditions.

Finally, a summary is given in Chapter 5. Experience with the numerical analyses and conclusions of the presented investigations are outlined, and suggestions for future work are discussed.

References

[1] Chopra, A. K. and Chakrabarti, K., "The Koyna earthquake of December 11, 1967 and the performance of Koyna Dam," *Report No. EERC 71-1*, University of California, Berkeley, April 1971.

[2] Hall, J. F., "Study of the earthquake response of Pine Flat Dam," *Earthquake Engineering and Structural Dynamics*, Vol. 14, No. 2, March-April, 1986.

[3] Thomas, Henry H., "The engineering of large dams," Part I, John Wiley & Sons, 1976.

[4] United States Department of the Interior, Bureau of Reclamation, "Design of gravity dams," Denver, 1975.

Chapter Two

DAM-WATER-FOUNDATION SYSTEM

2.1 Introduction

Concrete gravity dam-water-foundation systems are three-dimensional but are often idealized as two-dimensional sections in planes normal to the dam axis. This assumption requires that the geometry and material properties of the system as well as the seismic input vary slowly along the dam axis. A two-dimensional treatment is also often used when unkeyed contraction joints are present in the dam, on the basis that the monoliths will vibrate nearly independently under strong shaking; a plane stress condition is usually assumed. However, the presence of joints does not necessarily allow two-dimensional representations of the water and foundation since their responses may still be highly three-dimensional, for example, if adjacent monoliths are vibrating out of phase. Even so, since nonlinear analyses of three-dimensional systems are too expensive at present, only the planar problem will be dealt with here, although an approximate procedure to account for three-dimensional foundation effects will be incorporated.

The excitations associated with the two-dimensional idealization are the horizontal (stream component) and vertical components of the free-field ground motions. Fig. 2.1 depicts a two-dimensional profile of the system together with the associated boundaries, coordinate system, and applied loads. The sign convention employed in all media is tension positive.

2.2 Scope and Organization

The purpose of this chapter is to define the system model adopted throughout this study, a preliminary step to addressing the nonlinear phenomenon in following chapters. Section 2.3 presents the general form of the system matrix equation together with the set of equations defining the time marching scheme. For every subsystem, the assumptions involved are stated and the contributions to the system matrices are defined. Finally, in Section 2.4, the tendency towards anticipated nonlinear behavior, both in the water reservoir and the concrete dam, is demonstrated through a numerical example.

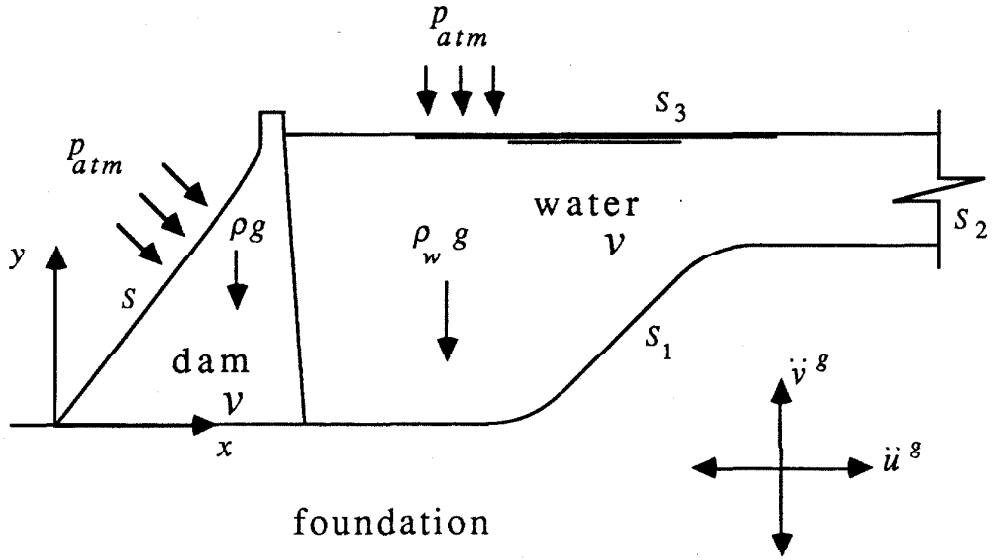

Figure 2.1. The dam-water-foundation system, associated boundaries, coordinate system, and applied loads.

2.3 Mathematical Formulation

Procedures for computing the dynamic response of concrete gravity dams often employ the displacement-based formulation since it provides a convenient approach for describing the mechanical behavior of solids. The formulation is in terms of the material particle displacements which are the physical quantities of interest. Standard finite element techniques are used to spatially discretize the field equations and produce the matrix equation of the dam. The finite element grid is embedded in the material and moves with it such that every nodal point has the same motion as the material particle it coincides with. The nodal unknowns, therefore, are the components of the particle displacements.

The same approach can be extended easily to model the water behavior. This is advantageous since it offers easy coding, full compatibility with the structure formulation leading to a single symmetric matrix equation for the water-structure system, and great capability of handling material nonlinearity within the fluid. However, from a computational point of view, the water displacement formulation produces more unknowns than the conventional formulation employing the scalar wave equation. Consequently, it increases the cost of two-dimensional analyses and renders three-dimensional analyses almost inaccessible.

Throughout this study, the dam-water system is regarded as an integral system that is formulated in terms of the particle displacements. Special treatment of the interface is required due to the inviscid behavior of the water. Small displacements are assumed everywhere in the system so that there is no distinction between any deformed configuration and the initial configuration.

Considering the whole domain of the dam-water system, application of the weighted residual method to the field equations gives rise to the following single matrix equation,

$$\mathbf{M}\{\ddot{U}\} + \mathbf{C}\{\dot{U}\} + \{\mathbf{P}(\{U\})\} = \{\mathbf{F}_{st}\} - \{\mathbf{F}_{eq}\} - \{\mathbf{F}_2\}, \qquad (2.1)$$

where the bold-faced symbols stand for the global system arrays ($\mathbf{M}$ = mass

matrix, $\mathbf{C}$ = damping matrix, $\{\mathbf{P}\}$ = vector of stiffness forces, $\{\mathbf{F}_{st}\}$ = static load vector, $\{\mathbf{F}_{eq}\}$ = earthquake load vector due to uniform free-field ground accelerations in both x and y directions, and $\{\mathbf{F}_2\}$ = earthquake load vector associated with the nonreflecting boundary of the water domain) that are formed by the conventional assembly methods of the corresponding element arrays which will be defined in the following subsections; $\{U\}$ is the vector of unknown nodal displacements relative to the specified free-field input ground motions; and a superdot indicates a material time derivative. At node i, the unknowns are translations u_i and v_i along the x and y axes, respectively.

In the absence of any nonlinear behavior, modal analyses and frequency domain methods are the most efficient and informative solution techniques available for solving equation (2.1). However, when nonlinear behavior is considered, the more expensive time domain integration of the matrix equation must be used instead. Time domain solutions are carried out incrementally using either a variable or a fixed time step size Δt. Knowing the solution at time t, the solution at time $t + \Delta t$ is obtained iteratively by treating the dynamic system as an equivalent static one with a tangent matrix.

Time integration schemes are categorized into implicit, explicit, and implicit-explicit schemes. The choice of the proper scheme depends on the type of problem. Implicit schemes are safer regarding convergence, and allow equilibrium to be satisfied to any degree through iteration. It is also highly desirable that the adopted time integration scheme enjoy second order accuracy, be unconditionally stable, and provide adequate numerical damping for the high frequency response components. The Bossak 'α-method' [1,10,15], a generalization of the Newmark method, meets these requirements, and hence, it is chosen. Linearization of the stiffness forces is performed in the standard way using the tangent stiffness matrix $\mathbf{K}_T$ and the resulting discretized version of equation (2.1) written at time $t + \Delta t$ is

$$\Big[(1-\alpha_B)\mathbf{M}+\gamma\Delta t\mathbf{C}+\beta\Delta t^2\mathbf{K}_T^k\Big]\{\Delta U^k\}=\beta\Delta t^2\{\mathbf{F}(t+\Delta t)\}$$
$$-\Big[(1-\alpha_B)\mathbf{M}+\gamma\Delta t\mathbf{C}\Big]\{U^k(t+\Delta t)\}-\beta\Delta t^2\{\mathbf{P}^k(t+\Delta t)\}$$
$$+\mathbf{M}\Big(\{U(t)\}+\Delta t\{\dot U(t)\}+\Delta t^2(\frac{1}{2}-\frac{\beta}{1-\alpha_B})\{\ddot U(t)\}\Big)(1-\alpha_B)$$
$$+\mathbf{C}\Big(\{U(t)\}+\Delta t(1-\frac{\beta}{\gamma})\{\dot U(t)\}+\Delta t^2(\frac{1}{2}-\frac{\beta}{\gamma})\{\ddot U(t)\}\Big)\gamma\Delta t, \quad (2.2)$$

where $\{\mathbf{F}\}$ stands for the right hand side of equation (2.1). The vector of displacement increments, $\{\Delta U^k\}$, is used to update the solution at time $t+\Delta t$ as follows,

$$\{U^{k+1}(t+\Delta t)\}=\{U^k(t+\Delta t)\}+\{\Delta U^k\}, \quad (2.3)$$

where the superscript $k=1,2,\ldots$ is an iteration counter and $\{U^1(t+\Delta t)\}$ is equal to $\{U(t)\}$, the accepted converged solution at time t. The internal force vector $\{\mathbf{P}^k\}$ and the tangent matrix $\mathbf{K}_T^k$ are updated at the element level as will be shown later in the following chapters. When convergence is attained, $\{U(t+\Delta t)\}$ is used to obtain the nodal velocities and accelerations as follows,

$$\begin{aligned}\{\ddot U(t+\Delta t)\}&=\frac{\{U(t+\Delta t)\}-\{U(t)\}}{\beta\Delta t^2}-\frac{\{\dot U(t)\}}{\beta\Delta t}-(\frac{1}{2\beta}-1)\{\ddot U(t)\},\\ \{\dot U(t+\Delta t)\}&=\{\dot U(t)\}+\Big((1-\gamma)\{\ddot U(t)\}+\gamma\{\ddot U(t+\Delta t)\}\Big)\Delta t.\end{aligned} \quad (2.4)$$

In the above, γ, β and α_B are the parameters of the numerical integration scheme (the two-parameter Newmark scheme is recovered by setting $\alpha_B=0$). For second order accurate integration with positive numerical damping, the following should be satisfied [10],

$$\begin{aligned}\alpha_B&<0,\\ \gamma&=1/2-\alpha_B,\\ \beta&=(1-\alpha_B)^2/4.\end{aligned} \quad (2.5)$$

In the following subsections, the dam, foundation, and water subsystems are defined, and the contributions to the global matrices and vectors appearing in equation (2.1) are given.

2.3.1 Concrete Gravity Dam

An independent dam monolith under plane stress conditions (open joints assumed) is considered. In the absence of cracks, the plain concrete throughout the monolith is assumed linear, elastic, isotropic, and homogeneous. The standard finite element discretization leads to the following element matrices and vectors,

$$\begin{aligned} M^e &= \int_{v^e} \rho N^T N dv, \\ K_T^e &= \int_{v^e} B^T D_T^e B dv, \\ \{F_{st}^e\} &= \int_{v^e} \rho N^T \begin{Bmatrix} g_x \\ g_y \end{Bmatrix} dv + \int_{S^e} N^T \begin{Bmatrix} n_x \\ n_y \end{Bmatrix} p_{atm} ds, \\ \{F_{eq}^e\} &= M^e \begin{pmatrix} 1 & 0 & 1 & 0 & \dots \\ 0 & 1 & 0 & 1 & \dots \end{pmatrix}^T \begin{Bmatrix} \ddot{u}^g \\ \ddot{v}^g \end{Bmatrix}, \end{aligned} \tag{2.6}$$

where N and B are the nodal displacements to element displacements and strains transformation matrices, respectively; ρ is the concrete mass density; g_x and g_y are the components of the gravitational acceleration; p_{atm} is the atmospheric pressure; n_x and n_y are components of the outward unit normal to the boundary; u^g and v^g are the free-field ground motions; D_T^e is the tangent constitutive matrix given, in absence of cracks, by

$$D_T^e = \begin{pmatrix} \frac{E}{1-\nu^2} & \frac{E\nu}{1-\nu^2} & 0 \\ \frac{E\nu}{1-\nu^2} & \frac{E}{1-\nu^2} & 0 \\ 0 & 0 & G \end{pmatrix}; \tag{2.7}$$

E is Young's modulus of plain concrete; ν is Poisson's ratio; and G is the shear modulus.

Modifications to D_T^e to account for cracks are discussed in Chapter 4. Note that $\{F_{eq}^e\}$ is written for an ordering of nodal unknowns as $u_1, v_1, u_2, v_2, \dots$ etc.

Structural damping is incorporated by means of the Rayleigh expression,

$$\mathbf{C}^e = a_d \, \mathbf{M}^e + b_d \, \mathbf{K}^e, \tag{2.8}$$

where the proportionality constants a_d and b_d are determined by specifying two damping ratios for the dam at two different frequencies; and $\mathbf{K}^e$ is the elastic

element stiffness matrix. Such a damping mechanism has often been favorably incorporated in mathematical models of linear dynamical systems because it leads to classical modes. However, it does not necessarily represent the actual internal dissipation mechanism. Probably, hysteretic damping would be more appropriate; however, this form of damping is difficult to incorporate in time domain analyses.

Within the context of crack opening in concrete, special treatment of the Rayleigh damping is required, as will be discussed later in Chapter 4.

Following standard procedures, the displacements in the interior of an element can be obtained by using the element interpolation functions and the element strains evaluated from the appropriate derivatives of the element displacements. The element stresses are calculated incrementally.

2.3.2 Rock Foundation

Inclusion of foundation interaction introduces some flexibility at the dam base and provides additional means for energy dissipation through radiation. The dynamic characteristics of the dam, therefore, are functions of the foundation flexibility and the radiation damping. In the finite element method, the dam base degrees of freedom are fixed if the foundation is assumed rigid; otherwise, stiffness and damping interaction coefficients can be assembled to the base degrees of freedom to represent the flexible foundation. These interaction coefficients are generally determined by substructuring methods. An exact mathematical formulation of the foundation leads to frequency dependent interaction coefficients that are applicable to frequency domain analyses. In time domain analyses, assumptions may be introduced to arrive at approximate frequency independent interaction coefficients [11].

The general discrete form of the foundation equilibrium equation at the dam base written in the frequency domain is as follows

$$\{F_f\} = \mathbf{K}_f(w)\{U_f\} + \mathbf{C}_f(w)\{\dot{U}_f\}, \tag{2.9}$$

where $\{F_f\}$ = vector of forces acting on the foundation; $\mathbf{K}_f(w)$ = foundation stiffness matrix; $\mathbf{C}_f(w)$ = foundation damping matrix; $\{U_f\}$ = vector of foundation degrees of freedom; and w is the frequency parameter. A suitable mathematical model for the foundation has to be devised in order to obtain the coefficients of $\mathbf{K}_f$ and $\mathbf{C}_f$.

Analytical representations of a two-dimensional viscoelastic half-space are in common usage [4,5], but have drawbacks of a zero static stiffness and possibly amounts of radiation damping in excess of that present in actual three-dimensional systems. Both of these disadvantages can be overcome by assigning to the two-dimensional dam model an equivalent length L_{eq} in the direction of the dam axis and attaching the dam to the surface of a three-dimensional half-space [6], see fig. 2.2.

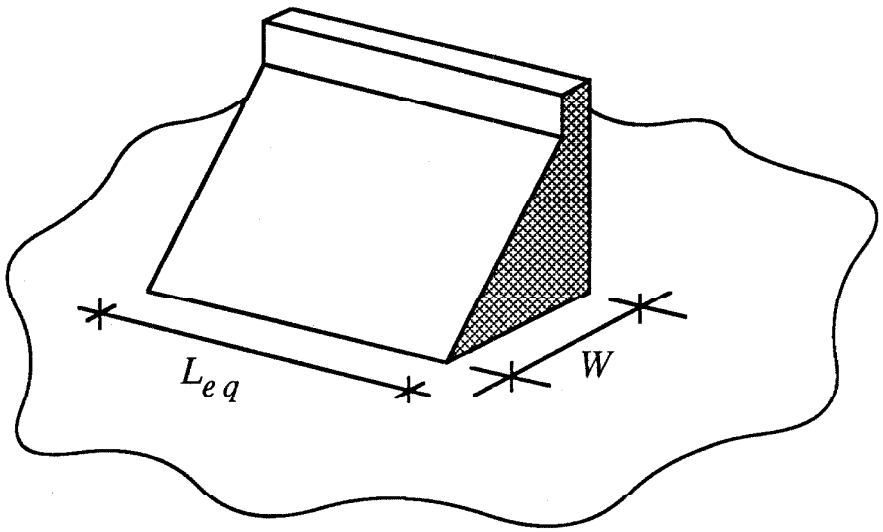

Figure 2.2. Equivalent dam attached to the surface of a three-dimensional half-space.

For the purpose of computing the foundation interaction coefficients, the foundation surface in contact with the dam is assumed to be a rigid plate of the same dimensions as the dam base ($L_{eq} \times W$, where W is the base width of the dam). All of the loads acting on the rigid plate and all of its possible modes of response are confined to the plane normal to the dam axis. For the three foundation degrees of freedom, U_f, V_f and θ_f (fig. 2.3b), equation (2.9) takes the form

$$\begin{Bmatrix} F_f^u \\ F_f^v \\ M_f/R \end{Bmatrix} = \begin{pmatrix} k_f^{uu} & 0 & k_f^{u\theta} \\ 0 & k_f^{vv} & 0 \\ k_f^{u\theta} & 0 & k_f^{\theta\theta} \end{pmatrix} \begin{Bmatrix} U_f \\ V_f \\ \theta_f R \end{Bmatrix} + \begin{pmatrix} c_f^{uu} & 0 & c_f^{u\theta} \\ 0 & c_f^{vv} & 0 \\ c_f^{u\theta} & 0 & c_f^{\theta\theta} \end{pmatrix} \begin{Bmatrix} \dot{U}_f \\ \dot{V}_f \\ \dot{\theta}_f R \end{Bmatrix}. \tag{2.10}$$

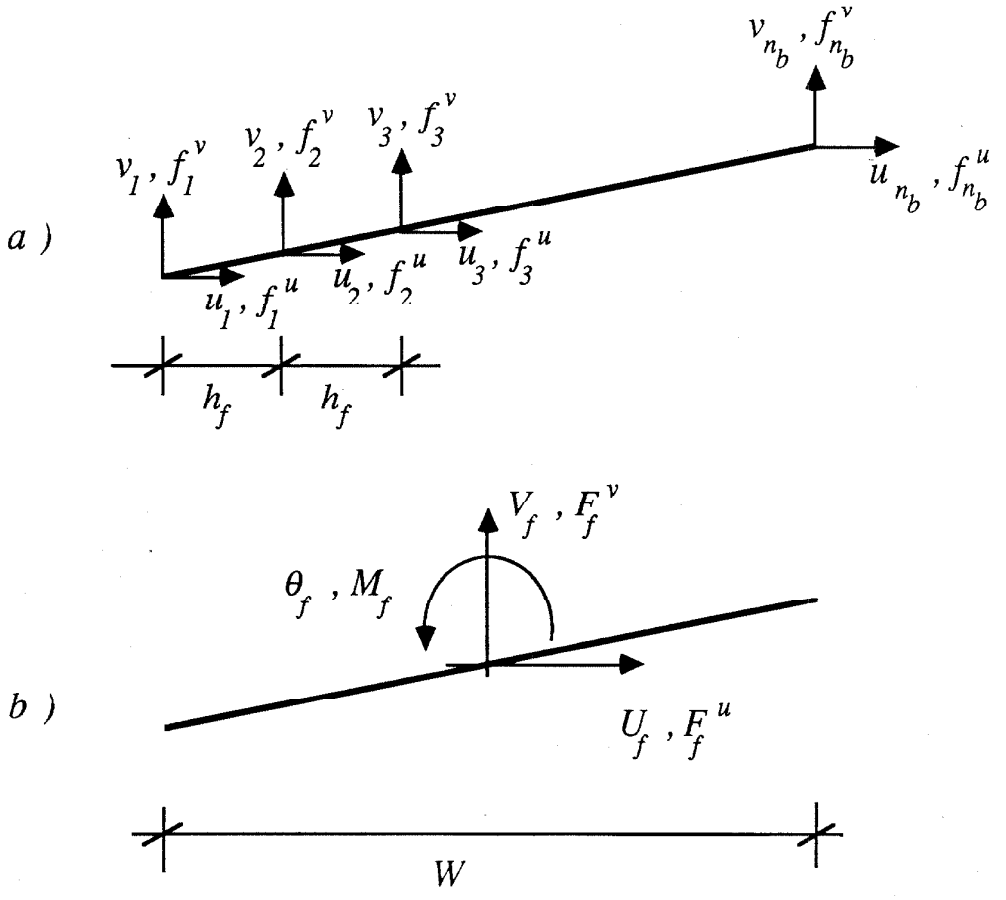

Figure 2.3. Degrees of freedom along the dam-foundation interface: a) base of dam, b) foundation plate.

For the analyses of Pine Flat Dam presented later, the equivalent length L_{eq} is chosen as twice the base width W, which is appropriate since Pine Flat Dam is built in a fairly narrow valley. The frequency dependence of the interaction coefficients $k_f^{uu} \ldots c_f^{u\theta}$ for $L_{eq}/W = 2$ is shown in table 2.1; the numerical values come from reference [14]. All coefficients are normalized using G_f and R, where G_f is the foundation shear modulus, and R is the radius of the circle of the same area as the foundation plate, given by $\sqrt{\frac{L_{eq}W}{\pi}}$. The dimensionless frequency w^* is given by $w^* = wR/v_s$, where v_s is the shear wave speed in the foundation.

w^*	$\frac{k_f^{uu}}{G_f R}$	$\frac{k_f^{vv}}{G_f R}$	$\frac{k_f^{\theta\theta}}{G_f R}$	$\frac{k_f^{u\theta}}{G_f R}$	$\frac{c_f^{uu} v_s}{G_f R^2}$	$\frac{c_f^{vv} v_s}{G_f R^2}$	$\frac{c_f^{\theta\theta} v_s}{G_f R^2}$	$\frac{c_f^{u\theta} v_s}{G_f R^2}$
0.0	5.17	6.32	2.65	0.348				
0.5	5.14	6.20	2.55	0.409	3.64	5.70	0.292	0.109
1.0	5.15	5.88	2.34	0.477	3.47	5.53	0.328	0.019
1.5	5.26	5.48	2.15	0.525	3.39	5.55	0.409	–0.038
2.0	5.41	5.02	1.99	0.539	3.29	5.60	0.470	–0.080
2.5	5.48	4.53	1.85	0.515	3.19	5.72	0.512	–0.105
3.0	5.46	4.08	1.70	0.463	3.12	5.87	0.550	–0.118
3.5	5.37	3.78	1.57	0.391	3.09	5.97	0.580	–0.122
4.0	5.27	3.64	1.44	0.305	3.08	6.08	0.608	–0.121
4.5	5.19	3.63	1.32	0.209	3.07	6.13	0.633	–0.115
5.0	5.11	3.65	1.21	0.105	3.06	6.16	0.656	–0.106

Table 2.1. Coefficients of the foundation stiffness and damping matrices, for $L_{eq}/W = 2$, Poisson's ratio $= 1/3$, and internal hysteretic damping ratio of 2%.

Considering the dimensions of Pine Flat Dam and typical properties of foundation rock ($G_f = 2.0 \times 10^6$ psi, $v_s = 7735$ ft/sec), a frequency of 10 hz, below which most of the earthquake response will occur, corresponds to $w^* = 2.0$. Between $w^* = 0.0$ and 2.0, the frequency variation of the coefficients is small enough to allow constant values to be used; the largest error will be associated with the rotational degree of freedom. Values for the frequency independent coefficients could be obtained by averaging the coefficients in the table between

$w^* = 0.0$ and 2.0, or could be set equal to those at the w^* equal to the dimensionless fundamental resonant frequency of the dam-water-foundation system [7].

To employ the rigid foundation interface model along with the flexible finite element discretization associated with the dam and shown in fig. 2.3a, the dam base is first restricted from all possible deformational type responses and only allowed to undergo rigid body motions. This is easily achieved through a penalty formulation described in Appendix 2.A which derives a $2n_b \times 2n_b$ constant symmetric stiffness matrix K_{rb} (rb for rigid base) to be assembled into the stiffness matrix of the dam at the nodal base degrees of freedom. Second, equation (2.10) needs to be recast in a form compatible with these nodal degrees of freedom. This is done by transformation in Appendix 2.B. The resulting foundation matrix equation, (2.B.1), includes the 3×3 foundation matrices K_{cf} and C_{cf} (cf for compatible foundation) that are analogous to their counterparts in equation (2.10). Foundation interaction is incorporated by assembling K_{cf} and C_{cf} into the stiffness and damping matrices of the dam, respectively, at the selected three nodal degrees of freedom at the dam base.

2.3.3 Water

The displacement-based fluid model adopted in this investigation is described in reference [13], where the fluid was assumed linear, compressible, inviscid, and irrotational. In this subsection, the water element matrices and vectors are defined, and the boundary conditions to the water, derived in Appendix 2.C, are incorporated into the finite element equations.

The element mass matrix M^e, static load vector $\{F^e_{st}\}$, and earthquake load vector $\{F^e_{eq}\}$ are identical to their counterparts for the dam given in (2.6) except for the use of the water mass density ρ_w and the addition of several boundary terms to $\{F^e_{st}\}$ which are defined later. Since the fluid is assumed inviscid, its strain energy is due only to deformational modes with volumetric strains. This leads to the following tangent element stiffness matrix

$$K^e_{vs} = \int_{v^e} B^T_{vs} k_T B_{vs} dv, \tag{2.11a}$$

where k_T is the tangent water compressibility, and B_{vs} is the nodal displacement-volume strain transformation matrix (vs for volume strain). Reduced integration is a must to obtain stiffness-free element bending modes. It should be mentioned that the presence of sediment, either saturated or unsaturated [2], can be approximately accounted for as a finite layer by adjusting the density and compressibility in the elements at the bottom of the reservoir.

The element stiffness matrix as defined above has mostly zero energy deformational modes, and hence, the global water stiffness matrix is expected to become singular, even after proper handling of the reservoir boundaries. This is remedied by enforcing the irrotationality condition and including the linearized small amplitude wave boundary condition at the free-surface.

Irrotationality is enforced through a penalty formulation that leads to an additional term in the element stiffness matrix given by

$$K^e_i = \int_{v^e} B^T_i \alpha_i B_i dv, \tag{2.11b}$$

where α_i is a penalty number, and B_i is the nodal displacement-vorticity transformation matrix (i for irrotational). Reduced integration is again used in integrating (2.11b) as required by penalty methods.

Including the boundary condition for small amplitude free-surface waves, as stated in Appendix 2.C.3, adds a third term given by

$$K^e_3 = \int_{S^e_3} \rho_w g N^T T N ds, \tag{2.11c}$$

in which

$$T = \begin{pmatrix} n_x n_x & n_x n_y \\ n_y n_x & n_y n_y \end{pmatrix},$$

and where n_x, n_y are components of the outward unit normal to the horizontal free-surface S_3, and g is the gravitational acceleration (32.2 ft/sec/sec).

Thus, the total element stiffness matrix becomes

$$K_T^e = K_{vs}^e + K_i^e + K_3^e. \tag{2.12}$$

It is to be noted that sloshing is insignificant in dam-water systems, and it is often neglected in formulations employing pressures or potential quantities as the independent variables. In the displacement-based formulation, however, it ought to be included to help suppress the singularity of the water stiffness matrix.

Energy dissipation associated with the water is due to radiation in the infinite upstream direction and absorption along the foundation interface. Assuming one-dimensional wave propagation in the foundation medium in the direction normal to the water-foundation interface S_1 and in the reservoir normal to and upstream of the vertical transmitting boundary S_2 (Sommerfeld condition), analytical explicit representation for the pressures along these boundaries can be obtained (Appendices 2.C.1 and 2.C.2),

$$p = -\frac{\rho_w}{q}\dot{u}_n + p_{st} \qquad on \qquad S_1, \tag{2.13a}$$

and

$$p = -c\rho_w\dot{u}_n - c\rho_w\dot{u}_n^g + p_{st} \qquad on \qquad S_2, \tag{2.13b}$$

where p = absolute pressure (static plus dynamic); p_{st} = static pressure (includes atmospheric); $\dot{u}_n$ = the n-component of the boundary velocity relative to the free-field velocity; $\dot{u}_n^g$ = the n-component of the free-field ground velocity; q = a damping coefficient related to the reflectivity of the pressure waves off the foundation medium; and c is the water pressure wave speed.

The discrete form produces the right-hand side force vector

$$\begin{aligned}\{F^e\} &= \int_{S^e} N^T \begin{Bmatrix} n_x \\ n_y \end{Bmatrix} p\,ds \\ &= -C_1^e\{\dot{U}^e\} - C_2^e\{\dot{U}^e\} - \{F_2^e\} + \{F_{st}^e\},\end{aligned} \tag{2.14}$$

where

$$C_1^e = \int_{S_1^e} \frac{\rho_w}{q} N^T T N \, ds,$$

$$C_2^e = \int_{S_2^e} c\rho_w N^T T N \, ds,$$

$$\{F_2^e\} = C_2^e \begin{pmatrix} 1 & 0 & 1 & 0 & \dots \\ 0 & 1 & 0 & 1 & \dots \end{pmatrix}^T \begin{Bmatrix} \dot{u}^g \\ \dot{v}^g \end{Bmatrix},$$

$$\{F_{st}^e\} = \int_{S_1^e, S_2^e} N^T \begin{Bmatrix} n_x \\ n_y \end{Bmatrix} p_{st} \, ds.$$

C_1^e and C_2^e are assembled to the system damping matrix, while $\{F_2^e\}$ is assembled to $\{\mathbf{F}_2\}$ and $\{F_{st}^e\}$ to $\{\mathbf{F}_{st}\}$ in equation (2.1). The vector $\{F_{st}^e\}$ augments the one mentioned earlier.

To improve the integrity of the water stiffness matrix, additional springs are added along the boundaries S_1 and S_2 in the direction normal to these boundaries. A stiffness value of order 1/1000 of the average diagonal of K_{vs}^e is assigned to these springs.

The dam-water interface deserves special treatment to allow for tangential slip by the inviscid water. Details appear in Appendix 2.C.4.

It should be noted that the nonreflecting boundary S_2, as incorporated in the present analysis, does not include the effect of vertical ground motions along the reservoir bottom beyond the discretized region. Depending on the length of the discretized region, this may actually be more realistic than application of vertical ground motion uniformly along the entire reservoir floor. Also, the nonreflecting boundary is only approximate, and the magnitude of the error depends on how far the boundary is placed from the dam and on the presence of dissipation mechanisms such as bottom absorption.

A numerical study is presented to assess the present finite element treatment of infinite reservoirs under earthquake type loading. Emphasis is on the appropriate extent of the mesh (i.e., position of the nonreflecting boundary), and the role of bottom absorption in dissipating some of the resulting reflections. The problem considered is pictured in fig. 2.4 together with three finite

element discretizations, a, b and c, of length-to-height ratios of 1, 1.5 and 2, respectively, each with the nonreflecting boundary, S_2, at the far end. These meshes use the four node square element with a single integration point at the center. The system is assumed linear with $\rho_w g$ equal to 62.4 lb/ft^3 and k_T equal to 3×10^5 psi. The input ground motion is the S00E component of the 1940 El Centro earthquake (fig. 2.8.a) applied in the stream direction.

Fig. 2.5 displays the obtained set of volume strain time histories (tension positive), shown by solid lines, at the centers of elements 2 and 8, and the corresponding exact solutions [3], shown by dashed lines. These results pertain to the case of rigid reservoir bottom (i.e., $\alpha_r = 1.0$, where α_r is the reflection coefficient, see Appendix 2.C.1). Some discrepancy is seen and is due to reflections off the approximate nonreflecting boundary. As shown, the accumulative effects of these reflections are delayed for the longer meshes where better agreement is evident. The case of absorptive reservoir bottom ($\alpha_r = 0.87$) is shown in fig. 2.6 where the exact solution was obtained by a frequency domain analysis using a finite element discretization with an exact nonreflecting boundary [8]. In this case, some of the reflected waves are absorbed at the bottom, thereby leading to a much better match between the two solutions. Incidentally, both sets of exact solutions were obtained by solving the pressure wave equation.

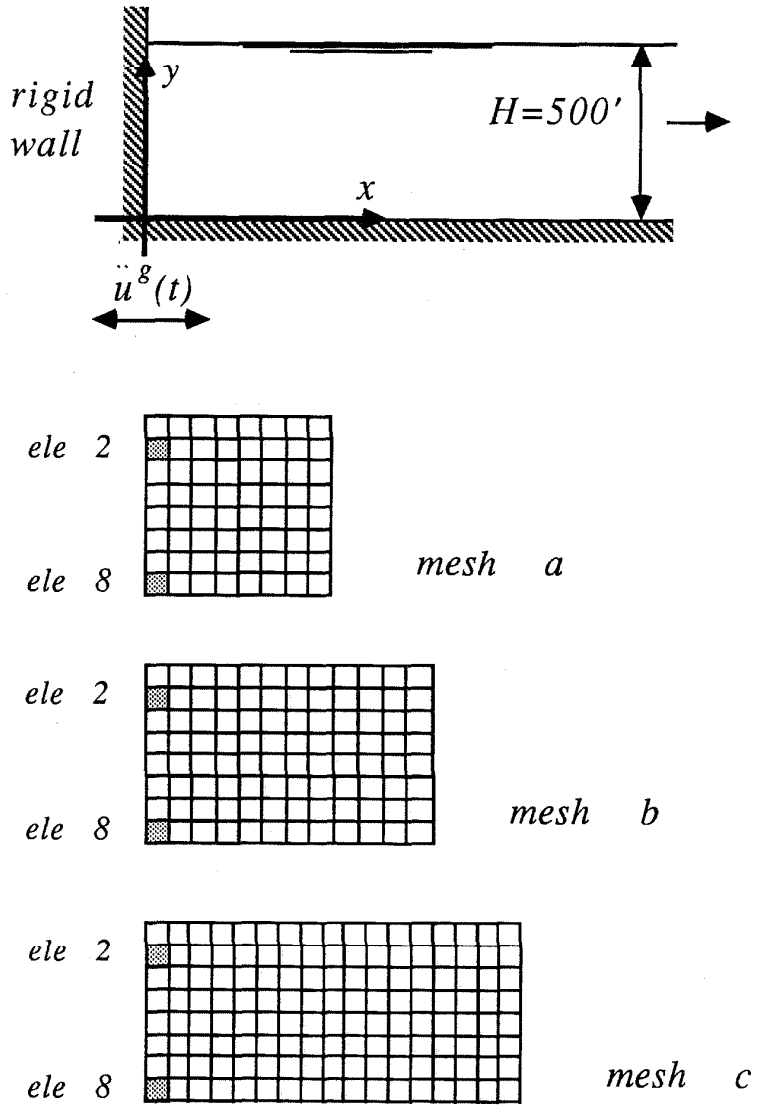

Figure 2.4. Test problem for examining the water response.

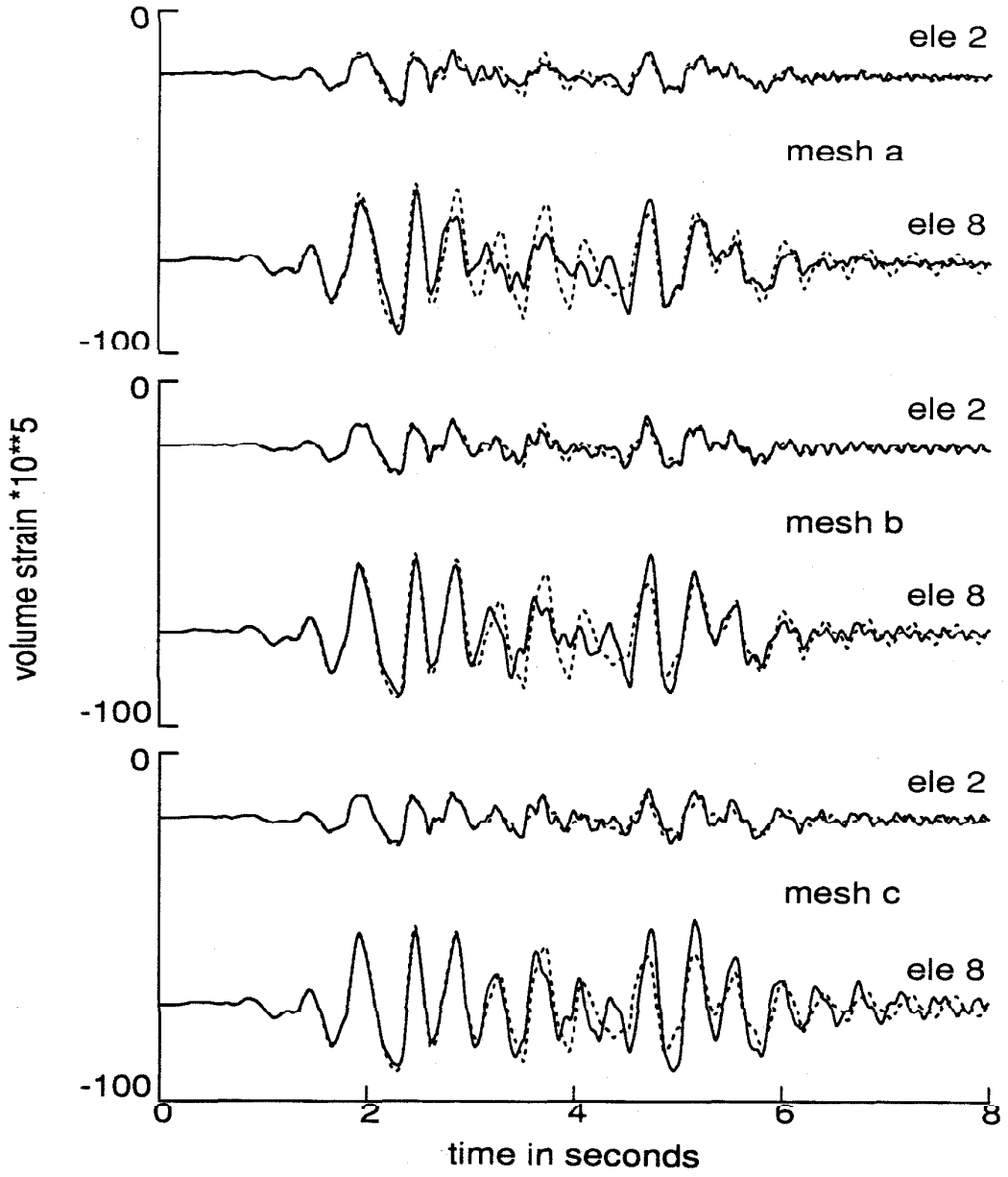

Figure 2.5. Comparison of the volume strain time histories between the current formulation (solid line) and the exact solution (dashed line) for the test problem (rigid bottom, $\alpha_r = 1.0$).

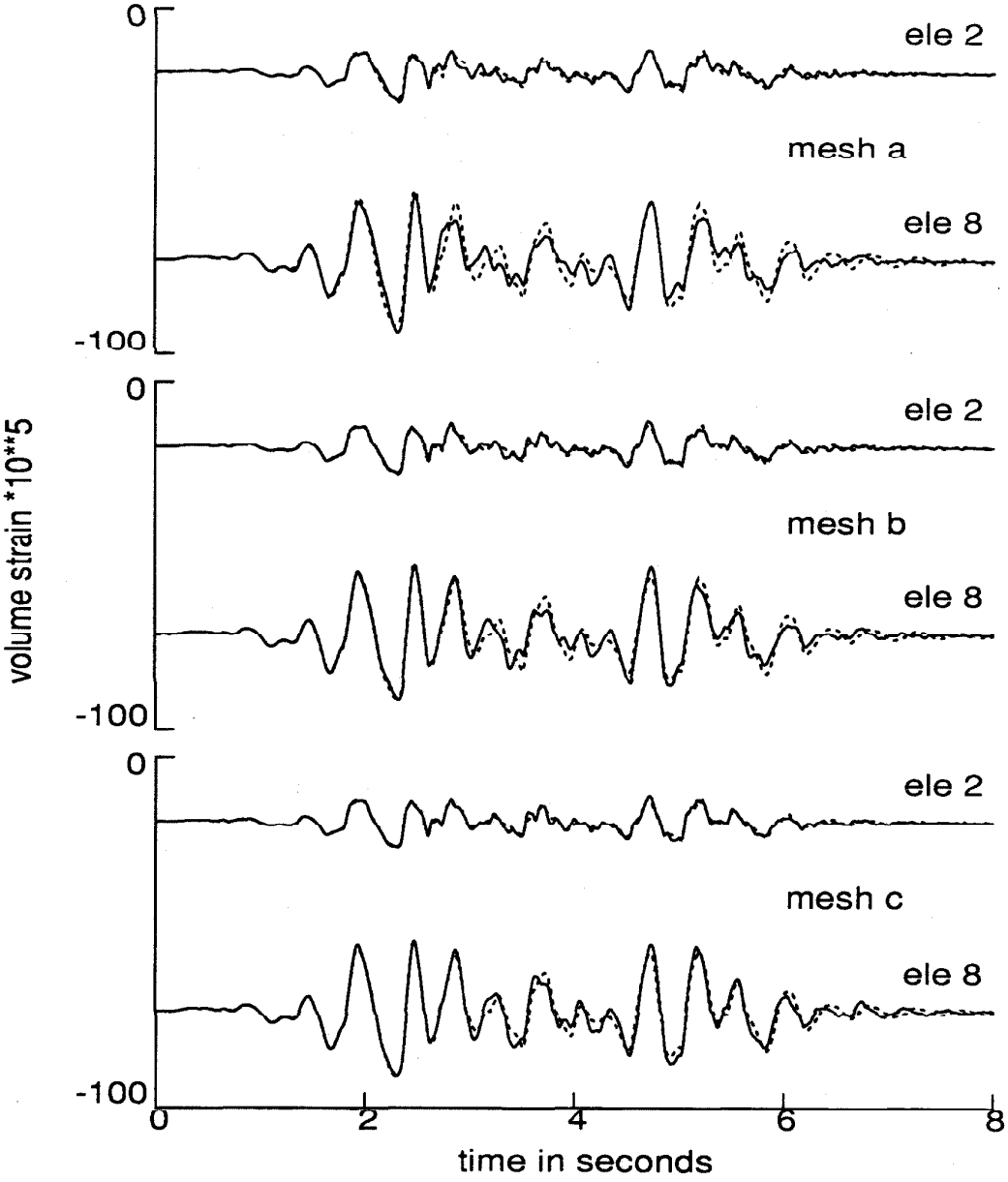

Figure 2.6. Comparison of the volume strain time histories between the current formulation (solid line) and the exact solution (dashed line) for the test problem (absorptive bottom, $\alpha_r = 0.87$).

2.4 Earthquake Response

In this section, a numerical example is presented to demonstrate that nonlinear behavior, mainly tension cracks in the dam and water cavitation in the reservoir, can be expected for moderately strong ground motions. A typical concrete gravity dam is considered, the 400 ft high Pine Flat Dam located near Fresno, California, with an infinite reservoir and constant water depth of 380 ft. The system is assumed linear with $\rho_w g = 62.4$ lb/ft^3; $k_T = 3 \times 10^5$ psi; $\rho g = 155$ lb/ft^3; $E = 4 \times 10^6$ psi; and $\nu = 0.2$. Stiffness-proportional damping is added to the dam to provide 3% critical damping at its fundamental mode. The reservoir bottom is assumed flexible with $\alpha_r = 0.87$. Values of the foundation stiffness and damping coefficients are taken as those at $\omega^* = 0.5$ in table 2.1 since this frequency is close to the fundamental frequency of the dam-water-foundation system (≈ 2.7 hz); the foundation is taken to be rather rigid with $G_f = 4.5 \times 10^6$ psi and $v_s = 11602$ ft/sec. The integration parameters, β, γ and α_B are set equal to $0.36, 0.7$ and -0.2, respectively.

The finite element mesh (fig. 2.7) is obviously very fine for the present case; however, it is used just for the purpose of later comparisons with nonlinear analyses in Chapters 3 and 4. The system is subjected to the S00E and vertical components of the 1940 El Centro earthquake ground motions (fig. 2.8) scaled amplitude-wise by 1.5.

Fig. 2.9 displays time histories of the vertical component of normal stress (tension positive) at the heel of the dam and near the top. Contours of the maximum principal (tensile) stress are shown in fig. 2.10. It is obvious that the heel of the dam and the neck at the level of slope change sustain considerable tensile stresses that are well above the tensile strength of plain concrete. (Of course, as sharp corners in linear elasticity, both the heel and the toe are points of stress singularity.) Practically, cracks may develop even under much lower tensile stresses due to existing weak planes, lift joints for example. It is evident that considerable cracking can be expected for the level of ground motion employed.

Volume strains in the water elements adjacent to the dam face at two instants of time during the earthquake are shown in fig. 2.11 together with the hydrostatic values. The strains are referenced to zero at zero absolute pressure and thus include the effect of atmospheric pressure. As shown, considerable dilatation develops in the water along the dam face near the top. Water behavior under tension is uncertain; it is expected that it would exhibit some nonlinearity and that the assumption of linear compressibility would not apply. Thus, some amount of cavitation can be expected in the reservoir under the 1.5 times El Centro ground motions.

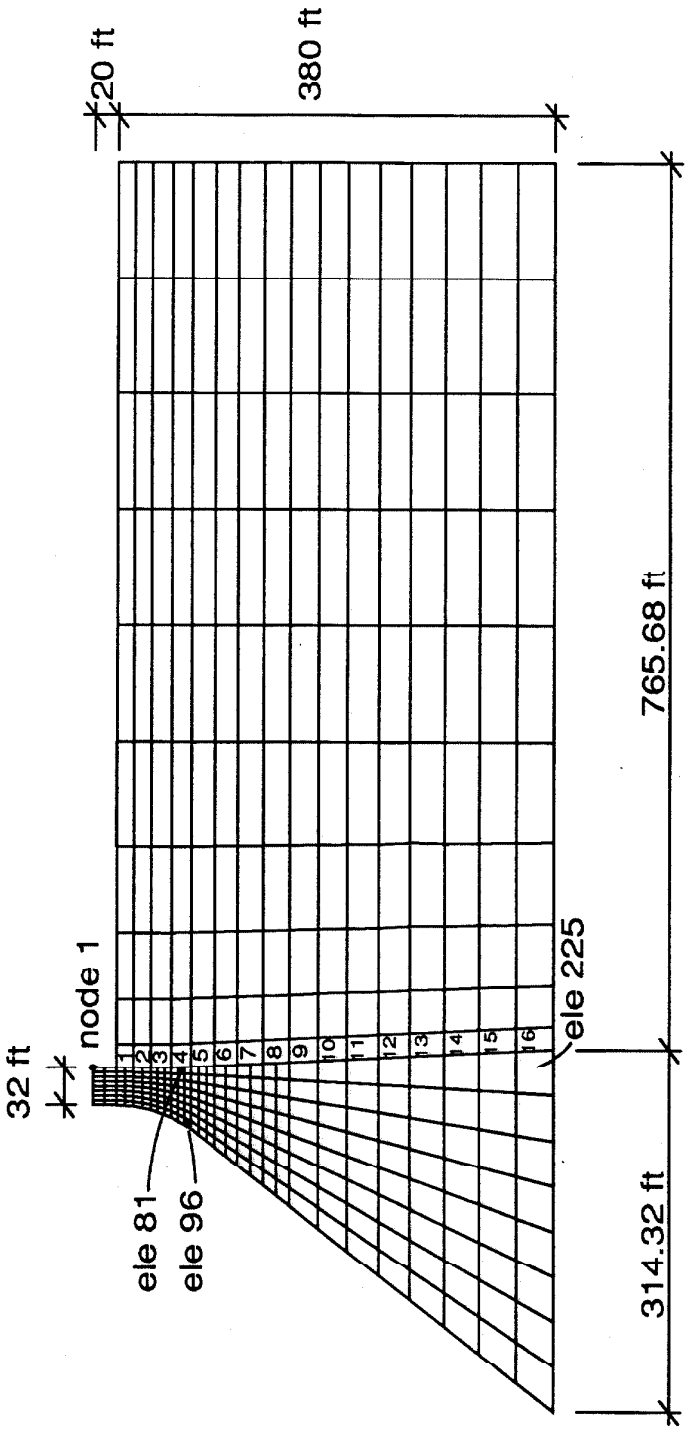

Figure 2.7. Finite element discretization of the Pine Flat Dam-water system.

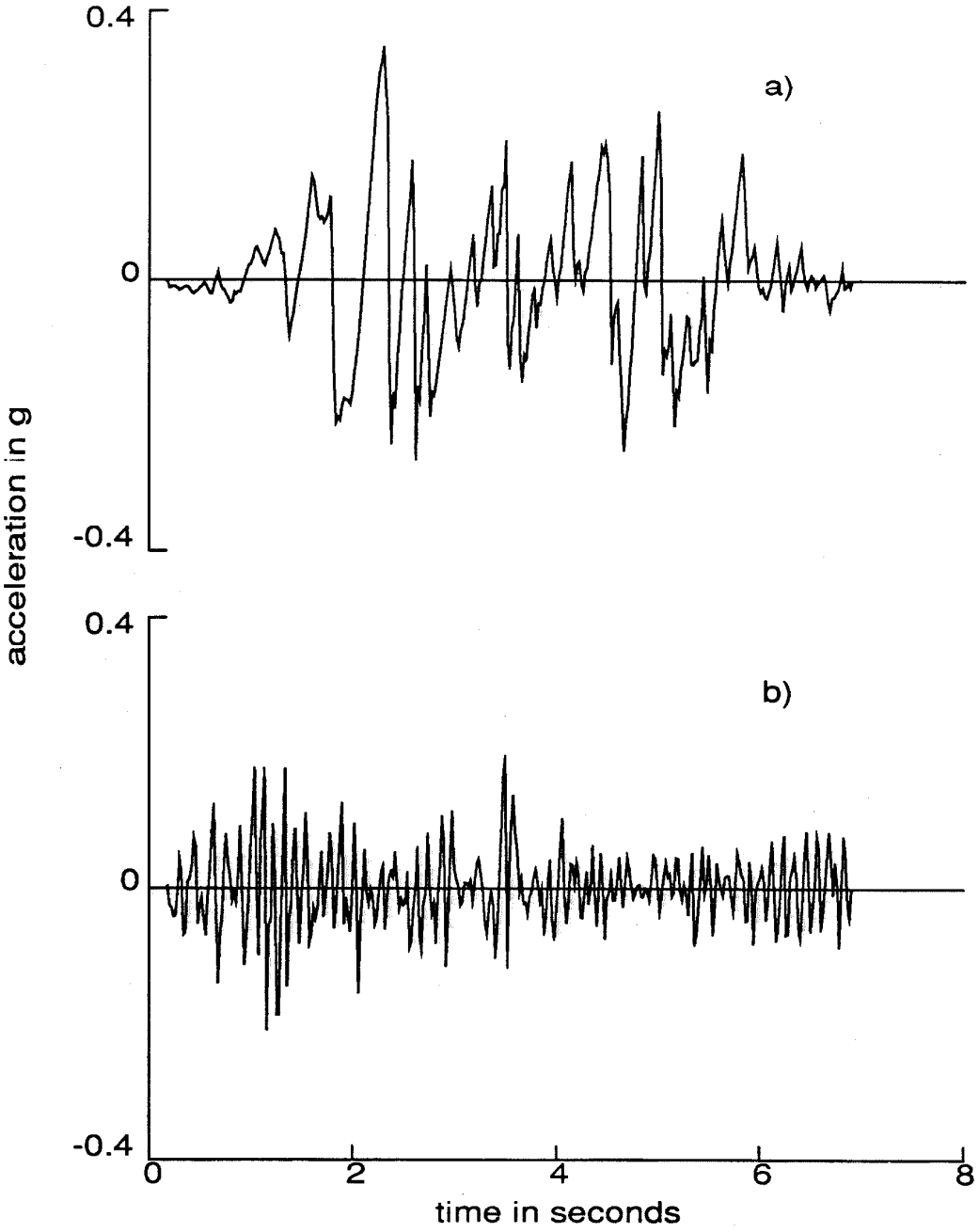

Figure 2.8. The 1940 El Centro Earthquake ground motions, a) S00E component, b) vertical component.

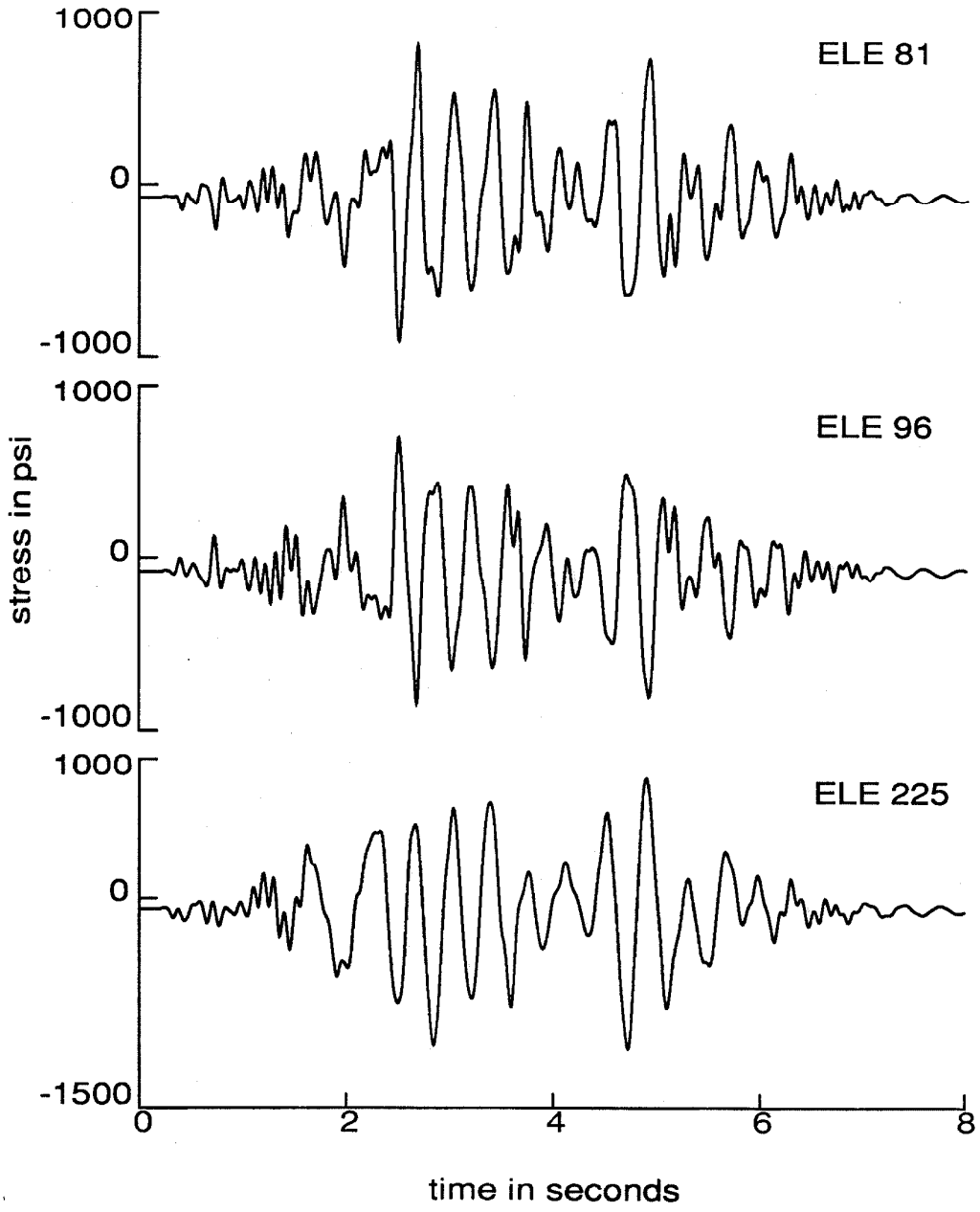

Figure 2.9. Time histories for the vertical component of normal stress for the Pine Flat Dam analysis.

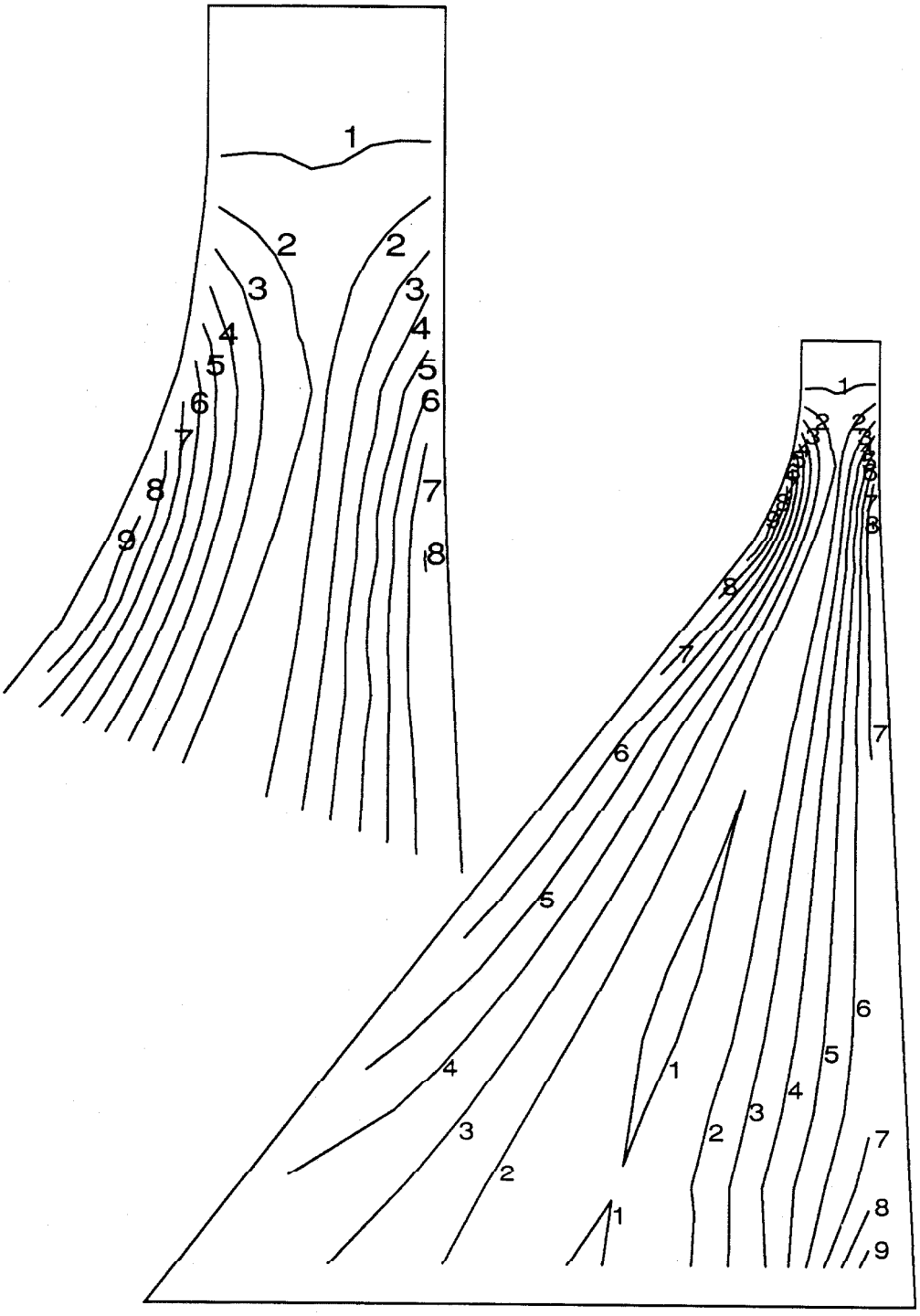

Figure 2.10. Contour lines of maximum principal stress (tension) for the Pine Flat Dam analysis. Numbers indicate contour values in hundreds of psi.

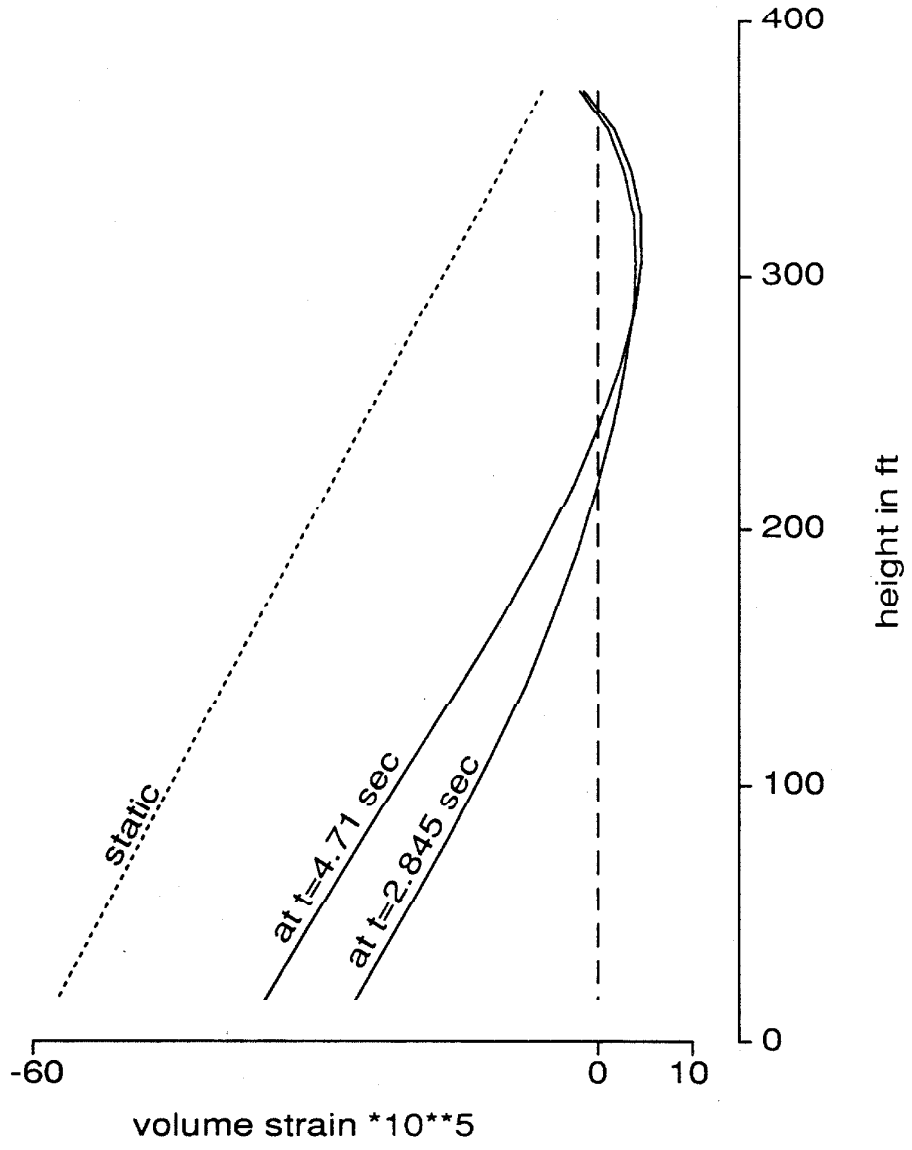

Figure 2.11. Profiles of the static and total volume strains in the water along the dam face at instants of time in the Pine Flat Dam analysis.

References

[1] Adams, D. D. and Wood, W. L., "Comparison of Hilber-Hughes-Taylor and Bossak 'α-methods' for numerical integration of vibration equations," *International Journal for Numerical Methods in Engineering*, Vol. 19, No. 5, May 1983.

[2] Cheng, A. D., "Effect of sediment on earthquake-induced reservoir hydrodynamic response," *Journal of Engineering Mechanics*, Vol. 112, No. 7, July 1986.

[3] Chopra, A. K., "Hydrodynamic pressures on dams during earthquakes," *Journal of the Engineering Mechanics Division*, Vol. 93, No. EM6, December 1967.

[4] Dasgupta, G. and Chopra, A. K., "Dynamic stiffness matrices for viscoelastic half planes," *Journal of the Engineering Mechanics Division*, Vol. 105, No. EM5, October 1979.

[5] Fenves, G. and Chopra, A. K., "Earthquake analysis and response of concrete gravity dams," *Report No. UCB/EERC-84/10*, Earthquake Engineering Research Center, University of California, Berkeley, August 1984.

[6] Finn, W. D. L., Varoglu, E. and Cherry, S., "Seismic water pressures against concrete dams," *Proceedings of the Symposium on Structural and Geotechical Mechanics,* held at the University of Illinois, Urbana, October 1975, A volume honoring N. M. Newmark, Edited by W. J. Hall, Prentice-Hall, 1977.

[7] Ghaffar-Zadeh, M. and Chapel, F., "Frequency-independent impedances of soil-structure systems in horizontal and rocking modes," *Earthquake Engineering and Structural Dynamics*, Vol. 11, No. 4, July 1983.

[8] Hall, J. F. and Chopra, A. K., "Dynamic response of embankment concrete gravity and arch dams including hydrodynamic interaction," *Report No. UCB/EERC-80/39*, Earthquake Engineering Research Center, University of California, Berkeley, October 1980.

[9] Hatano, T. and Nakagawa, T., "Seismic analysis of arch dams - coupled vibrations of dam body and reservoir water," *Technical Report*, Central Research Institute of Electric Power Industry, Tokyo, November 1972.

[10] Hughes, T. J. R., "The finite element method, Linear static and dynamic finite element analysis," Prentice-Hall, 1987.

[11] Richart, F. E., Hall, J. R. and Woods, R. D., "Vibration of soils and foundations," Prentice-Hall, 1970.

[12] Rosenblueth, E., "Presión hidrodinámica en presas debida a la aceleración vertical con refracción en el fondo," II Congreso Nacional de Ingeniería Sísmica, Veracruz, Mexico, May 1968.

[13] Wilson, E. L., "New approaches for the dynamics of large structural systems," *Report No. UCB/EERC-82/04*, Earthquake Engineering Research Center, University of California, Berkeley, June 1982.

[14] Wong, H. L. and Luco, J. E., "Tables of impedance functions and input motions for rectangular foundations," *Report No. CE 78-15*, University of Southern California, Los Angeles, December 1978.

[15] Wood, W. L., Bossak, M. and Zienkiewicz, O. C., "An alpha modification of Newmark's method," *International Journal for Numerical Methods in Engineering*, Vol. 15, No. 10, October 1980.

Appendix 2.A: Rigid Dam-Foundation Interface

Fig. 2.3a depicts a discretized dam base with n_b nodal points; each has two degrees of freedom u and v. To conform with the rigid foundation interface model adopted in Chapter 2, the dam degrees of freedom along the base are restricted from any deformational type response through a penalty formulation. A certain arrangement of stiff springs is conceived among the base nodal points in such a way as to constrain all possible deformational modes. The potential energy associated with these stiff springs can be defined (let $n_b = 9$ for simplicity) as follows:

$$\begin{aligned}\pi_{rb} = 1/2\,\alpha_{rb}\{&(u_5-u_1)^2+(u_5-u_2)^2+(u_5-u_3)^2+(u_5-u_4)^2\\ &+(u_5-u_6)^2+(u_5-u_7)^2+(u_5-u_8)^2+(u_5-u_9)^2\\ &+(v_2-v_1-\frac{v_9-v_1}{8})^2\\ &+(v_3-v_2-\frac{v_9-v_1}{8})^2\\ &+(v_4-v_3-\frac{v_9-v_1}{8})^2\\ &+\cdots\\ &+(v_9-v_8-\frac{v_9-v_1}{8})^2\},\end{aligned} \tag{2.A.1}$$

where α_{rb} is a penalty number representing the stiffness of constraining springs. Minimizing π_{rb} w.r.t. each of the degrees of freedom appearing in the above formula produces the following two sets of constraint equations,

$$\begin{aligned}\alpha_{rb}(u_5-u_1)&=0\\ \alpha_{rb}(u_5-u_2)&=0\\ \alpha_{rb}(u_5-u_3)&=0\\ \alpha_{rb}(u_5-u_4)&=0\\ \alpha_{rb}(8u_5-u_1-u_2-u_3-u_4-u_6-u_7-u_8-u_9)&=0\\ \alpha_{rb}(u_5-u_6)&=0\\ &\vdots\\ \alpha_{rb}(u_5-u_9)&=0,\end{aligned} \tag{2.A.2}$$

and

$$\begin{aligned}
\alpha_{rb}(7v_1/8 - v_2 + v_9/8) &= 0 \\
\alpha_{rb}(-v_1 + 2v_2 - v_3) &= 0 \\
\alpha_{rb}(-v_2 + 2v_3 - v_4) &= 0 \\
\alpha_{rb}(-v_3 + 2v_4 - v_5) &= 0 \\
&\vdots \\
\alpha_{rb}(-v_7 + 2v_8 - v_9) &= 0 \\
\alpha_{rb}(v_1/8 - v_8 + 7v_9/8) &= 0,
\end{aligned} \tag{2.A.3}$$

or in matrix form

$$\mathbf{K}_{rb} \begin{Bmatrix} u_1 \\ v_1 \\ u_2 \\ v_2 \\ \vdots \\ u_o \\ v_9 \end{Bmatrix} = 0, \tag{2.A.4}$$

where $\mathbf{K}_{rb}$ is a constant symmetric constraint matrix defined on the next page. Similar relations to (2.A.4) can be written for other values of n_b following the same procedure.

$$K_{rb} = \alpha_{rb} \begin{pmatrix}
1 & 0 & 0 & 0 & 0 & 0 & 0 & 0 & -1 & 0 & 0 & 0 & 0 & 0 & 0 & 0 & 0 & 0 \\
0 & 7/8 & 0 & -1 & 0 & 0 & 0 & 0 & 0 & 0 & 0 & 0 & 0 & 0 & 0 & 0 & 0 & 1/8 \\
0 & 0 & 1 & 0 & 0 & 0 & 0 & 0 & -1 & 0 & 0 & 0 & 0 & 0 & 0 & 0 & 0 & 0 \\
0 & -1 & 0 & 2 & 0 & -1 & 0 & 0 & 0 & 0 & 0 & 0 & 0 & 0 & 0 & 0 & 0 & 0 \\
0 & 0 & 0 & 0 & 1 & 0 & 0 & 0 & -1 & 0 & 0 & 0 & 0 & 0 & 0 & 0 & 0 & 0 \\
0 & 0 & 0 & -1 & 0 & 2 & 0 & -1 & 0 & 0 & 0 & 0 & 0 & 0 & 0 & 0 & 0 & 0 \\
0 & 0 & 0 & 0 & 0 & 0 & 1 & 0 & -1 & 0 & 0 & 0 & 0 & 0 & 0 & 0 & 0 & 0 \\
0 & 0 & 0 & 0 & 0 & -1 & 0 & 2 & 0 & -1 & 0 & 0 & 0 & 0 & 0 & 0 & 0 & 0 \\
-1 & 0 & -1 & 0 & -1 & 0 & -1 & 0 & 8 & 0 & -1 & 0 & -1 & 0 & -1 & 0 & -1 & 0 \\
0 & 0 & 0 & 0 & 0 & 0 & 0 & -1 & 0 & 2 & 0 & -1 & 0 & 0 & 0 & 0 & 0 & 0 \\
0 & 0 & 0 & 0 & 0 & 0 & 0 & 0 & -1 & 0 & 1 & 0 & 0 & 0 & 0 & 0 & 0 & 0 \\
0 & 0 & 0 & 0 & 0 & 0 & 0 & 0 & 0 & -1 & 0 & 2 & 0 & -1 & 0 & 0 & 0 & 0 \\
0 & 0 & 0 & 0 & 0 & 0 & 0 & 0 & -1 & 0 & 0 & 0 & 1 & 0 & 0 & 0 & 0 & 0 \\
0 & 0 & 0 & 0 & 0 & 0 & 0 & 0 & 0 & 0 & 0 & -1 & 0 & 2 & 0 & -1 & 0 & 0 \\
0 & 0 & 0 & 0 & 0 & 0 & 0 & 0 & -1 & 0 & 0 & 0 & 0 & 0 & 1 & 0 & 0 & 0 \\
0 & 0 & 0 & 0 & 0 & 0 & 0 & 0 & 0 & 0 & 0 & 0 & 0 & -1 & 0 & 2 & 0 & -1 \\
0 & 0 & 0 & 0 & 0 & 0 & 0 & 0 & -1 & 0 & 0 & 0 & 0 & 0 & 0 & 0 & 1 & 0 \\
0 & 1/8 & 0 & 0 & 0 & 0 & 0 & 0 & 0 & 0 & 0 & 0 & 0 & 0 & 0 & -1 & 0 & 7/8
\end{pmatrix}$$

Appendix 2.B: Foundation Interaction Matrices

The finite element discretization of the dam leads to $2 \times n_b$ translational degrees of freedom along the base that can be restricted to preclude deformational type responses of the base, see Appendix 2.A. Foundation matrices developed for a rigid plate conform with the degrees of freedom U_f, V_f and θ_f defining its rigid motion as employed in equation (2.10). These degrees of freedom are shown in fig. 2.3b. Before the matrices of equation (2.10) can be assembled into the nodal equations of the dam base, a transformation is necessary. The horizontal displacement, U_f, is replaced by any of the horizontal nodal degrees of freedom (take $n_b = 9$, for example), $u_1, \ldots, u_9$, say u_9. The vertical displacement, V_f, and the angle of rotation, θ_f, are replaced by any pair from the vertical nodal degrees of freedom, $v_1, \ldots, v_9$, say v_1 and v_9.

The foundation equilibrium equation as defined in equation (2.10) is recast in a new form compatible with the selected base degrees of freedom. Thus,

$$\begin{Bmatrix} f_1^v \\ f_9^u \\ f_9^v \end{Bmatrix} = \mathbf{K}_{cf} \begin{Bmatrix} v_1 \\ u_9 \\ v_9 \end{Bmatrix} + \mathbf{C}_{cf} \begin{Bmatrix} \dot{v}_1 \\ \dot{u}_9 \\ \dot{v}_9 \end{Bmatrix}. \qquad (2.B.1)$$

The coefficients of the foundation matrices $\mathbf{K}_{cf}$ and $\mathbf{C}_{cf}$ can be determined from the matrices of equation (2.10) using transformations defined by the simple geometrical relations

$$U_f = u_9$$

$$V_f = (v_9 + v_1)/2$$

$$\theta_f = (v_9 - v_1)/8h_f$$

together with the following equilibrium relations,

$$f_1^v = F_f^v/2 - M_f/8h_f$$

$$f_9^u = F_f^u$$

$$f_9^v = F_f^v/2 + M_f/8h_f,$$

which gives the following:

$$
\begin{aligned}
k_{cf}^{11} &= k_f^{vv}/4 + k_f^{\theta\theta}(R/8h_f)^2 \\
k_{cf}^{12} &= -k_f^{u\theta}(R/8h_f) \\
k_{cf}^{13} &= k_f^{vv}/4 - k_f^{\theta\theta}(R/8h_f)^2 \\
k_{cf}^{22} &= k_f^{uu} \\
k_{cf}^{23} &= -k_{cf}^{12} \\
k_{cf}^{33} &= k_{cf}^{11},
\end{aligned}
\qquad (2.B.3)
$$

and similar relations for the foundation damping coefficients.

Appendix 2.C: Water-Reservoir Boundary Conditions

The geometry of the water-reservoir system and the associated boundaries are defined in fig. 2.1. To be consistent with the displacement-based description adopted in Chapter 2, the boundary conditions need to be mathematically formulated in terms of the displacements $\underset{\sim}{u}(\underset{\sim}{x},t)$ and/or the stresses $\underset{\sim}{\sigma}(\underset{\sim}{x},t)$ at these boundaries. Since the water is inviscid, only the displacement component normal to the boundary, $u_n(\underset{\sim}{x},t)$, and the pressure, $p(\underset{\sim}{x},t)$, need to be considered. The latter notation refers to absolute pressure.

2.C.1 Reservoir Bottom

In early work in dam-water systems, it was customary to assume a rigid reservoir bottom. This, however, led to severe resonances in the compressible water body, especially under vertical excitation. To reduce the compressible water resonance, Rosenblueth [12] treated vertical excitation as a one-dimensional wave propagation from a flexible foundation into the water, and Hatano [9] provided some absorption at the reservoir bottom through a damping boundary condition.

Hall [8] later combined these concepts into a general boundary condition to be applied along the reservoir floor which, for absolute pressure p in the time domain, takes the form

$$\frac{\partial p}{\partial n}(\underset{\sim}{x},t) = \rho_w\left(\ddot{u}_n^g(t) + g_n\right) - q\dot{p}(\underset{\sim}{x},t), \qquad \forall \underset{\sim}{x} \in S_1, \qquad (2.C.1)$$

where

n indicates the direction of the outward normal,

$\ddot{u}_n^g =$ the n-component of the free-field ground acceleration,

$g_n =$ the n-component of the gravitational acceleration,

$q =$ the reservoir bottom damping coefficient,

$= (1-\alpha_r)/c(1+\alpha_r)$,

$\alpha_r =$ the reflection coefficient, i.e., the ratio of the reflected to incident amplitude of a pressure wave striking the reservoir floor,

$c =$ the water pressure wave speed,

$\rho_w =$ mass density of water.

Equation (2.C.1) assumes a one-dimensional wave propagation in the foundation medium normal to the interface.

The water equilibrium equation at the reservoir bottom in the n-direction is

$$\frac{\partial p}{\partial n}(\underset{\sim}{x},t) = \rho_w\big(\ddot{u}_n^t(\underset{\sim}{x},t) + g_n\big), \qquad \forall \underset{\sim}{x} \in S_1, \qquad (2.C.2)$$

in which $\ddot{u}_n^t$ is the n-component of the total boundary acceleration.

Equations (2.C.1) and (2.C.2) can be used to reformulate the boundary condition (2.C.1) in terms of the pressure p, rather than the pressure gradient $\partial p/\partial n$. By eliminating $\partial p/\partial n$ between (2.C.1) and (2.C.2), one gets

$$\rho_w \ddot{u}_n^t(\underset{\sim}{x},t) = \rho_w \ddot{u}_n^g(t) - q\dot{p}(\underset{\sim}{x},t), \qquad \forall \underset{\sim}{x} \in S_1. \qquad (2.C.3)$$

Integrating once w.r.t. time,

$$\rho_w \dot{u}_n^t(\underset{\sim}{x},t) = \rho_w \dot{u}_n^g(t) - q\big(p(\underset{\sim}{x},t) - p_{st}(\underset{\sim}{x})\big), \qquad \forall \underset{\sim}{x} \in S_1, \qquad (2.C.4.)$$

where p_{st} is the static pressure (including atmospheric), $\dot{u}_n^t$ is the n-component of the total boundary velocity, and $\dot{u}_n^g$ is the n-component of the free-field ground velocity. Rearranging,

$$p(\underset{\sim}{x},t) = -\frac{\rho_w}{q}\dot{u}_n(\underset{\sim}{x},t) + p_{st}(\underset{\sim}{x}), \qquad \forall \underset{\sim}{x} \in S_1, \qquad (2.C.5)$$

where $\dot{u}_n$ is the n-component of the boundary velocity relative to the free-field ground motion. Equation (2.C.5) is the reservoir bottom boundary condition and can readily be incorporated in displacement-based formulations.

2.C.2 Upstream Radiation Boundary

Infinite reservoirs require a vertical nonreflecting boundary placed some distance upstream to absorb outgoing pressure waves. An approximate nonreflecting boundary condition applicable in the time domain is the Sommerfeld condition,

$$\frac{\partial p}{\partial n}(\underset{\sim}{x},t) = -\frac{1}{c}\dot{p}(\underset{\sim}{x},t), \qquad \forall \underset{\sim}{x} \in S_2. \qquad (2.C.6)$$

Equation (2.C.6) is a special case of (2.C.1) for a vertical boundary with water beyond ($q = 1/c$) and no free-field motions.

The water equilibrium equation at S_2 in the n-direction is

$$\frac{\partial p}{\partial n}(\underset{\sim}{x},t) = \rho_w \ddot{u}_n^t(\underset{\sim}{x},t), \qquad \forall \underset{\sim}{x} \in S_2, \qquad (2.C.7)$$

which, using (2.C.6), leads to

$$\frac{1}{c}\dot{p}(\underset{\sim}{x},t) = -\rho_w \ddot{u}_n^t(\underset{\sim}{x},t), \qquad \forall \underset{\sim}{x} \in S_2. \qquad (2.C.8)$$

Integrating w.r.t. time yields

$$p(\underset{\sim}{x},t) = -c\rho_w \dot{u}_n^t(\underset{\sim}{x},t) + p_{st}(\underset{\sim}{x}), \qquad \forall \underset{\sim}{x} \in S_2. \qquad (2.C.9)$$

Splitting $\dot{u}_n^t$ into $\dot{u}_n$ and $\dot{u}_n^g$ results in

$$p(\underset{\sim}{x},t) = -c\rho_w \dot{u}_n(\underset{\sim}{x},t) - c\rho_w \dot{u}_n^g(t) + p_{st}(\underset{\sim}{x}), \qquad \forall \underset{\sim}{x} \in S_2, \qquad (2.C.10)$$

which is the boundary condition at S_2.

2.C.3 Reservoir Free-Surface

The free-surface condition that is often adopted is given by

$$p(\underset{\sim}{x},t) = p_{atm}, \qquad \forall \underset{\sim}{x} \in S_3, \qquad (2.C.11)$$

which states that the surface pressure is always equal to the atmospheric pressure (-14.7 psi), thus neglecting the free-surface water waves. This is acceptable since, although free-surface waves may be important in cases of small reservoirs, as tanks, they can be neglected in the large reservoirs of dams [3]. However, because the displacement-based formulation gives rise to a singular water stiffness matrix and because the inclusion of the free-surface water waves reduces the degree of singularity, equation (2.C.11) is modified to account for the free-surface waves. Assuming small displacements and making use of fig. 2.C.1,

$$p(\underset{\sim}{x},t) = p_{atm} - \rho_w g u_n(\underset{\sim}{x},t), \qquad \forall \underset{\sim}{x} \in S_3, \qquad (2.C.12)$$

in which the term proportional to the free-field ground displacement, u_n^g, has been omitted.

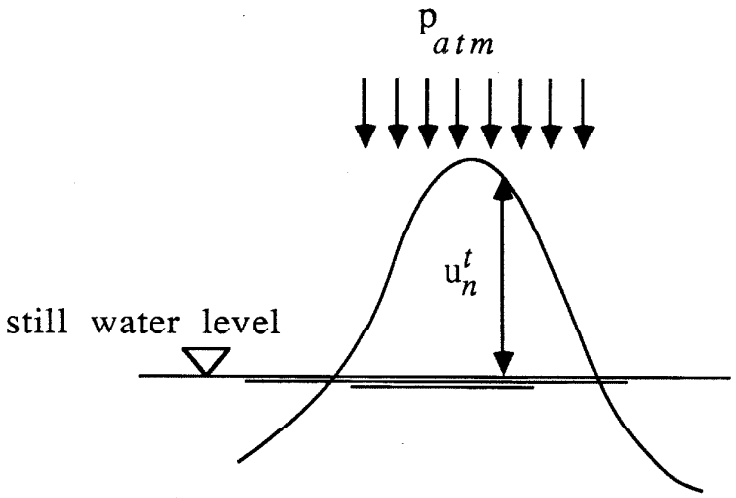

Figure 2.C.1. Free-surface small amplitude waves.

2.C.4 Water-Structure Interface

Along the water-structure boundary, continuity of displacements and equilibrium of stresses must be ensured. Since the water is inviscid, only those components normal to the interface need to be compatible, while in the tangential direction, the water and the adjacent structure should be allowed to move independently. There are two ways to achieve such compatibility, as depicted in fig. 2.C.2. The first is by introducing special nodes along the interface with three degrees of freedom each: a common normal degree of freedom and two tangential degrees of freedom. In the second method, double nodes along the interface are used; in each pair, one node belongs to the water while the other belongs to the structure. The nodes coincide geometrically and are connected together by a stiff spring element in the direction normal to the interface. The former method produces fewer degrees of freedom; on the other hand, it requires some transformations that depend on the geometry of the interface. With the latter method, attention should be given to avoid numerical ill-conditioning due to the high spring stiffness used. The latter method (fig. 2.C.2b) is used here.

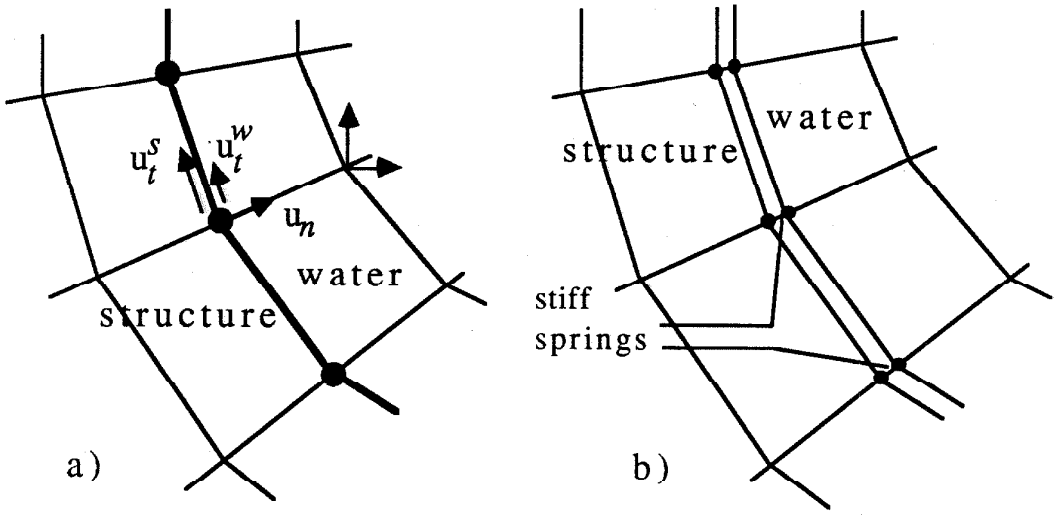

Figure 2.C.2. Modeling of water-structure interface.

Chapter Three

WATER CAVITATION

3.1 Introduction

When a water-structure system is subjected to severe dynamic excitations, the absolute water pressure may drop to the water vapor pressure producing the phenomenon known as water cavitation. Analytical studies of dam-water systems subjected to earthquake excitations show that reservoir cavitation is likely under typical strong ground motions [4]. The importance of cavitation in dam-water systems stems from its possible effects on the hydrodynamic forces acting on the dam which play an important role in the dam response.

The main difficulty in modeling reservoir cavitation is the lack of knowledge of the actual physical mechanism involved. It is expected that the mechanical behavior within cavitated regions will depend on sizes of the resulting bubbles in the reservoir and their distribution. To develop an analytical model, in absence of sufficient experimental data, three possibilities may be considered. Case 1: Cavities form of essentially zero mass (containing only water vapor and air) which may close at a later time with resulting impact. Case 2: A region of micro-bubbles forms in which the volume of bubbles is small compared to the volume of the cavitated region. This allows the simplifying assumption that the mass is uniform throughout the reservoir. Case 3: Something between cases

1 and 2 results. Unfortunately, no physical evidence exists to indicate which cavitation process is correct.

With regard to computational requirements, a numerical formulation of case 1 is cumbersome since the mesh of the reservoir must be continually modified to follow the geometry of the cavities. On the other hand, the assumption contained in case 2 is a great convenience because the nonlinearity can be incorporated entirely into the constitutive model of the water; no remeshing is required.

3.2 Scope and Organization

The purpose of this chapter is to present a simple analytical approach to simulate reservoir cavitation in dam-water systems based on the case 2 mechanism. First, a brief review of reported literature is given in Section 3.3. Then, in Section 3.4, the adopted cavitation model is presented and incorporated into the finite element model described in Chapter 2. The behavior of the model is investigated in Section 3.5 with emphasis on element size effects. In Section 3.6, the influence of reservoir cavitation on the earthquake response of Pine Flat Dam is demonstrated through a numerical study.

3.3 Previous Work

Cavitation studies in dam-water systems subjected to dynamic excitations are very few. No observations of cavitation in an actual water reservoir under earthquake-induced ground motions have been reported. Most experimental work on cavitation has been directed to high speed flow problems such as around moving turbine blades or through pipe bends. In only one experiment, that by Niwa and Clough [6], has cavitation been observed in the water reservoir of a dam under excitation provided by a shaking table. The dam model, a 27 in high single monolith of Koyna Dam (prototype height 338 ft), was separated from the water by a plastic membrane. Since air could access the dam-membrane interface, separation (i.e., cavitation) occurred whenever the absolute water pressure reduced to the atmospheric pressure. Ideally, the membrane (necessary to pre-

vent water leakage and contact with the plaster dam) would be omitted and the vapor and atmospheric pressures reduced by the length scale, but these are near impossible to accomplish. Note that the unscaled atmospheric pressure acting on the water in the experiment confined possible cavitation to separation between the dam and membrane; i.e., no cavitation in the water could occur. For strong excitations, these separations extended over the top third of the dam face and were followed by compressive pressures upon impact. Although it was stated that the impact action definitely increased these pressures, a careful examination of the pressure time histories does not indicate that this effect was great. Some of the large pressures were not preceded by cavitation, and many cavitation closures did not produce large pressures. The peak pressure amplitude generated in the cavitation region was about the same as that which occurred in the lower part of the reservoir; this distribution is not untypical of linear response.

Several two-dimensional analytical studies have been carried out to investigate the consequences of water cavitation. Clough and Chu-Han [2] employed the case 1 mechanism with the cavity confined to a separation at the dam face. The pressure formulation (dynamic pressure as the independent variable) was used for water assumed incompressible, and all degrees of freedom away from the dam were condensed out (possible because of the incompressibility assumption). For a 160 m high gravity dam subjected to the 1940 S00E El Centro ground motion scaled amplitude-wise by two (maximum horizontal acceleration of 0.65 g), impacts of the water against the dam following separation increased the tensile stresses by 20-40 % in the upper part of the dam. It was also pointed out that since water compressibility can significantly affect the water pressure response, it should be included in cavitation studies.

Another analytical study by Zienkiewicz, Paul and Hinton [7] employed a displacement potential formulation for compressible water [5] for two-dimensional gravity dams. A bilinear pressure-volume strain relation [1] was used for the water to include cavitation (case 2 mechanism). The formulation

led to coupled matrix equations for the dam and water which were solved iteratively at each time step in a staggered scheme; linearization of the equations could not be performed as the fluid nonlinearity entered into a mass-like term. No energy absorption was employed in the water except for an upstream transmitting boundary. The model was capable of capturing cavitation anywhere in the reservoir; in fact, isolated regions of cavitation occurred at considerable distances from the dam, a behavior not elaborated on in the reference. Analyses of Koyna, Pine Flat and Bhakra Dams (338, 400 and 610 ft heights, respectively) were made for the 1967 Koyna and 1940 El Centro ground motions scaled amplitude-wise by 1.5 (maximum horizontal accelerations of 0.94 and 0.49 g, respectively). Effects of the cavitation on the dam response were moderate and, in general, tended to reduce the peak responses somewhat. However, time histories of the water pressure responses were very different depending on whether or not cavitation was included. Peak compressive pressures, attained after closure of the cavitated regions, increased considerably. Possible drawbacks of the displacement potential formulation are the dependence of the pressures on the second time derivative of the potential function, which may be inaccurate, and the necessity to use ground displacements to define the earthquake motion, which seldom can be determined accurately.

Recently, Fenves and Vargas-Loli [3] have proposed a mixed displacement-pressure formulation for the water that leads to a symmetric matrix equation for the dam-water system. They used the bilinear model mentioned above. A close examination of their water element reveals it to be essentially identical to that employed here, in spite of different derivations. An analysis of Pine Flat Dam used the S69E component of the 1952 Taft Lincoln School Tunnel ground motion scaled to a peak acceleration of 1 g. A stiffness-proportional damping was added to the water to give 0.1 % damping in the fundamental pressure mode of the water. The envelope of cavitation spanned the top half of the reservoir near the dam and extended over the top few layers of elements to the end of the mesh 1200 ft away from the dam where a transmitting condition was applied.

Effects of cavitation on the dam response were less than in [7], and still tended to reduce the peak amplitudes. Cavitation again strongly affected the water pressures.

In both [7] and [3], closure of a region of cavitation resulted in a sharp spike of compressive pressure followed by high frequency oscillations. The degree to which this behavior depended on the numerical discretization was not examined, although damping added in [3] was intended to stabilize the high frequency response. This behavior can be troublesome if large enough, leading to additional cycles of cavitation and spread of a cavitated zone. Some of the studies presented in this chapter investigate the mesh dependence of the solution when cavitation occurs.

In all the foregoing analytical investigations, the dam was assumed to behave linearly. However, under the high levels of excitations required to trigger water cavitation, the dam can experience high tensile stresses that exceed the plain concrete strength. Consequently, concrete cracking should be expected. As will be seen in Chapter 4, the behavior of cracked dams alters the hydrodynamic pressures on the upper part of the dam where most of the cavitation takes place. Hence, in a complete cavitation study, the dam should be treated as the situation warrants.

3.4 Mathematical Formulation

The displacement-based water model defined in Chapter 2 is extended to account for case 2 water cavitation. It is assumed that the pressure-volume strain relation obeys the bilinear model mentioned earlier and that the mass distribution throughout the reservoir is uniform. Thus, the nonlinearity is fully contained in the stiffness term leading to straight-forward linearization and solution by the standard Newton-Raphson methods.

Cavitation is assumed to initiate when the absolute water pressure drops to the water vapor pressure p_v. The incipience of cavitation is associated with a local sudden drop in the tangent water compressibility k_T from k_w to a much smaller value k_c that lasts as long as the total volume strain exceeds V_v (fig. 3.1). The original compressibility, k_w, is regained upon closure of the cavities (i.e., when the volume strain drops below V_v). The special case of $k_c = 0$ implies that cavitated water completely loses its stiffness locally and behaves under its own inertia only.

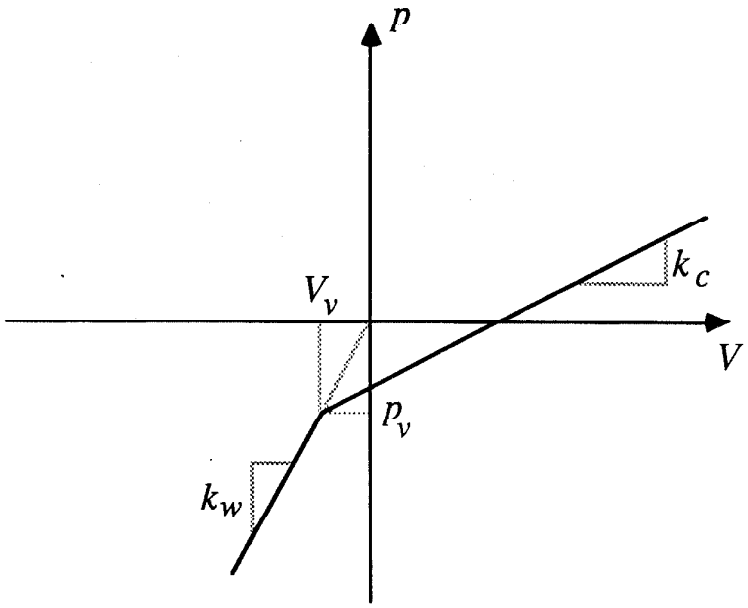

Figure 3.1. The bilinear model used for cavitation. p = absolute pressure; V = volume strain.

Following fig. 3.1, the bilinear model can be mathematically described by

$$p^e = \begin{cases} k_w V^e & \text{if} \quad V^e \leq p_v/k_w; \\ p_v + (V^e - V_v)k_c & \text{otherwise,} \end{cases} \tag{3.1}$$

where p^e is the absolute water pressure at a point in element e; V^e is the corresponding volume strain given by

$$V^e = B_{vs}\{U^e\}, \tag{3.2}$$

where B_{vs} is the nodal displacement-volume strain transformation matrix; $\{U^e\}$ is the vector of relative nodal displacements of element e; and p_v is the water vapor pressure (-0.34 psi at 70^o).

Reforming the vector of the stiffness forces, $\mathbf{P}^k$ in equation (2.1), is done at the element level. At every iteration, the volume strain V^e is calculated at the integration point of each element. The corresponding pressures are then calculated according to the constitutive relation (3.1). For every element, the vector of the stiffness forces is computed as

$$P^e = \int_{v^e} B_{vs}^T p^e dv, \tag{3.3}$$

and then assembled to the global array $\mathbf{P}^k$.

The element tangent stiffness matrix as defined by equations (2.11) and (2.12) depends on the tangent water compressibility of the element, k_T. Once an element cavitates, its tangent water compressibility drops from k_w to k_c and its tangent stiffness matrix changes accordingly. The computer code stores the global linear stiffness matrix, $\mathbf{K}$, computed with $k_T = k_w$ for every element. At each iteration k, the current global tangent stiffness matrix, $\mathbf{K}_T^k$, is formed by adjusting $\mathbf{K}$ to account for currently cavitated elements. The adjustment for element e is given by

$$\Delta K^e = -k_w(1 - k_c/k_w)K_{vs}^e, \tag{3.4}$$

where K^e_{vs} is given by equation (2.11a). The adjustments for cavitated elements are then assembled into $\mathbf{K}$. In the special case of $k_c = 0$, the adjustment for element e is simply $-K^e_{vs}$. It should be noted that K^e_i and K^e_3 remain untouched throughout the cavitation process.

This numerical treatment of water cavitation is analogous to the smeared cracking approach for introducing cracks in solid media.

3.5 Numerical Studies

This section presents preliminary numerical studies to evaluate qualitatively the present numerical model. The basic problem considered herein consists of a rigid vertical wall that impounds a body of water occupying an infinite reservoir of constant depth (fig. 3.2.a). The reservoir floor is assumed rigid, and the rigid wall moves with horizontal acceleration consisting of a double pulse (fig. 3.2.b). The excitation is designed to induce reservoir cavitation followed later by closure of the cavitated region. The water compressibility k_w was set equal to 3×10^5 psi, the water unit weight $\rho_w g$ to 62.4 lb/ft^3, the vapor pressure p_v to -0.34 psi, the compressibility of cavitated regions k_c to 0.0, and the atmospheric pressure p_{atm} to -14.7 psi. It was desired to have zero numerical damping in this study; hence, the integration parameters β, γ and α_B were set equal to 1/4, 1/2 and zero, respectively.

In the finite element discretization, a length of the reservoir equal to the water depth is meshed. The nonreflecting boundary described in Chapter 2 is placed at the far end. The mesh uses four node square elements with a single integration point at the center. Three different element sizes were employed in this study as shown in fig. 3.3. The size of the time step, Δt, used with each mesh was chosen small enough to capture all possible features of the numerical behavior.

Considering the bilinear constitutive model, the water volume strain, V^e, is, in general, a more informative quantity than the water absolute pressure, p^e. Hence, the former is preferred over the latter as the representative response

quantity of the water. Note that on the compression side, the volume strain is proportional to the pressure.

Fig. 3.4 displays the obtained time histories of the volume strain, V^e, at the center points of all elements along the moving boundary. These results pertain to mesh a in fig. 3.3. The corresponding responses assuming linear behavior (no cavitation) are shown by dashed lines. It can be seen that cavitated elements experience larger expansions and undergo high frequency oscillations after closure of the cavitated region. The period of oscillation was observed to be about 0.05 sec which compares to the free vibration period of a single element in its volume mode of 0.03 sec ($\pi l_e \sqrt{\frac{\rho_w}{2k_w}}$ with element length l_e = 62.5 ft). Additional analyses of the finer meshes of figs. 3.3 b and c (results not shown) showed that while the amplitude of the high frequency oscillation did not reduce, the vibration period decreased nearly linearly with element size. Thus, these oscillations are judged to be spurious, and, to minimize their participation, an internal damping mechanism in the form

$$C^e = b_w \, K^e_{vs} \tag{3.5}$$

is added, similar to that used in [3]. The damping is calculated at the element level, then assembled to the water damping matrix. Choice of the damping constant, b_w, should be made to dissipate most of the spurious components without significantly affecting the "true" response.

Results of fig. 3.4 were recomputed by a second analysis (fig. 3.5.a) where damping from (3.5) has been provided in the amount of 1 % critical in the fundamental pressure mode of the water (period = 0.42 sec). From fig. 3.5.a, this amount of damping eliminates enough of the spurious high frequency components to reveal the nature of the impact following closure of the initial cavitation (elements 1, 2 and 3). Results from the finer meshes using the same amount of damping (i.e., the same b_w) appear in figs. 3.5.b and c, and it is evident that the latter represents a converged solution at the level of damping employed.

Note that the spurious components are more effectively eliminated from the finer meshes because of the use of stiffness-proportional damping. This suggests that these components can be removed from finer and finer meshes by using successively less and less damping, approaching the zero damped case in the limit. While this has not been attempted because of the expense, it is believed that such a result would differ little from the responses in fig. 3.5.c because of the small amount of damping employed there.

For the analyses performed with damping, fig. 3.6 depicts the regions of cavitation at instants of time during the initial cavitation and a later one. Good agreement is obtained among the three meshes. The region of initial cavitation is elongated along the moving boundary while the second is thinner and extends further into the reservoir. This latter shape may be influenced by pressure wave reflections off the free-surface and reservoir floor.

The stiffness-proportional damping used here to eliminate the spurious high frequency components creates internal damping forces that act to constrain a cavitated element's expansion and which also pull on neighboring elements. Even with small damping, such forces may become significant if the volume strain rates are high. A result may be to exaggerate the extents of cavitation somewhat, and the zones in fig. 3.6 may reflect this. On the other hand, too little damping may result in very unrealistic extents of cavitation because of the spurious oscillations.

It is noteworthy that energy radiation through the transmitting boundary at the upstream end of the reservoir does not provide adequate means of dissipation of the spurious components. Also, incorporation of some amount of numerical damping ($\alpha_B = -0.2, \gamma = 0.7$, and $\beta = 0.36$) had little effect.

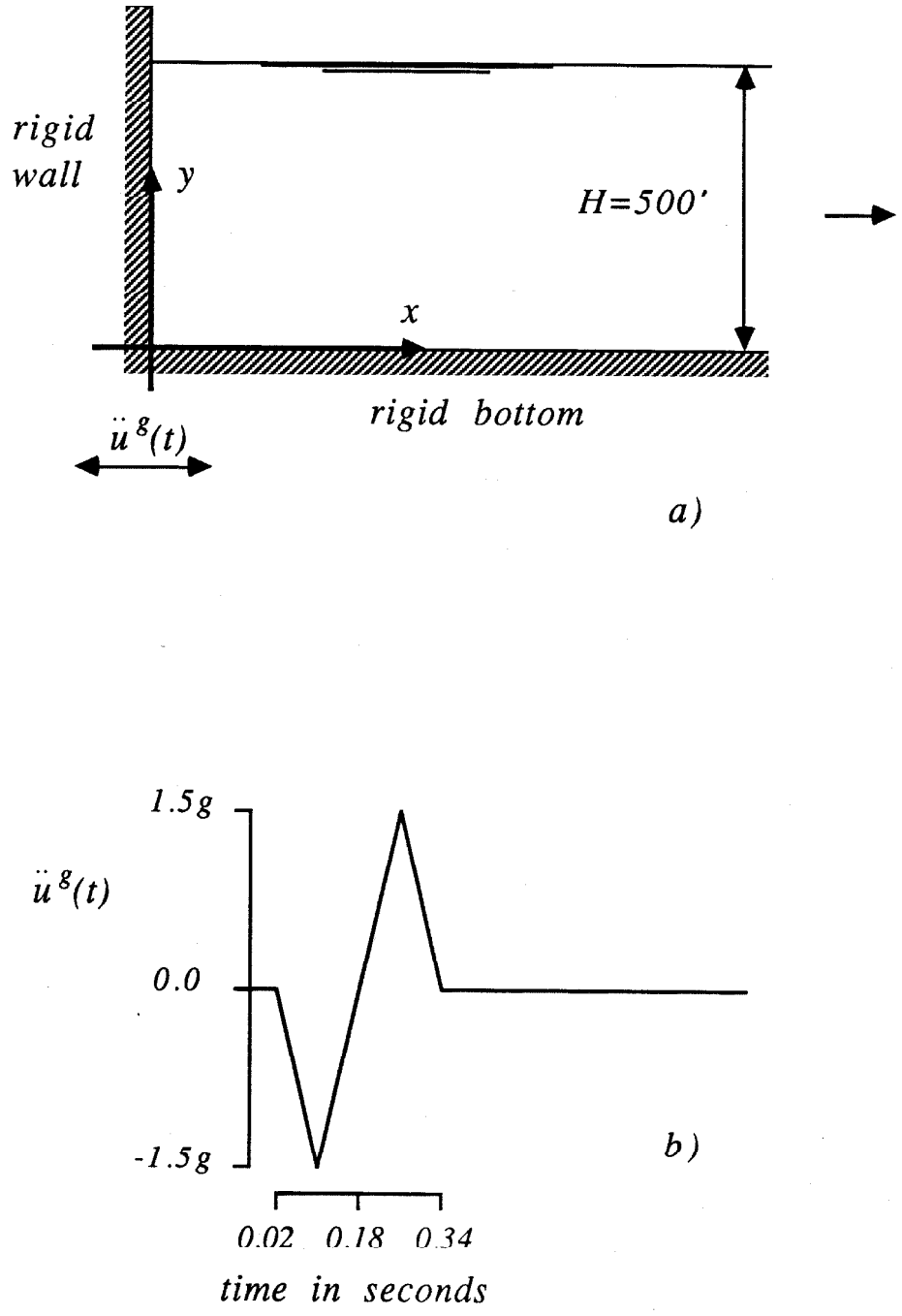

Figure 3.2. The test problem showing the water-reservoir system and the applied excitation.

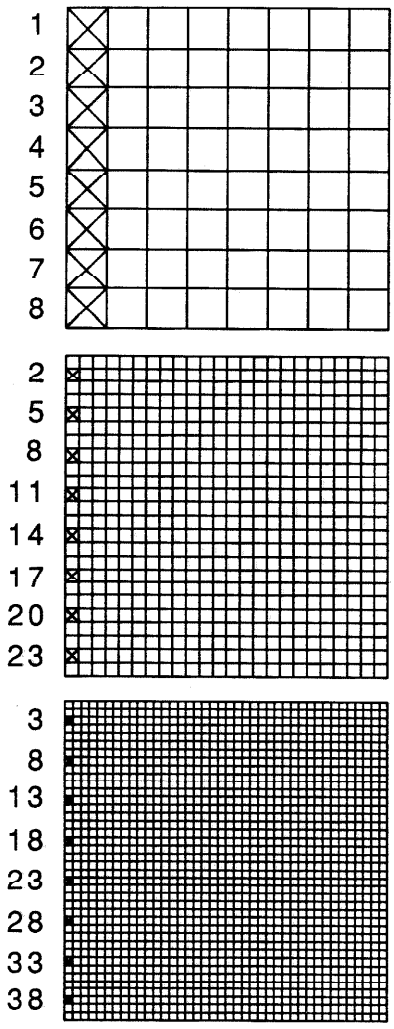

a) 64 elements
$\Delta t = 0.005$ sec.

b) 576 elements
$\Delta t = 0.002$ sec.

c) 1600 elements
$\Delta t = 0.001$ sec.

Figure 3.3. Finite element discretizations of the water.

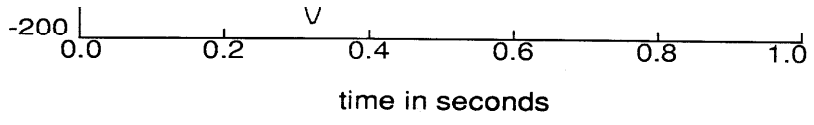

Figure 3.4. Volume strain time histories of mesh a (test problem). Solid line - cavitation included, no damping. Dashed line - linear response, no damping.

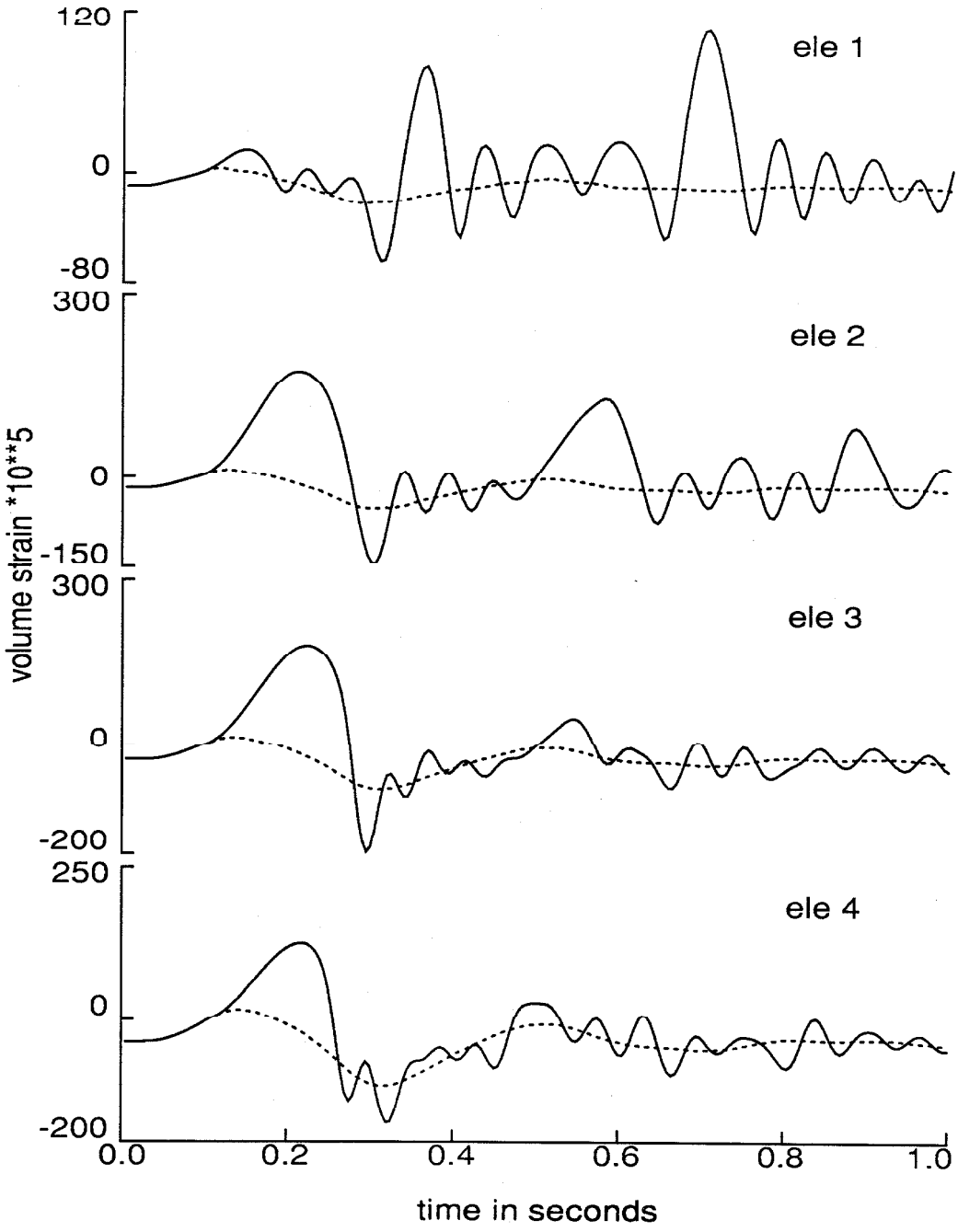

Figure 3.4. Volume strain time histories of mesh a (test problem). Solid line - cavitation included, no damping. Dashed line - linear response, no damping.

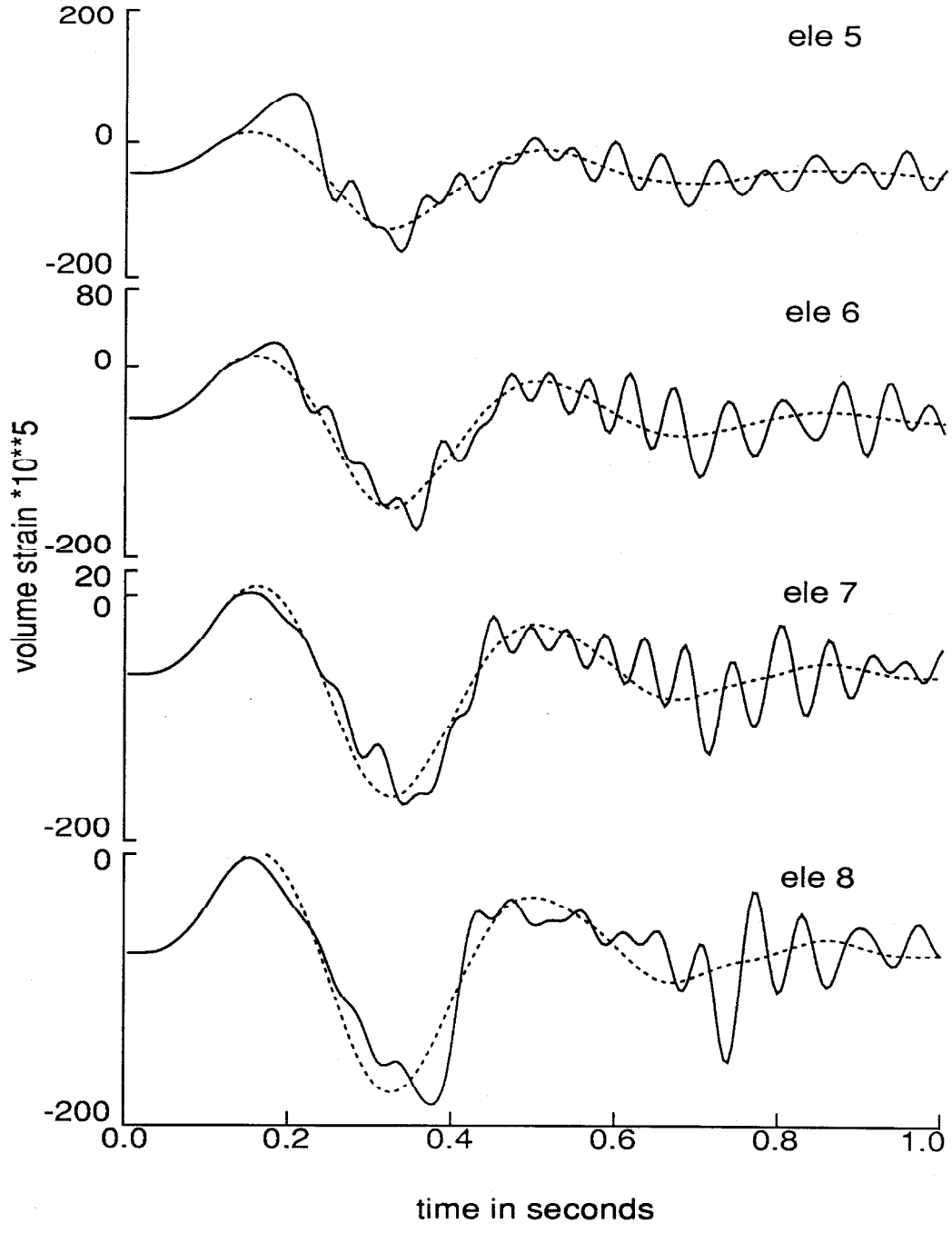

Figure 3.4. Continued.

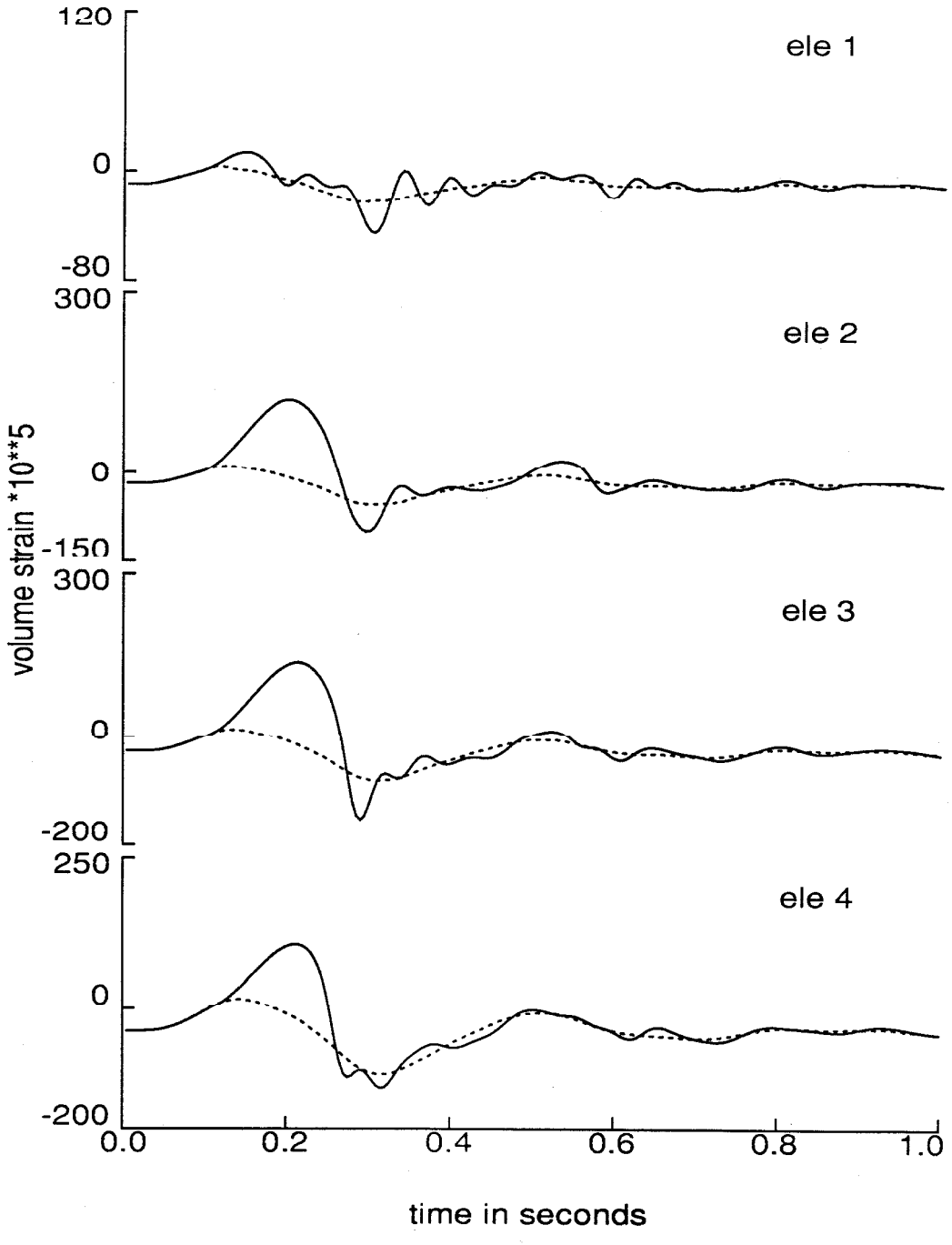

Figure 3.5.a. Volume strain time histories of mesh a (test Problem). Solid line - cavitation included, 1 % critical damping. Dashed line - linear response, no damping.

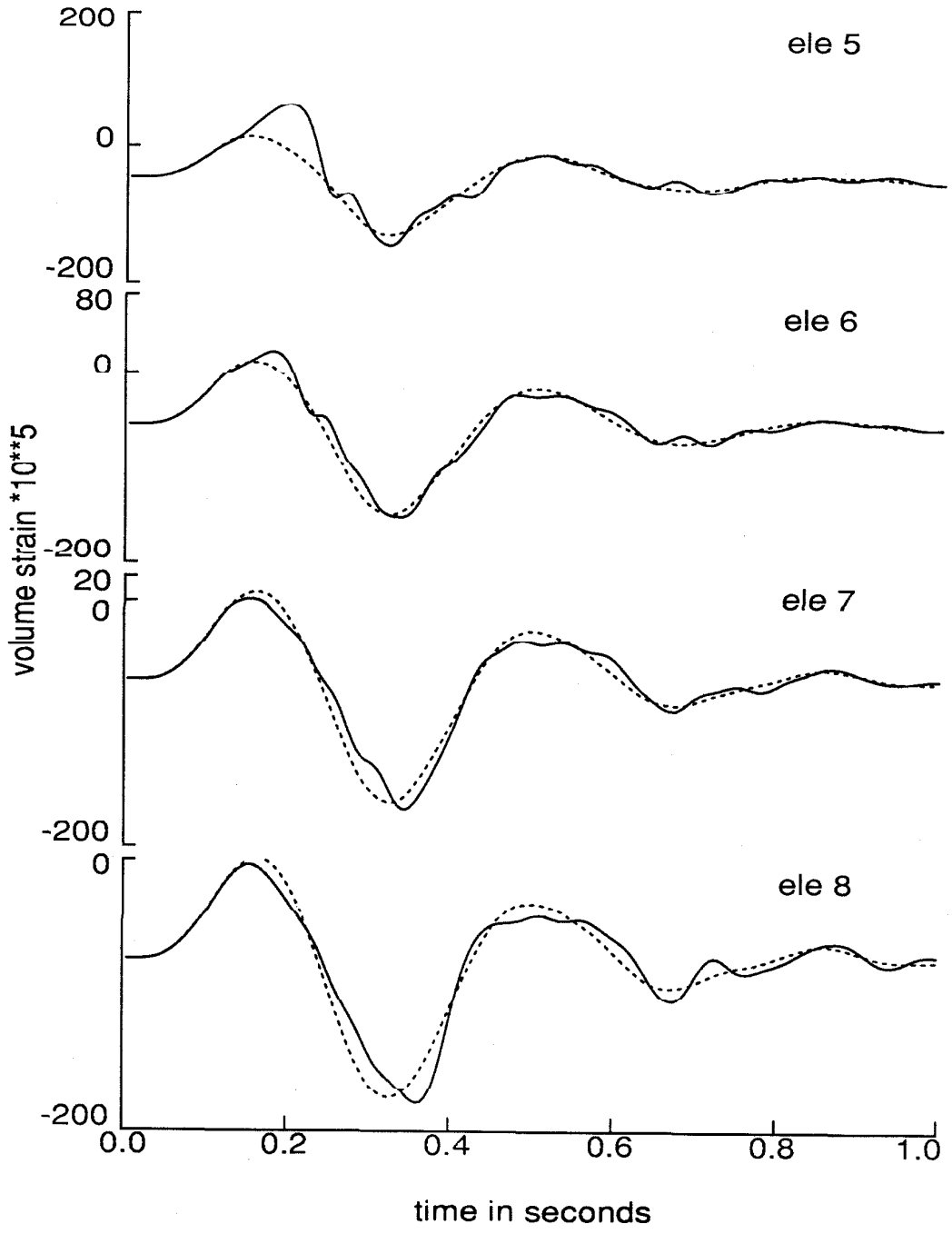

Figure 3.5.a. Continued.

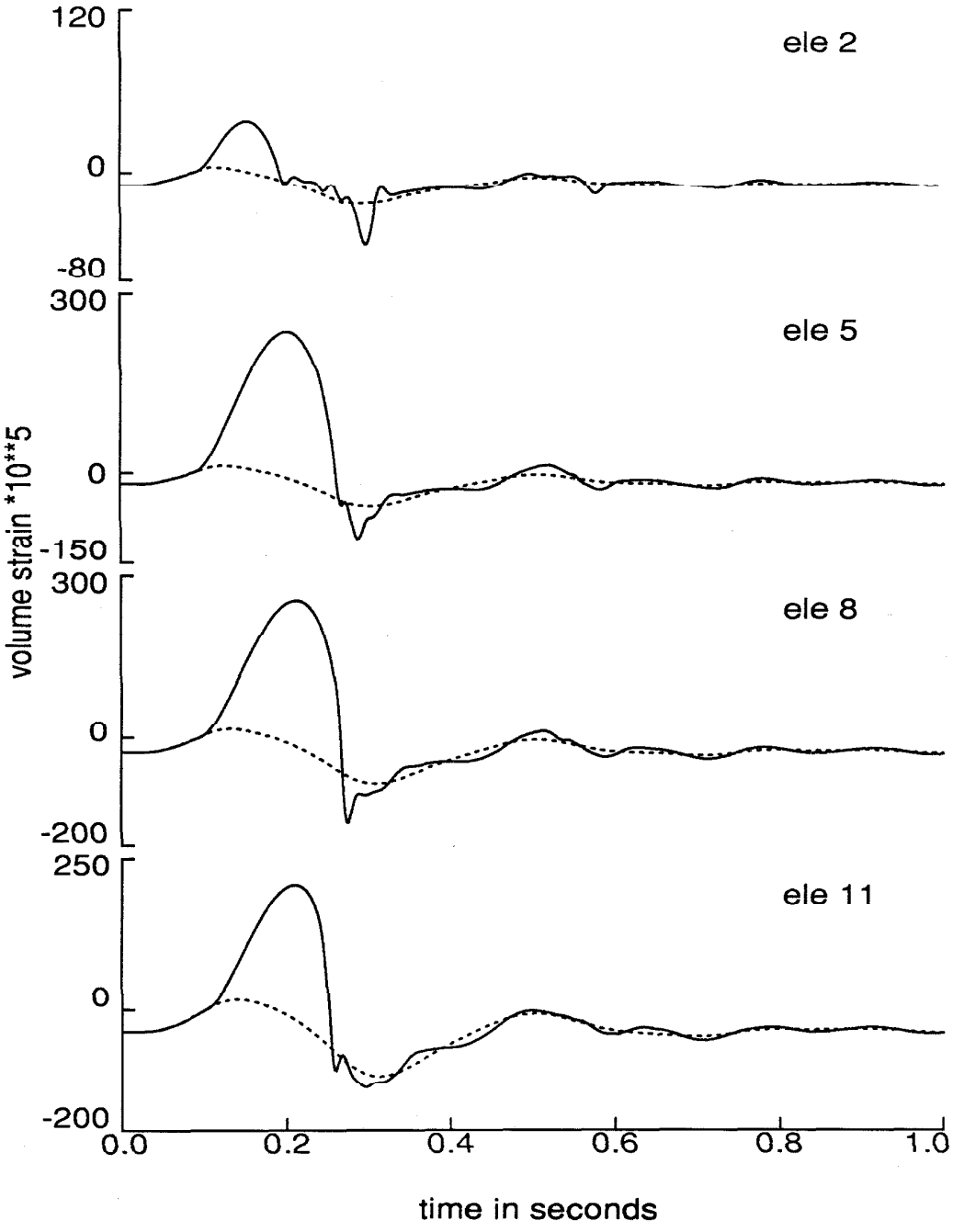

Figure 3.5.b. Volume strain time histories of mesh b (test problem). Solid line - cavitation included, 1 % critical damping. Dashed line - linear response, no damping.

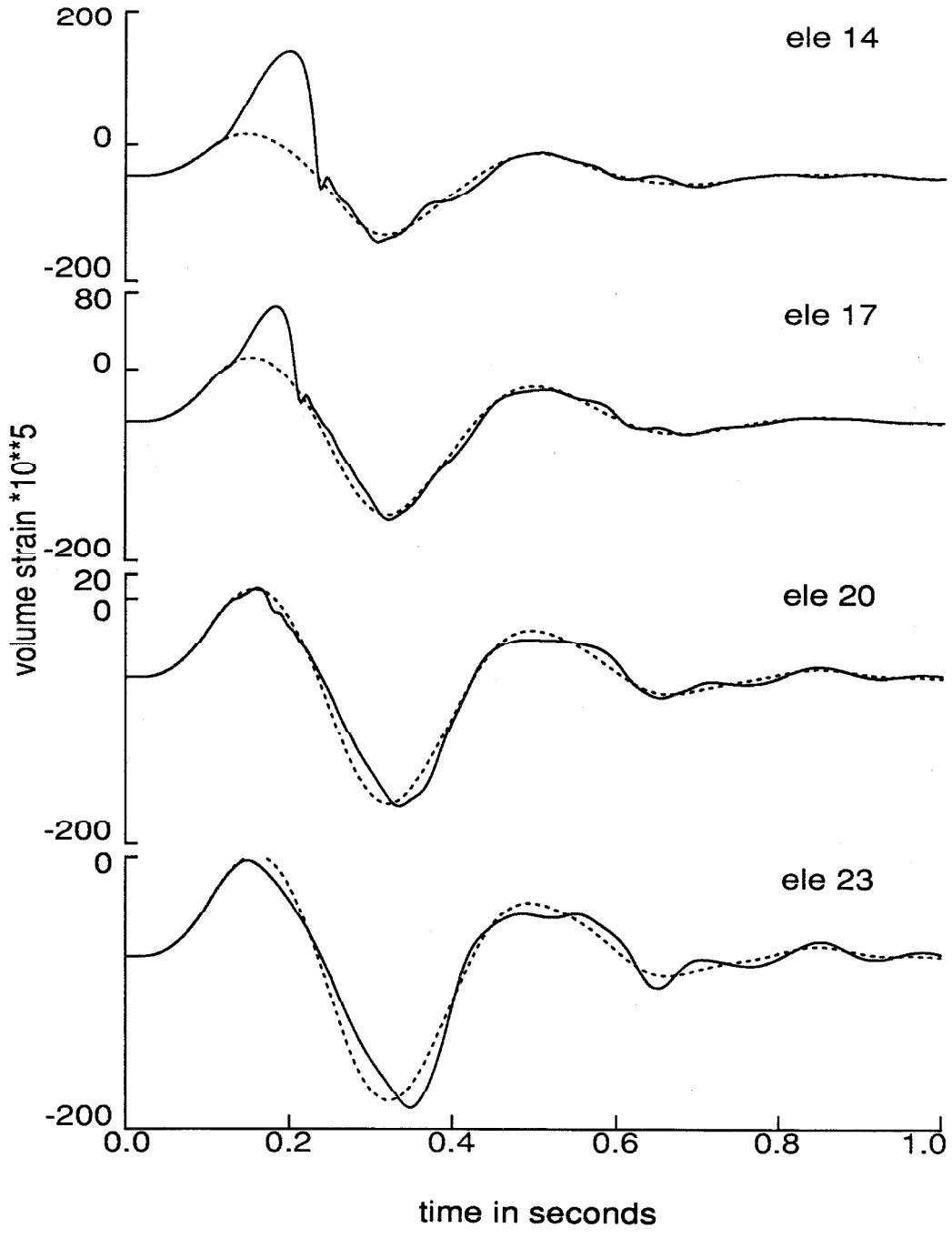

Figure 3.5.b. Continued.

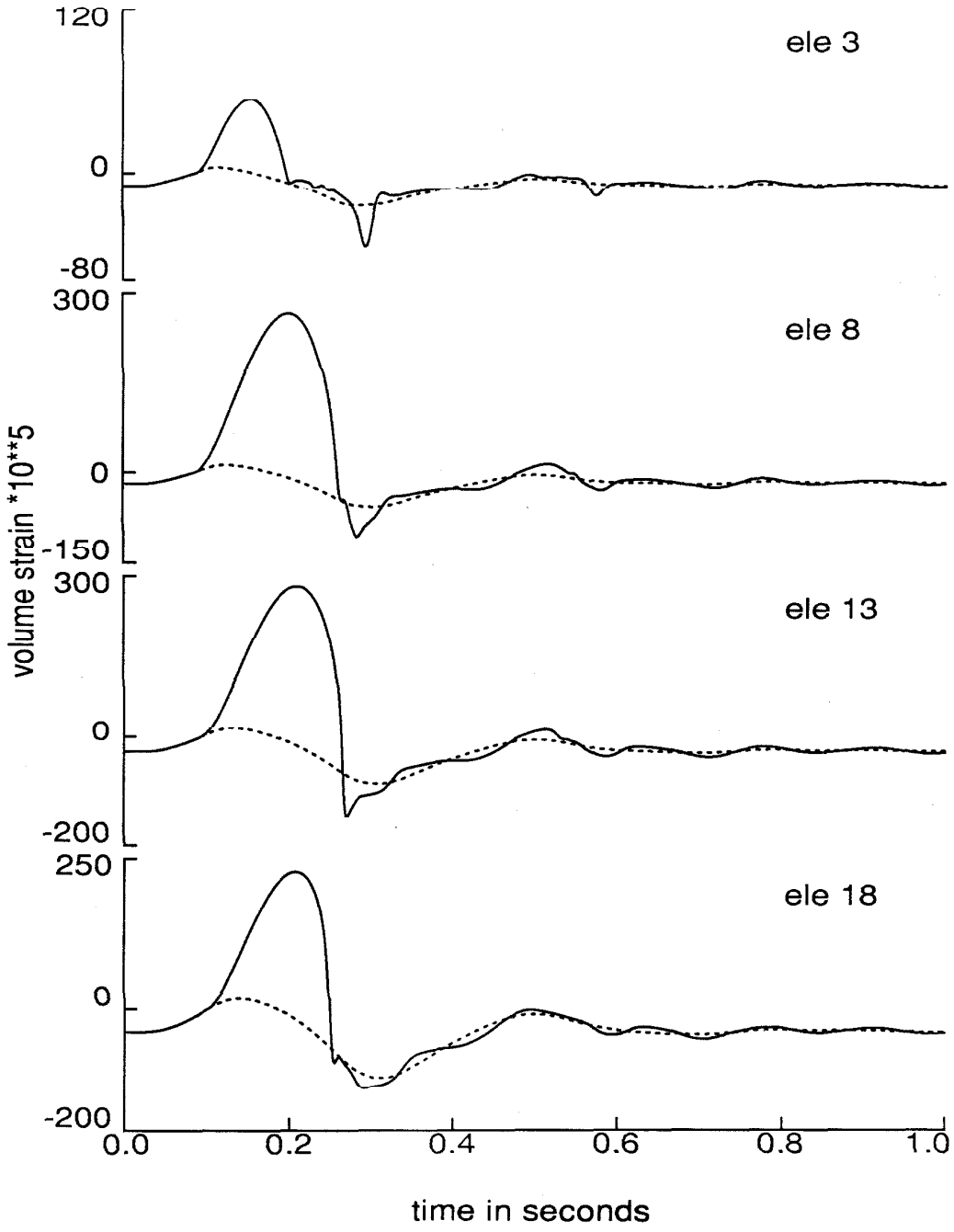

Figure 3.5.c. Volume strain time histories of mesh c (test problem). Solid line - cavitation included, 1 % critical damping. Dashed line - linear response, no damping.

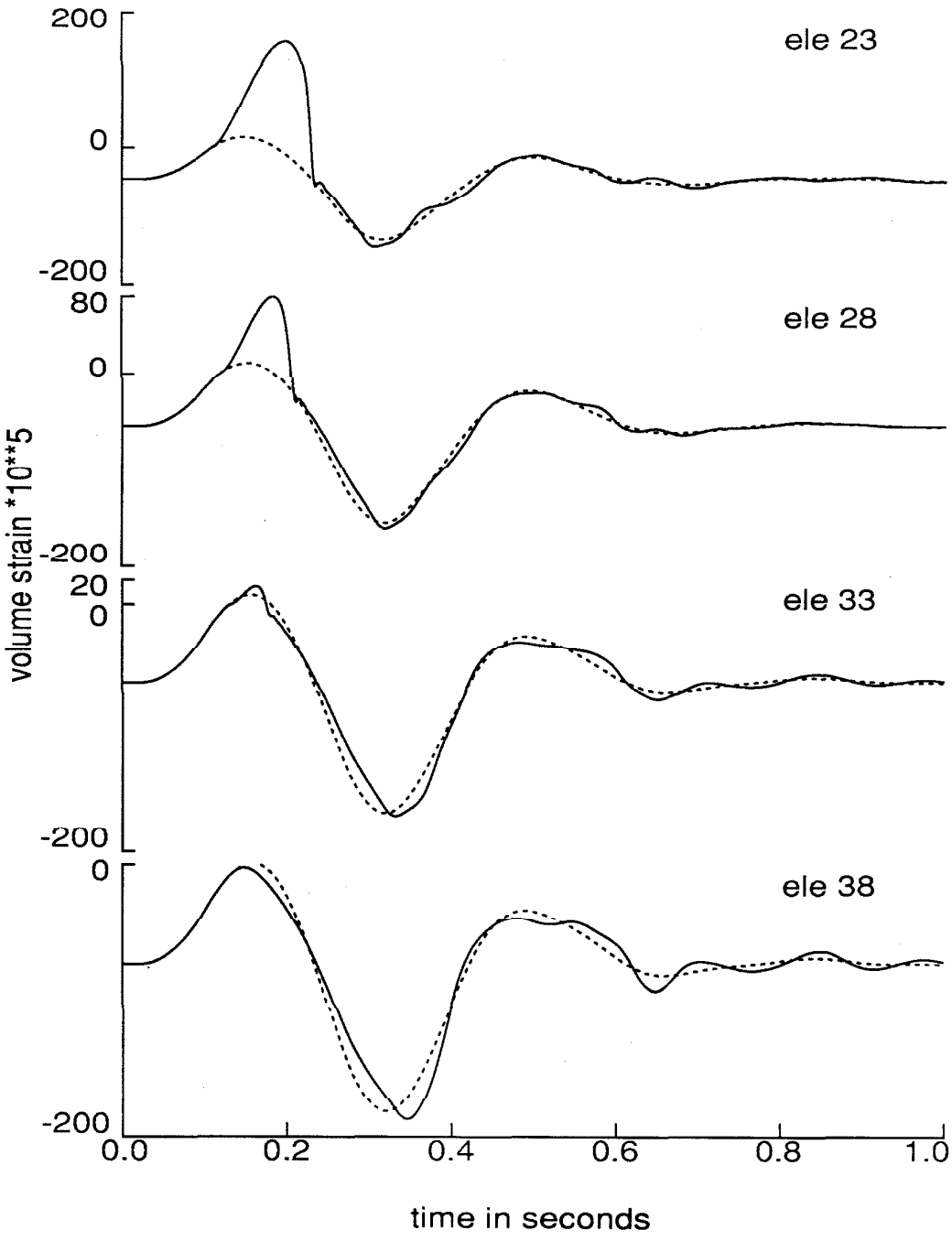

Figure 3.5.c. Continued.

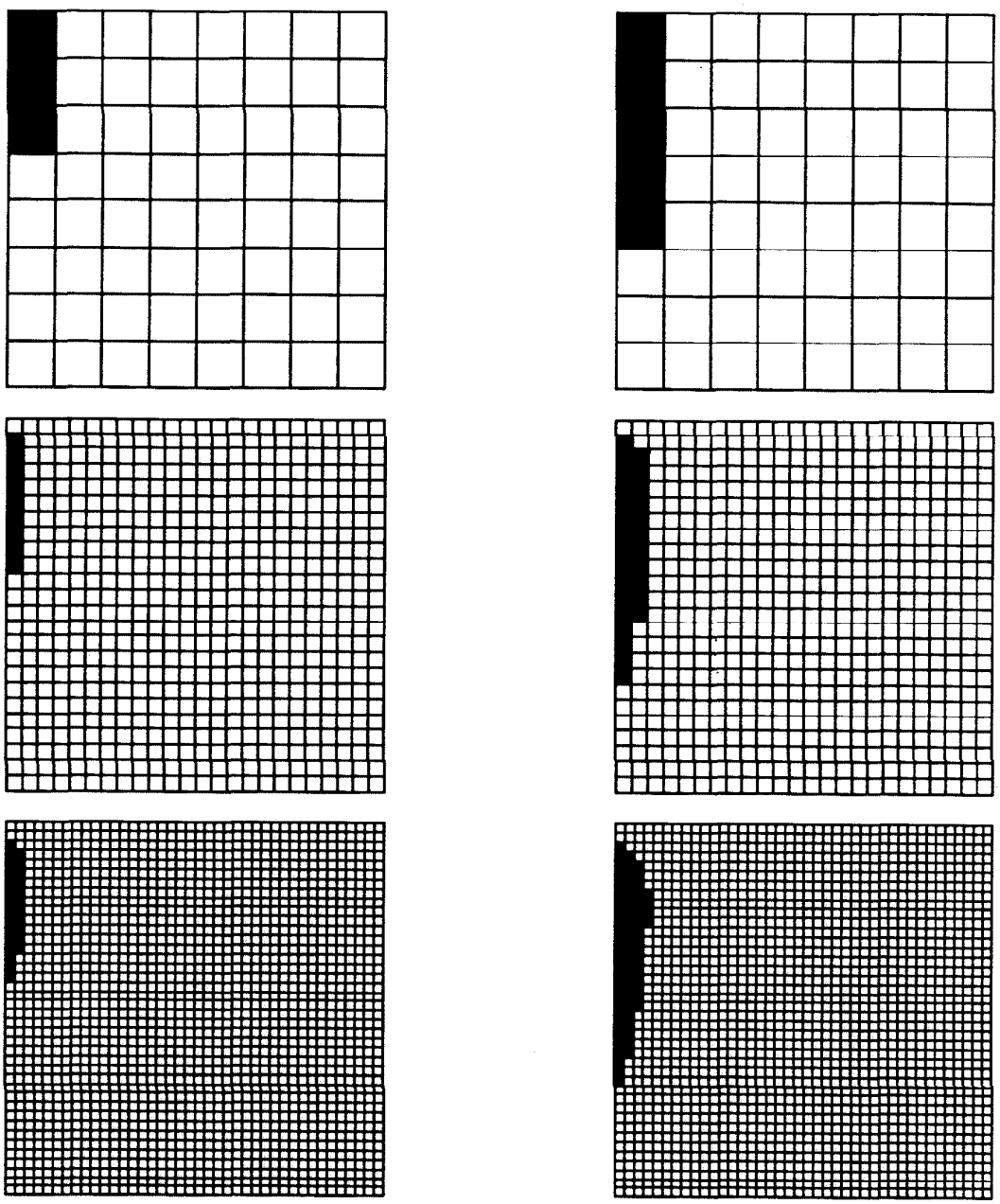

at 0.1 seconds

at 0.12 seconds

Figure 3.6. Cavitation patterns for the test problem at instants of time (with 1 % critical damping).

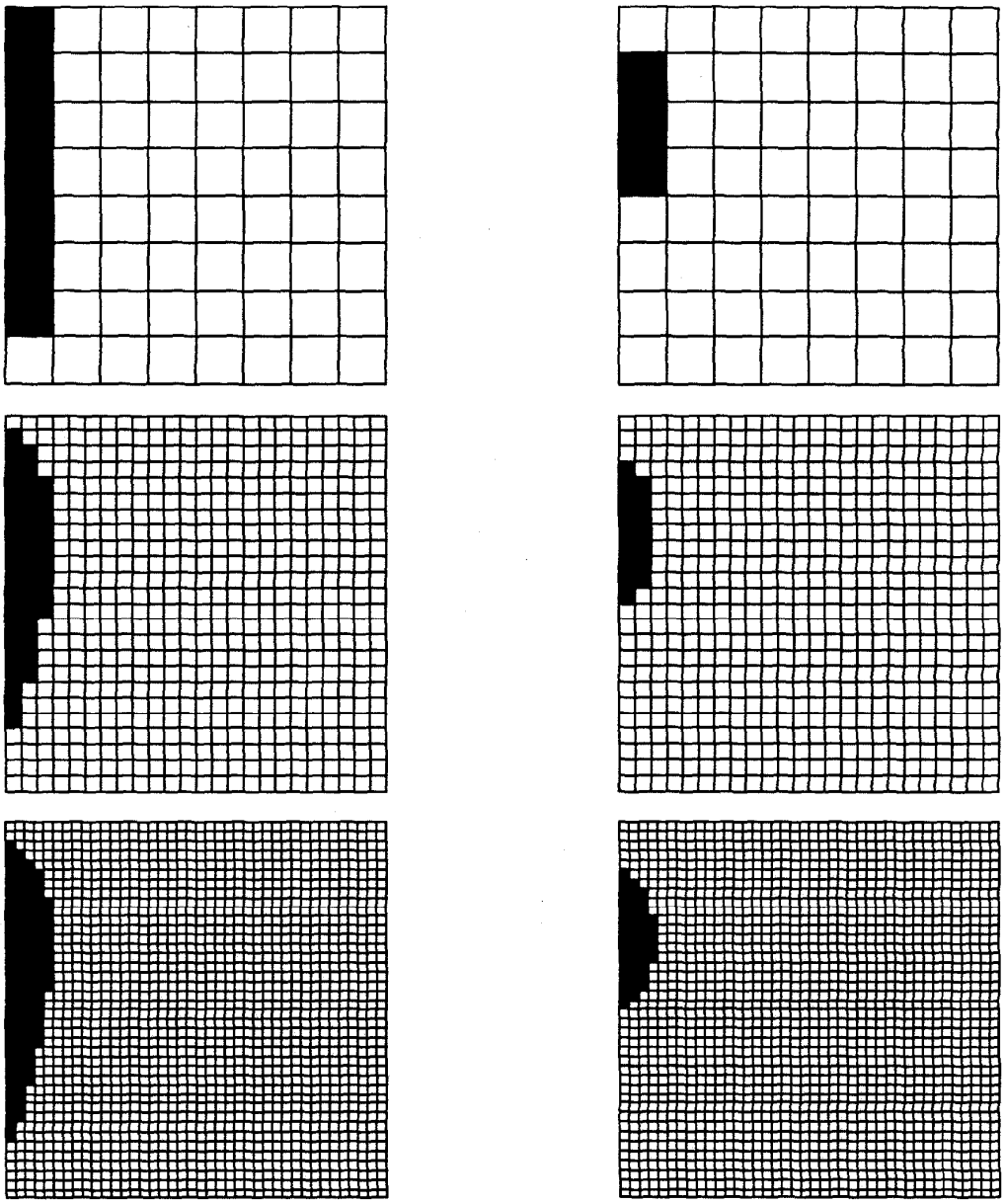

at 0.16 seconds

at 0.24 seconds

Figure 3.6. Continued.

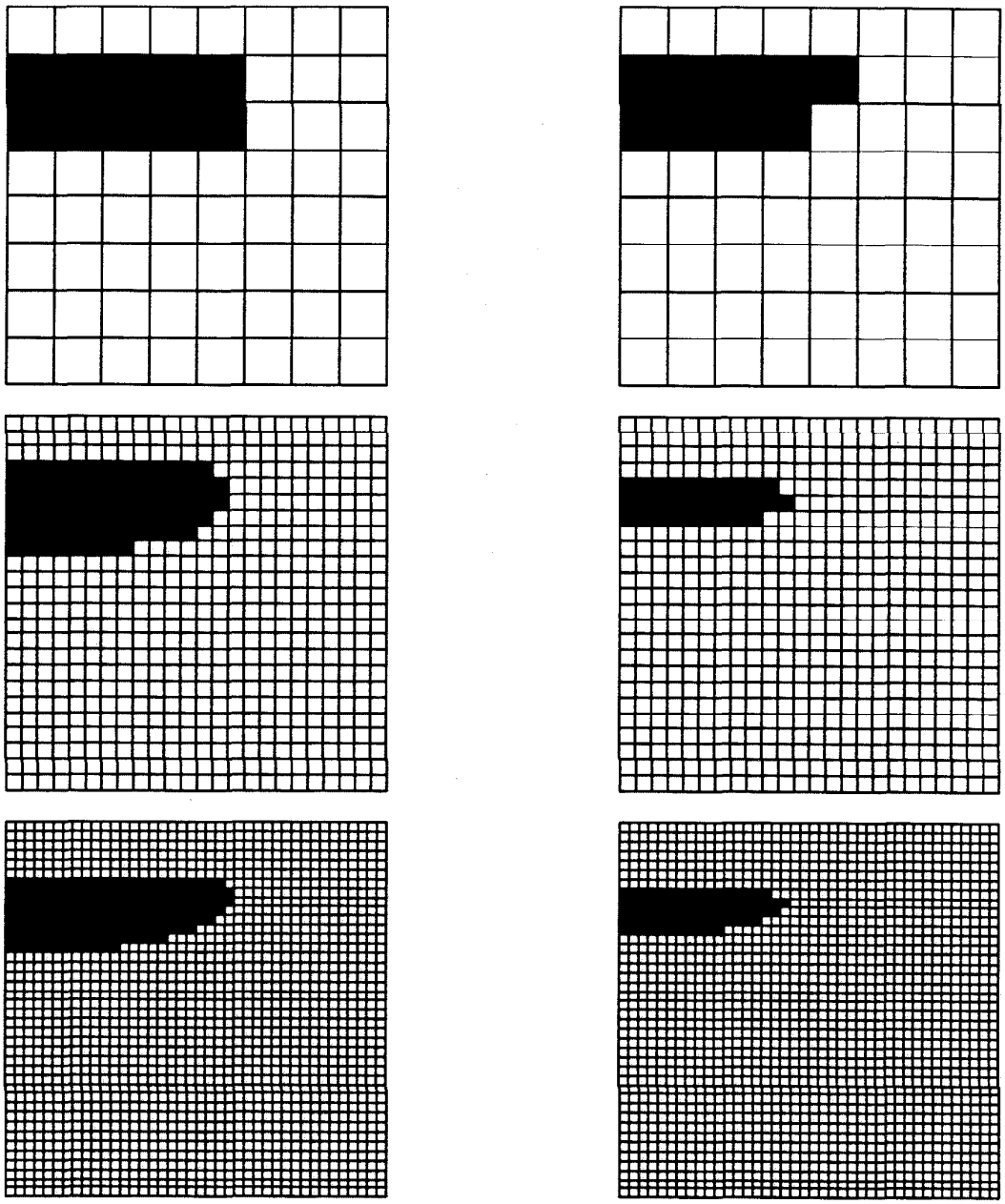

at 0.51 seconds

at 0.53 seconds

Figure 3.6. Continued.

3.6 Cavitation Effects on Dam Response

In this section, reservoir cavitation effects on the earthquake response of a concrete gravity dam are investigated. Nonlinear behavior is confined to water cavitation, while the dam is assumed to respond linearly as described in Chapter 2. Cases of cracked dams will be considered in Chapter 4.

A typical concrete gravity dam-water-foundation system represented by Pine Flat Dam is considered. The geometry and the finite element mesh used are shown in fig. 2.7, and the system parameters are the same as those in Section 2.4 with the water vapor pressure $p_v = -0.34$ psi, the tangent compressibility of cavitated regions $k_c = 0.0$, and 1 % critical damping in the fundamental pressure mode of the water (period = 0.32 sec). Simultaneous horizontal and vertical components of the El Centro earthquake ground motions (fig. 2.8) scaled amplitude-wise by 2 provided the excitation; the unscaled level of excitation is almost enough to trigger water cavitation [4]. The integration parameters α_B, γ and β were set equal to -0.2, 0.7 and 0.36, respectively.

Results of the analysis appear in figs. 3.7 to 3.11; results of the linear analysis (no cavitation, no internal damping in the water) are also shown. Fig. 3.7 presents time histories for volume strain in the water elements adjacent to the dam face. To provide more detail of the impact responses following cavitation closure, only the compressive strains (proportional to pressure) are shown in fig. 3.8. It is evident that the amount of stiffness-proportional damping employed for the water in the cavitation analysis (1 % of critical in the fundamental pressure mode) is insufficient to prevent the high frequency oscillations which are more severe than in the test problem discussed in the previous section. This is due to the stronger excitation (provided by the amplification in the upper part of the flexible dam) which produces greater cavitation (compare positive strains in figs. 3.5 and 3.7). The high frequency oscillations die out in a few cycles after which the response returns remarkably close to that of the linear case. The frequency of the impact response is too great to significantly influence the dam response,

and the tension cutoffs have little effect as well (figs. 3.9 and 3.10). As shown in fig. 3.11, the extent of cavitation is confined to the first and second columns of elements upstream of the dam. No isolated regions of cavitation occurred.

The high frequency oscillations noted in fig. 3.8 are similar to those of fig. 3.4 and are again judged to be spurious. Their removal was accomplished by increasing the stiffness-proportional damping in the water to 3 % of critical in the fundamental pressure mode; results appear in figs. 3.12 to 3.16 which parallel figs. 3.7 to 3.11. Again, the linear responses shown are for zero internal damping in the water. As with the 1 % damping case, effects of the cavitation on the dam response are small (figs. 3.14 and 3.15) and the extent of cavitation is similar (fig. 3.16). Indications are from the figures that the 3 % damping in the water is still low enough not to significantly affect the fundamental components of the system response.

Part of the success of the increased damping to eliminate the spurious oscillations lies in its reduction of the expansive strains associated with cavitation (compare positive strains in figs. 3.7 and 3.12) which, in turn, may have reduced the subsequent compressive impact, so its use may be viewed as somewhat dubious. However, because of the high cost of analyzing the finer meshes which are needed to reduce the damping requirement, the impact responses following cavitation closure seen in fig. 3.13 are the best available estimates for the "true" behavior. Each impact involves a single pressure spike of moderate amplitude and short duration and is too small to noticeably affect the dam response. The tension cutoffs would appear to have greater potential in this regard, but their effect is small as well.

The domination of the hydrodynamic response by high frequency components seen in [7] and [3] when cavitation was included is due, apparently, to their use of either no internal damping for the water or a much smaller amount than used here. Also, their more extensive spread of cavitation in the upstream direction can likely be attributed to the same feature. Incidentally, the measured pressure responses of [6] show impacts without any subsequent high frequency

oscillation and with only moderate increases, if any, in compressive pressures. This is in qualitative agreement with the results achieved here with stiffness-proportional damping in the water on the order of 1 % to 3 % of critical in the fundamental pressure mode. The final conclusion with regard to the effect of cavitation on the dam response is that it was found to be small in [7], [3], and here.

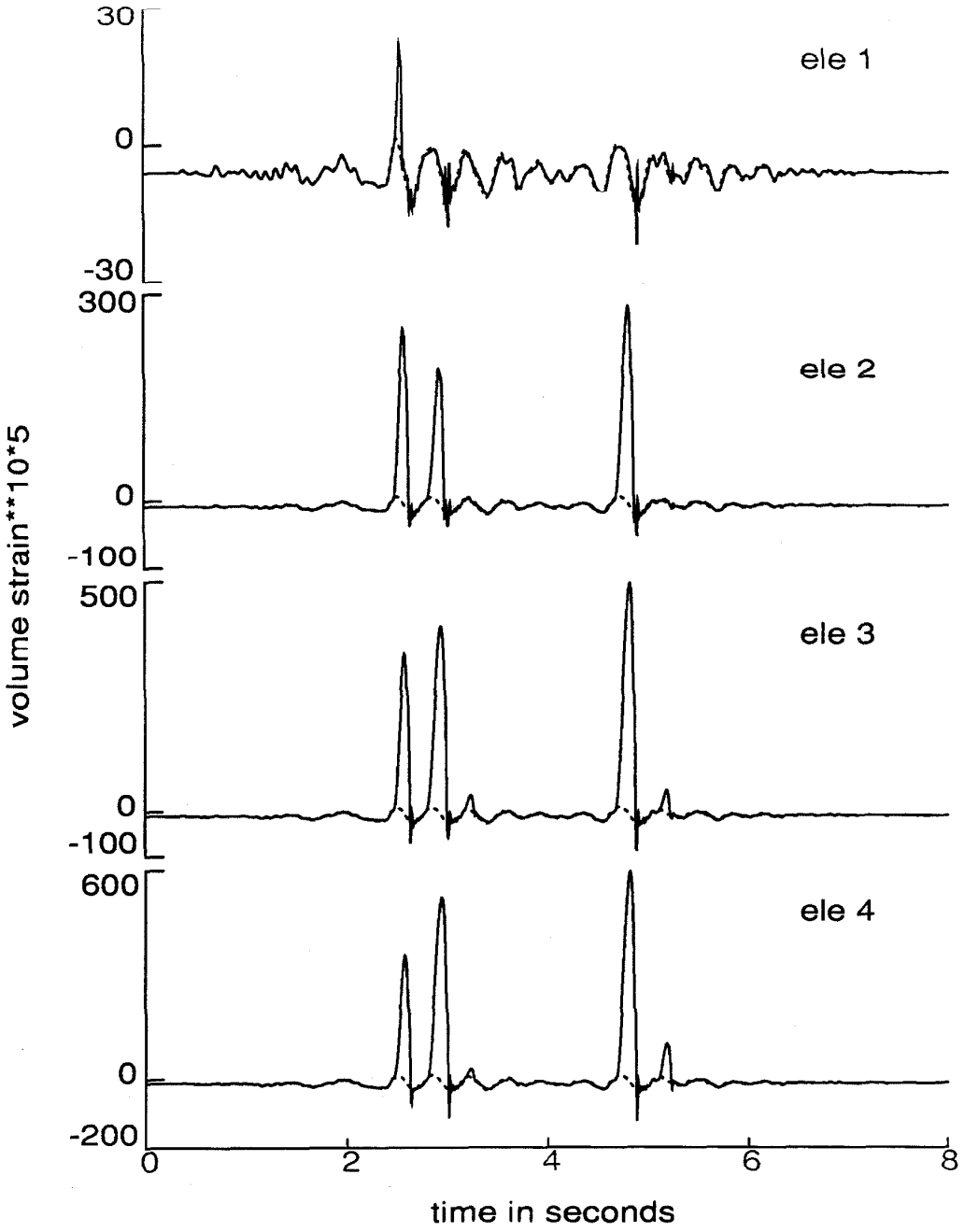

Figure 3.7. Volume strain time histories along the dam face (Pine Flat Dam analysis). Solid line - cavitation included, 1 % critical damping in the water. Dashed line - linear response, no added damping in the water.

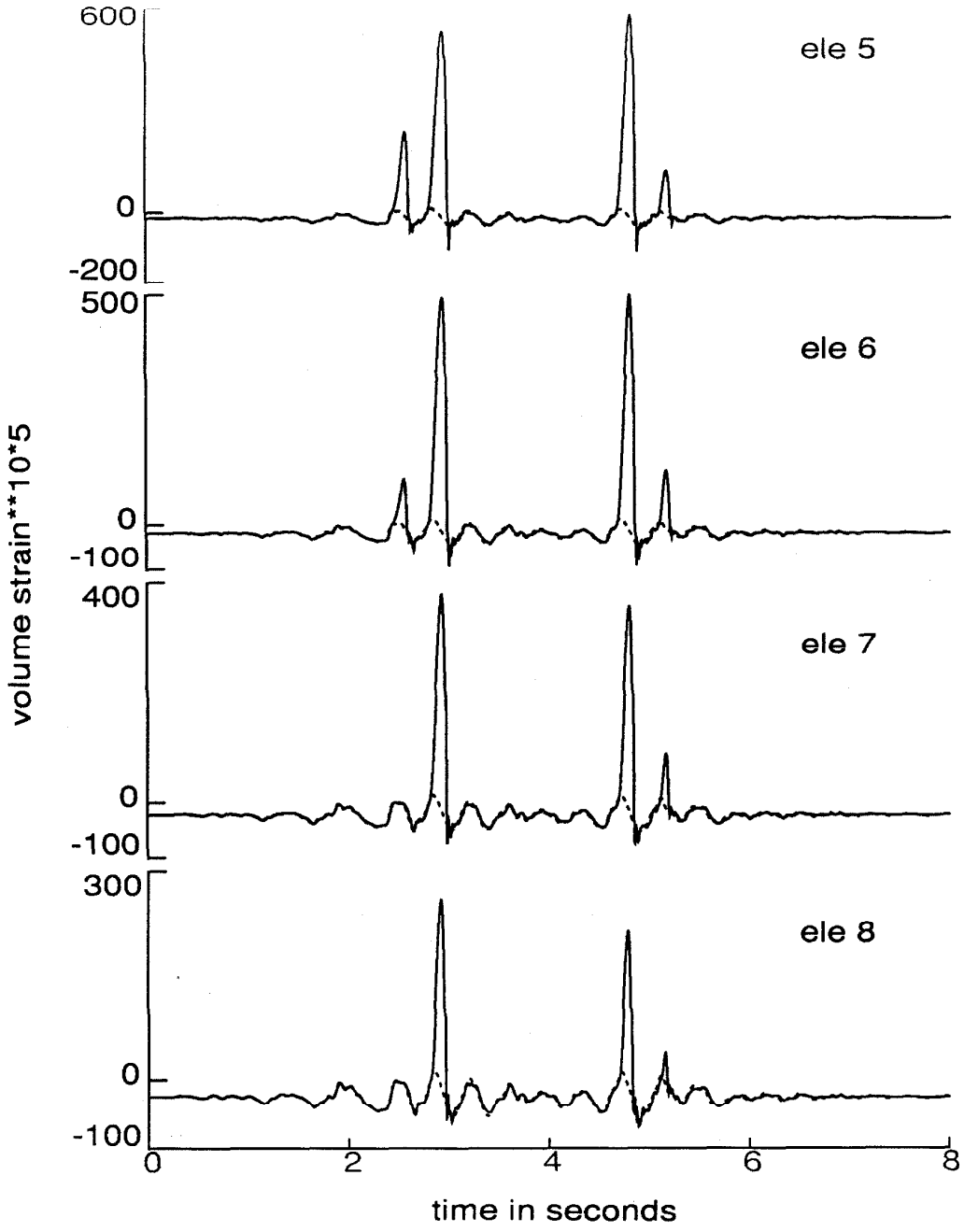

Figure 3.7. Continued.

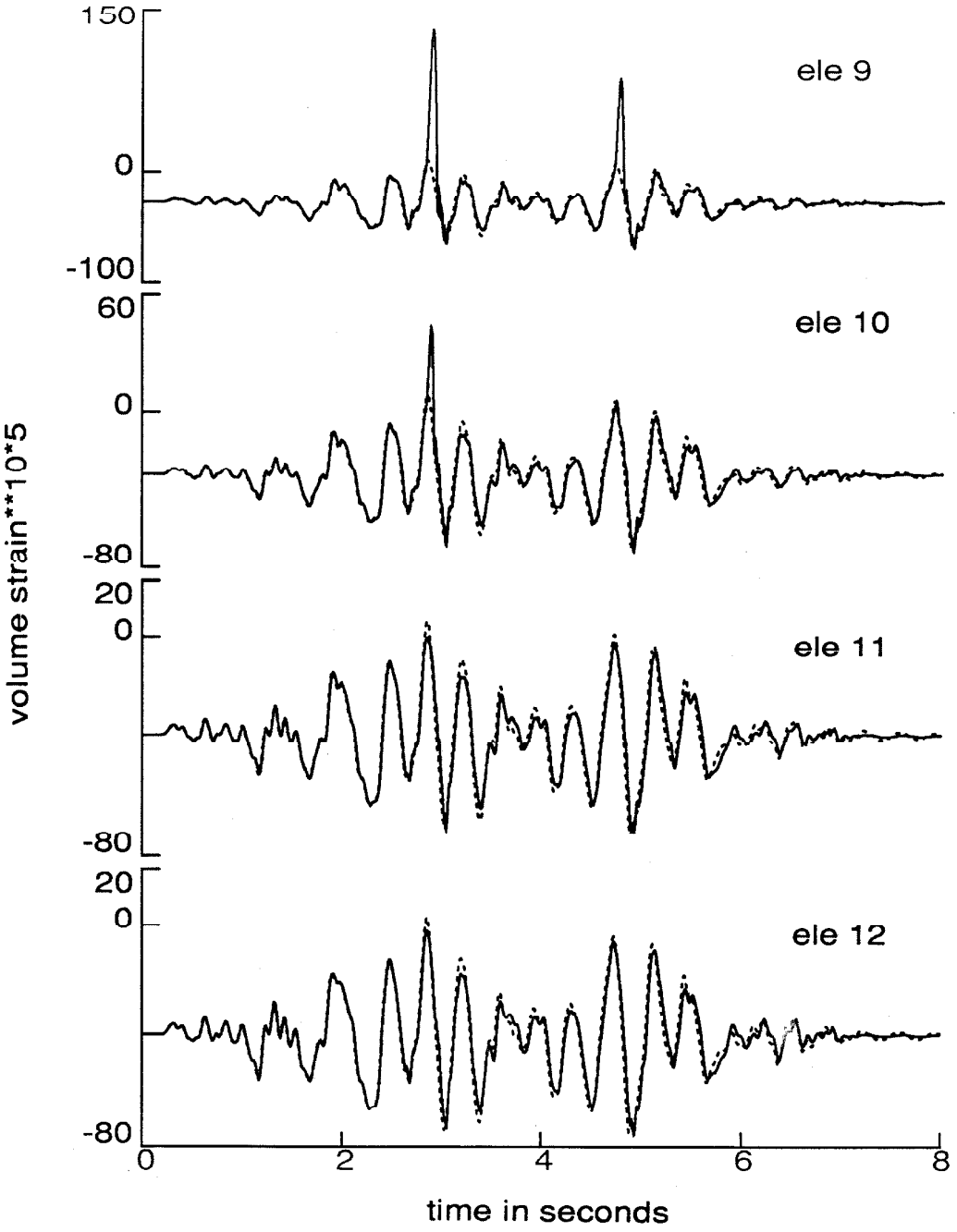

Figure 3.7. Continued.

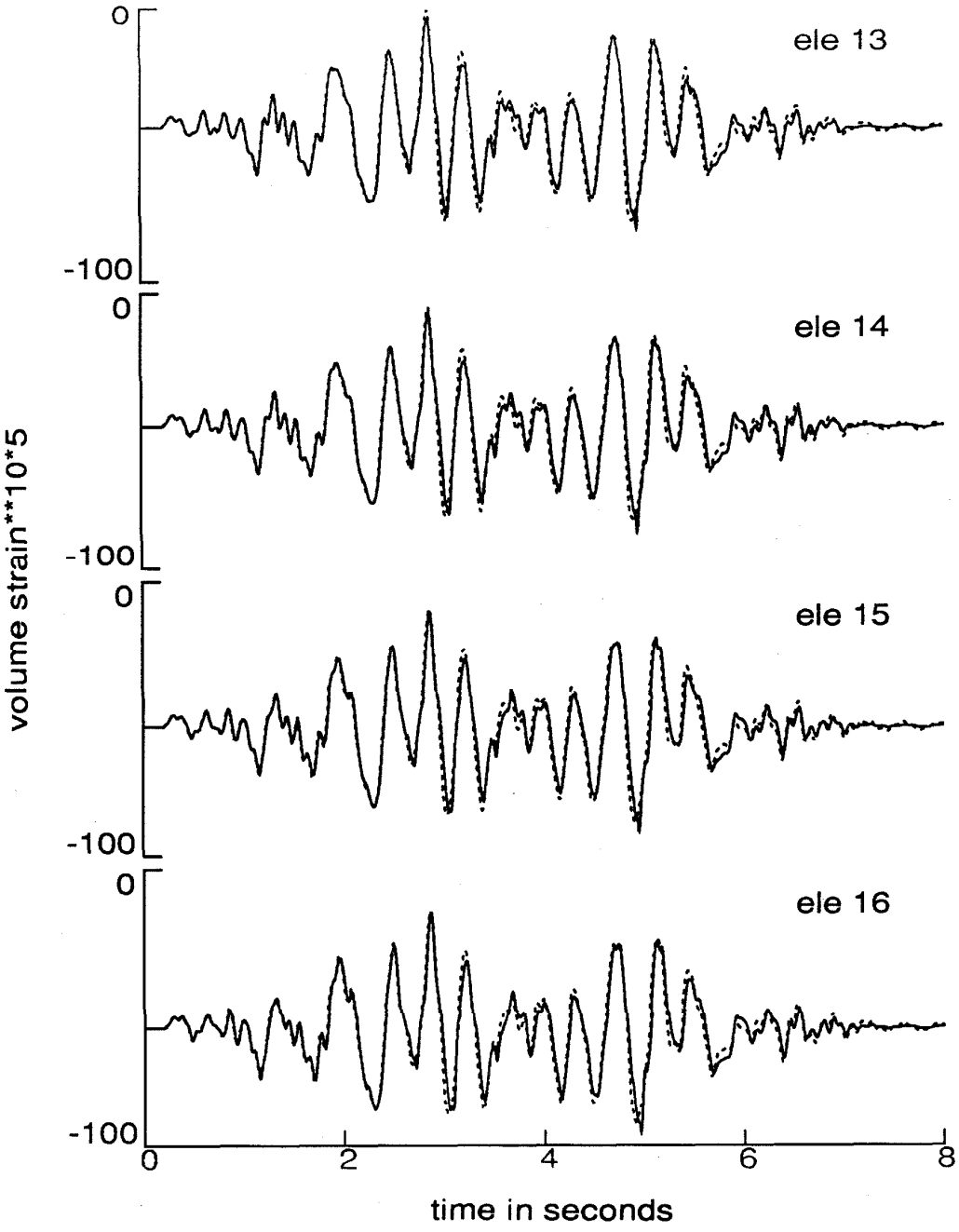

Figure 3.7. Continued.

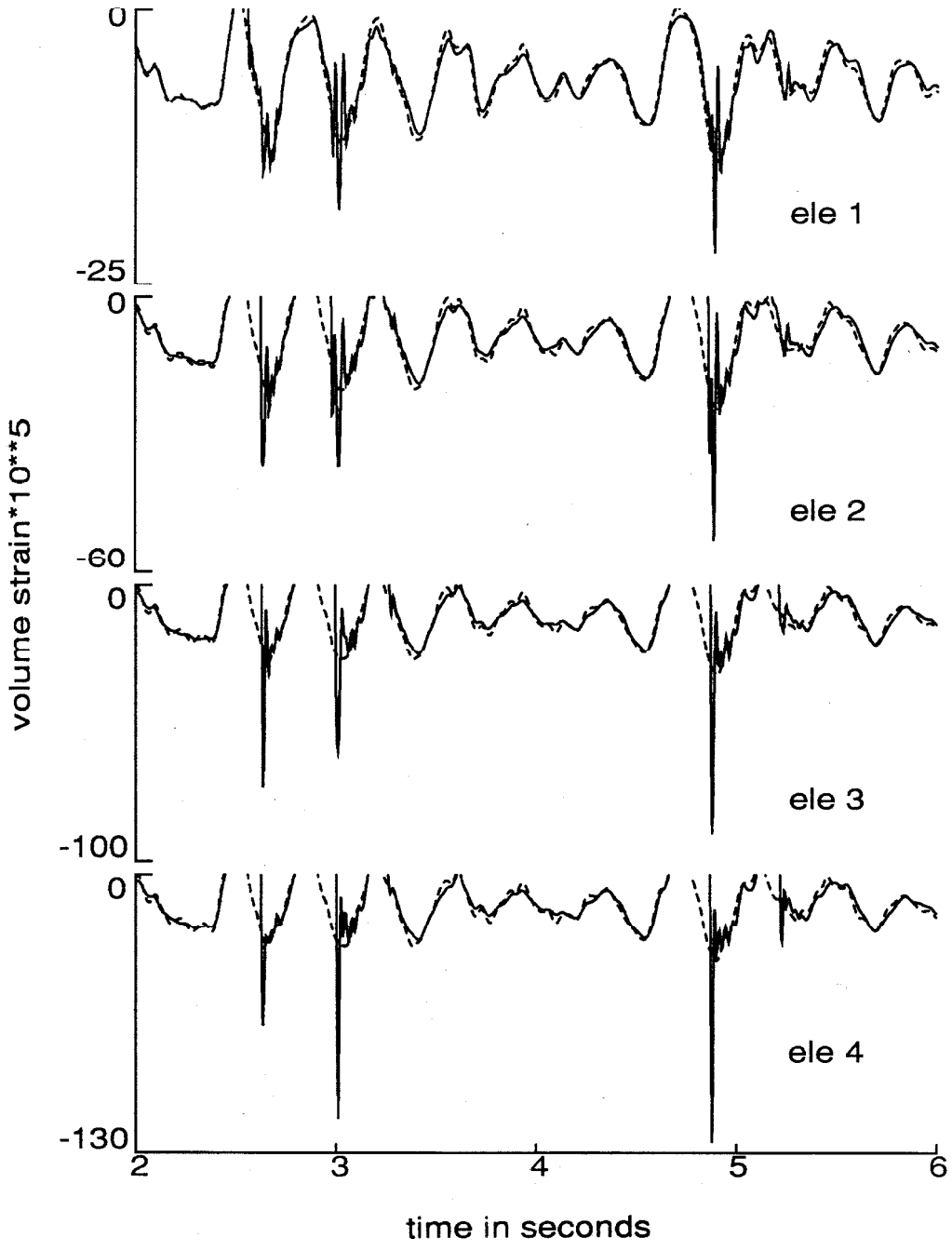

Figure 3.8. Detailed view of the compressive volume strains shown in fig. 3.7.

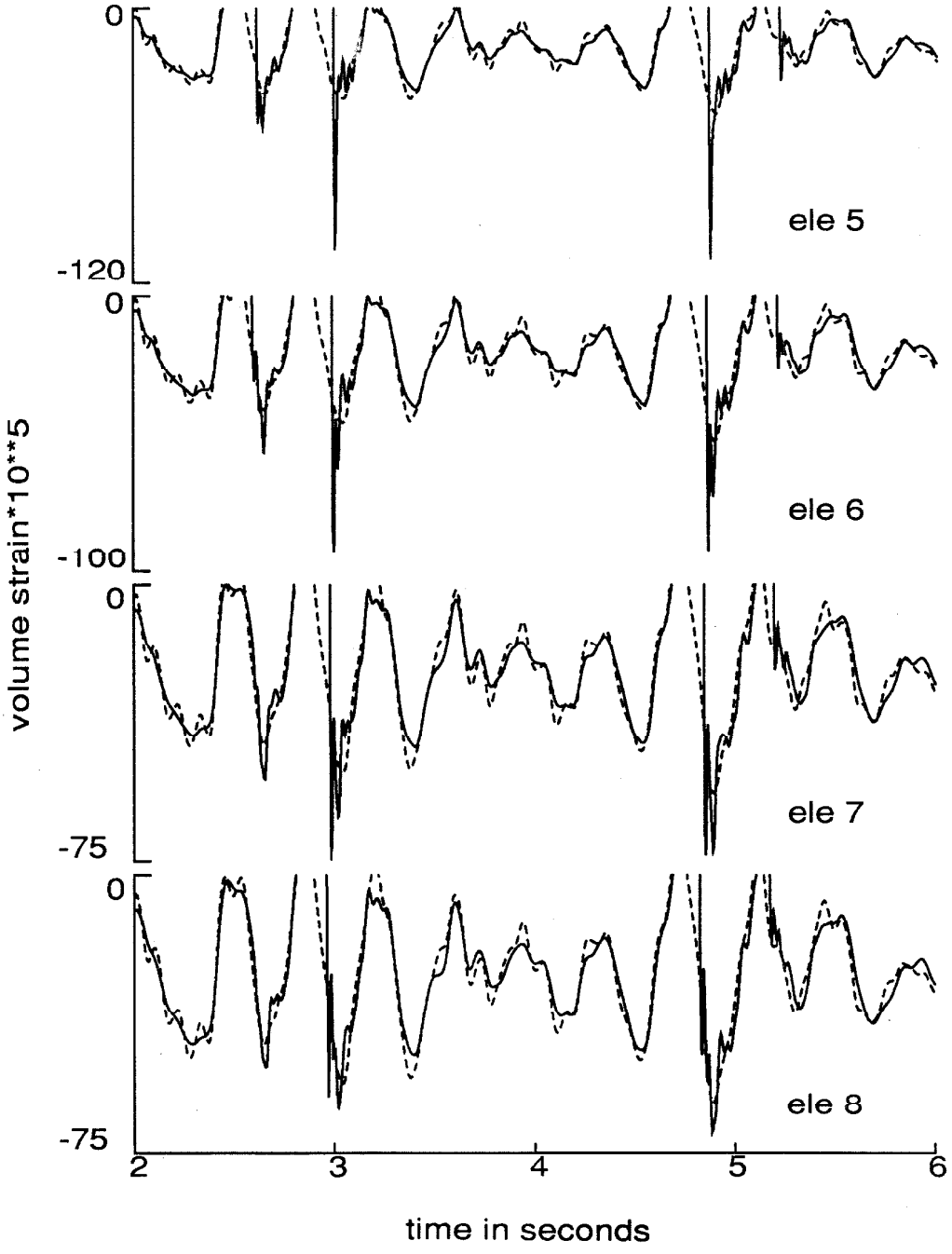

Figure 3.8. Continued.

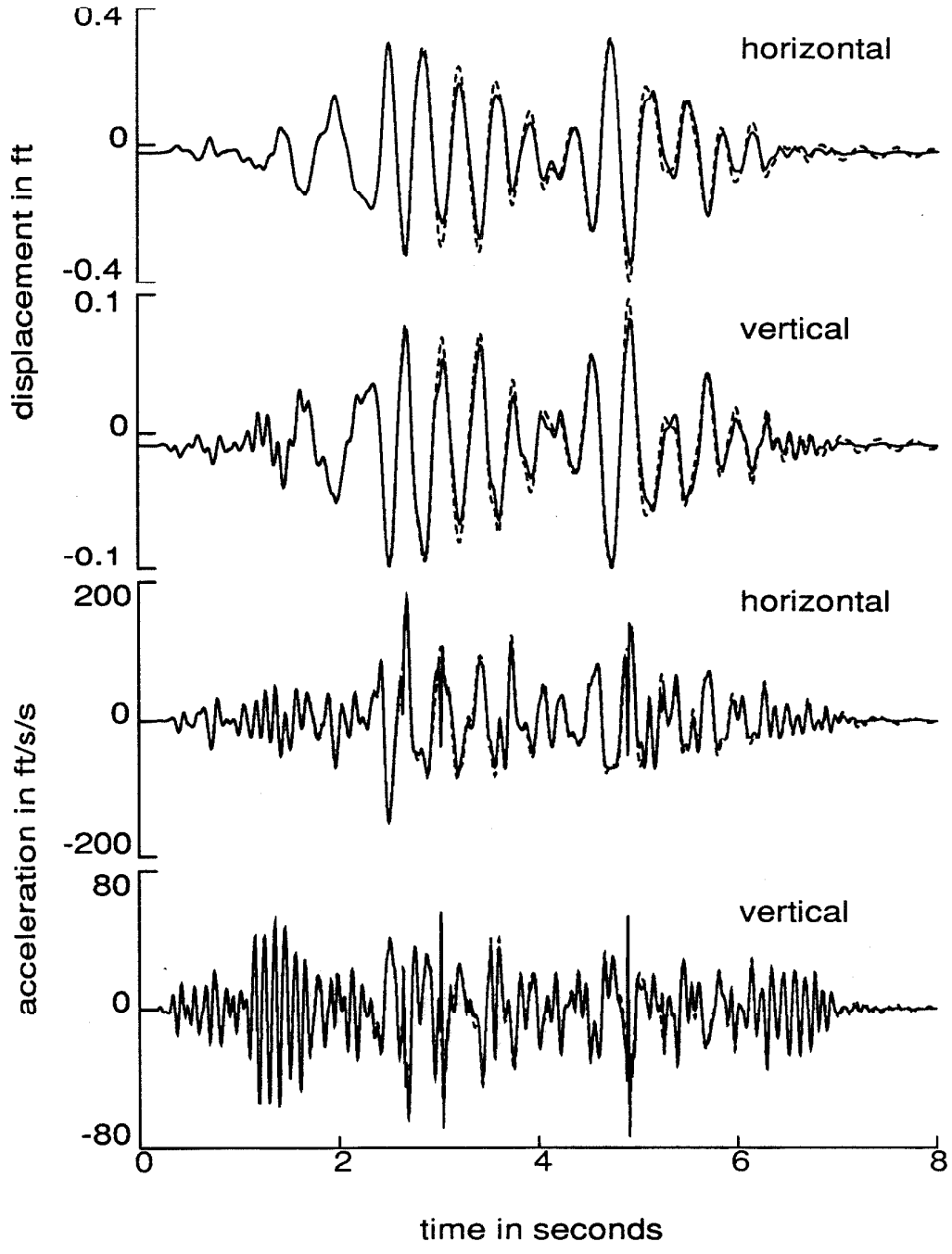

Figure 3.9. Horizontal and vertical motions of the dam crest at node 1 (Pine Flat Dam analysis). Solid line - cavitation included, 1 % critical damping in the water. Dashed line - linear response, no added damping in the water.

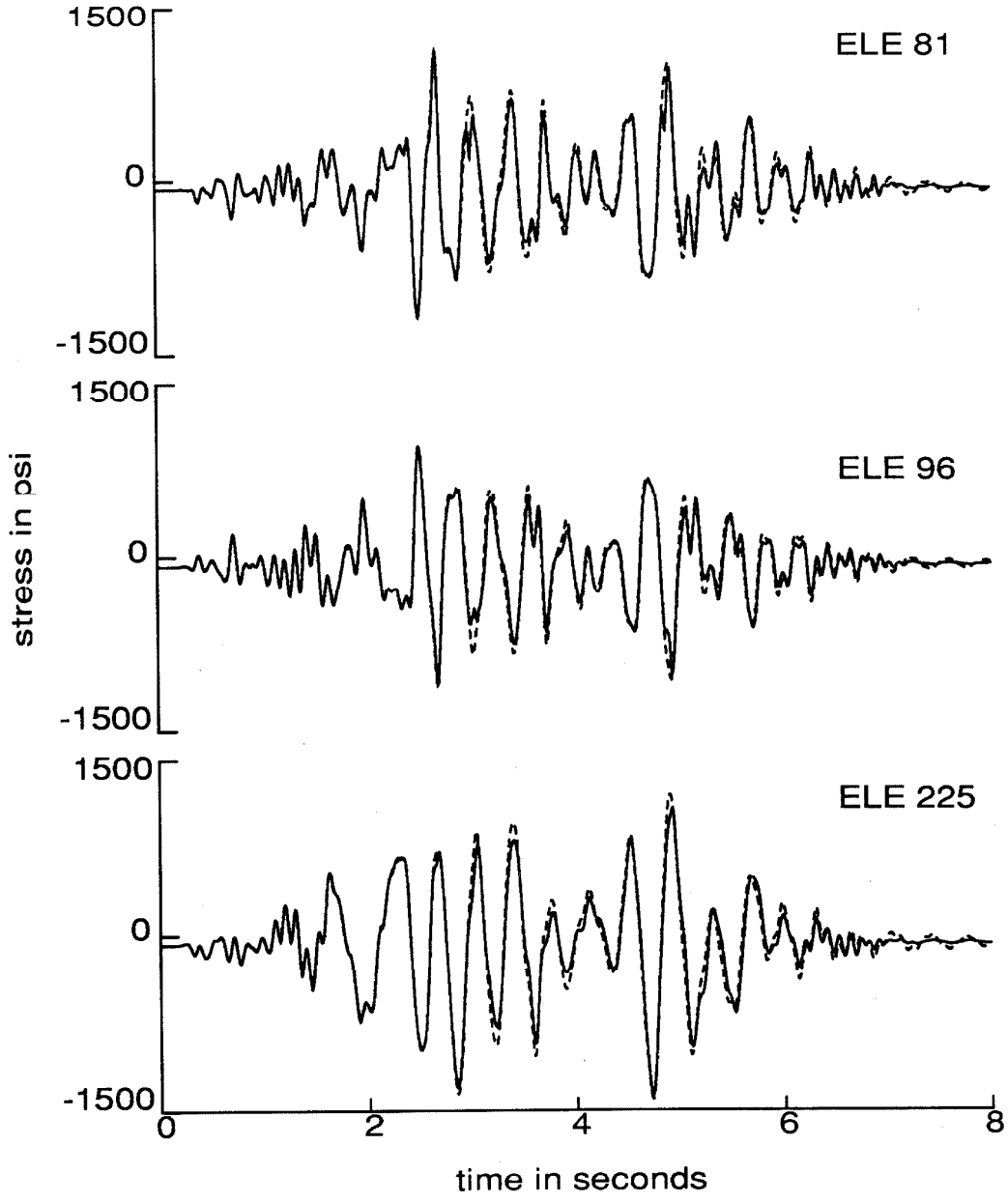

Figure 3.10. Vertical component of the normal stress in the dam (Pine Flat Dam analysis). Solid line - cavitation included, 1 % critical damping in the water. Dashed line - linear response, no added damping in the water.

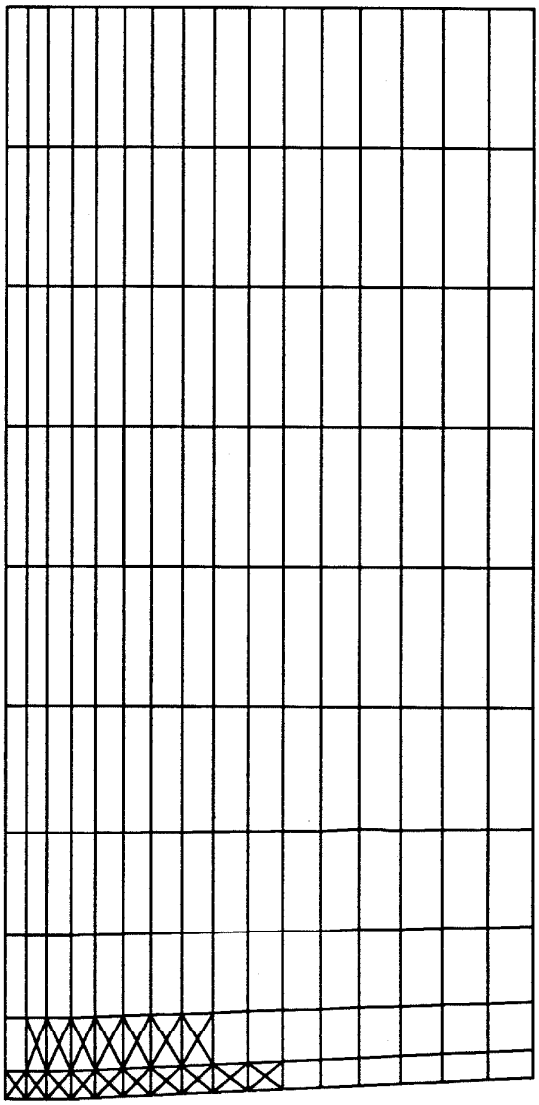

Figure 3.11. Envelope of cavitation for the Pine Flat Dam analysis (1 % critical damping in the water).

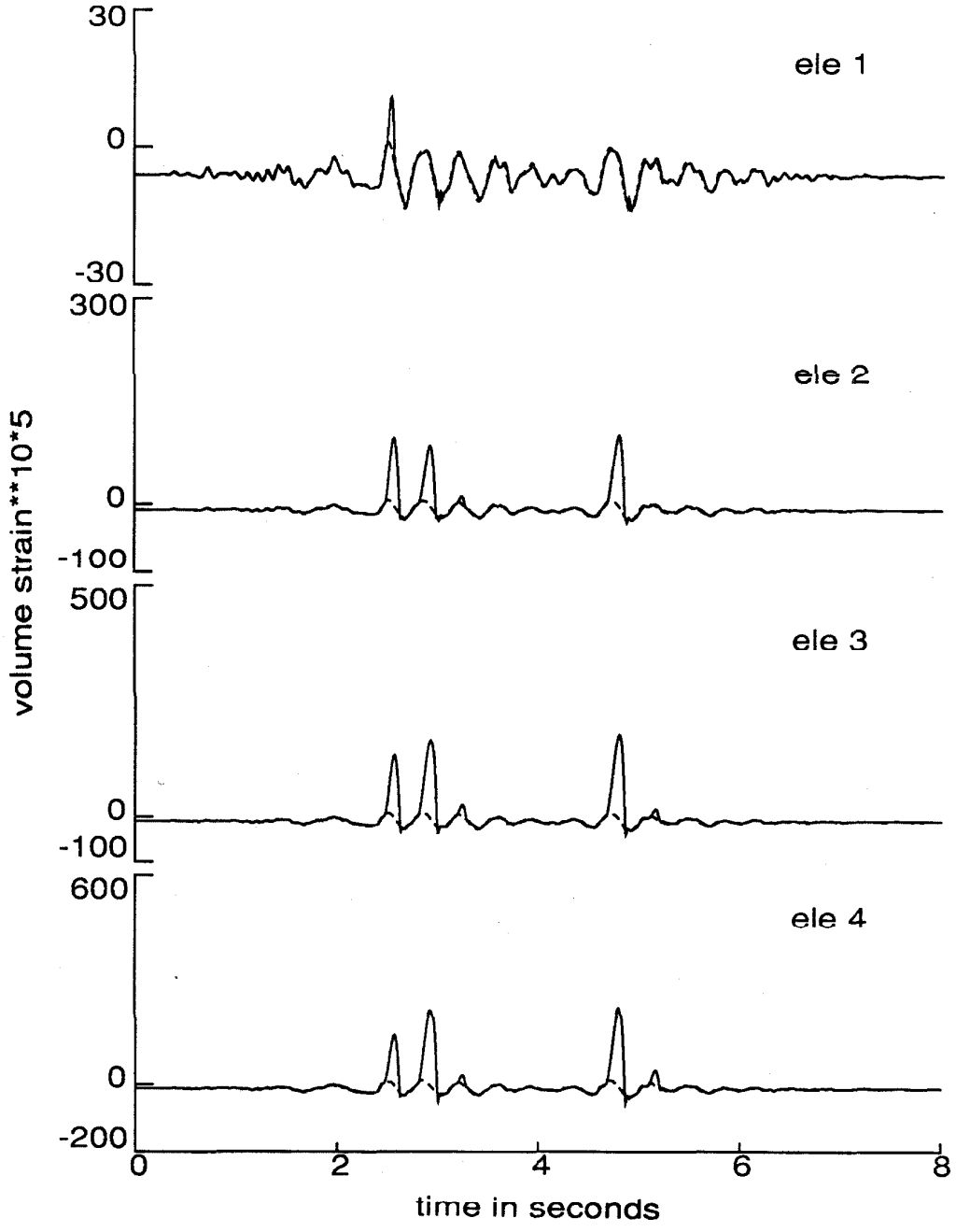

Figure 3.12. Volume strain time histories along the dam face (Pine Flat Dam analysis). Solid line - cavitation included, 3 % critical damping in the water. Dashed line - linear response, no added damping in the water.

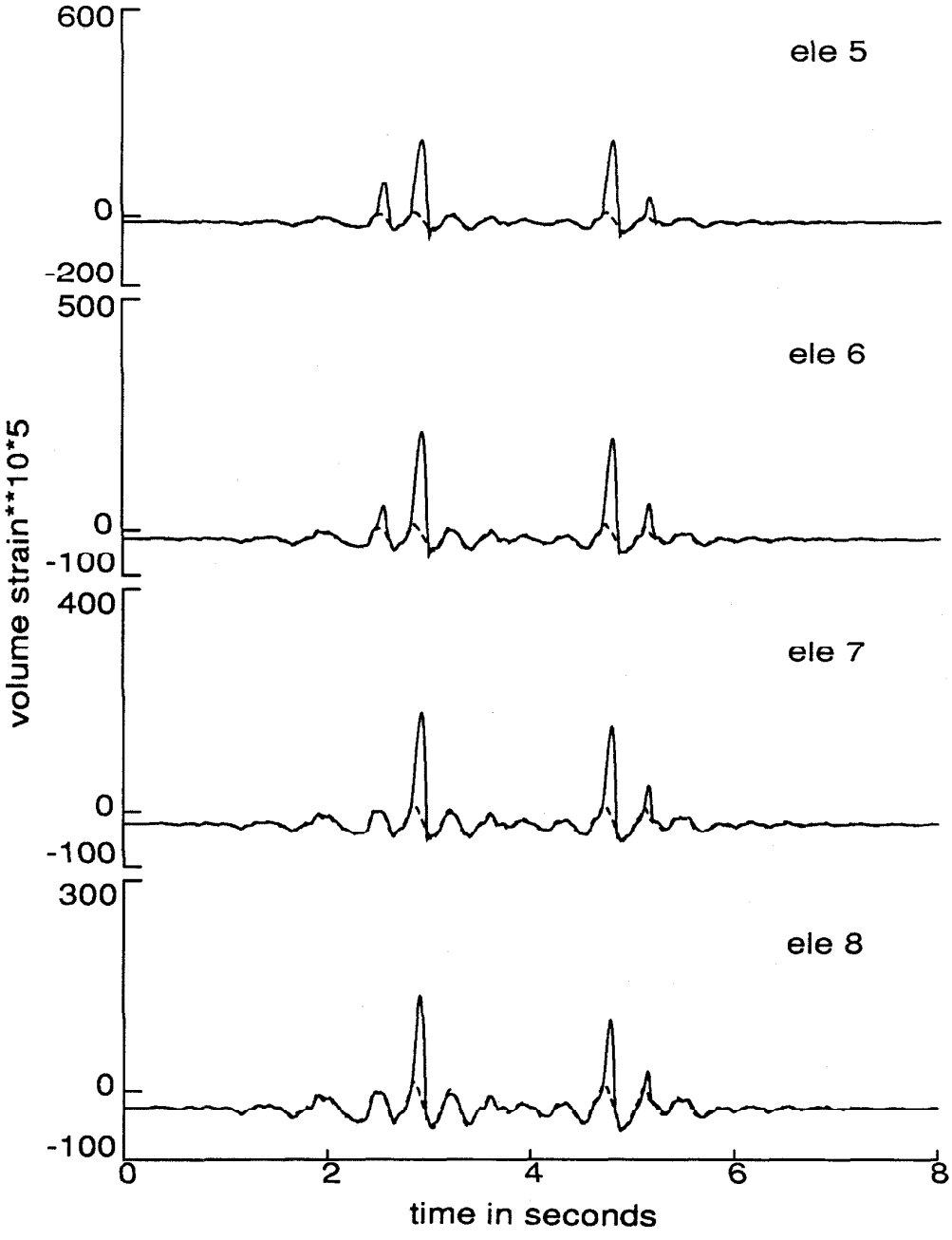

Figure 3.12. Continued.

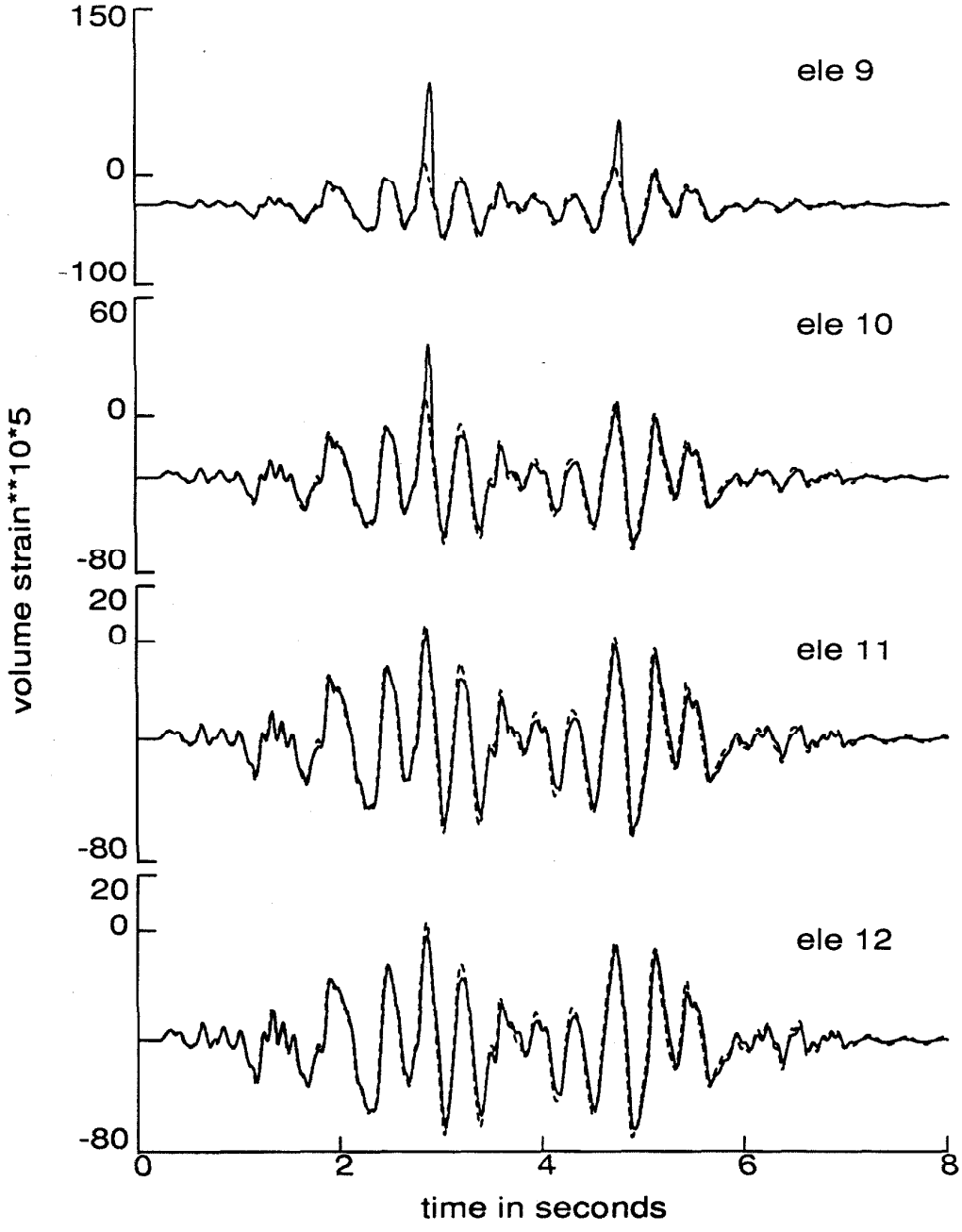

Figure 3.12. Continued.

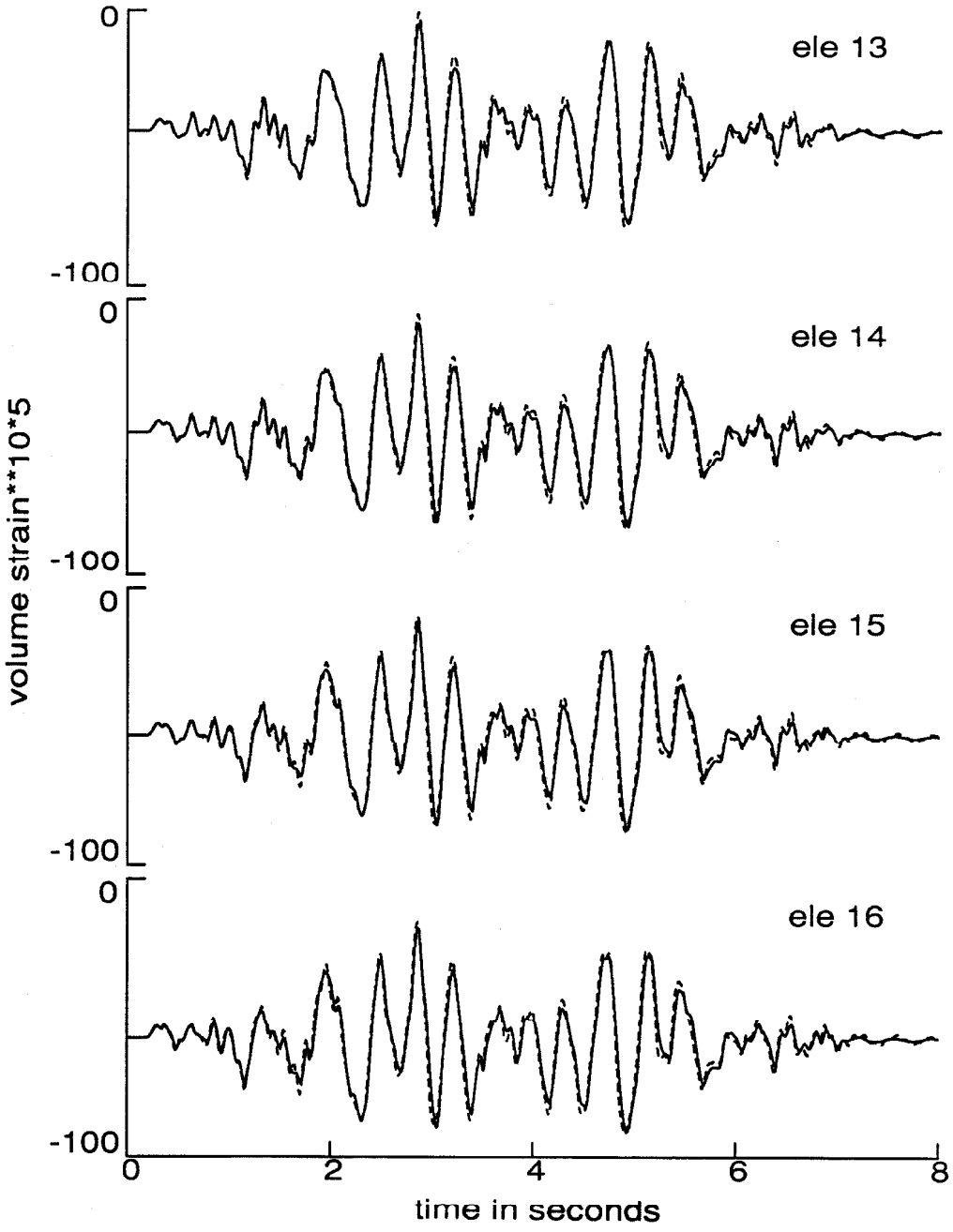

Figure 3.12. Continued.

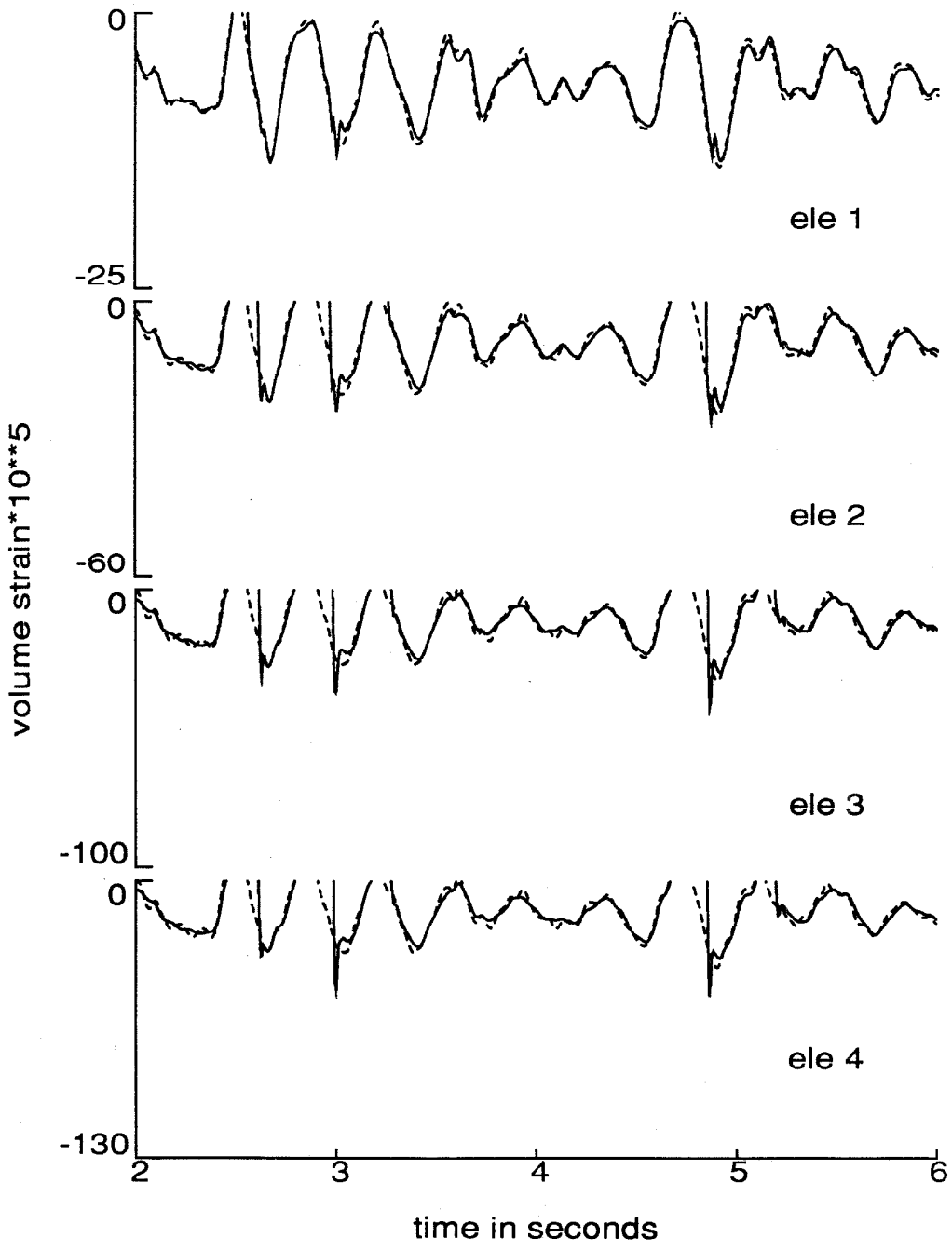

Figure 3.13. Detailed view of the compressive volume strains shown in fig. 3.12.

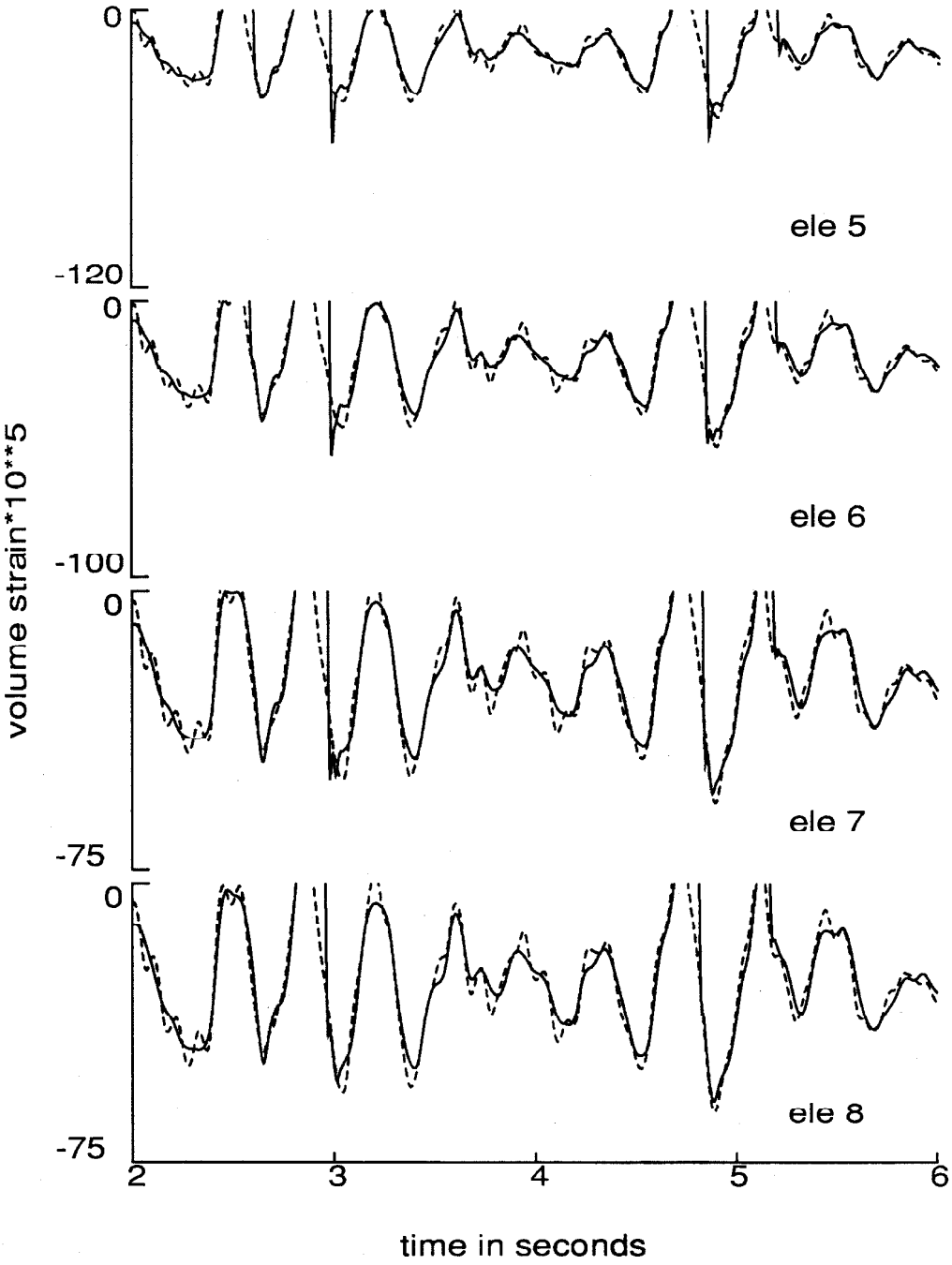

Figure 3.13. Continued.

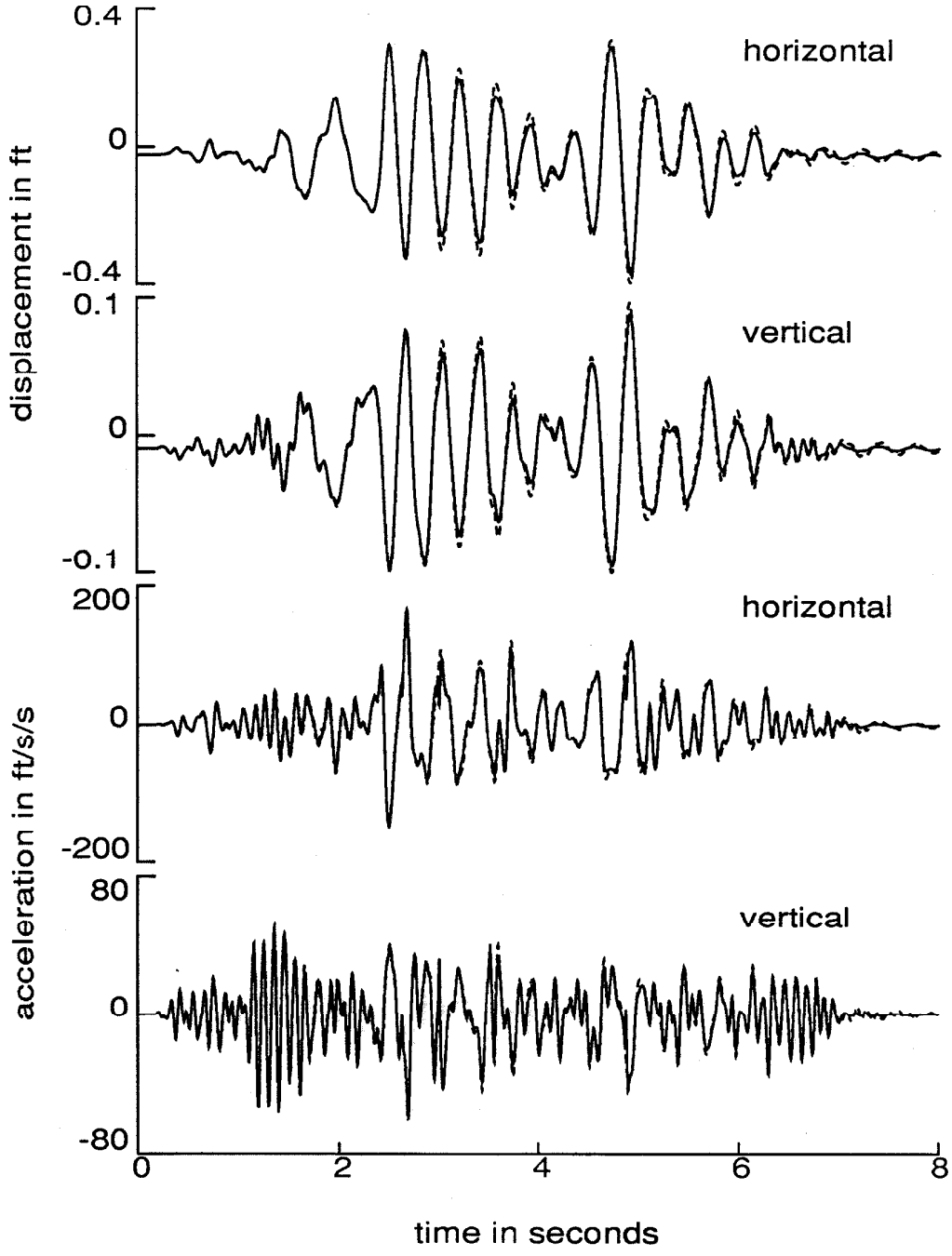

Figure 3.14. Horizontal and vertical motions of the dam crest at node 1 (Pine Flat Dam analysis). Solid line - cavitation included, 3 % critical damping in the water. Dashed line - linear response, no added damping in the water.

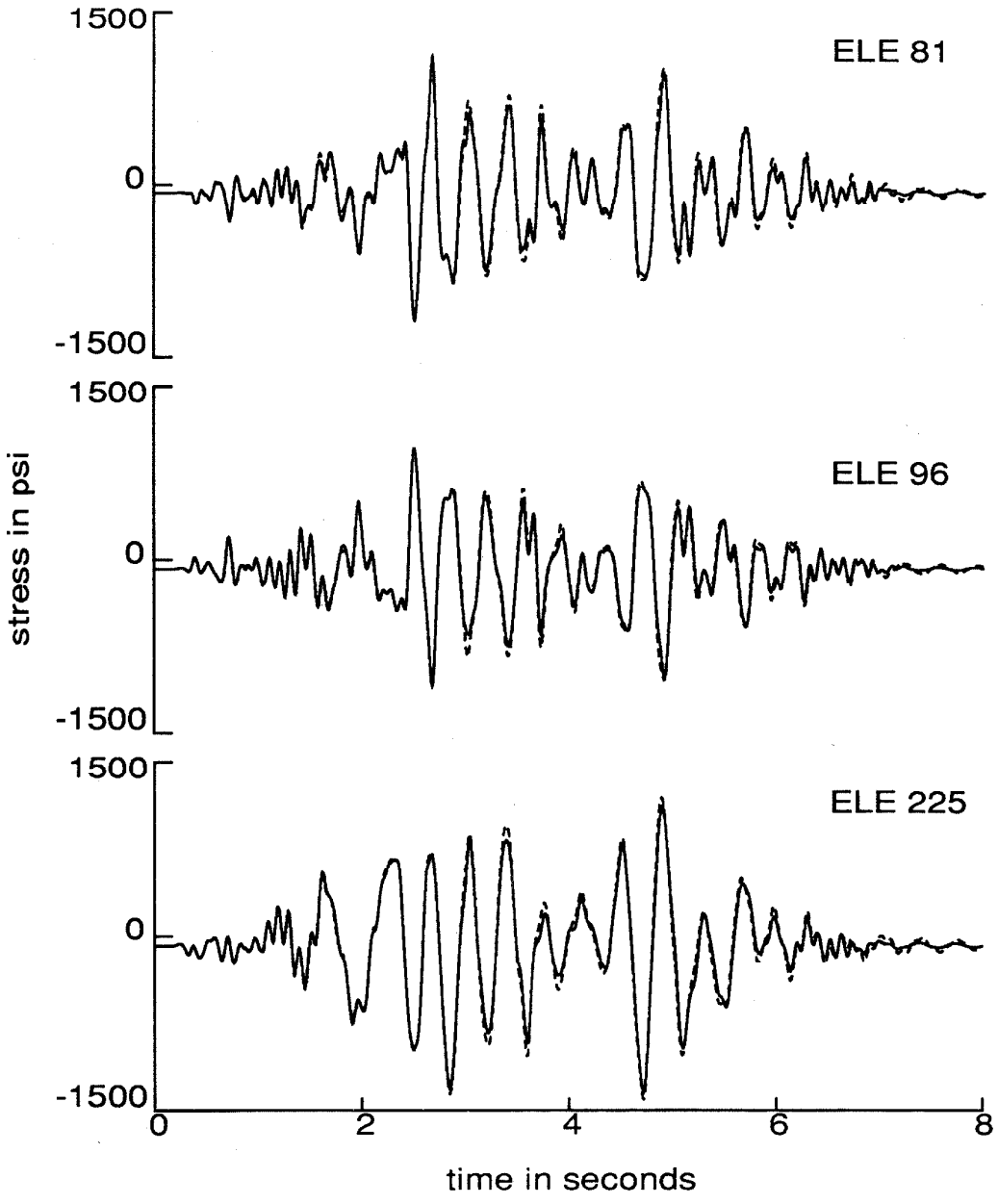

Figure 3.15. Vertical component of the normal stress in the dam (Pine Flat Dam analysis). Solid line - cavitation included, 3 % critical damping in the water. Dashed line - linear response, no added damping in the water.

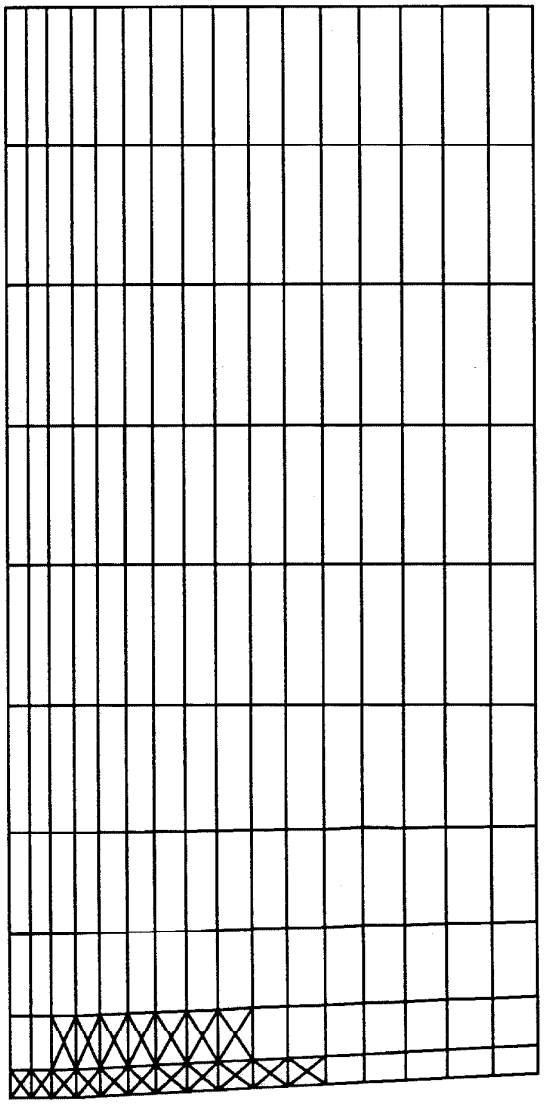

Figure 3.16. Envelope of cavitation for the Pine Flat Dam analysis (3 % critical damping in the water).

References

[1] Bleich, H. H. and Sandler, I. S., "Interaction between structures and bilinear fluids," *International Journal for Solids and Structures*, Vol. 6, No. 5, 1970.

[2] Clough, R. W. and Chu-Han, C., "Seismic cavitation effects on gravity dams," *Numerical Methods in Coupled Systems*, edited by R. W. Lewis, P. Bettes and E. Hinton, John Wiley & Sons Ltd., 1984

[3] Fenves, G. and Vargas-Loli, L. M., "Nonlinear dynamic analysis of fluid-structure systems," *Journal of Engineering Mechanics*, Vol. 114, No. 2, February 1988.

[4] Hall, J. F., "Study of the earthquake response of Pine Flat Dam," *Earthquake Engineering and Structural Dynamics*, Vol. 14, No. 2, March-April 1986.

[5] Newton, R. E., "Effects of cavitation on underwater shock loading - Part I," *NPS-69-78-013,* Naval Postgraduate School, Monterey, California, July 1978.

[6] Niwa, A. and Clough, R. W., "Shaking table research on concrete dam models," *Report No. UCB/EERC-80/05*, University of California, Berkeley, September 1980.

[7] Zienkiewicz, O. C., Paul, D. K. and Hinton E., "Cavitation in fluid-structure response (with particular reference to dams under earthquake loading)," *Earthquake Engineering and Structural Dynamics*, Vol. 11, No. 4, July-August 1983.

Chapter Four

TENSILE CRACKS IN CONCRETE GRAVITY DAMS

4.1 Introduction

Experience has shown that strong ground motions are capable of producing tensile stresses in concrete gravity dams that are well above the tensile strength of plain concrete. From a practical viewpoint, geometrical stress concentrations, joints, weak zones, and initial cracks constitute potential factors that may lead to cracking even under moderate shaking. Long term effects including gravity loadings, temperature gradients, and chemical activities (alkali aggregate reaction) are also capable of producing cracks in absence of dynamic loadings.

There are two distinct approaches that are in common usage in finite element studies of cracks in solid media: the smeared crack approach and the discrete crack approach. In the former, cracks are smeared in the finite elements by adjusting the element constitutive description for open and closed crack cases. The mesh, in general, can accommodate random crack patterns without modifications in geometry. The mechanics at the crack tip, however, are crudely represented and may depend on the mesh design. The discrete crack approach, on the other hand, models individual cracks which, therefore, are better defined allowing for more accurate representation of the crack tip field. However, continual remeshing is required as crack extension takes place.

4.2 Scope and Organization

The study presented in this chapter is concerned with tension cracks in planar sections of concrete gravity dams under earthquake-induced ground motions. Of interest are the location and extent of cracks and, since an important part of the dam response to a strong earthquake may take place after cracks have formed, the dynamic behavior of the dam in the presence of cracks. In the following section, a survey of relevant previous work is presented. In Section 4.4, a simple smeared crack model, which avoids remeshing to follow the crack tip, is introduced. Crack propagation is monitored in an interactive environment that provides for decision-making by the user. Some computational implications associated with the analysis are explained and investigated. In Section 4.5, extensive numerical studies of the earthquake response of the idealized Pine Flat Dam system are presented. Several cases of cracking are considered and analyzed.

4.3 Previous Work

4.3.1 Field and Laboratory Experience

Koyna Dam [23,7], completed in 1963 in India, is a 338 ft high gravity structure constructed of rubble concrete (fig. 4.1). In 1967, a magnitude 6.5 earthquake struck with an epicenter within 8 miles. At this time, the water level was 37 ft below the crest, or 22 ft below the design level. An accelerograph located at mid-height of a short monolith near one abutment recorded peak accelerations of 0.63 g cross-stream, 0.49 g stream and 0.34 g vertical and a duration of strong shaking of about 6 seconds. Because of the high stiffness of this monolith, these records are often taken as representative of the ground motions.

The earthquake caused significant cracking of the dam (fig. 4.2). The 218 ft level in the figure coincides with the level of slope change on the downstream face. Evidence was strong that cracking extended all the way through the dam

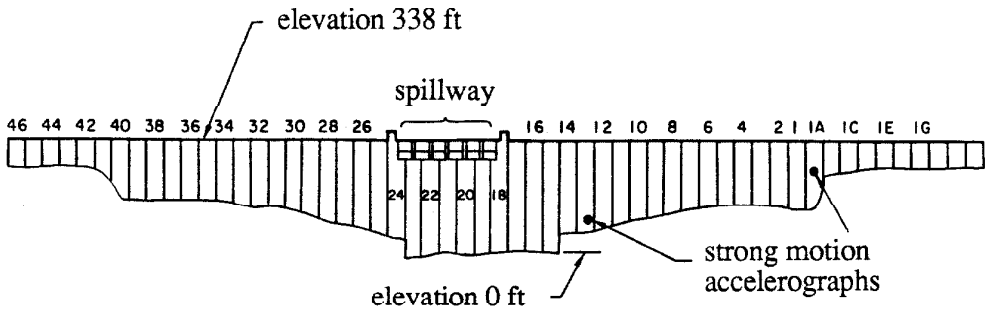

Downstream elevation view

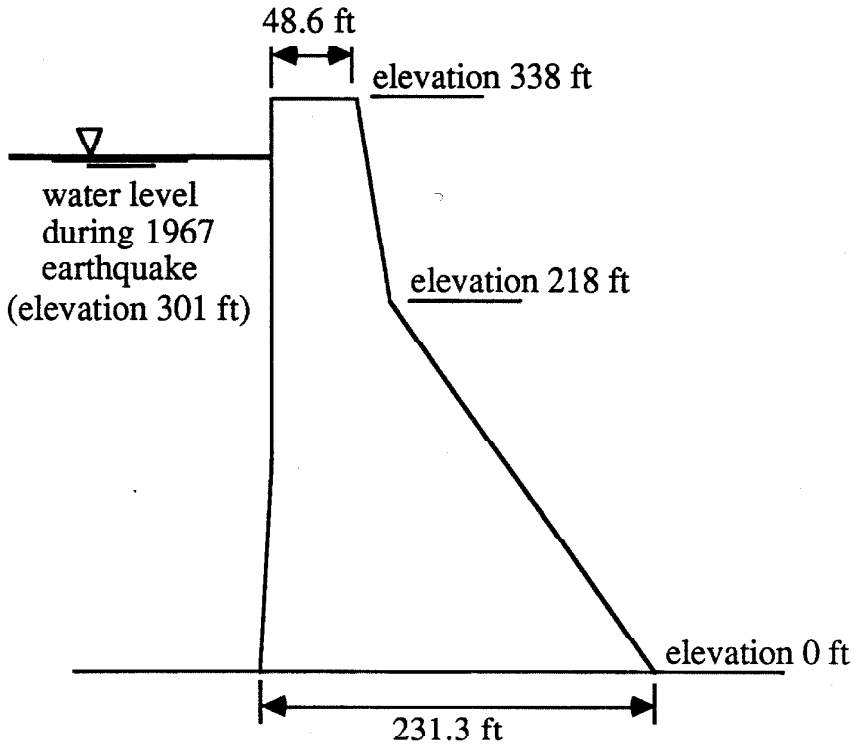

Cross-section of tallest nonoverflow monolith

Figure 4.1. Koyna Dam

from the upstream face to the downstream face and included leakage at the 218 ft level on the downstream face of a number of monoliths and a seeping crack at the same elevation in an elevator shaft where dye released at the upstream face appeared in as quickly as 5 minutes [3]. Even so, the dam remained stable, and no release of the water occurred. Spalling of concrete in the contraction joints indicated that some individual vibration of the monoliths took place.

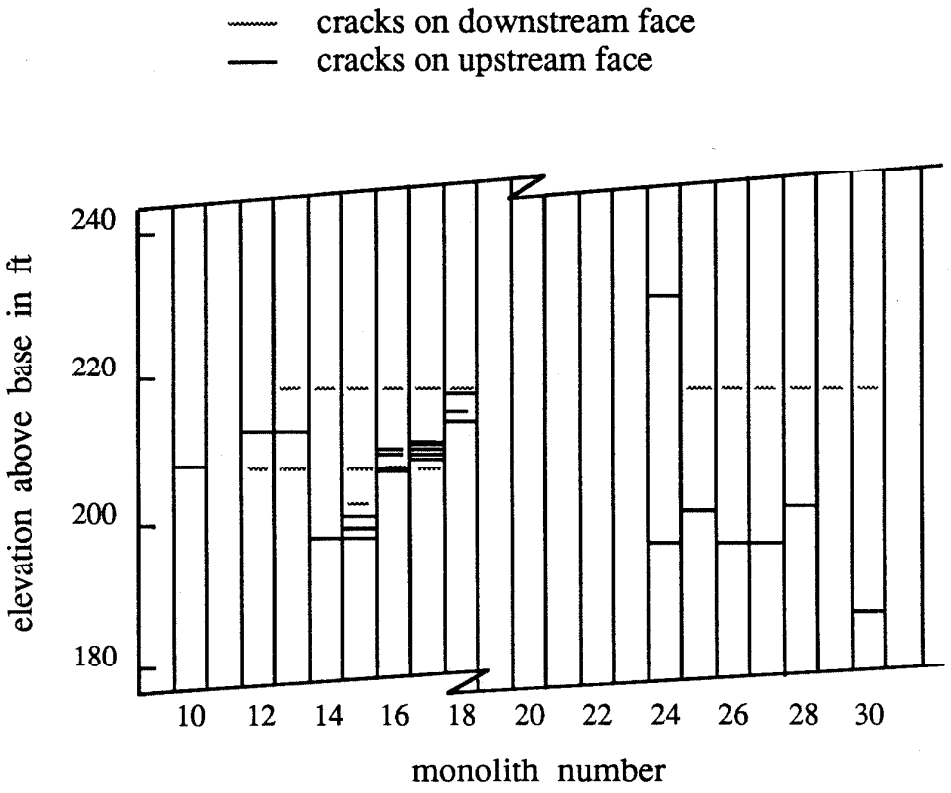

Figure 4.2. Cracks in Koyna Dam after the Koyna earthquake of 1967 [23].

The only experimental investigation of Koyna Dam worth mentioning is a shaking table test on a 27 in high model of a single monolith with a water reservoir carried out by Niwa and Clough [16]; cavitation aspects of this experiment were described in Section 3.3. A weak plaster-lead material provided proper similitude for density, stiffness and strength. Due to high frequency limitations of the shaking table, an artificial accelerogram was employed which combined harmonics at 6 hz, 20 hz and 33 hz. During a test with the table excitation applied in the stream direction at a peak acceleration of 1.21 g, a crack initiated at the point of slope change on the downstream face and propagated through to the upstream face (fig. 4.3). Following cracking, a rocking mode which locked onto the 6 hz harmonic in the base input became prominent. Peak displacements at the crest reached 0.47 in (5.9 ft prototype), a large value. However, even in the presence of the water pressure, the stabilizing effect of gravity sufficed to prevent overturning and significant sliding. A repeat of the 1.21 g test on the cracked dam caused some damage at the downstream end of the crack due to impact, but stability was maintained.

An experience similar to that at Koyna had taken place at Hsinfengkiang Dam (344 ft high diamond head buttress structure) in China in 1961 [11,21]. The earthquake magnitude was 6.1, and the water stood 43 ft below the crest, 16 ft below full level. The major crack spanned four buttresses at a level 52 ft below the crest where a structural discontinuity existed and was felt to have passed all the way through the dam. As at Koyna, the cracking did not constitute failure of the dam, and no release of water occurred.

A set of model tests has been carried out at 1 : 176 scale on a single buttress of Hsinfengkiang Dam constructed of hard rubber [6]. A horizontal cut all the way through the dam was made at the elevation of the observed fracture to represent a pre-existing crack. Although the detached block rocked and slid under earthquake-like excitations, it remained stable. However, the presence of water was not directly included, and, since material strengths did not scale, the observed stability was solely kinematic.

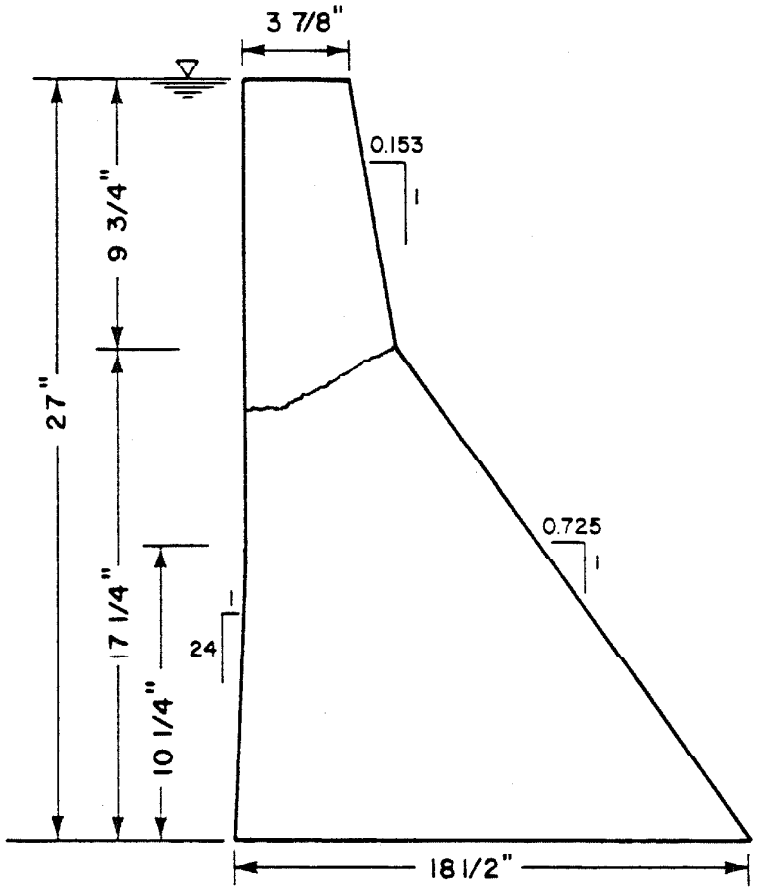

Figure 4.3. A single monolith model of the Koyna Dam showing cracks from a shaking table test at the University of California, Berkeley [16].

4.3.2 Mathematical Studies

Linearly elastic analyses of concrete gravity dams subjected to at least moderate ground motions reveal that tensile stresses large enough to produce cracking occur [9], which is substantiated by the field and laboratory experience mentioned above. The potential importance of cracking has spurred a number of attempts to account for this effect in mathematical models. These formulations can be classified into four groups which are discussed individually below. All deal with a single non-overflow monolith idealized as two-dimensional.

(I) Pre-existing crack, rigid detached block

An early analysis [19] of Koyna Dam using the ground motions recorded during the earthquake computed the horizontal acceleration at the level of slope change and applied it as base input to a rigid block representing the portion of the dam above a pre-existing crack that extended horizontally through the dam at the level of slope change. The 120 ft high block was allowed only to rock with a single rotational degree of freedom; no sliding was permitted. Water at a level 21 ft below the crest entered the analysis statically as a pressure on the upstream face and in the crack (uplift) and dynamically as an added mass. Upon impact, the angular velocity of the rigid block was assumed to reverse with a coefficient of restitution of 0.5; this reversal does not appear to be realistic. Results of the analysis predicted a stable response, i.e., no overturning. However, this stability was solely a kinematic one as no stresses were computed. Because of the many assumptions, some questionable, used in the analysis, the results should be viewed with much caution.

A rigid block analysis was used in a study of Hsinfengkiang Dam, described above, employing a 52 ft high block [6]. Both rocking and sliding were considered, but only in separate analyses; the rocking analysis examined different rotational impact assumptions including the case where the sense of the angular velocity was maintained through impact. Results for four earthquake ground motions (identified as Koyna, Hsinfengkiang, Helena and El Centro) revealed a stable structure; however, water was omitted. As for Koyna Dam [19], interpretation of the results is hampered by the many severe assumptions involved.

Recently, an improved treatment of the rigid block model has been mentioned [14]. A scheme developed by Lindvall, Richter and Associates allows simultaneous sliding and rocking as well as lift-off and also provides for possible cracking off of the corners of the block at the crack level. An analysis of Morris Dam has been carried out but has not yet been published.

(II) Pre-existing crack, finite element model

Although the capability of performing dynamic, finite element analyses of

structures with pre-existing cracks, either smeared or discrete, has been around for some time, almost no such work on gravity dams has been carried out. This is surprising since this technique can remove the assumptions involved in the rigid block model discussed above, except, of course, for the pre-existence and location of the crack. The only study reported used an extremely coarse mesh (two 8-node quadratic elements for Koyna Dam) with a horizontal discrete crack extending half-way through the dam from the upstream face to the mid-thickness [13]. However, such an arrangement could not provide valid results. A number of finite element analyses of a pre-cracked gravity dam (smeared crack model) are presented in this thesis.

(III) Smeared propagating cracks, finite element model

The first analysis of a concrete gravity dam which attempted to model actual crack propagation employed a full nonlinear constitutive representation for concrete which included stress-strain nonlinearity in both compression and tension, hysteresis, strain rate effects and a smeared crack capability [18]. Cracking occurred in an element upon reaching a critical tensile strain independent of rate effects. A number of analyses of Koyna Dam without water were carried out with meshes having either 4 or 6 elements in the thickness direction. An analysis using the finer mesh and the ground motions recorded during the earthquake showed cracking on both the upstream and downstream faces at the elevation of slope change, but the cracks penetrated only a single element into the interior. This behavior repeated in other analyses which used the coarse mesh and somewhat stronger ground motions and which excluded strain rate effects. One of these analyses showed that lowering the crack initiation strain caused the cracked zone to spread upward and downward along the faces of the dam, but not into the interior. No explanation for this behavior, which is thought to be unreasonable, was apparent.

A nonlinear finite element analysis of the 246 ft high Norris Dam [1] included compressive stress-strain nonlinearity, hysteresis and smeared cracking (critical tensile stress). The moderate excitation consisted of the horizontal and vertical

components of the 1957 Golden Gate Park motions, both scaled to 0.2 g peak acceleration. Dynamic water pressures for a reservoir level 33 ft below the crest were computed from a linear analysis and input as loads to the dam in the nonlinear analysis, an approximate procedure involving unknown error. Energy dissipation was via hysteresis only as no viscous damping was included. The tensile strength equalled 350 psi in the dam interior and 100 psi at the upstream and downstream faces due to the presence of surface cracks in the actual dam from nonuniform cooling. In the earthquake analysis, nearly all of the surface elements cracked as well as most of the interior elements in the upper third of the dam. In this region, two horizontal sections cracked all the way through - one at a level 20 ft below the crest (3 elements in the thickness direction) and the other at a level 65 ft below the crest (6 elements in the thickness direction). Many neighboring elements cracked as well.

Another analysis of Koyna Dam employed a rate-sensitive, elasto-viscoplastic constitutive model for concrete with smeared cracking [25]. However, the finite element meshes were extremely coarse (2 or 3 elements in the thickness direction), and the only results presented were a number of time histories of crest displacement from which little information could be gained.

A recent study [15] of the nonlinear response of gravity dams used the program ADINA and its nonlinear constitutive model of concrete with smeared cracking (critical tensile stress). Three dams were analyzed: 185 ft high Richard B. Russell Dam (tensile strength = 380 psi), a 300 ft high standard cross-section (380 psi), and the 638 ft high Dworshak Dam (740 psi). The meshes consisted of from 13 to 16 horizontal rows of 9-node quadratic elements with 5 elements in each row. Excitation was provided by the horizontal and vertical components of the 1966 Parkfield ground motion (peak acceleration 0.3 g in the horizontal component), which was tripled for the shorter Russell Dam. All of the dams cracked clear through: Russell at the base, the standard section at two levels in the upper part, and Dworshak at the level of slope change. A number of additional cracks initiated at other elevations but did not propagate all the way

through to the opposite face. All of the crack zones spanned at least several integration points in the vertical direction and often several elements.

Another recent study [24] modeled only the nonlinearity due to cracking and used an equivalent tensile strength based on fracture mechanics criteria (similar to that employed in this chapter). For a discretization of Pine Flat Dam, this equivalent strength varied from 130 psi in the elements at the top to 96 psi for the bottom row (fine mesh with eight elements in the thickness direction). However, these values were scaled up by a factor of 5.5 to avoid early cracking at the heel where a stress concentration existed (deemed unnecessary here). In an analysis using the 1952 S69E Taft ground motion scaled by two (maximum acceleration of 0.36 g) and a full reservoir, one of a number of analyses performed, half the bottom row of elements cracked as well as most of the neck region clear through the dam; the latter area was 5 elements deep. Computations in several of the analyses went unstable which was noted as a possible sign of imminent failure.

Still another recent investigation [8] employing smeared cracking incorporated special discontinuous shape functions to overcome some of the extraneous stiffness of a finite element containing a smeared crack (see appendices). The surfaces of discontinuity, connected together from element to element, form the cracks which, thus, have some similarity to discrete cracks. Fracture mechanics criteria were included through the use of the stress intensity factors, computed via a surface integral around the crack tip, to control the crack propagation. In an earthquake analysis of Pine Flat Dam using the 1957 Golden Gate Park accelerograms scaled to 0.2 g (no water, fine mesh with 12 elements in the thickness direction), cracks initiated from the upstream and downstream faces near the base of the neck. The former propagated only a short distance inward while the latter turned sharply downward and ran parallel to and not far from the upstream face almost to the base of the dam; they did not appear to meet. Each of these cracks was a single trace; no spread crack zones resulted.

The traditional smeared crack approaches described in [18], [1], [15], and [24] were all characterized by crack zones which spanned a number of elements in

width, unlike the results in [8]. Such behavior is not intuitive because the stress release which accompanies cracking relieves the surrounding tensile stresses except those ahead of the crack; thus, the crack should propagate in a narrow zone. As discussed later in the chapter, spread crack zones can artificially result from at least three sources. The first is the use of stiffness-proportional viscous damping in cracked elements, which prevents full stress release. Such damping was not employed in [18] and [1], may have been in [15] (not stated), and in [24] was computed using the tangent stiffness matrix to avoid the difficulty. Secondly, the use of the tangent stress-strain matrix of equation (4.1) for an open crack can cause unwanted stiffness in the opening mode for certain crack orientations (Appendix 4.A). Treatments were as follows: [18] - used equation (4.2), so no problem, [1] - no information, [15] and [24] - used equation (4.1) with $\alpha_s = 0.5$ and 0.1, respectively. Third is the satisfaction of the cracking criterion in a number of elements simultaneously, i.e., in an iteration of a time step (avoided here by imposing a limit of one new crack per iteration). Simultaneous element cracking is more likely to occur with larger time steps; those used in [18], [1], [15] and [24] were 0.0025, 0.005, 0.02 and 0.01 seconds, respectively. Thus, only for [15] and [24] do some possible explanations exist for the spread in the crack zones, although these are by no means definitive.

(IV) Discrete propagating cracks, finite element model

One investigation of earthquake-induced cracking in gravity dams which employed discrete cracks used a critical tensile stress criterion and located the cracks along interelement boundaries [22]. So that a crack could propagate perpendicular to the direction of principal tensile stress, existing element boundaries were adjusted by shifting the locations of the nodes, or new boundaries were generated by element subdivision. Each interelement crack was represented by a crack element which considered aggregate interlock in shear stress transfer. Outside of the cracks, the behavior was taken to be linearly elastic. A number of analyses of Koyna Dam investigated variations in viscous damping, tensile strength, aggregate interlock, strength of earthquake excitation, and mesh fine-

ness. An analysis with the finest mesh (5 elements in the thickness direction) using a cracking strength of 435 psi, empty reservoir, and an artificial accelerogram of 0.2 g peak showed a crack to initiate at the point of slope change on the downstream face and propagate along a generally horizontal path to the upstream face over several periods of the dam vibration. However, the crack profile included many side cracks and sharp turns in direction which appeared to be unrealistic. Possibly, the modifications to the mesh geometry generated local disturbances. A repeat of the analysis on a coarse mesh resulted in a crack profile which was very different in detail.

Another study [5] combined both the smeared and discrete crack approaches (apparently) with a separate, local finite element analysis of the crack tip zone to determine the stress intensity factors which were used to control the crack propagation. The local mesh was subjected to the current displacement field from the dam mesh. Apparently, inertial and hydrodynamic forces were precomputed from a linear analysis and applied to the dam in the nonlinear analysis (not accurate if significant cracking occurs). In an analysis of Pine Flat Dam using the 1957 Golden Gate Park accelerogram scaled to 0.1 g, a single crack was allowed to initiate on the upstream face near the base of the neck, and it turned down smoothly as it propagated inward to become parallel to the downstream face. However, the computations ceased at this point.

Finally, some significant finite element analyses of cracking in gravity dams which combined discrete crack modeling, fracture mechanics, and automatic remeshing in an interactive computer graphics environment [20,4] are mentioned here. To date, however, only static analyses have been published.

4.4 Crack Modeling

Analyses of cracked bodies require dealing with three different states: uncracked, open crack and closed crack. Appropriate criteria are also sought to govern the transition among different phases of behavior. The uncracked phase has already been defined in Chapter 2 (linearly elastic case).

In this section, the adopted smeared crack approach is presented. Open and closed crack states are described. Criteria for crack initiation, propagation, closing and reopening are introduced. No provisions are taken to simulate water contact with crack-generated surfaces on the water side; nor is atmospheric pressure applied to crack surfaces.

The discussion in this section is specialized for 4-node finite elements employing linearly interpolated displacements. A 2×2 Gauss integration is used for uncracked elements, and the potential for cracking is monitored at the center point. Once cracking takes place in an element, a one point Gauss integration (center point) is used for all time thereafter. The algorithm is capable of handling only a single crack orientation in each element.

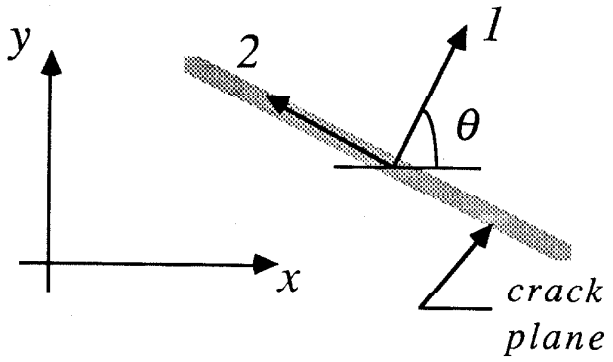

Figure 4.4. Local frame at a cracked integration point.

4.4.1 Open Crack Representation

At an integration point where crack opening is detected, the normal stress perpendicular to the crack plane is reduced to zero, and one possibility for the tangent constitutive matrix (in the 1-2 frame in fig. 4.4) is

$$D_T^{oc} = \begin{pmatrix} 0 & 0 & 0 \\ 0 & E & 0 \\ 0 & 0 & \alpha_s G \end{pmatrix}, \tag{4.1}$$

where α_s is a constant shear stiffness retention coefficient for shear transfer across an open crack due to aggregate interlock.

It has been observed that the coupling inherent in the finite element method may lead to some unwanted stiffness in smeared crack elements when D_T^{oc} of equation (4.1) is employed [10]. This is demonstrated in Appendix 4.A for a rectangular 4-node element where it is shown that unwanted stiffness is present for an open crack in both crack opening and sliding modes when the crack is not oriented parallel to one of the element sides. For such a crack, the extra stiffness can only be removed by taking

$$D_T^{oc} = \begin{pmatrix} 0 & 0 & 0 \\ 0 & 0 & 0 \\ 0 & 0 & 0 \end{pmatrix}, \tag{4.2}$$

which also works for nonrectangular elements. This, however, results in an undesirable zero normal stiffness for fibers oriented parallel to the crack. For a trapezoidal element with the crack parallel to the two parallel sides (as employed in Problems 4.1 to 4.6 later in the chapter), equation (4.1) may be safely used because no coupling results.

If the point under consideration never experienced cracking before, crack opening follows either crack initiation or crack propagation criteria (Sections 4.4.3 and 4.4.4) as the situation warrants. Reopening is detected by $\epsilon_1 + \nu\epsilon_2 > 0$ for equation (4.1) and by $\epsilon_1 > 0$ for equation (4.2).

Improvements in the representation of open cracks may be possible by using discontinuous interpolation functions for the cracked finite elements [8,17].

4.4.2 Closed Crack Representation

One possibility for the tangent constitutive matrix to represent the state of a closed crack is the original elastic matrix,

$$D_T^{cc} = \begin{pmatrix} \frac{E}{1-\nu^2} & \frac{E\nu}{1-\nu^2} & 0 \\ \frac{E\nu}{1-\nu^2} & \frac{E}{1-\nu^2} & 0 \\ 0 & 0 & G \end{pmatrix}, \tag{4.3}$$

which should be used in conjunction with D_T^{oc} of equation (4.1) for an open crack. However, this choice of D_T^{cc} can result in unwanted stiffness in the sliding mode. This is shown in Appendix 4.B for a rectangular 4-node element when the crack is not oriented parallel to one of the element sides. The extra stiffness can be removed by the choice

$$D_T^{cc} = \begin{pmatrix} E & 0 & 0 \\ 0 & 0 & 0 \\ 0 & 0 & G \end{pmatrix}, \tag{4.4}$$

which also works for nonrectangular elements and which should be used in conjunction with equation (4.2) for the open crack. Again, however, zero normal stiffness tangent to the crack results. For the trapezoidal case mentioned in the previous section, equation (4.3) may be safely used.

Sliding along closed crack planes is allowed according to the conventional friction theory

$$\tau_{12}^{k+1} \not> \mu_c \, \sigma_1^{k+1}, \tag{4.5}$$

where μ_c is an appropriate constant coefficient of friction of plain concrete. The full shear stiffness, G, is used in the tangent stiffness, hence, iterations will be required (when sliding occurs) until convergence is attained.

Crack closing is detected by $\epsilon_1 + \nu\epsilon_2 \leq 0$ when equation (4.3) is used and by $\epsilon_1 \leq 0$ for equation (4.4).

Improvements in the representation of sliding along an existing crack may be possible by using discontinuous interpolation functions [17].

4.4.3 Crack Initiation

Although formation of new cracks is permitted anywhere, it can be expected to occur only on the upstream and downstream faces of the dam and on the sides of existing open cracks as shown in fig. 4.5. A new crack is introduced along the plane of the maximum principal (tensile) stress, σ_{pt}, when this stress exceeds the tensile strength of plain concrete, σ_{ct}. Regarding the capability of having only a single crack orientation in each element, the matrices of equations (4.2) and (4.4) should be used for an existing crack to allow crack initiation off its side.

One difficulty often encountered during trial analyses was that, at the end of a time step, the condition $\sigma_{pt} > \sigma_{ct}$ was satisfied in a number of adjacent elements for which crack initiation was permitted. However, instead of the multiple cracks which could be introduced in this situation, the first crack to form would relieve the tensile stresses over the adjacent region (except ahead of the crack tip) and reduce the possibility of other similarly oriented cracks initiating

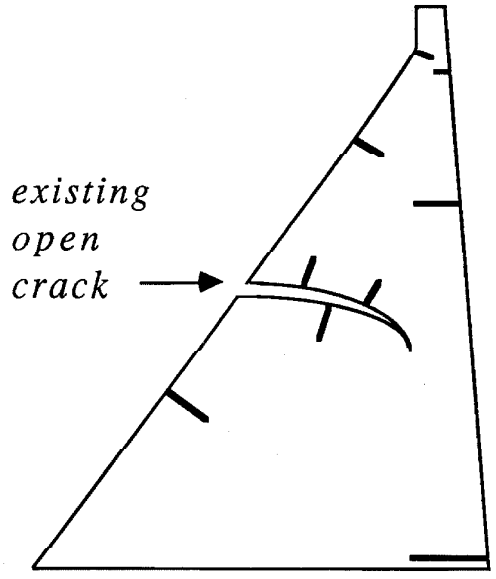

Figure 4.5. Possible locations for crack initiation.

nearby. This difficulty of the numerical solution could be avoided by reducing the time step until only a single crack initiation was indicated or, alternatively, as employed here, by allowing only a single crack initiation to occur in each iteration of each time step. In the latter procedure, the crack is introduced in the element for which the ratio σ_{pt} to σ_{ct} is maximum. The crack orientation is obtained by linear interpolation to the point in time when σ_{pt} equals σ_{ct}. (Actually, the user has ultimate control over decisions regarding crack initiation through interactive programming as discussed in the next section.)

Once a crack is initiated, its growth will be according to an appropriate propagation criterion.

4.4.4 Crack Propagation

Crack propagation in concrete is associated with a fracture zone which represents a transition between uncracked and fully cracked states. The fracture zone is characterized by a softening type of behavior. In order to adequately represent such behavior in the finite element idealization, the mesh should be fine with respect to the size of the fracture zone. This may be possible in the case of a small structure where the fracture zone constitutes a relatively sizable part. In large structures, however, the computational requirements would be very great. Another difficulty arises from the uncertainty about the constitutive behavior of the fracture zone.

Alternatively, suitable fracture mechanics techniques may be employed. Assuming mode-I crack opening and employing a regular arrangement for the mesh, Bazant used the energy release rate concept to devise a very simplified propagation criterion (equivalent strength criterion) [2]. When the principal tensile stress in the element just ahead of the crack front exceeds the critical element strength given by

$$\sigma_{cr} = \hbar k_{cr} a^{-1/2}, \tag{4.6}$$

the crack is allowed to extend into the element. The critical stress intensity factor for plain concrete, k_{cr}, is assumed given; a is a characteristic element

length and $\hbar$ is a constant that depends on the element type [2]. The dependence on element size approximately atones for not capturing the stress concentration at the crack tip. Values of σ_{cr} are, typically, less than the tensile strength, σ_{ct}. This technique is similar to that discussed in [24].

The crack propagation algorithm employed here uses the equivalent strength criterion. In an early version of this algorithm, the computer program automatically kept track of the elements adjacent to the current crack tip (fig. 4.6) and identified them as candidates for crack extension. The particular element chosen, limited to one per iteration, was the element with the maximum ratio of σ_{pt} to σ_{cr}. This fully automated procedure often resulted in crack orientations in the individual elements which were not tangent to the general trend of the crack as defined by the profile of cracked elements (fig. 4.7, results of an actual analysis incorporating release of viscous forces as described below). Such behavior is thought not to be realistic and to be caused by the constraints imposed by the finite element discretization.

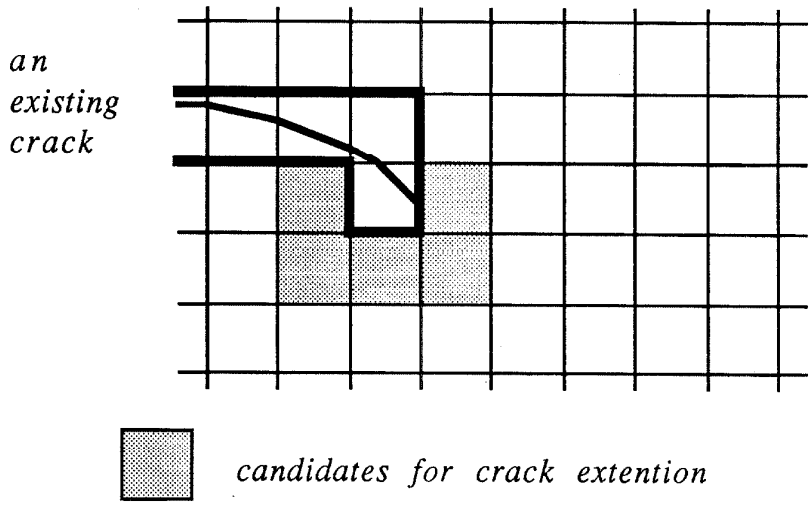

Figure 4.6. Candidates for extension of the crack tip in an early, automated version of the propagation algorithm.

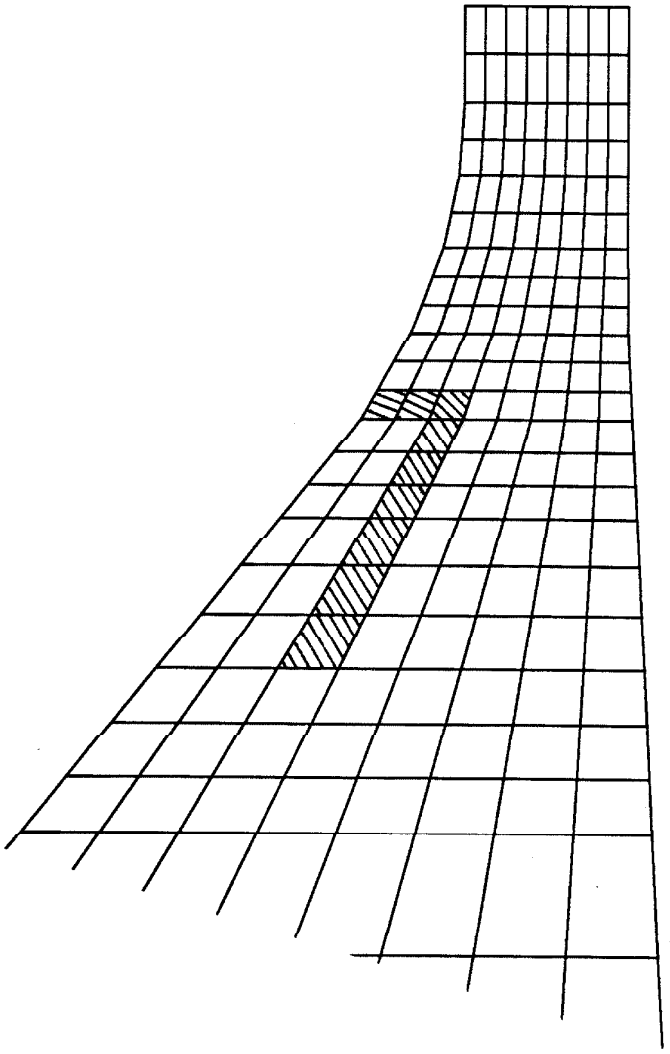

Figure 4.7. Crack location from a trial analysis using an early, automated version of the propagation algorithm.

The present version of the computer program allows the user to control the crack extensions through interactive programming. At every iteration in which the initiation or propagation criterion is satisfied in an element or a group of elements, the program displays all relevant information for these elements and accepts the user's decision of which element (or no element) to initiate or propagate a crack. For the example in fig. 4.8, for which the propagation criterion is satisfied in both elements A and B, the user should choose element A whether or not it had the greatest ratio of σ_{pt} to σ_{cr} because it makes the extension of the crack most consistent with the orientation of the existing crack. Extension to element C is probable in a later iteration.

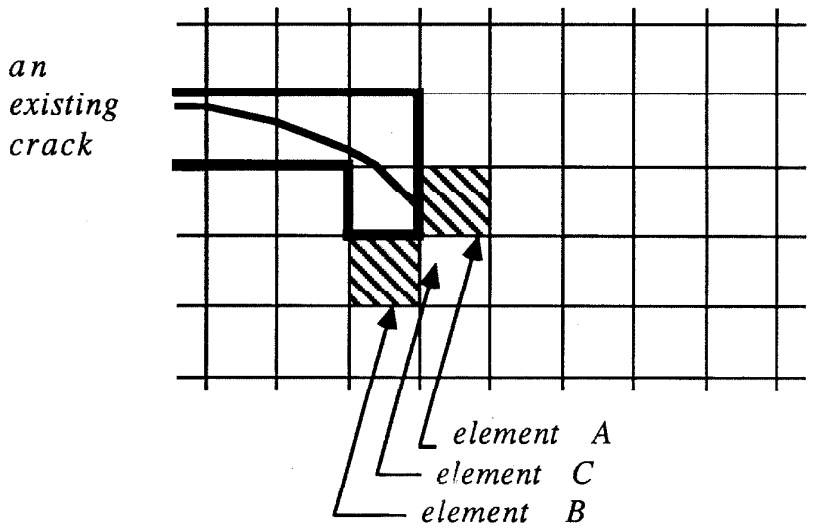

Figure 4.8. User chooses crack extension to element A or B in the interactive crack propagation algorithm.

Trial analyses have also revealed that the tensile stresses in elements on the sides of a crack were not reduced when the crack propagated by as would be expected from the stress release associated with cracking (see example in Section 4.5.1). Investigation showed that the tensile stress carried by the concrete prior to cracking is transferred almost entirely to the viscous damping mechanism in time steps subsequent to cracking due to the large increase in relative velocity which occurs across the crack. Recall that only stiffness-proportional damping is employed. To avoid this artificial transfer of load, the damping is removed from an element after cracking. This modification is made for all time because of additional difficulties encountered in restoring the damping following crack closure, i.e., the large impulse which results due to the high crack closing velocity.

At the heel of the dam, a stress concentration exists, and, therefore, the crack initiation stress there is taken as the propagation strength σ_{cr} rather than the concrete tensile strength σ_{ct}. It will be assumed that the crack which initiates at the heel propagates horizontally along the dam-foundation interface (fig. 4.9a) without dipping into the rock (fig. 4.9b). This implies that the rock is sufficiently stronger than the dam-foundation joint. When such a crack is allowed (see Problems 4.4, 4.5 and 4.6), it is treated as a smeared crack in the bottom row of elements in the dam mesh. The presence of shear keys into the foundation is not explicitly considered although sliding can be prevented by specifying the coefficient of friction to be a large number.

4.4.5 Planes of Weakness

The present version of the computer program accounts for planes of weakness in the dam such as construction joints and initial cracks. A plane of weakness can be defined at the center point of an element by its orientation and either a reduced tensile strength σ'_{ct} or a reduced propagation strength σ'_{cr}. Cracking in such an element can occur along the plane of weakness if the tensile stress normal to the plane, σ_{nt}, exceeds σ'_{ct} (initiation) or σ'_{cr} (propagation), or it can occur on the plane of the maximum principal tension σ_{pt} if this stress exceeds

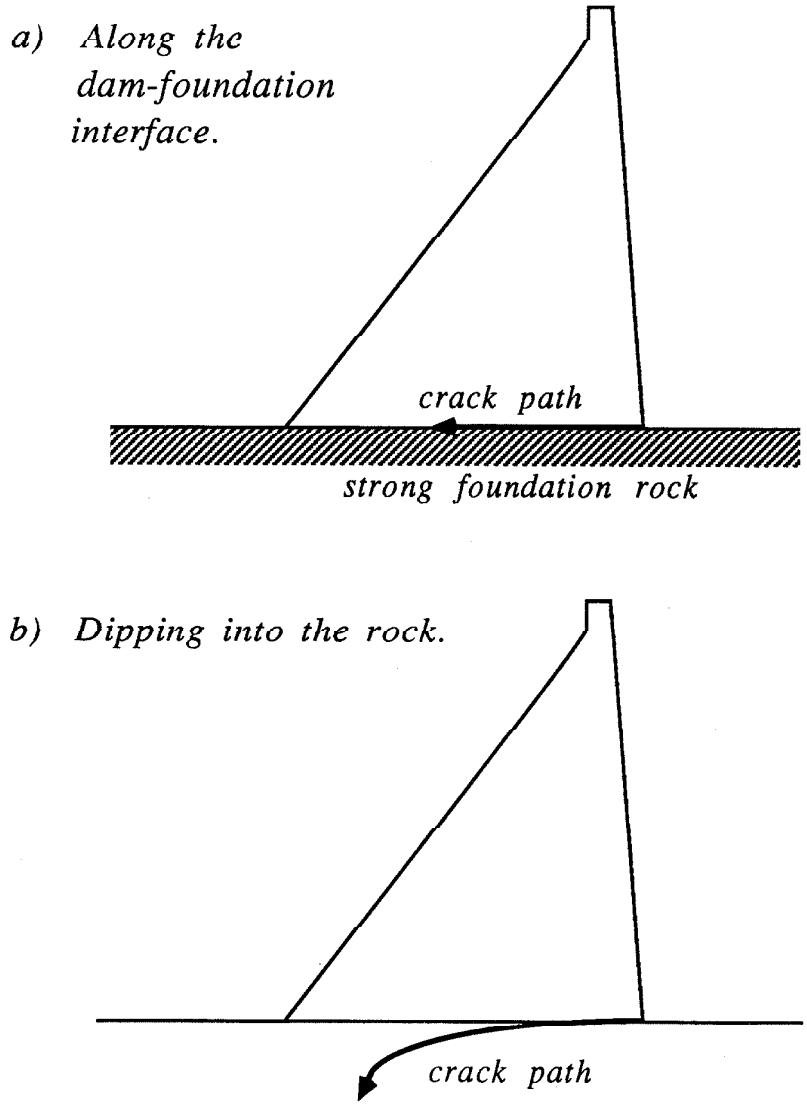

Figure 4.9. Crack propagation from the heel of the dam.

σ_{ct} (initiation) or σ_{cr} (propagation). The ratios σ_{pt}/σ_{ct} and σ_{nt}/σ'_{ct} (initiation) as well as σ_{pt}/σ_{cr} and σ_{nt}/σ'_{cr} (propagation) are output by the program when they exceed unity to aid in the selection of which crack to form. The ultimate decision lies with the user through interactive programming.

4.5 Numerical Analyses

In safety evaluation studies of concrete gravity dams, a precise definition of the initial state throughout the body of the dam is required a priori. Weak planes and previously developed cracks influence the dynamic response of the dam. As will be seen later, the assumed initial state affects the resulting pattern of cracks.

In this section, six numerical examples are presented (Problems 4.1 through 4.6). Several cases of cracks are considered to obtain insight into the nonlinear dynamic behavior of the system. Rocking and sliding of fully cracked sections are investigated, and possible modes of failure are identified. The influence of cracks on dam-water interaction is also demonstrated.

The basic problem considered and the finite element discretization were described in Section 3.6. In Problems 4.2 and 4.3, slanted grids are employed to avoid the coupling effects in cracked elements since the stiffness parallel to the crack is retained. The coefficient of friction μ_c is set equal to 0.75, the shear retention coefficient α_s to 0.0, the concrete tensile strength σ_{ct} to 600 psi, and the critical stress intensity factor k_{cr} to 2000 lb/in$^{1.5}$ (see, for example, [4]); other parameters are kept the same as in Section 3.6. The tangent constitutive matrices given in equations (4.1) and (4.3) are used for open and closed crack cases, respectively, except for Problem 4.6, which involves unspecified crack patterns, where the definitions of equations (4.2) and (4.4) are adopted instead. Water cavitation is monitored following the procedures of Chapter 3, with 0.5% stiffness-proportional damping added to the water in its fundamental mode. Numerical damping is added to provide some damping to the high frequency response; the integration parameters γ, β and α_B are set equal to 0.7, 0.36 and -0.2, respectively.

The ground motions used are the S00E and vertical components of the 1940 El Centro earthquake pictured in fig. 2.8; both components are scaled amplitude-wise by 1.5. The sampling points of the input ground accelerations are 0.02 sec apart, and the time step used for the time domain analysis is 0.005

sec; linear interpolation is employed to obtain the ground accelerations at these intervals. According to reference [12], features of numerical time integration schemes (such as stability and convergence) may depend not only on the integration parameters but also on the chosen time step size. No difficulties were apparent in this regard.

4.5.1 Problem 4.1

Consider first the simple problem of an initial horizontal crack near the top of the dam. The crack is placed along the $10th$ row (elements 73 through 80), 70.4 ft from the crest (fig. 4.10). Such a crack could develop in the presence of reduced tensile strength along lift joints. Only the single crack was considered; no other cracks were allowed to initiate.

The analysis was carried out first with the stiffness-proportional viscous damping retained in cracked elements at all times. This was the very first computer run attempted, and it is included here to demonstrate the role of stiffness-proportional damping in connection with crack modeling. Fig. 4.11 displays the time histories of the vertical component of normal stress in elements 65 and 81 which show remarkably high tensile stresses; elements 65 and 81 are on the upstream face above and below the cracked row, respectively. The peaks of these tensile stresses were synchronized with crack opening in element 73. Such high tension close to and normal to the open crack is certainly unrealistic and, as was mentioned before, is a consequence of the large viscous forces developed across the cracked elements at times of crack opening.

The algorithm was modified by removing the stiffness-proportional damping from an element as soon as it experiences cracking, and the previous results were recomputed by a second analysis (fig. 4.12). The modification leads to virtually tension free crack surfaces and was included for all other results.

Fig. 4.13 shows the time history of crack opening and closing in elements 73 through 80. Since the crack state is monitored at the center point of each cracked element, the obtained profile of the crack state is represented in a discrete fash-

ion. The rocking motion pivots on elements 73 and 80 with a maximum period of about 0.6 seconds. In a finer mesh, the pivots would each include several elements; in such a case, the contact would be better represented. This dependence on mesh fineness certainly affects the predicted stresses at the pivots and possibly the rocking and sliding motions as well. In the present analysis, the maximum compressive stresses in elements 73 and 80 (fig. 4.14) are within the linear range of typical concrete, as were the compressive stresses elsewhere.

Despite the release of the tensile stresses normal to the crack (fig. 4.12), contours of the maximum principal stress (tension) shown in fig. 4.15 reveal a zone of substantial tension nearby. This tension occurs on a plane nearly perpendicular to that of the crack near the upstream end, and separate analyses showed that the tension increases in cases of higher coefficient of friction. Investigation of the stresses in the vicinity of the crack indicated that such tension results from high shear stresses transferred across the pivot element 73. However, inadequate mesh fineness prevented an accurate assessment of this mechanism which could lead to a vertically oriented crack. The only other tension large enough to initiate cracking occurs at the heel of the dam as shown in fig. 4.15.

The relationship between the shear in the pivot element 73 and the horizontal tension in element 82 is shown in fig. 4.16; similar results for elements 80 and 87 on the downstream side appear in fig. 4.17. The smaller tensions generated in element 87 are believed due to the inclination of the downstream face which gives the upward thrust parallel to the downstream face a horizontal component (fig. 4.18).

In fig. 4.19 the time histories of the vertical displacements at nodes 1, 130 and 139 are shown. Despite the fact that the smeared crack model does not provide for a precise geometric definition of cracks, reasonable estimates of the opening displacements may be obtained from the displacements normal to the crack line; as shown, a maximum opening displacement of about 0.1 ft is predicted at the upstream face with a duration of 0.2 to 0.3 sec. Any water inflow into the crack was neglected; open cracks were subjected to absolutely

zero normal stress.

In addition to the rocking motion of the detached block, the time histories of the horizontal displacements at nodes 1, 130, and 139 (fig. 4.20) show noticeable sliding in the downstream direction leading to a permanent slip of about 1.9 ft. The actual sliding displacement, obtained by multiplying the element shear strain by the element height, appears in fig. 4.21. Incidentally, in the first analysis (retaining the stiffness-proportional damping of the cracked elements) the permanent slip reached only 0.05 ft.

Direction and magnitude of the sliding motion depend, among other factors, on the ground motions, water level in the reservoir, orientation of cracks (see Problems 4.2 and 4.3), and the shear transfer mechanism. Elevation of the crack was also found to be an important factor. For instance, in a separate analysis an initial crack was assumed in the $12th$ row instead of the $10th$ (about 12 ft lower), and the predicted permanent slip was only 0.75 ft. Increasing the frictional resistance along the crack diminishes the sliding while enhancing the rocking motion. Numerical experience has confirmed that increasing the coefficient of friction results in more side sway at the top, larger crack opening displacements, and longer rocking periods.

The cracking of the dam also affects the hydrodynamic pressures in the reservoir and, in turn, the amount of cavitation. This is demonstrated via fig. 4.22 which displays the time histories of the volume strain in the water elements along the dam face (elements 1 through 16) together with the corresponding case without any crack in the dam. When crack opening takes place, virtually no cavitation occurs because of a reduction in the excitation to the water from the dam motion. Fig. 4.23 shows that, although the accelerations of the cracked dam are higher, the peaks occur as sharp spikes, and the low frequency response (which is more effective in generating hydrodynamic pressure) is actually reduced.

To examine the role of the mass-proportional damping in restraining the response of the top part of the dam, a separate analysis was carried out with both mass and stiffness-proportional damping in the amount of 1.5% of critical

each in the fundamental mode of the dam (i.e., a total of 3% of critical at the fundamental mode of the dam). The predicted permanent slip was about 1.7 ft, and the rocking response as indicated by crack opening and closing was also very similar to that presented in fig. 4.13. Despite such rather mild effects observed in this particular case, mass-proportional damping was excluded throughout this study.

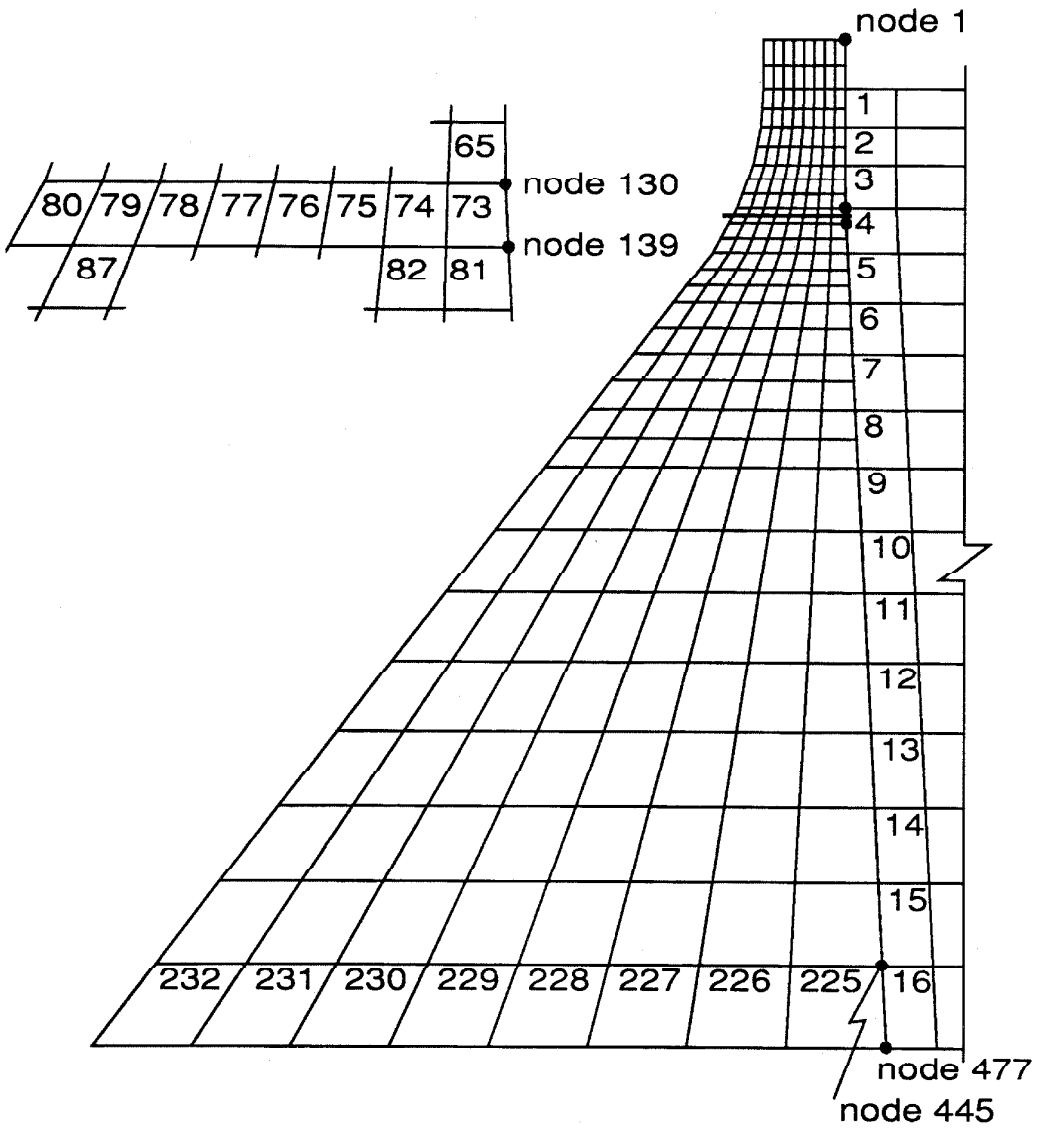

Figure 4.10. Finite element mesh and element and node numbering for Problem 4.1. See fig. 2.7 for the complete mesh.

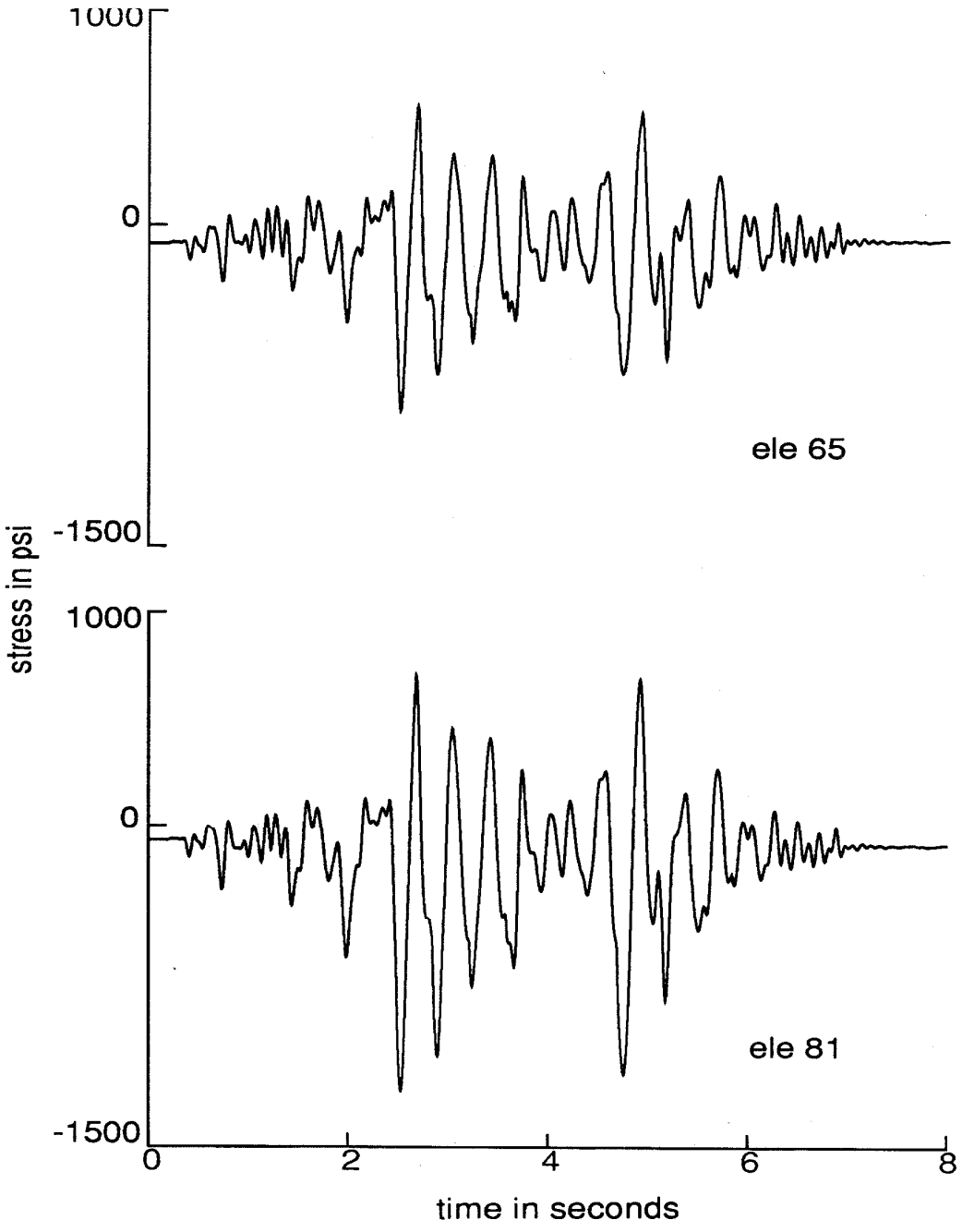

Figure 4.11. Time histories of the vertical component of normal stress above and below the crack for Problem 4.1. Stiffness-proportional damping is retained at all times.

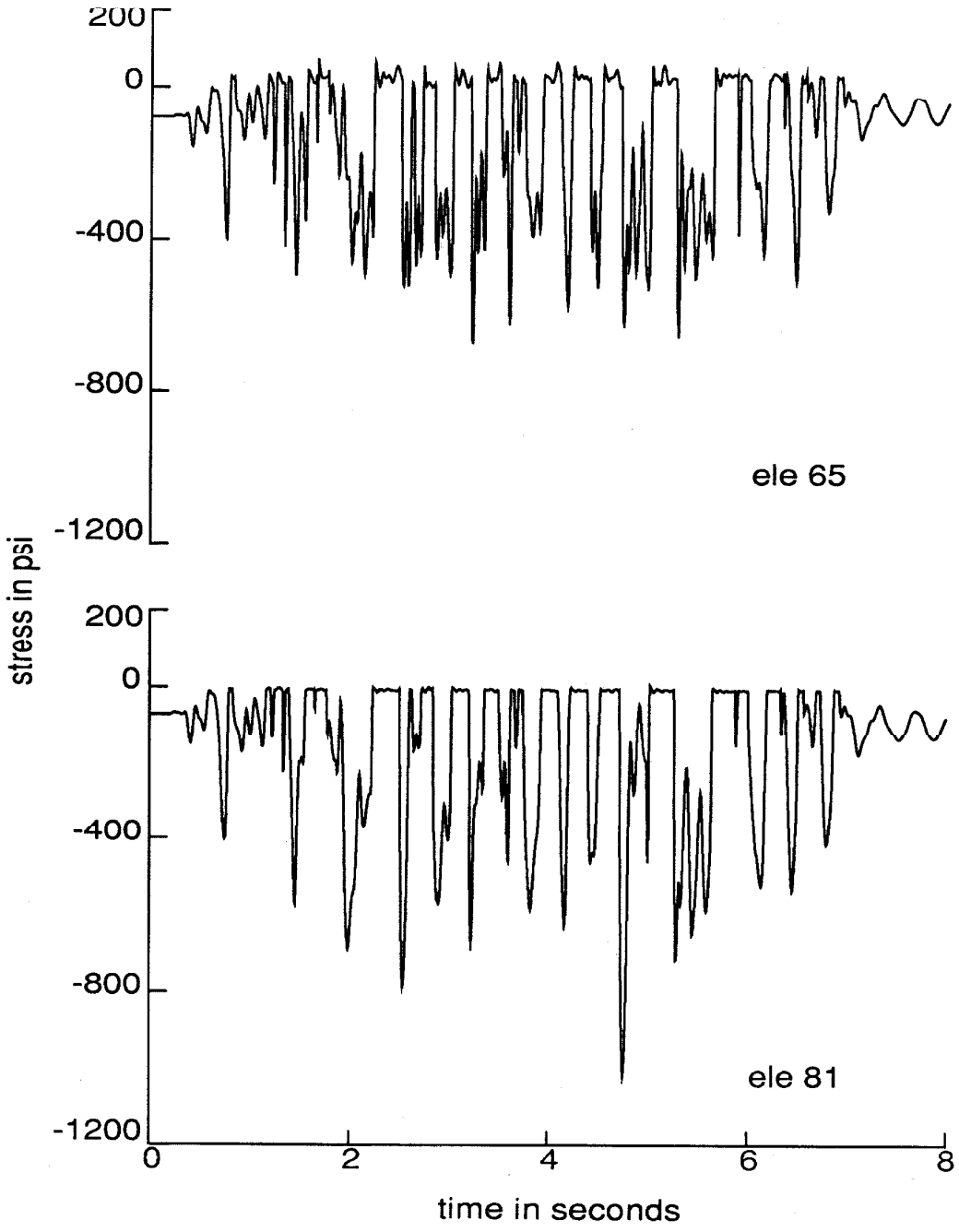

Figure 4.12. Time histories of the vertical component of normal stress above and below the crack for Problem 4.1. Stiffness-proportional damping is removed in cracked elements after cracking.

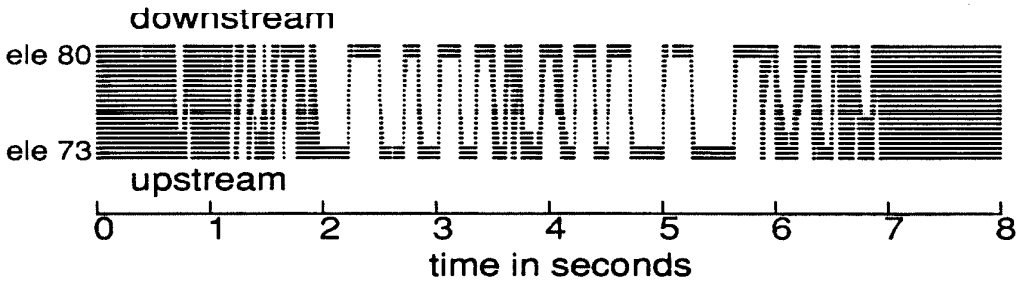

Figure 4.13. Time history of crack opening and closing at elements 73 through 80 for Problem 4.1. Solid lines (three per element) denote a closed crack.

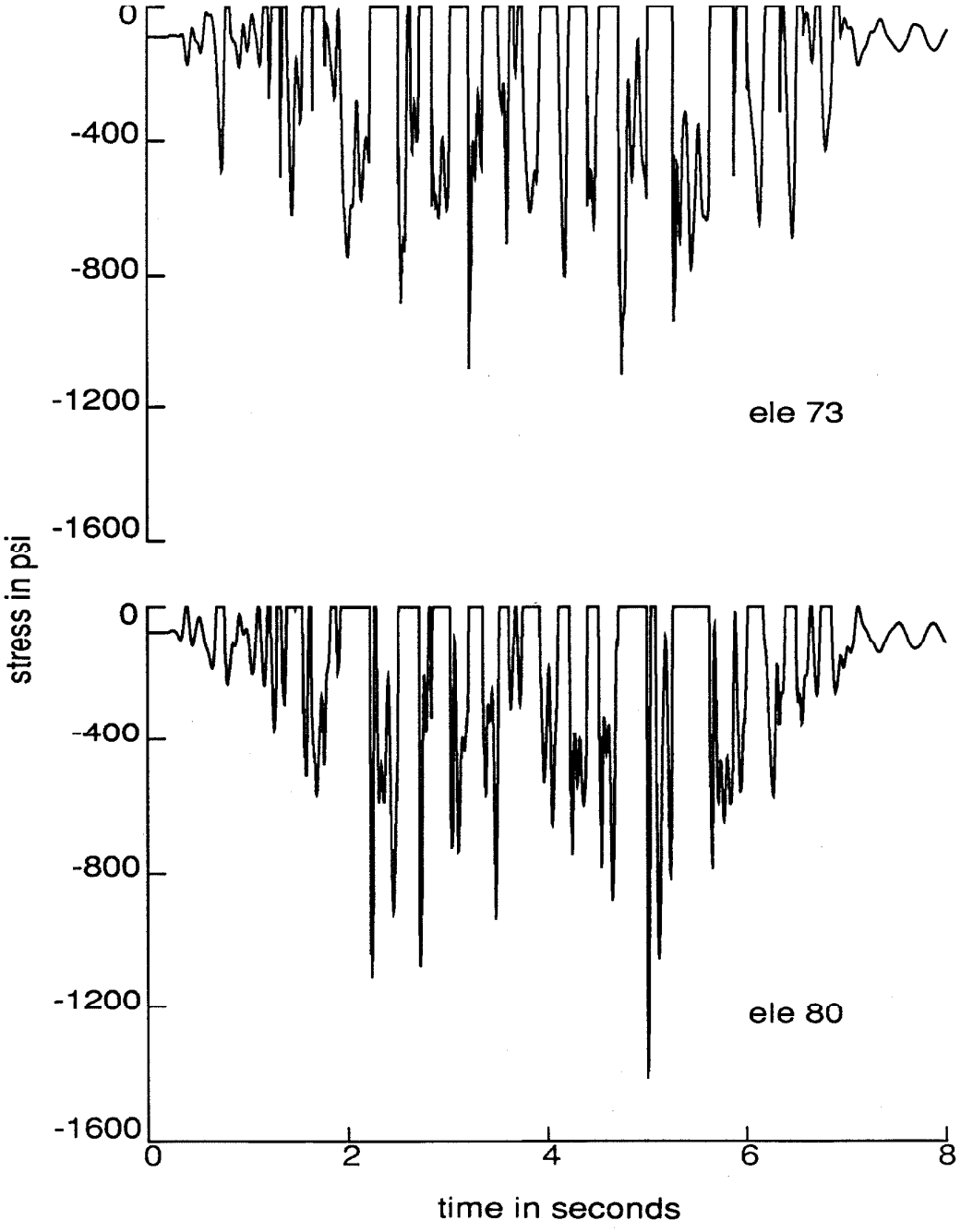

Figure 4.14. Time histories of the vertical component of normal stress at the crack level (elements 73 and 80) for Problem 4.1.

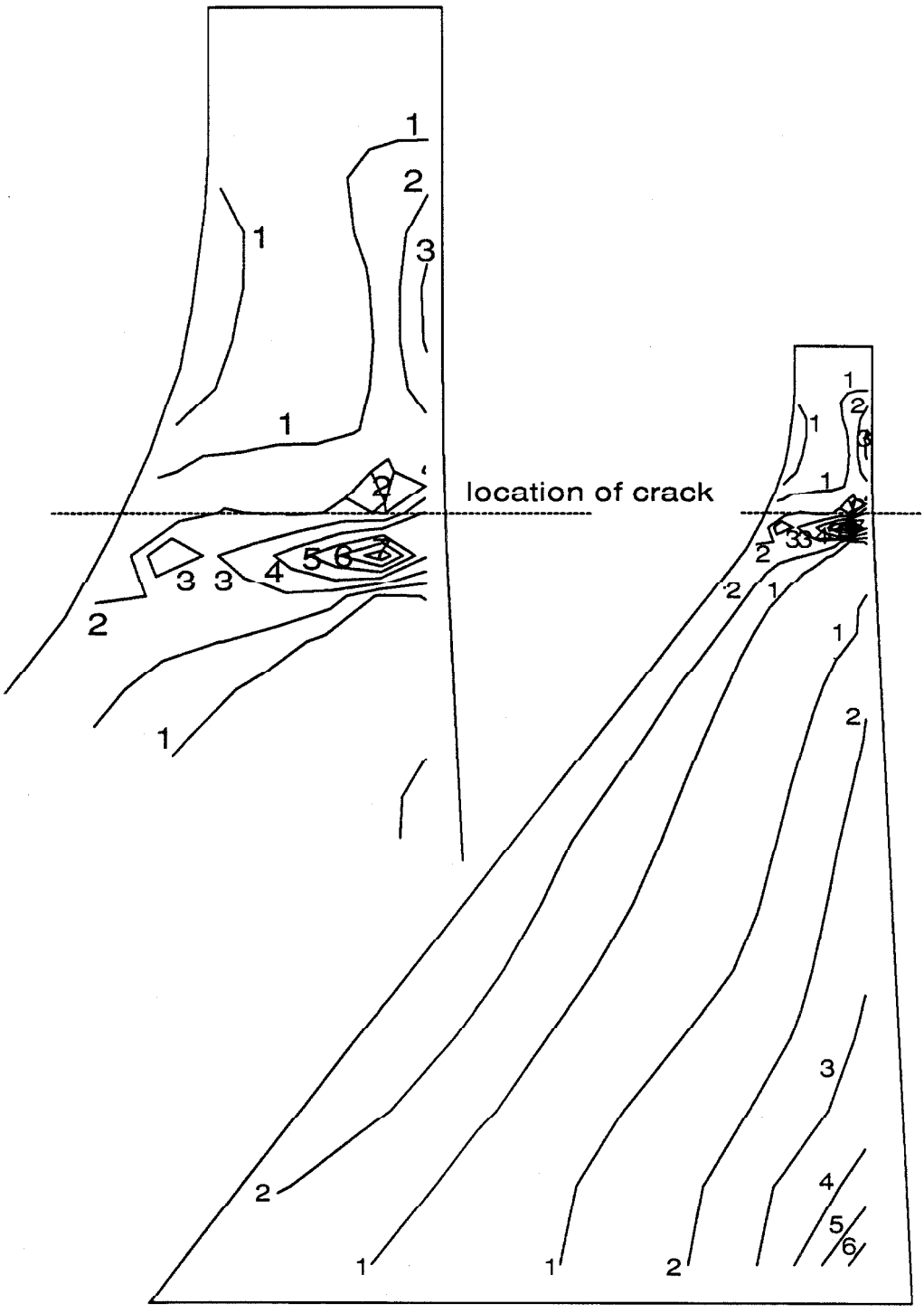

Figure 4.15. Contours of the maximum principal stress (tension) in the dam for Problem 4.1. Numbers indicate contour values in hundreds of psi.

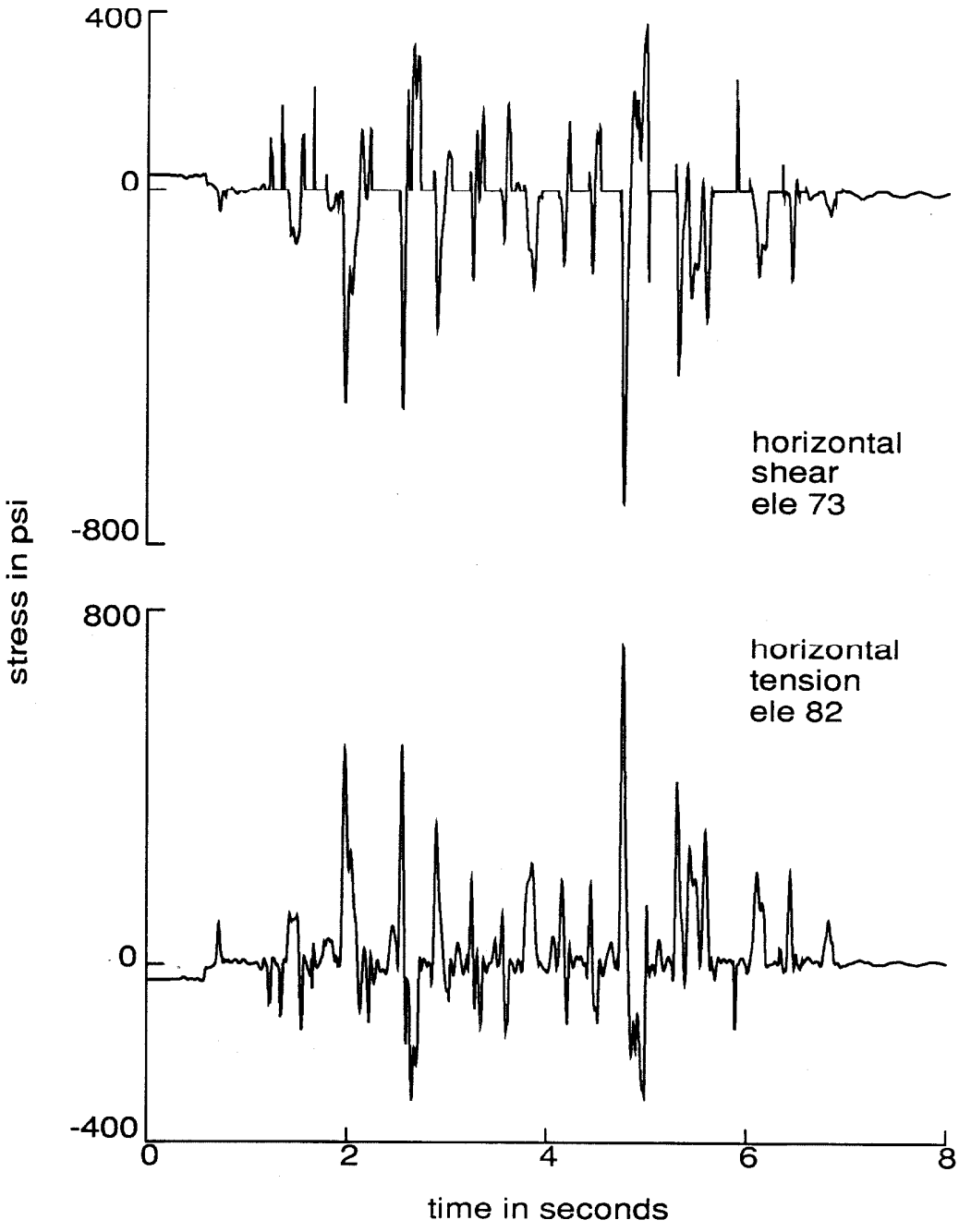

Figure 4.16. Horizontal crack shear in element 73 and horizontal tension in element 82 for Problem 4.1.

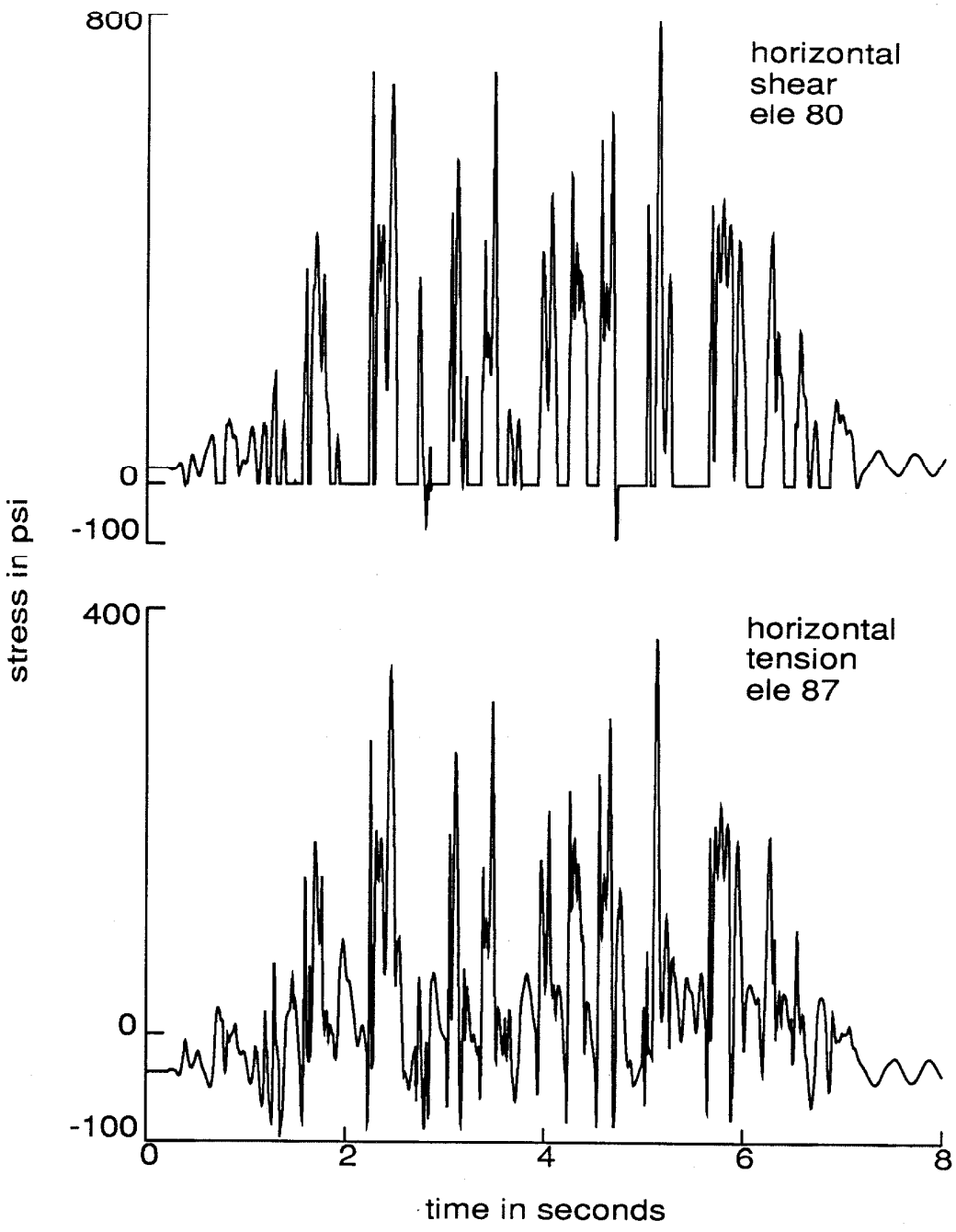

Figure 4.17. Horizontal crack shear in element 80 and horizontal tension in element 87 for Problem 4.1.

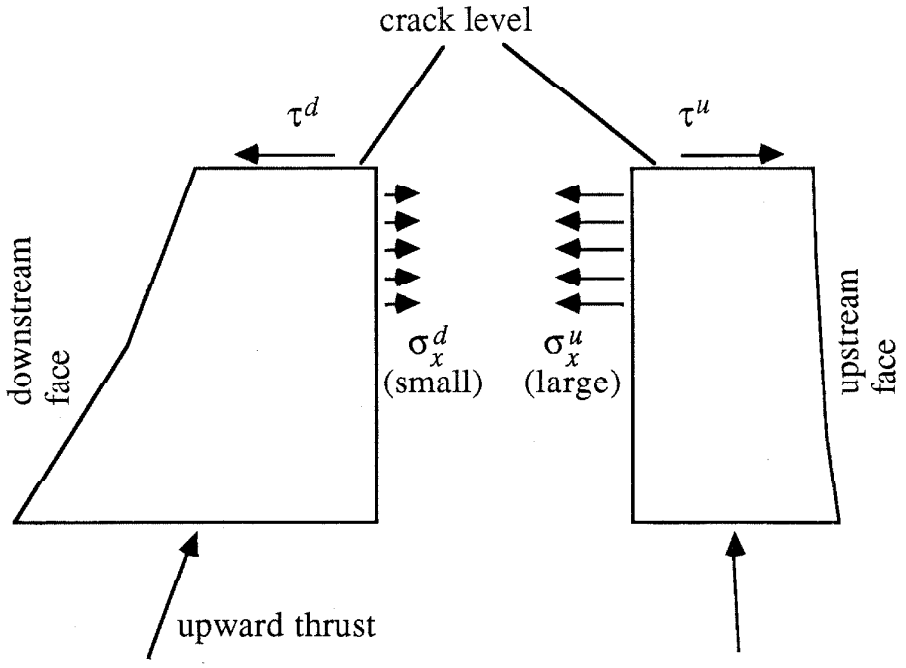

τ = shear stress transferred across the crack

σ_x = horizontal tension on vertical plane

u = upstream side

d = downstream side

Figure 4.18. Equilibrium of horizontal forces at times of development of maximum horizontal tension for Problem 4.1.

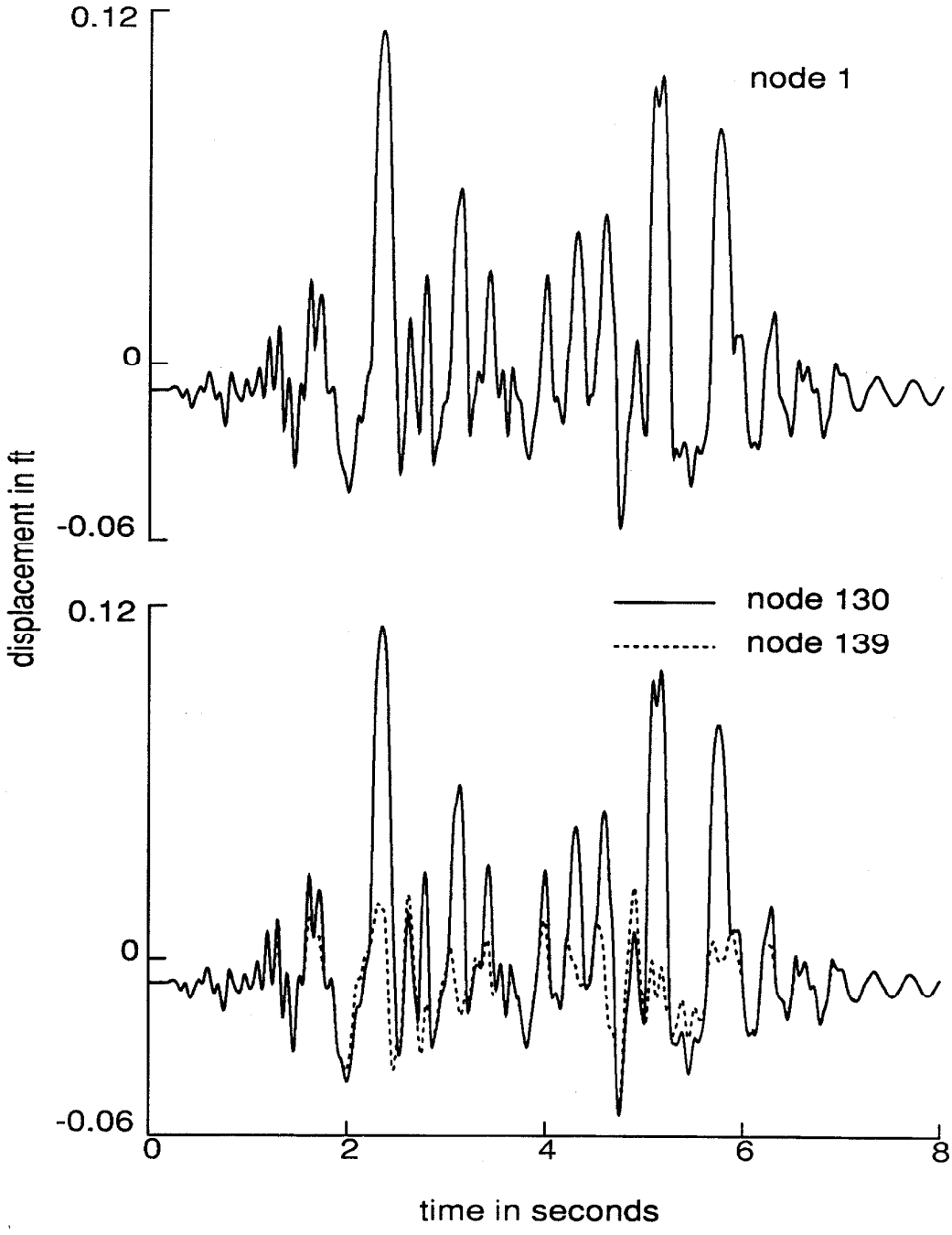

Figure 4.19. Time histories of the vertical displacements at nodes 1, 130, and 139 for Problem 4.1.

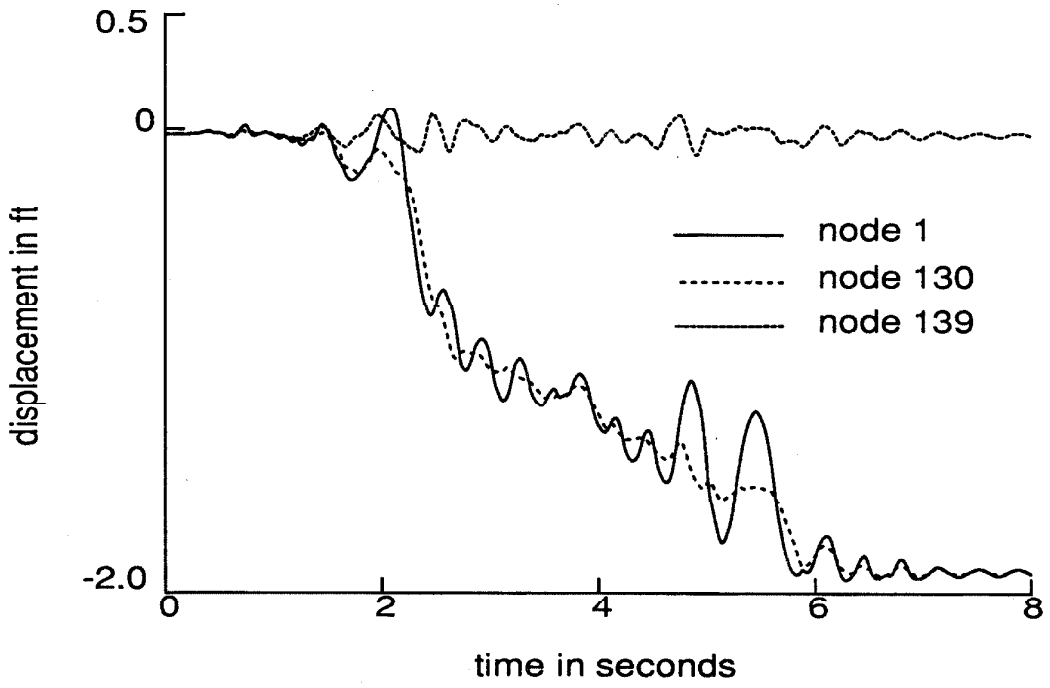

Figure 4.20. Time histories of the horizontal displacements at nodes 1, 130, and 139 for Problem 4.1.

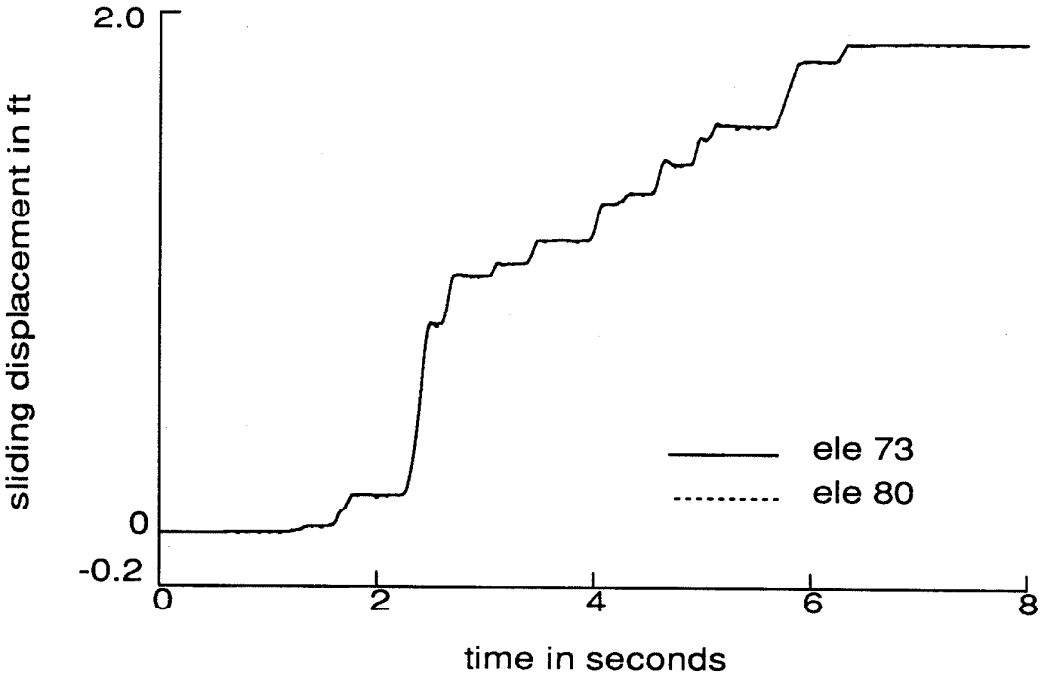

Figure 4.21. Time histories of the sliding displacements along the crack plane (elements 73 and 80) for Problem 4.1.

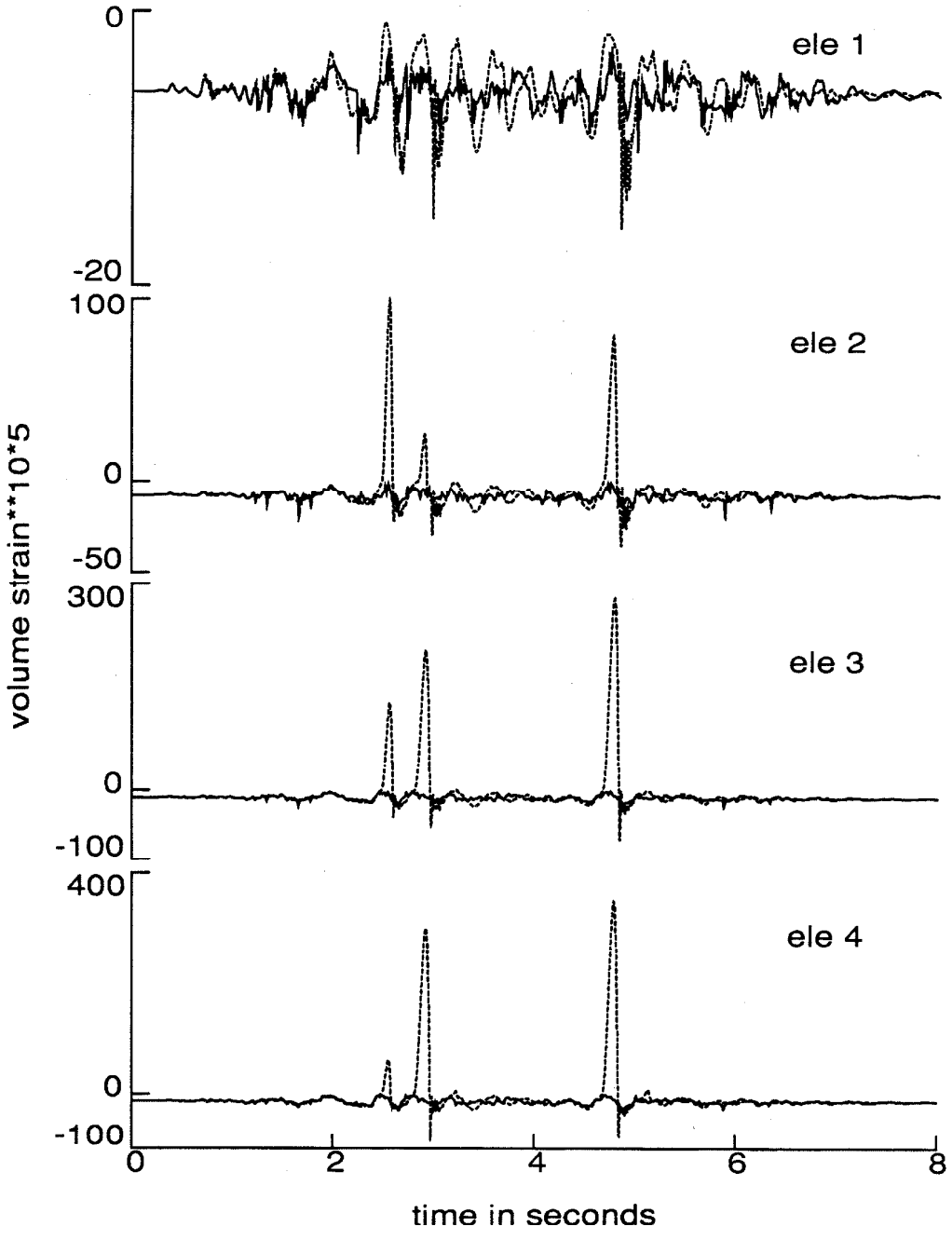

Figure 4.22. Time histories of the absolute volume strain in the water along the dam face with cavitation permitted. Cracked dam (solid line, Problem 4.1) and uncracked dam (dashed line).

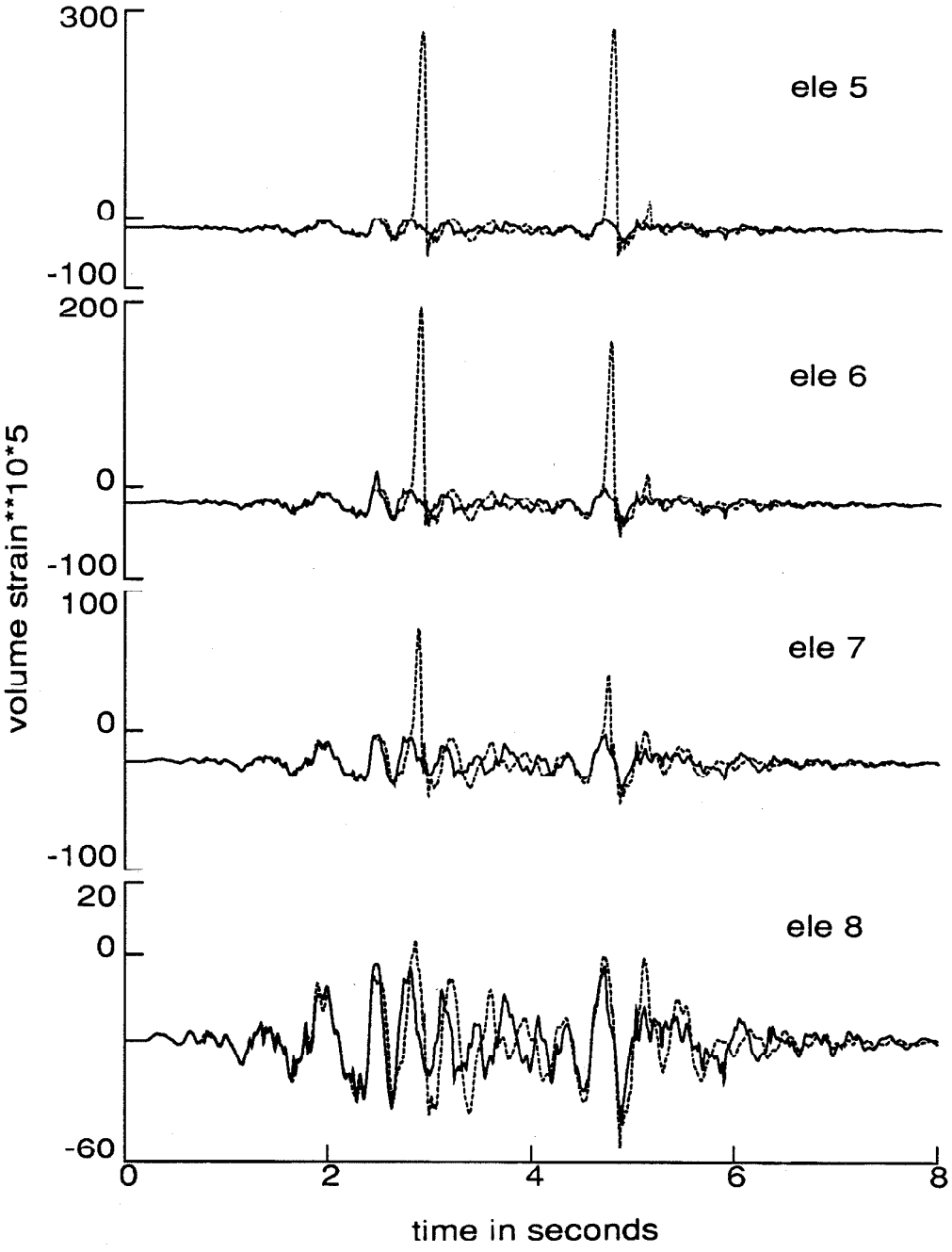

Figure 4.22. Continued.

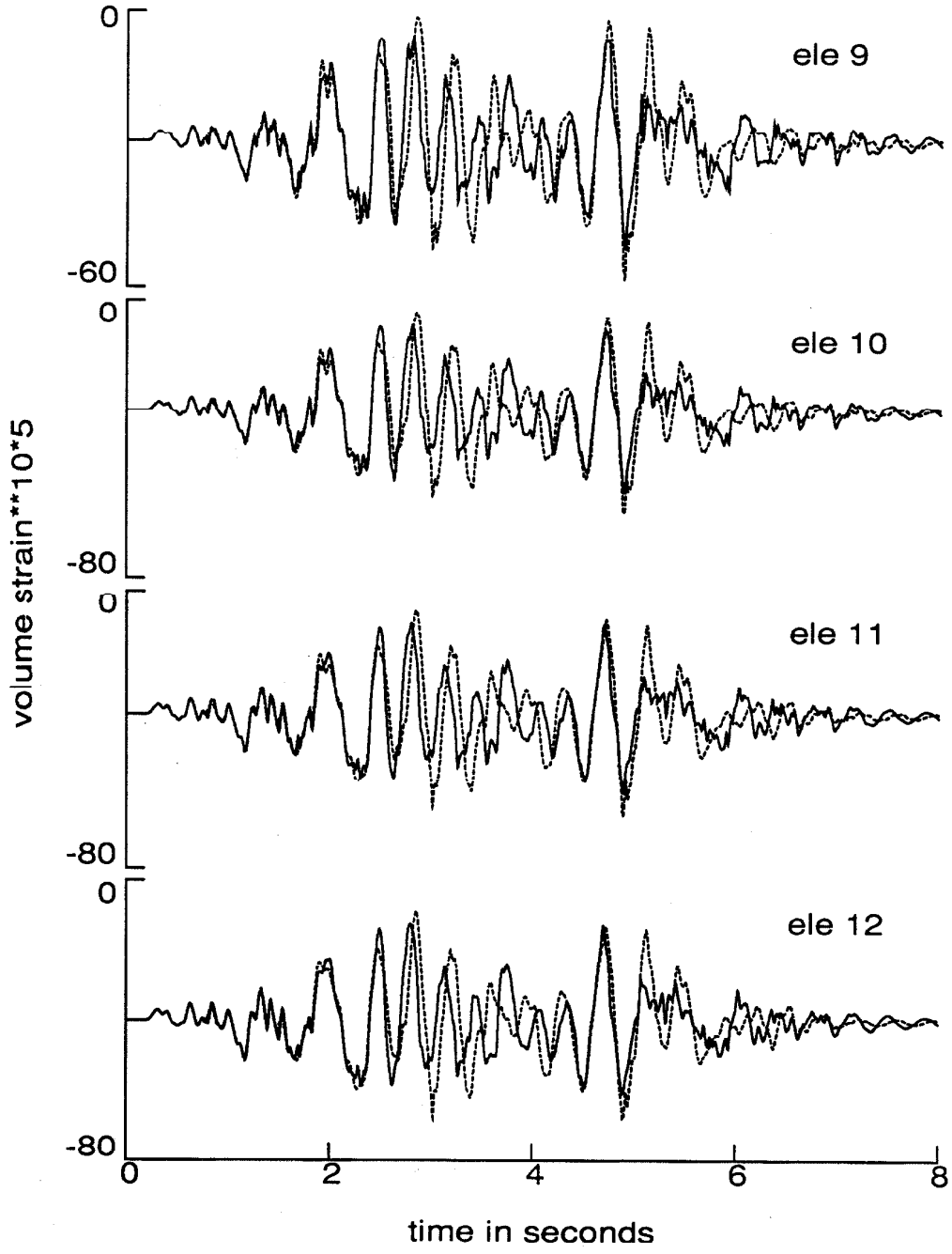

Figure 4.22. Continued.

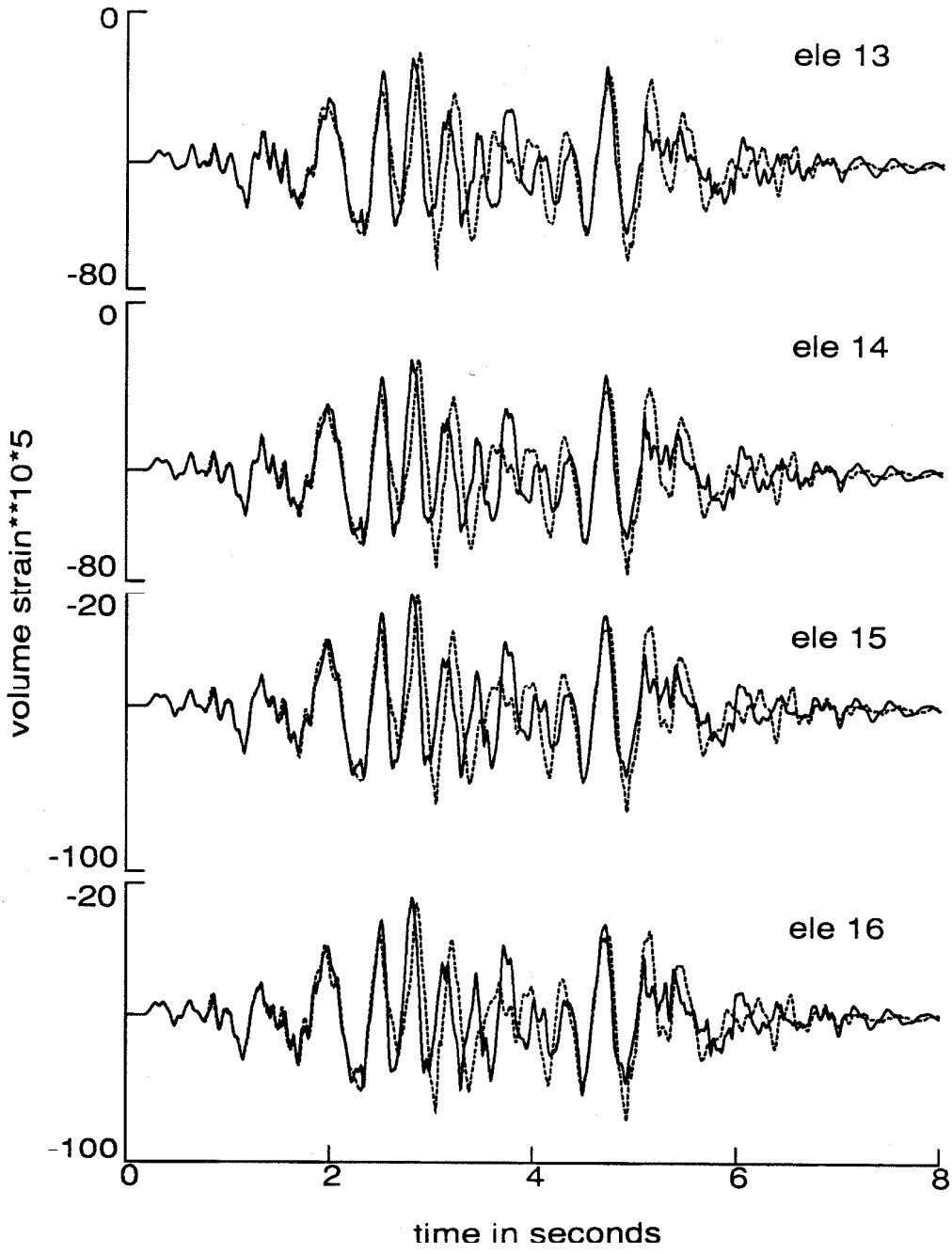

Figure 4.22. Continued.

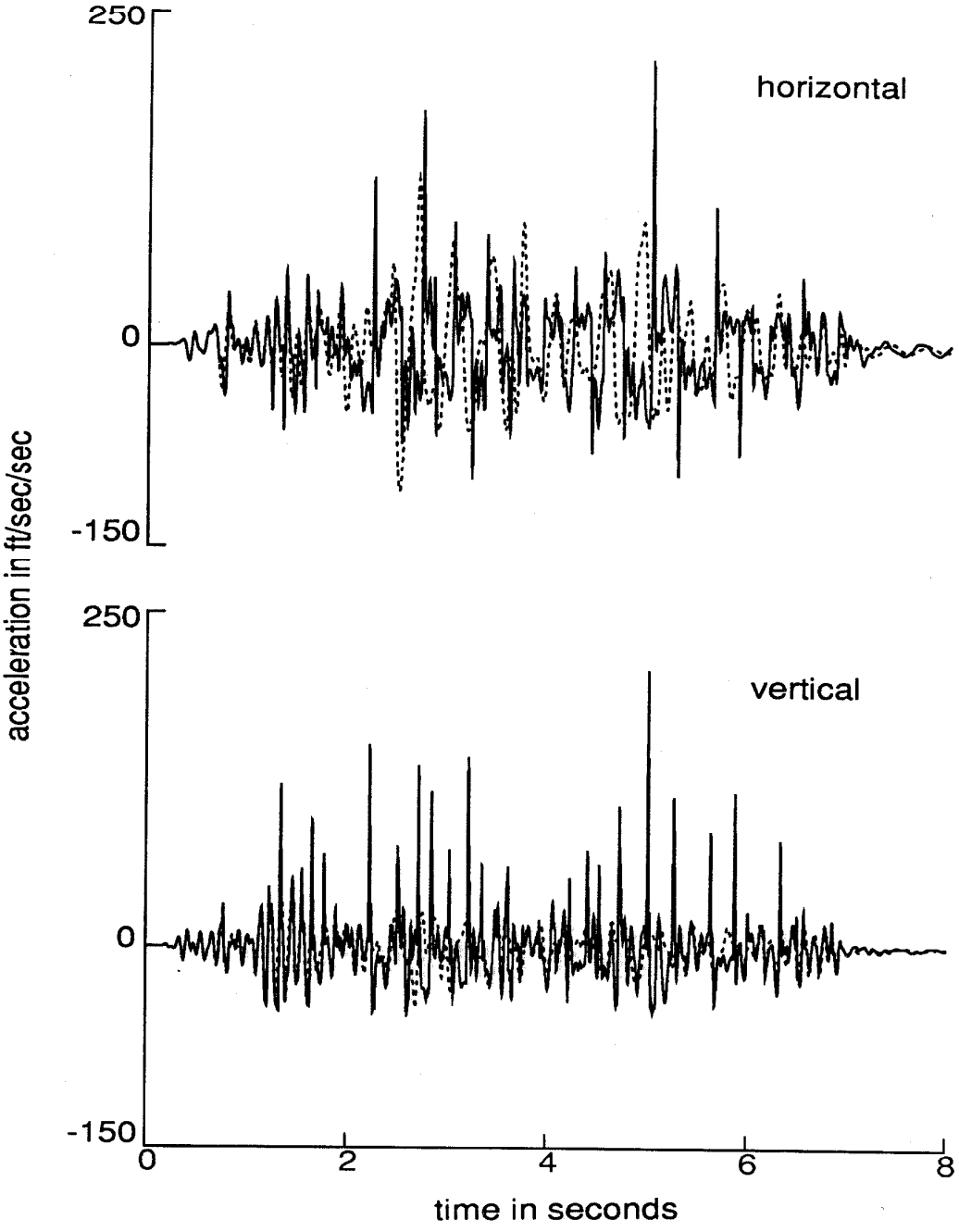

Figure 4.23. Time histories of the accelerations at node 1 with cavitation permitted. Cracked dam (solid line, Problem 4.1) and uncracked dam (dashed line).

4.5.2 Problem 4.2

In cases where the tensile strength along lift joints is comparable to that of plain concrete, propagating cracks will not necessarily follow the lift joints; inclined cracks may result depending on the stress field and isotropy of the fracture strength. This study considers the case of an initial straight crack (fig. 4.24) which inclines at an angle of 19^o and meets the upstream face 86 ft below the crest. The dip of the crack upstream could result from an initiation at the downstream face. No further cracking was permitted in the analysis which was carried out with the same system parameters used in Problem 4.1. The results are displayed in figs. 4.25 through 4.28.

The time history of crack opening and closing (fig. 4.25) is similar to that of the horizontal crack (fig. 4.13) although the maximum opening of 0.08 ft (fig. 4.26) is somewhat smaller. Inclining the crack reduces its permanent slip from 1.9 ft to 0.9 ft (fig. 4.27) because the sliding now takes place "uphill". Absence of downhill slip is probably due to characteristics of the ground motions and to the presence of the static water pressure. Tensile stresses high enough to initiate additional cracking again occur close to the crack on a plane nearly perpendicular to it and also at the heel of the dam (fig. 4.28). These stresses close to the crack occur at the downstream end due to the upstream dip of the crack. Although not shown in the figures, little cavitation was present (some in elements 3 and 4), and the compressive stresses in the dam remained everywhere within the linear range.

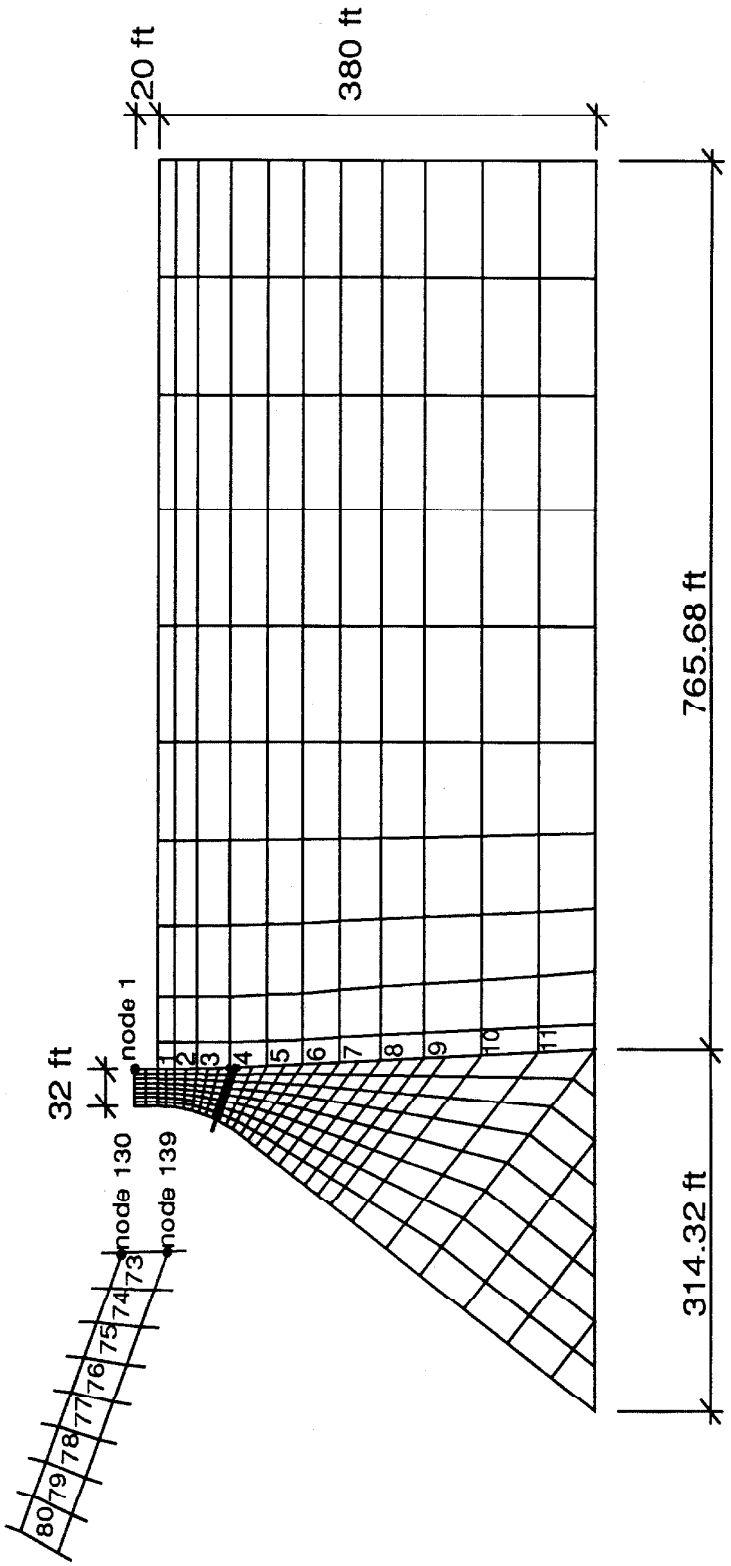

Figure 4.24. Finite element mesh and element and node numbering for Problem 4.2.

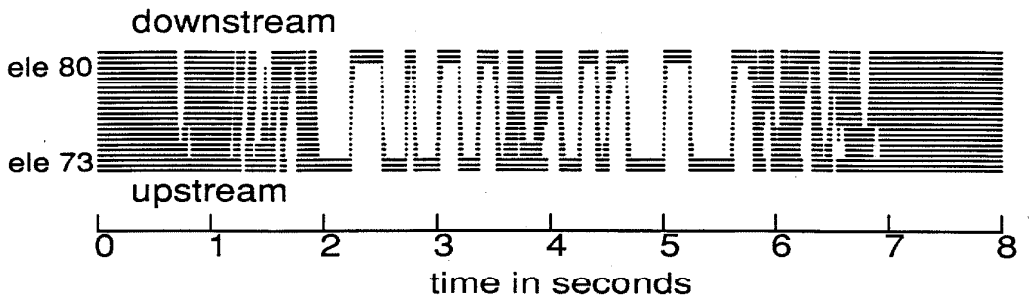

Figure 4.25. Time history of crack opening and closing at elements 73 through 80 for Problem 4.2. Solid lines (three per element) denote a closed crack.

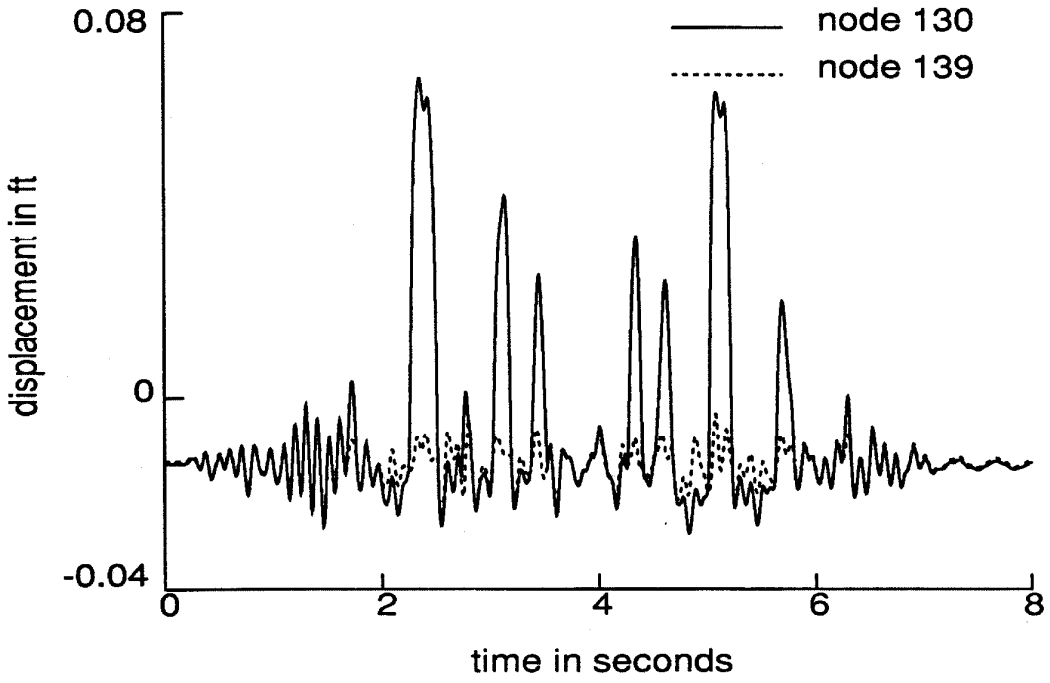

Figure 4.26. Time histories of the displacements at nodes 130 and 139 in the direction normal to the crack for Problem 4.2.

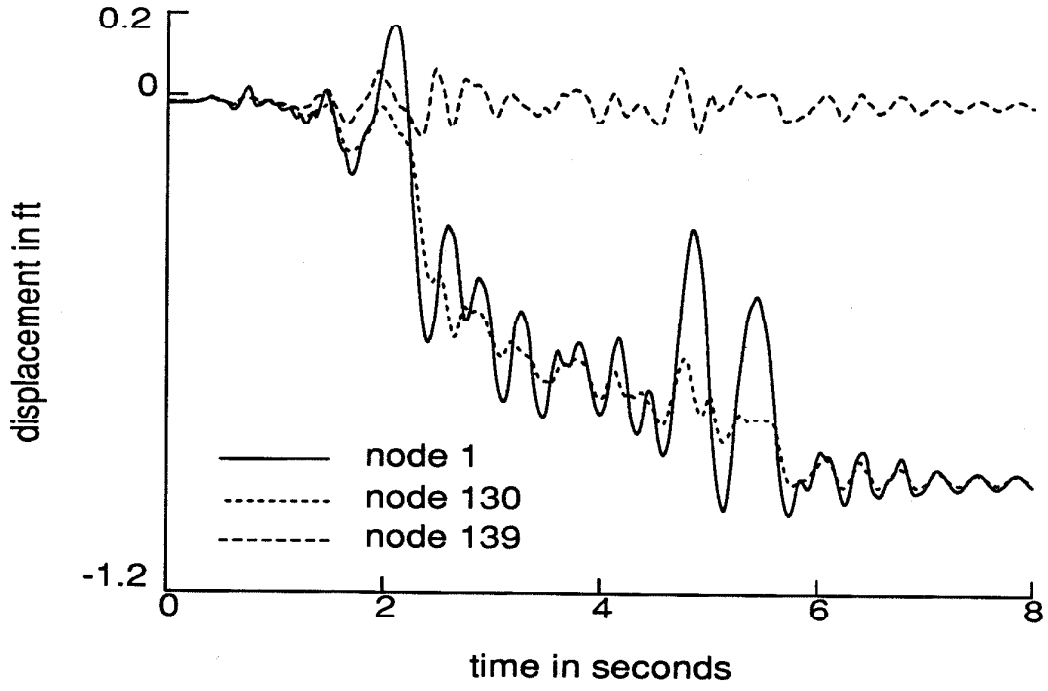

Figure 4.27. Time histories of the displacements at nodes 1, 130 and 139 in the direction tangent to the crack for Problem 4.2.

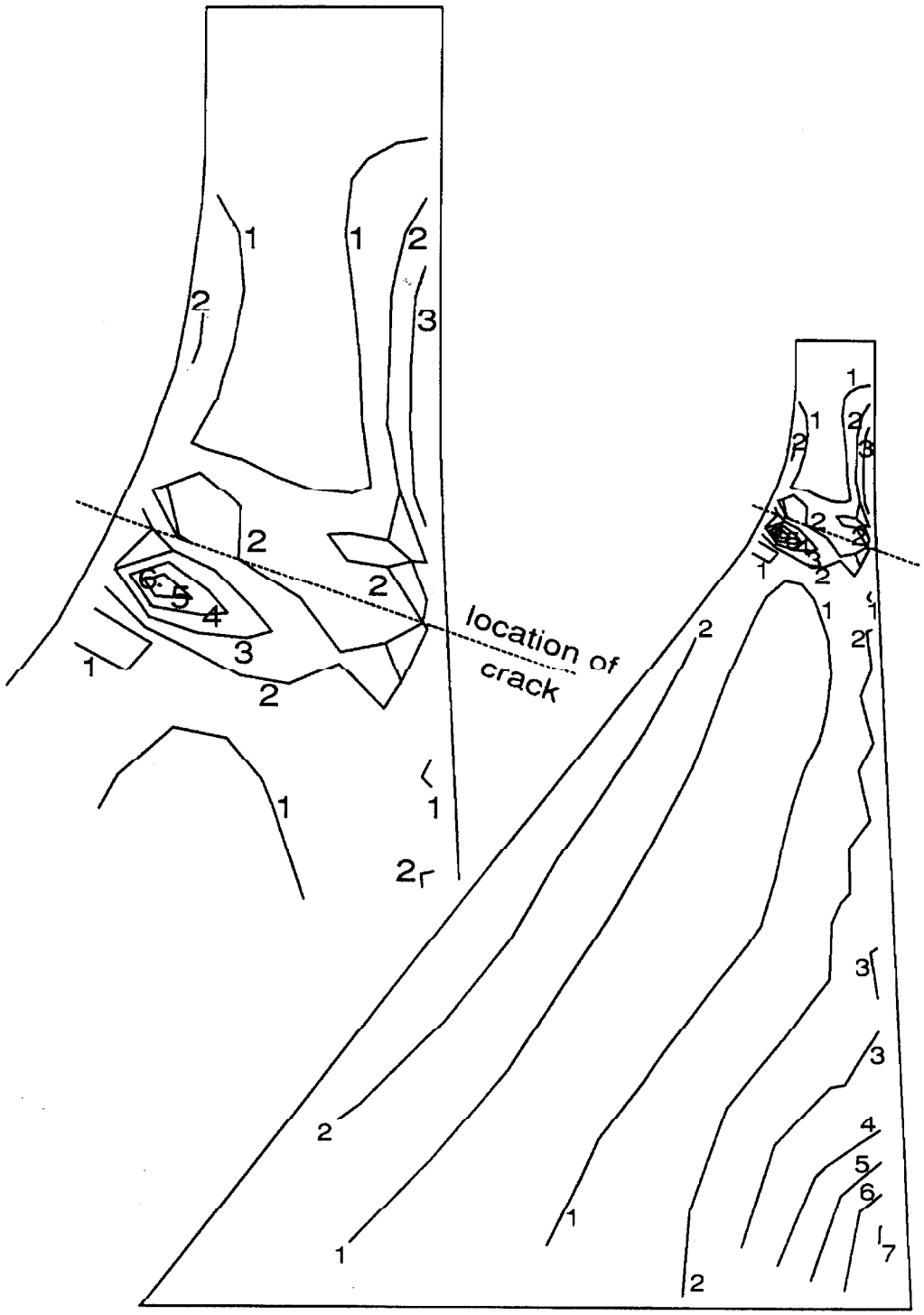

Figure 4.28. Contours of the maximum principal stress (tension) in the dam for Problem 4.2. Numbers indicate contour values in hundreds of psi.

4.5.3 Problem 4.3

Results of Problems 4.1 and 4.2 showed the tendency for the top part of the dam to slide in the downstream direction. Accordingly, the detached block would certainly be susceptible to more sliding if the initial crack dips downstream as shown in fig. 4.29. The crack inclines 18^o downstream and meets the upstream face 76 ft below the crest. The downstream dip could result from an initiation on the upstream face.

To study this case, the slanted mesh of fig. 4.29 is employed with the same system parameters used previously (no other cracking permitted). Figs. 4.30 through 4.33 display the obtained responses. Obviously, the rocking motion has significantly diminished in comparison with that in Problems 4.1 and 4.2. On the other hand, more sliding is evident resulting in larger permanent slip, about 3.4 ft. Contours of the maximum principal stress (fig. 4.33) show similar patterns to those observed in the preceding Problems. The large tension which occurs near the crack returns to the upstream end. Again, little cavitation occurred (some in elements 5, 6 and 8), and compressive stresses remained in the linear range.

It should be noted that the sliding displacements in the cracked elements may be large enough to cause noticeable errors in the small displacement formulation, and a remeshing capability is called for. Significant errors would be present in the stresses at the ends of the crack, but the computed slip of 3.4 ft may be approximately correct because the length of the sliding plane decreased only from 63.8 ft to 60.4 ft, a 5.3% reduction.

Regarding the coupling effects in cracked elements, an interesting observation was made during the course of the computations. Accidently, some nodal coordinates were mistyped which caused the grid lines bounding the crack to deviate about 1.0 degree from being parallel. This resulted in a very stiff response in sliding (permanent slip of only 0.8 ft) and, consequently, larger rocking motion, and also gave rise to a totally erroneous stress field around the crack.

When the stiffness parallel to the crack was removed in the cracked elements (i.e., using equations (4.2) and (4.4)), there was no coupling, and the results were very similar to the present case. Thus, equations (4.1) and (4.3) should be used with great caution.

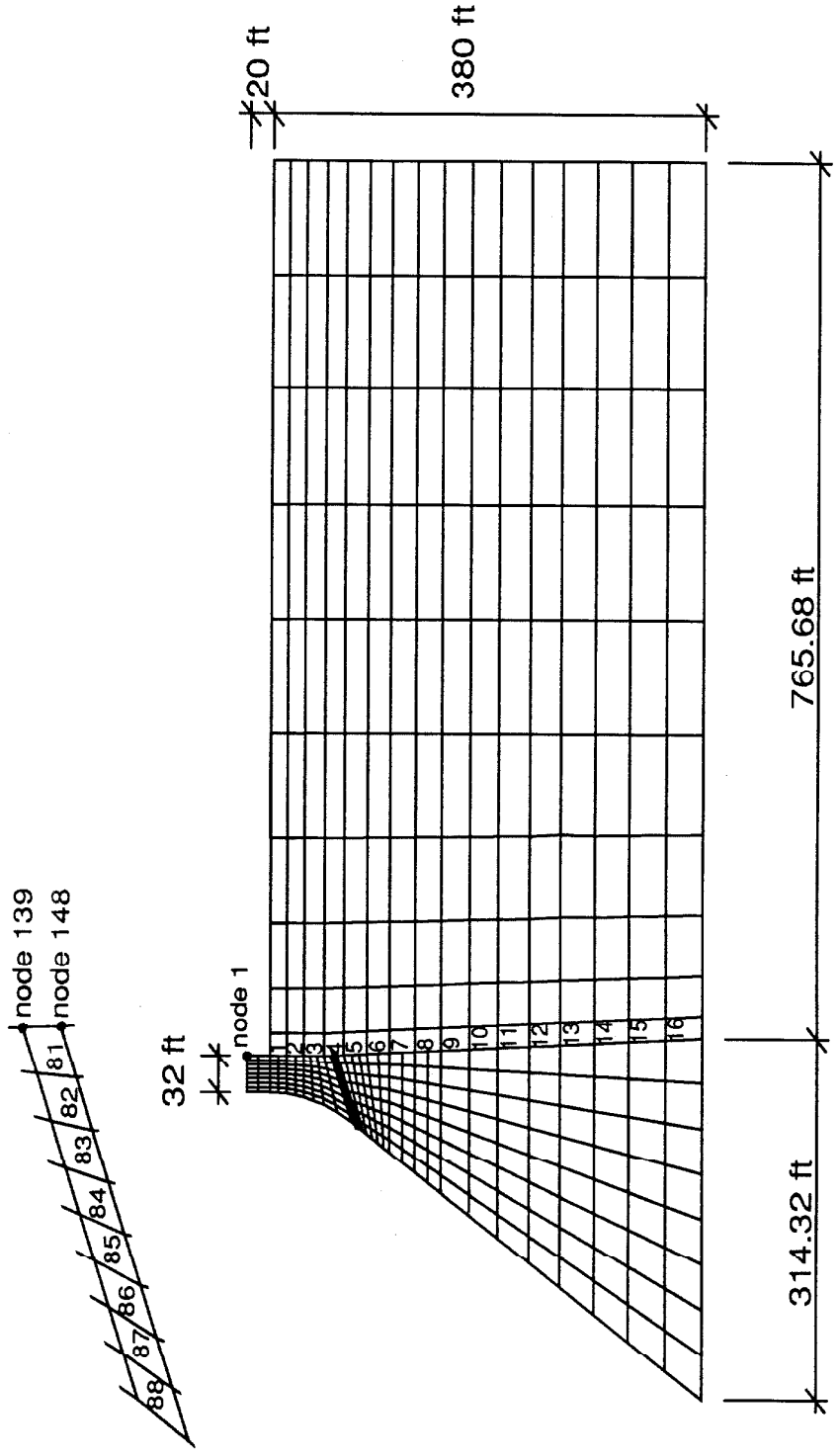

Figure 4.29. Finite element mesh and element and node numbering for Problem 4.3.

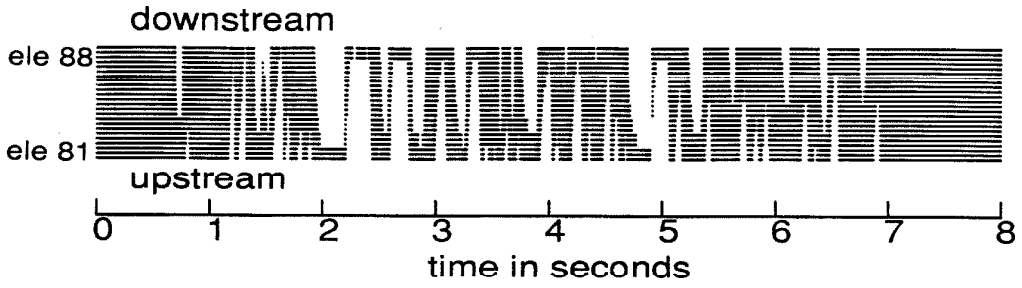

Figure 4.30. Time history of crack opening and closing at elements 81 through 88 for Problem 4.3. Solid lines (three per element) denote a closed crack.

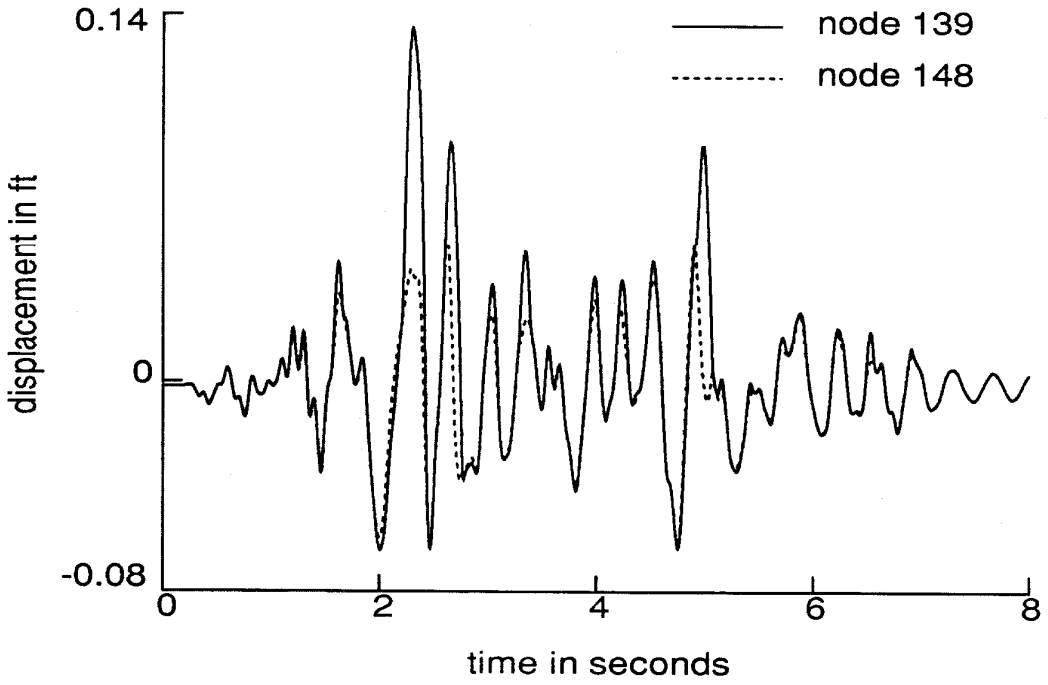

Figure 4.31. Time histories of the displacements at nodes 139 and 148 in the direction normal to the crack for Problem 4.3.

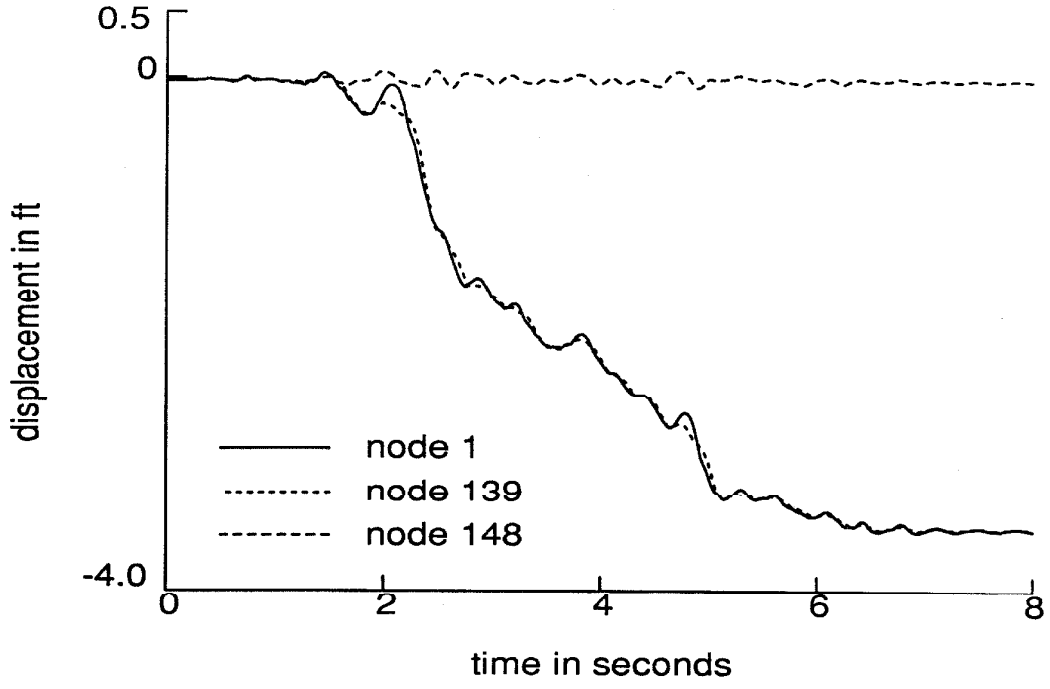

Figure 4.32. Time histories of the displacements at nodes 1, 139 and 148 in the direction tangential to the crack for Problem 4.3.

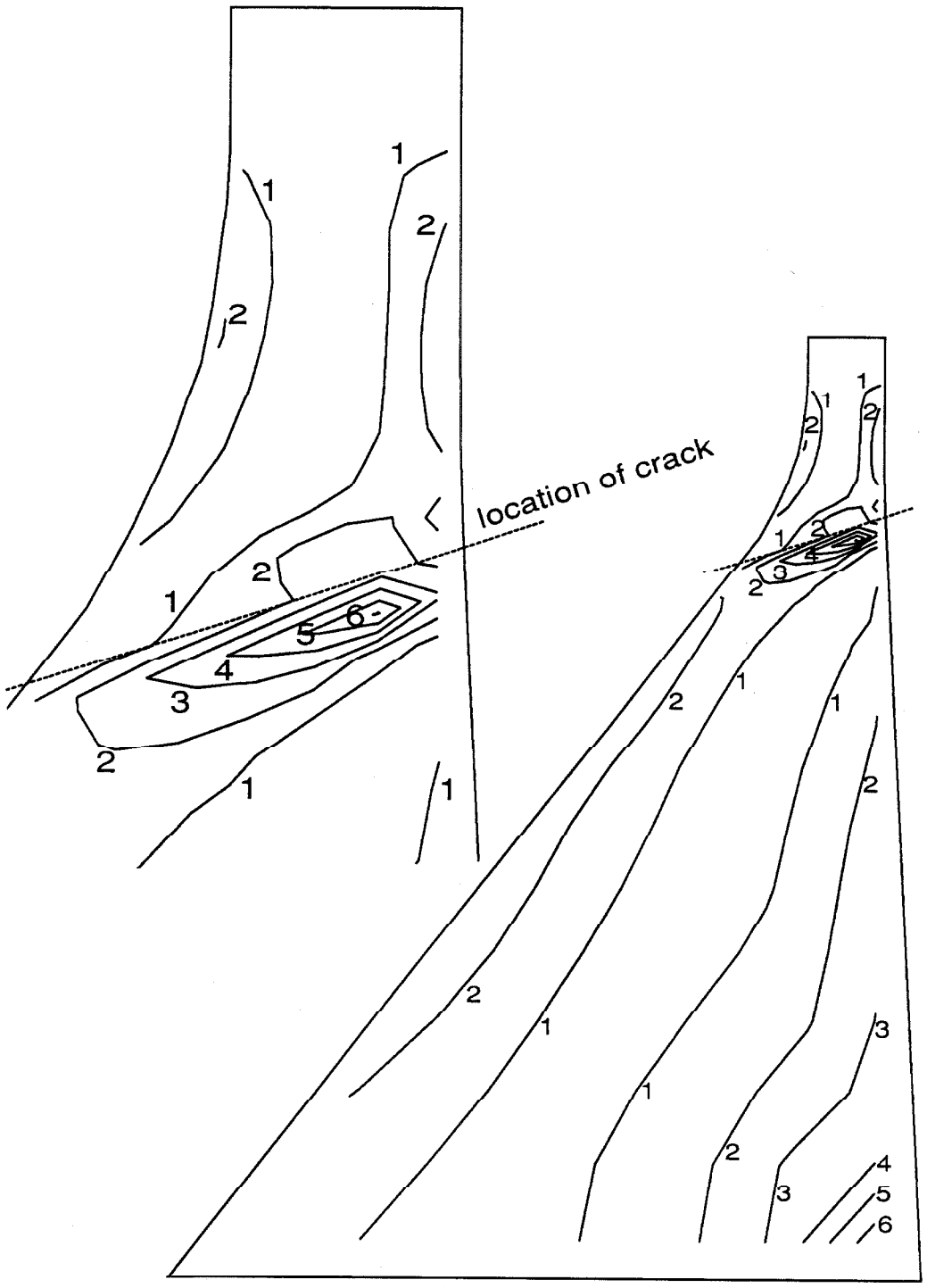

Figure 4.33. Contours of the maximum principal stress (tension) in the dam for Problem 4.3. Numbers indicate contour values in hundreds of psi.

4.5.4 Problem 4.4

This problem examines the behavior of the dam with a single initial crack along the dam-foundation joint. Using the mesh of fig. 4.10, the crack is smeared through the bottom row of dam elements, 225 through 232. No other cracking was permitted. The analysis was carried out using the same parameters as before, and the results are displayed in figs. 4.34 through 4.37. Rocking motion about the base (figs. 4.34 and 4.35) is less pronounced than that of the detached top part of the dam examined earlier; the dam never lifts off along more than five elements out of the total of eight. The sliding motion shown in fig. 4.36 shows a permanent slip of about 0.6 ft, also less than that of the detached top part. Contours of the maximum principal stress (fig. 4.37) reveal tensile stresses near the base of the neck large enough to initiate cracking. Water cavitation was recorded in elements 2, 3, and 4, but the amount was appreciably less than that in the case of a linear dam (dashed line in fig. 4.22). Compressive stresses were again within the linear range.

Ideally, dam-foundation joints are keyed to improve the sliding resistance at the base. However, nearby weak planes such as unkeyed lift joints and weak seams running through the foundation rock may actually compromise the overall resistance against sliding.

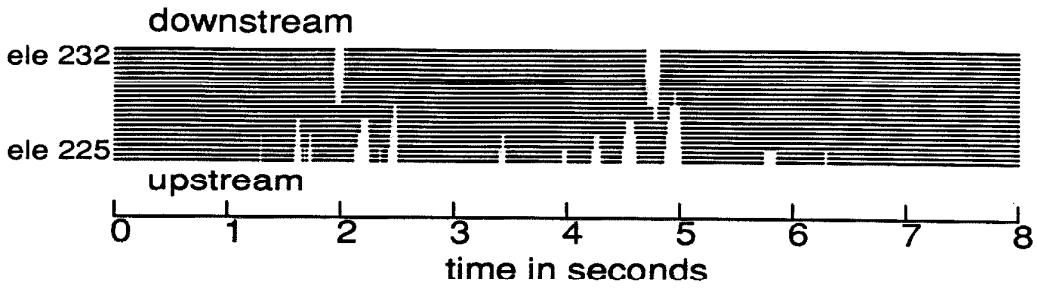

Figure 4.34. Time history of crack opening and closing (elements 225 through 232) for Problem 4.4. Solid lines (three per element) denote a closed crack.

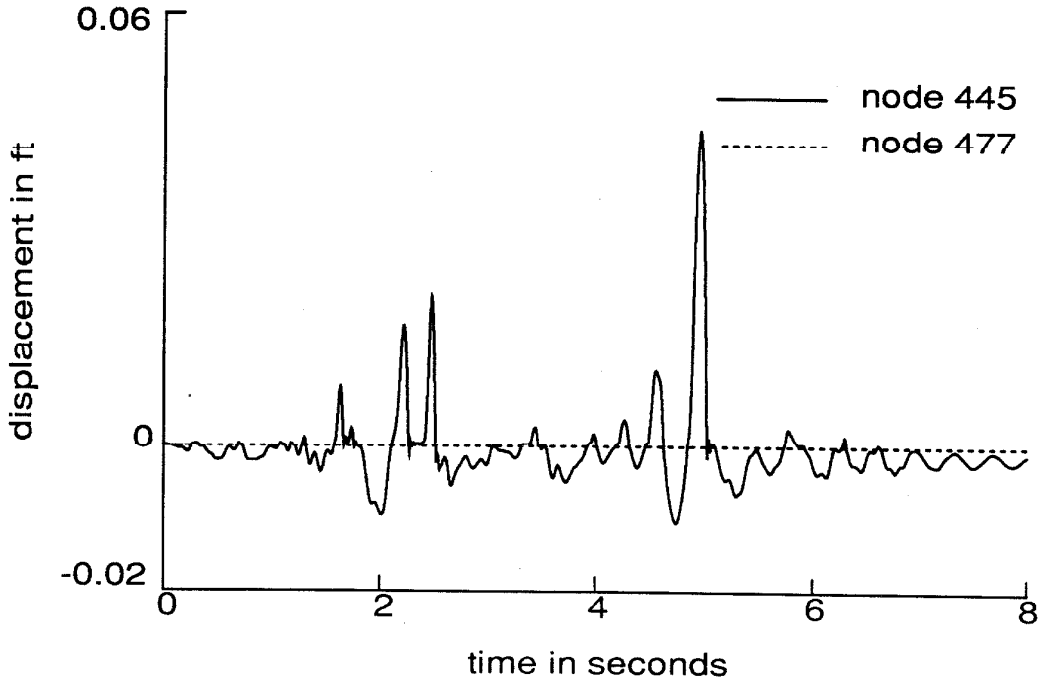

Figure 4.35. Time histories of the vertical displacements at nodes 445 and 477 for Problem 4.4.

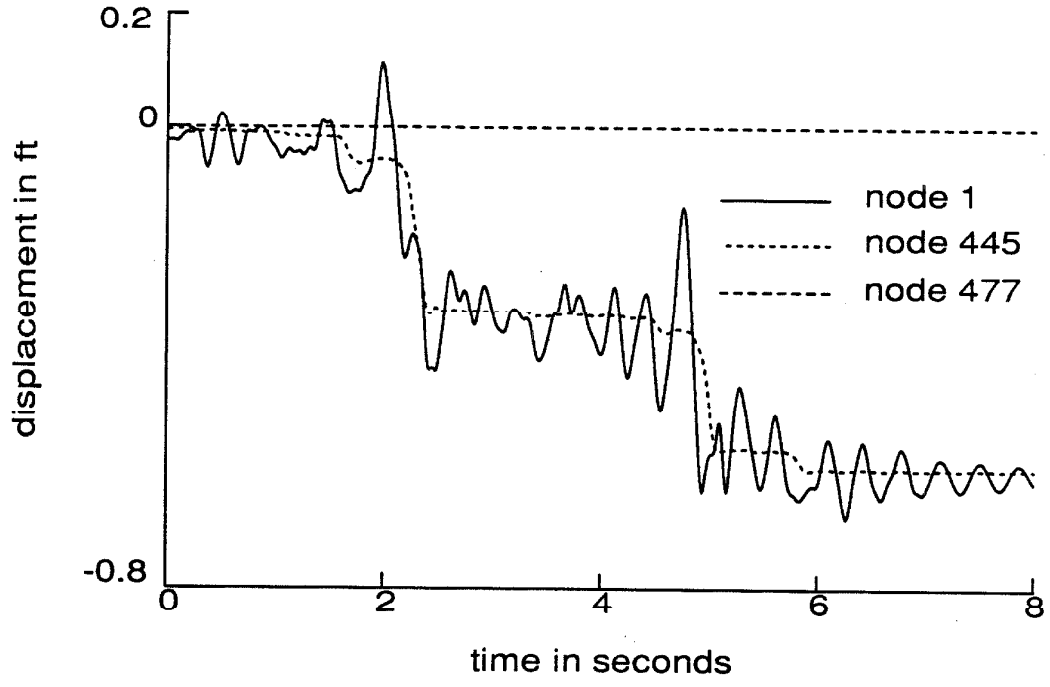

Figure 4.36. Time histories of the horizontal displacements at nodes 1, 445 and 477 for Problem 4.4.

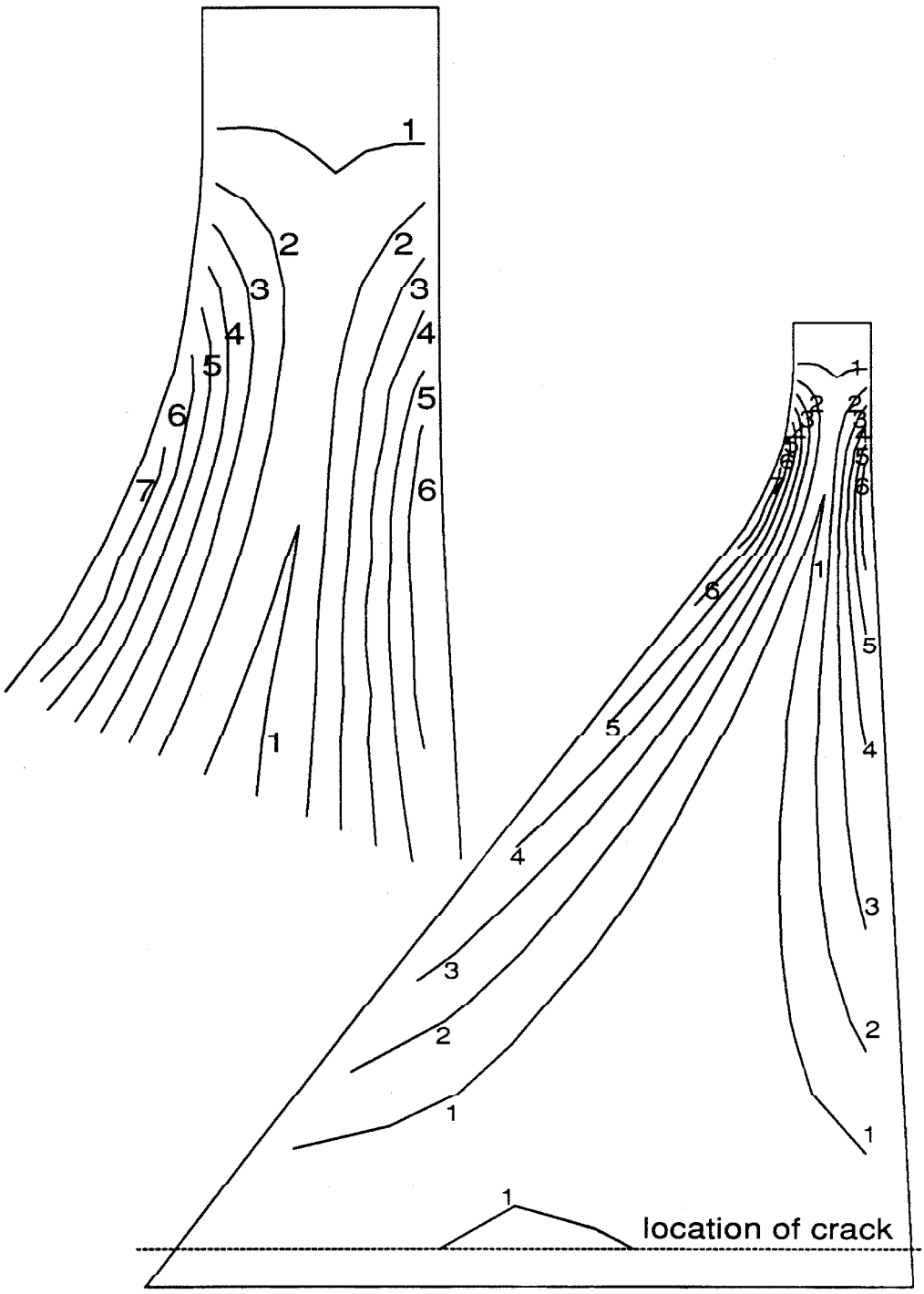

Figure 4.37. Contours of the maximum principal stress (tension) in the dam for Problem 4.4. Numbers indicate contour values in hundreds of psi.

4.5.5 Problem 4.5

The earthquake response of a dam monolith is influenced by initial cracks and existing weak planes. Of particular importance is the case of crack propagation in a dam with lift joints of low tensile strength. In an attempt to model such a problem, horizontal lift joints were assumed through every row of dam elements in the mesh shown in fig. 4.10; no initial cracks were considered. The reduced strengths along the joints were assumed to be half those taken for the concrete; $\sigma'_{ct} = 300$ psi, and σ'_{cr} is computed from equation (4.6) using a critical stress intensity factor of 1000 lb/in$^{1.5}$. Thus, σ'_{cr} varies from 100 psi in the region of the neck to 40 psi at the base of the dam. Cracking other than along the horizontal lift joints is prevented.

Time histories of crack opening and closing are shown in fig. 4.38. Initiation first occurred at the heel (element 225) at 1.09 seconds, and this crack propagated later to elements 226, 227, 228, and 229 at 1.19, 1.61, 2.32, and 4.925 seconds, respectively. The rest of the base (elements 230 through 232) never experienced cracking. A second crack initiated in element 80 at 1.95 seconds and quickly propagated through to element 74; the last element of this joint (element 73) cracked on the following back swing of the dam. No further cracking occurred.

Interestingly, in the midst of propagation of the top crack, it wanted to deviate from the joint and turn downward due to large shear stresses in the element at the crack tip. According to Section 4.4.5, the criteria to determine whether the crack should follow the joint or not utilizes the values σ_{pt}/σ_{cr} and σ_{nt}/σ'_{cr}. With σ_{cr} computed using the critical stress intensity factor of 2000 lb/in$^{1.5}$, on occasion the former ratio exceeded both unity and the latter ratio. The tendency to dip away from the horizontal lift joint would diminish as the ratio σ'_{cr}/σ_{cr} gets smaller and eventually vanish in the limit when the joints are actually initial cracks ($\sigma'_{ct} = \sigma'_{cr} = 0$). Contours of the maximum principal stress (not shown) contained tensile stresses large enough to initiate cracking on a plane nearly

perpendicular to the top crack and close to it. These stresses, which were not permitted to initiate cracks, are similar to those seen near the initial cracks of Problems 4.1 to 4.3.

Figs. 4.39 and 4.40 show the time histories of displacements at nodes 1, 130, 139, 445 and 477. For the top crack, the opening reaches 0.18 ft and the permanent slip is 1.75 ft; these compare to values of 0.1 ft and 1.9 ft, respectively, for the initial crack of Problem 4.1 (which was in the same location). The maximum opening is 0.04 ft for the bottom crack, comparable to that of the initial base crack of Problem 4.4; no sliding takes place at the base in the present case because the crack does not propagate through. The hydrodynamic response (not shown) contained only a small amount of cavitation, even less after the top crack had fully developed. Compressive stresses remained in the linear range.

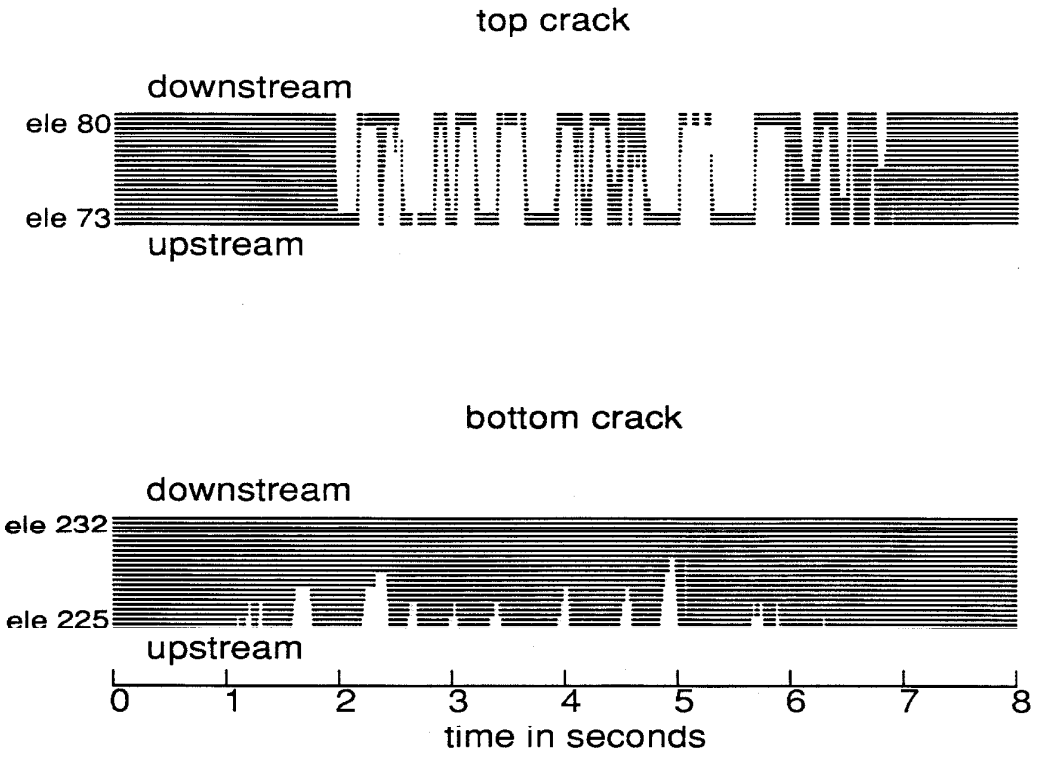

Figure 4.38. Time histories of crack opening and closing at elements 73 through 80 (top crack) and elements 225 through 232 (bottom crack) for Problem 4.5. Solid lines (three per element) denote a closed crack.

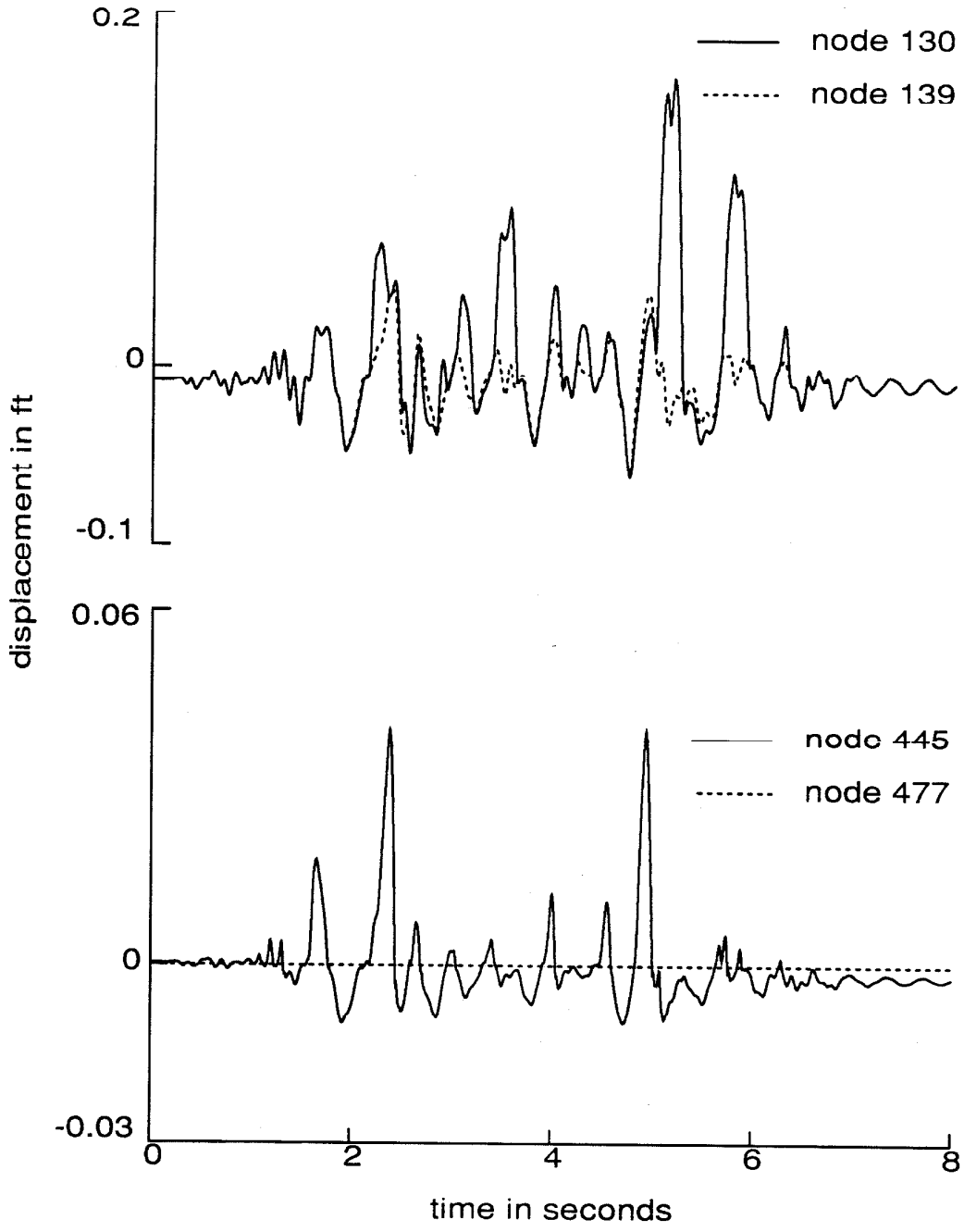

Figure 4.39. Time histories of the vertical displacements at nodes 130, 139, 445 and 477 for Problem 4.5.

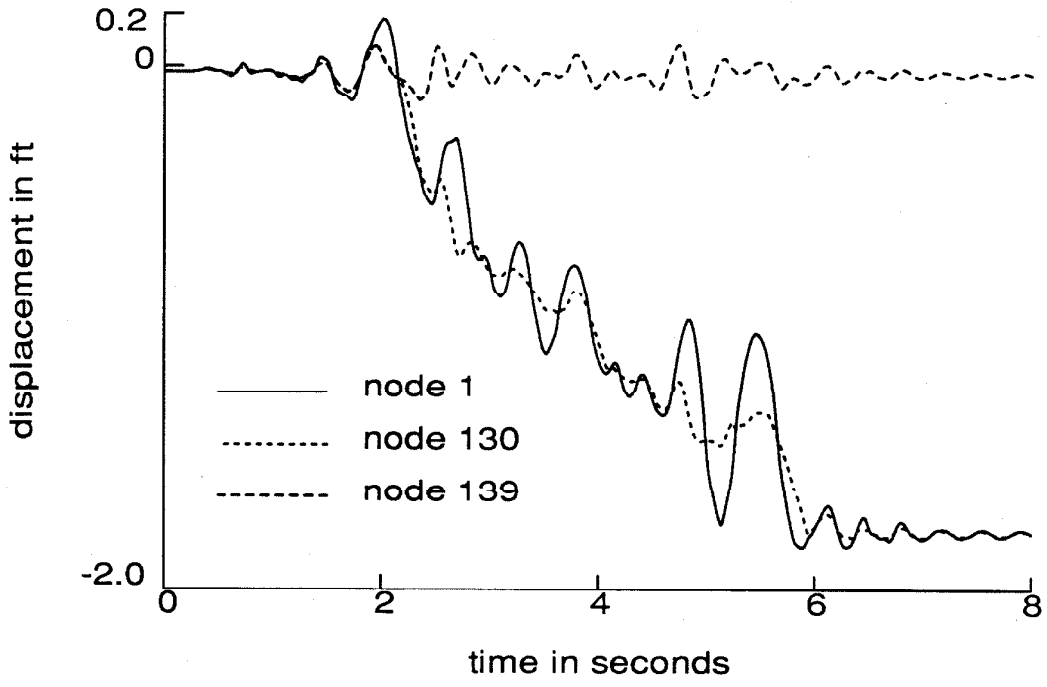

Figure 4.40. Time histories of the horizontal displacements at nodes 1, 130 and 139 for Problem 4.5.

4.5.6 Problem 4.6

The last study examines cracking in a dam section with no initial cracks or planes of weakness. The crack initiation strength σ_{ct} equals 600 psi, and the propagation strength σ_{cr} (from equation (4.6) with a critical stress intensity factor of 2000 $lb/in^{1.5}$) ranges from 200 psi in the region of the neck to 80 psi at the bottom. Cracking at the base is assumed to follow the horizontal dam-foundation joint as in Problem 4.5.

Similar to the preceding Problem, crack initiation was first detected at the heel (element 225) after 1.18 seconds and extended later through elements 226, 227, and 228 at 1.2, 1.61, and 2.25 seconds, respectively; the rest of the dam-foundation joint remained uncracked. In the meantime, a second crack initiated in element 96 at 1.965 seconds. The propagation of this crack is summarized in table 4.1 and pictured in fig. 4.41.

time step	time in sec	element no.	row no.
393	1.965	96	12
		95	12
		103	13
		102	13
		101	13
		109	14
394	1.970	108	14
		116	15
		124	16
395	1.975	123	16
396	1.980	131	17
397	1.985	139	18
399	1.995	138	18
403	2.015	146	19
502	2.510	154	20
503	2.515	162	21
505	2.525	170	22

Table 4.1. Details of crack propagation in the top of the dam for Problem 4.6.

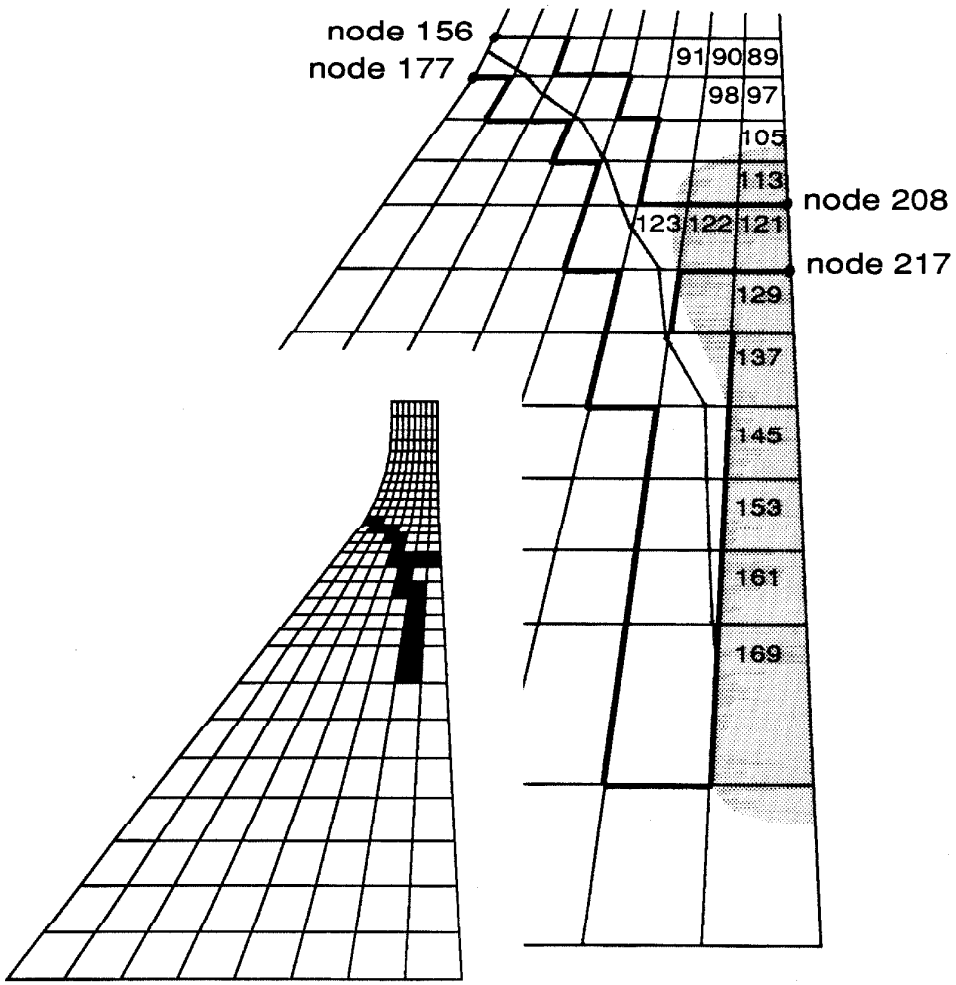

Figure 4.41. Profiles of the cracks in the top part of the dam for Problem 4.6.

During the time gap noted between cracking of elements 146 and 154, the dam reversed its motion and the top crack closed; the base crack opened and extended to element 228 as was mentioned above. Vertical tension developed in the upstream elements at the base of the neck but never peaked to 600 psi through this cycle.

It should be mentioned here that the proximity of the top crack shown in fig. 4.41 to the upstream face makes modeling the shaded zone shown in the figure difficult since only a few elements exist across its width. Recall also that in the adopted smeared crack model, the element loses its normal stiffness in the direction parallel to the crack whether the crack is open or closed. This means that most of the cracked elements can carry only a little vertical load because of the near vertical orientation of the crack. To carry the analysis further, considerable judgement is necessary to interpret the results and to account for further cracking in the dam.

During the next opening of the top crack, it extended downward to elements 154, 162 and 170. Following closure up to the level of elements 122 and 121 at 2.645 seconds, the principal tensile stress in element 122 (acting on a nearly horizontal plane) exceeded 600 psi, a result of cantilever bending in the shaded region. Cracking of element 122 confined the cantilever bending moment to element 121, which was under a net vertical compression. At 2.655 seconds, tensile stresses exceeding 600 psi existed in several nearby elements above because of the vertical tensile force being transferred through the left side of element 121 (the tension leg of the cantilever bending moment). The next step should have been to continue the horizontal crack through the left side of element 121, but, since the stresses were only monitored at the center Gauss point (which showed vertical compression), this was not possible. It was decided to crack element 121 horizontally at this center Gauss point anyway which, although no opening occurred, relieved the high tensions above since the stiffness of the bending mode of element 121 reduces to zero with one point integration. Had element 121 been initially integrated with one point quadrature, the high tensions in

the elements above would not have developed. Element 121 did not open until the dam deflected downstream; it would have cracked horizontally then anyway since its neighbor, element 122, had cracked previously.

The analysis was carried out to the end of the time history (8 seconds) with no further crack initiation or extension. However, tensile stresses high enough to cause crack initiation were seen on planes nearly perpendicular to the sloping crack at two locations: below the crack near the downstream face and to the right of it above element 122. This behavior is similar to that observed in previous problems, and no additional cracks were initiated because of a lack of mesh fineness. No cavitation occurred in the reservoir during the response.

Figs 4.42 to 4.46 show time histories of crack opening and closing and of the displacements at nodes 1, 156, 177, 208 and 217. Deflections of the dam toward the reservoir are particularly significant, and, in the largest excursion, the sloping crack stays open for 0.75 seconds, and the width of the opening reaches 0.5 ft at the downstream face (figs. 4.42 and 4.44). At the upstream face, the maximum width of the opening is 0.15 ft (fig. 4.46). Although the dam remained stable and experienced little sliding (figs. 4.43 and 4.45), the top portion of the dam appears to be precariously close to sliding into the reservoir, especially if the wedge below elements 122 and 121 is lost. It should be emphasized that the discretization in the shaded zone is too coarse to affirm that such an event does not occur. For example, although the compressive stresses sampled at the center Gauss points remained in the linear range, the cantilever bending stress in the wedge at the upstream face is poorly represented by the stresses at the element centers, especially near the bottom of the wedge where the width is a single element. Also, vertical impact loadings on the wedge during closing of the crack through elements 121 and 122 would be particularly detrimental and may not be well captured by the analysis. Finally, it is mentioned that response of the dam subsequent to loss of the wedge would involve considerable sliding along the curved crack, and questions remain as to how well the analysis procedure could capture this behavior. Depending on the crack profile, such sliding would

create open segments and local regions of high contact stresses along the crack, and possibly form additional cracks.

As revealed by a separate analysis, a different crack pattern was obtained at the top of the dam when the ground motions were reversed. This pattern resembled an inverse picture of that shown in fig. 4.41; the crack initiated almost horizontally off the upstream face and dipped as it propagated, ending close and approximately parallel to the downstream face. Geometrical problems hampered the analysis in a very similar way as discussed above.

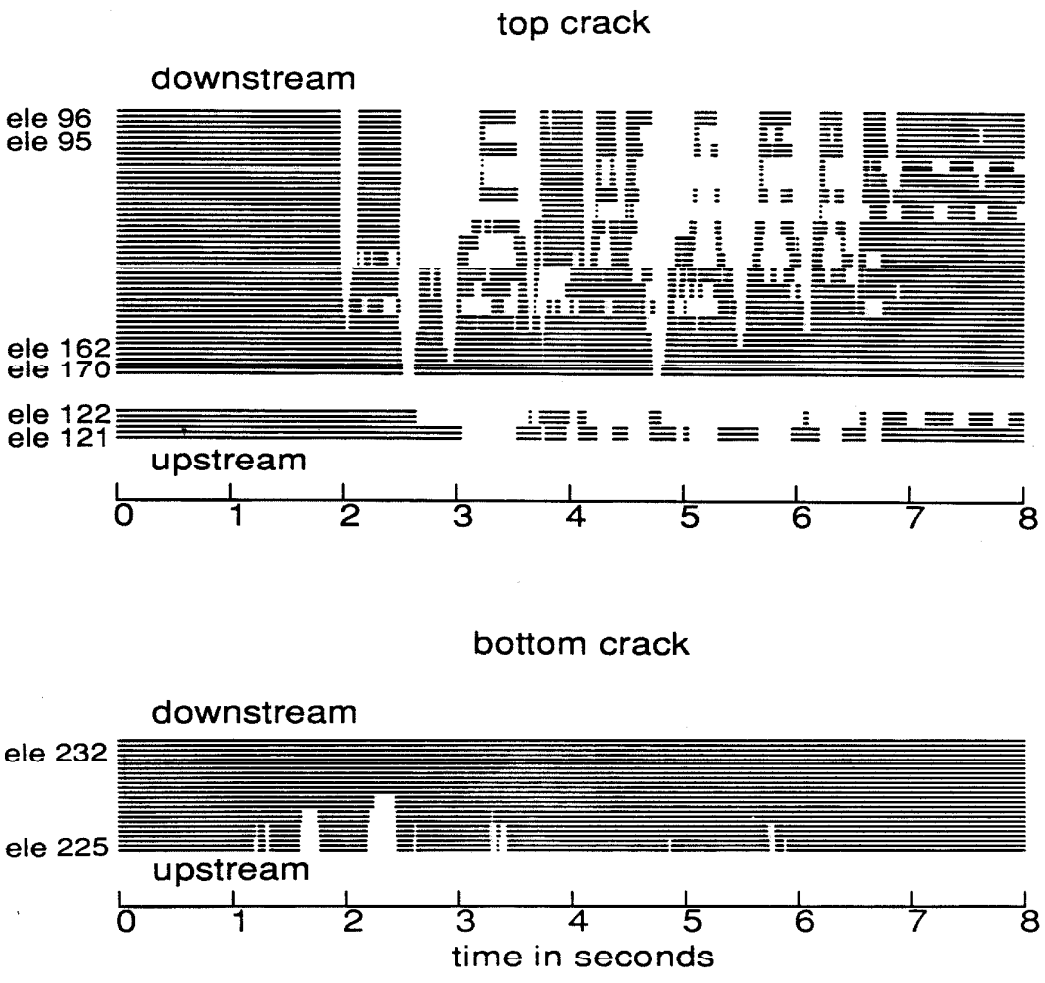

Figure 4.42. Time histories of crack opening and closing for the cracks in Problem 4.6. Solid lines (three per element) denote a closed crack.

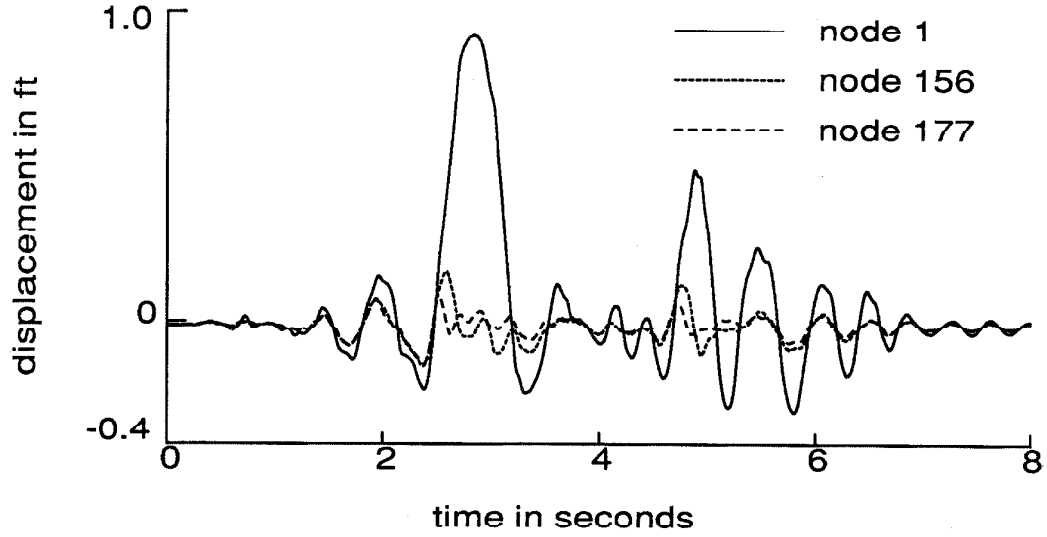

Figure 4.43. Time histories of the displacements at nodes 1, 156 and 177 in the direction tangent to the crack for Problem 4.6.

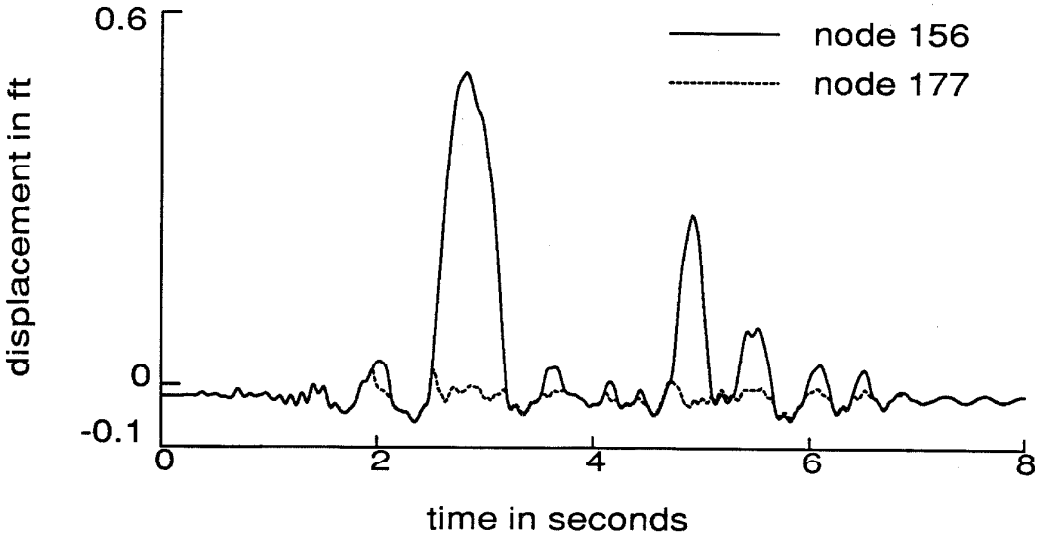

Figure 4.44. Time histories of the displacements at nodes 156 and 177 in the direction normal to the crack for Problem 4.6.

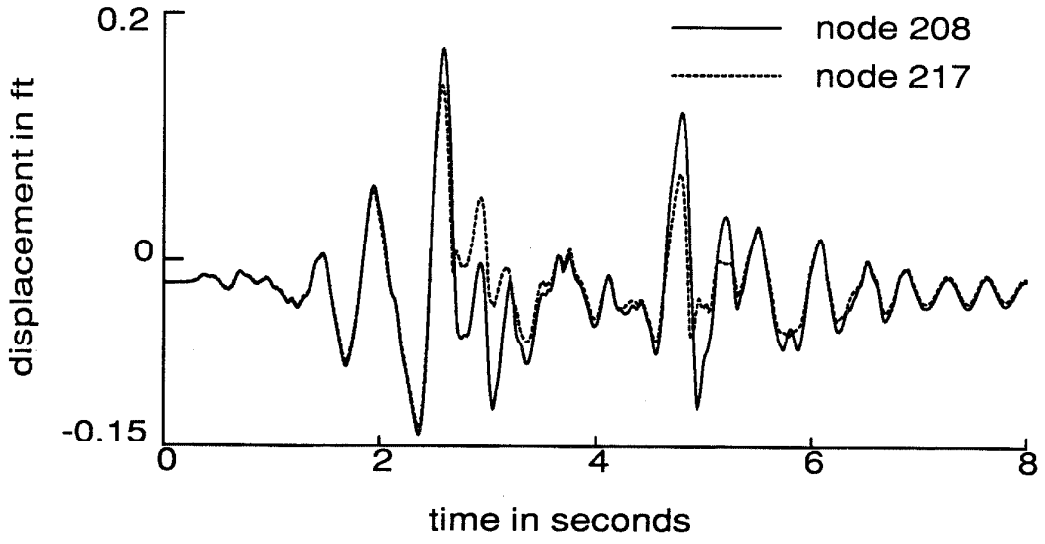

Figure 4.45. Time histories of the horizontal displacements at nodes 208 and 217 for Problem 4.6.

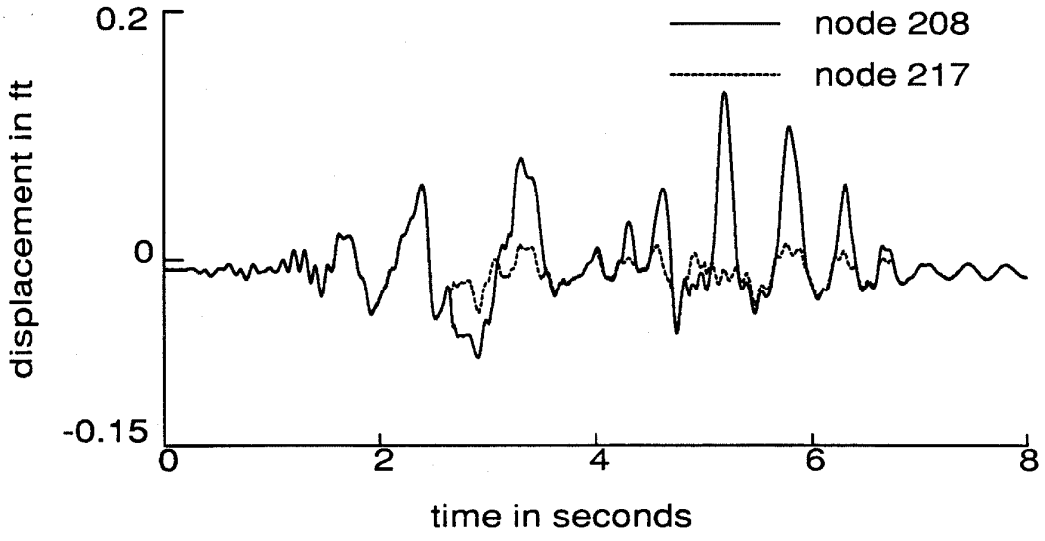

Figure 4.46. Time histories of the vertical displacements at nodes 208 and 217 for Problem 4.6.

References

[1] Agbabian Associates, "Nonlinear analysis of Norris Dam for seismic loads," El Segundo, California, June 1975.

[2] Bazant, Z. P. and Cedolin, L., "Blunt crack band propagation in finite element analysis," *Journal of the Engineering Mechanics Division*, Vol. 105, No. EM2, April 1979.

[3] Berg, G.V., et al., "The Koyna, India, Earthquakes," *Proceedings of the 4th World Conference on Earthquake Engineering*, Vol. 3, Santiago, Chile, 1969.

[4] Chappell, J. F., "A fracture mechanics investigation of the cracking of Fontana Dam," A Master of Science Thesis, Cornell University, Ithaca, New York, May 1981.

[5] Chapuis, J., Rebora, B. and Zimmermann, Th., "Numerical approach of crack propagation analysis in gravity dams during earthquakes," *Commission International Des Grands Barrages*, Quinzième Congrès des Grands Barrages, Lausanne, 1985.

[6] Chen, H.-Q., et al., "Dynamic stability analysis of cracked top portion of the Xinfengjiang Concrete Diamond Head Buttress Dam," *Proceedings of US-PRC Bilateral Workshop on Earthquake Engineering*, Harbin, China, August 1982.

[7] Chopra, A. K. and Chakrabarti, P., "The Koyna Earthquake of December 11, 1967 and the performance of the Koyna Dam," *Report No. EERC 71-1*, Earthquake Engineering Research Center, University of California, Berkeley, April 1971.

[8] Droz, Patrice, "Modèle numérique du comportement non-linéaire d'ouvrages massifs en beton non armé," *Thesis No. 682*, Department de Génie Civil, Ecole Polytechnique Féderal de Lausanne, EPFL 1987.

[9] Hall, J. F., "Study of the earthquake response of Pine Flat Dam," *Earthquake Engineering and Structural Dynamics*, Vol. 14, No. 2, March-April 1986.

[10] Haugeneder, E., "A note on finite element analysis of blunt crack band propagation," *Proceedings of the International Conference on Constitutive Laws for Engineering Materials, Theory and Application*, University of Arizona, Tucson, January 10-14, 1983.

[11] Hsu, T.-H., et al., "Strong motion observation of water induced earthquake at Hsinfengkiang reservoir in China," *Engineering Geology*, Vol. 10, 1976.

[12] Hughes, T. J. R., "Stability, convergence and growth and decay of energy of the average acceleration method in nonlinear structural dynamics," *Computers and Structures*, Vol. 6, No. 4/5, August-October, 1976.

[13] Kaldjian, M.J. and Berg, G.V., "A method for computing the response of cracked gravity dams to earthquake forces," *Paper No. 118, Bulletin of the Indian Society of Earthquake Technology*, Vol. 9, No. 1, March 1972.

[14] Kollgaard, E.B., "Criteria for seismic safety-approaches for evaluation of analytical results," *Proceedings of the China-US Workshop on Earthquake*

Behavior of Arch Dams, Beijing, China, June 1987.

[15] Mlakar, P. F., "Nonlinear response of concrete gravity dams to strong earthquake-induced ground motion," *Computers & Structures*, Vol. 26, No. 1/2, 1987.

[16] Niwa, A. and Clough, R. W., "Shaking table research on concrete dam models," *Report No. UCB/EERC-80/05*, Earthquake Engineering Research Center, University of California, Berkeley, September 1980.

[17] Ortiz, M., Leroy, Y. and Needleman, A., "A finite element method for localized failure analysis," *Computer Methods in Applied Mechanics and Engineering* , Vol. 61, No. 2, March 1987.

[18] Pal, N., "Nonlinear earthquake response of concrete gravity dams," *Report No. EERC 74-14*, Earthquake Engineering Research Center, University of California, Berkeley, December 1974.

[19] Saini, S. S. and Krishna, J., "Overturning of top profile of the Koyna Dam during severe ground motion," *Earthquake Engineering and Structural Dynamics*, Vol. 2, No. 3, January-March 1974.

[20] Saouma, V. E., "Interactive finite element analysis of reinforced concrete; a fracture mechanics approach," A Ph.D. Thesis, Cornell University, Ithaca, New York, January 1981.

[21] Shen, C.-K. et al., "Earthquakes induced by reservoir impounding and their effect on Hsinfengkiang Dam," *Scientia Sinica*, April 1974, **17**, 2, also *Proceedings of the 11th International Congress on Large Dams*, Question 51, New Delhi, India, 1979.

[22] Skrikerud, P. E., and Bachmann, H., "Discrete crack modelling for dynamically loaded unreinforced concrete structures," *Earthquake Engineering and Structural Dynamics*, Vol. 14, No. 2, March-April 1986.

[23] UNESCO, "Koyna Earthquake December 11, 1967," *Report of the Committee of Experts*, New Delhi, India, April 1968.

[24] Vargas-Loli, L.M. and Fenves, G., "Nonlinear earthquake response of concrete gravity dams," Department of Civil Engineering, University of Texas, Austin, December 1987.

[25] Zienkiewicz, O. C., Fejzo, R. and Bićanić, N., "Experience in analyzing plain concrete structures using a rate senstive model with crack monitoring capabilities," *Proceedings of the International Conference on Constitutive Laws for Engineering Materials, Theory and Application*, University of Arizona, Tucson, January 10-14, 1983.

Appendix 4.A:

Coupling Effects in a Smeared Crack Element (Open Crack)

Consider a 4-node, linearly interpolated, rectangular element that contains an open crack as shown in fig. 4.A.1a. Such a crack splits the element in one of the two cases in fig. 4.A.1b according to the cracking situation in neighboring elements as shown in fig. 4.A.1c. Take the first case as an example. The two modes of deformation shown in fig. 4.A.1d and e are of interest; one is an opening mode with nodes A and B displacing an amount Δr_1 normal to the crack, and the other is a sliding mode with A and B displacing Δr_2 tangent to the crack. Because the crack is initially open, the opening mode should have zero stiffness, while the sliding mode should receive stiffness only from the shear retention term $\alpha_s G$ in D_T^{oc}. Such, however, is not the case for a crack not parallel to one of the sides of the rectangular element.

Strain and stress increments, the latter computed with D_T^{oc} from equation (4.1), in the element are

$$\begin{Bmatrix} \Delta\epsilon_1 \\ \Delta\epsilon_2 \\ \Delta\gamma_{12} \end{Bmatrix} = \frac{\Delta r_1}{h} \begin{Bmatrix} sin\theta \\ 0 \\ cos\theta \end{Bmatrix} \quad , \quad \begin{Bmatrix} \Delta\sigma_1 \\ \Delta\sigma_2 \\ \Delta\tau_{12} \end{Bmatrix} = \alpha_s G \frac{\Delta r_1}{h} \begin{Bmatrix} 0 \\ 0 \\ cos\theta \end{Bmatrix}$$

for the opening mode (where θ = the angle between the crack normal and the horizontal, and h = element height) and are associated with nodal force increments

$$\Delta F_1 = \frac{l}{2h} \alpha_s G \Delta r_1 cos^2\theta$$

$$\Delta F_2 = \frac{l}{2h} \alpha_s G \Delta r_1 cos\theta sin\theta,$$

where l = element width. For the sliding mode,

$$\begin{Bmatrix} \Delta\epsilon_1 \\ \Delta\epsilon_2 \\ \Delta\gamma_{12} \end{Bmatrix} = \frac{\Delta r_2}{h} \begin{Bmatrix} 0 \\ cos\theta \\ sin\theta \end{Bmatrix} \quad , \quad \begin{Bmatrix} \Delta\sigma_1 \\ \Delta\sigma_2 \\ \Delta\tau_{12} \end{Bmatrix} = \frac{\Delta r_2}{h} \begin{Bmatrix} 0 \\ E cos\theta \\ \alpha_s G sin\theta \end{Bmatrix}$$

and

$$\Delta F_1 = \frac{l}{2h} \alpha_s G \Delta r_2 sin\theta cos\theta$$

$$\Delta F_2 = \frac{l}{2h}(E cos^2\theta + \alpha_s G sin^2\theta)\Delta r_2.$$

The nonzero nodal force increments for the opening mode indicate the presence of an unwanted stiffness which arises from the nonzero shear strain increment $\Delta\tau_{12}$ for a crack orientation off horizontal. To examine the magnitude of this extra stiffness, set $\alpha_s = 0.5, G = 0.4E, \theta = 60^o$ and $\Delta r_1 = 1.0$ resulting in $\Delta F_1 = 0.025\frac{El}{h}$ and $\Delta F_2 = 0.043\frac{El}{h}$ and compare to the nodal force increment $\Delta F_y = 0.5\frac{El}{h}$ necessary to extend the uncracked element vertically a unit amount. Thus, the unwanted stiffness is not negligible but can be made so by taking a small value for α_s. For the sliding mode, the nonzero strain increment $\Delta\epsilon_2$ tangent to the crack produces additional unwanted stiffness. To examine this effect, set $\alpha_s = 0.0, \theta = 60^o$ and $\Delta r_2 = 1.0$ resulting in $\Delta F_1 = 0.0$ and $\Delta F_2 = 0.125\frac{El}{h}$ and compare to the nodal force increment $\Delta F_x = 0.2\frac{El}{h}$ (with $G = 0.4E$) necessary to displace the top of the uncracked element horizontally a unit amount. The magnitude of ΔF_2 is large and can only be made negligible by taking E small. This, however, has the undesirable effect of eliminating the normal stiffness in the direction tangent to the crack.

It should also be mentioned that for an open crack extending through a number of elements at different angles (as in fig. 4.A.1.c), retention of the stiffness E tangent to the crack contributes stiffness to an opening deformation because some of the sliding mode depicted in fig. 4.A.1.e will be present in some of the elements.

Appendix 4.B:

Coupling Effects in a Smeared Crack Element (Closed Crack)

Consider the sliding mode (fig. 4.A.1.e) for a closed crack in a rectangular element. Increments of strain, stress (computed using D_T^{cc} from equation (4.3) and nodal forces are

$$\begin{Bmatrix} \Delta\epsilon_1 \\ \Delta\epsilon_2 \\ \Delta\tau_{12} \end{Bmatrix} = \frac{\Delta r_2}{h} \begin{Bmatrix} 0 \\ cos\theta \\ sin\theta \end{Bmatrix} \quad , \quad \begin{Bmatrix} \Delta\sigma_1 \\ \Delta\sigma_2 \\ \Delta\tau_{12} \end{Bmatrix} = \frac{\Delta r_2}{h} \begin{Bmatrix} \frac{\nu E}{1-\nu^2} cos\theta \\ \frac{E}{1-\nu^2} cos\theta \\ G sin\theta \end{Bmatrix}$$

and

$$\Delta F_1 = \frac{l}{h}(\frac{\nu E}{1-\nu^2} + G)\Delta r_2 sin\theta cos\theta$$

$$\Delta F_2 = \frac{l}{h}(\frac{E}{1-\nu^2} cos^2\theta + G sin^2\theta)\Delta r_2.$$

The nonzero strain increment $\Delta\epsilon_2$ parallel to the crack produces unwanted stiffness which restrains the sliding along a nonhorizontal crack. To examine this extra stiffness, set $G = 0, \nu = 0.25, \theta = 60^o$ and $\Delta r_2 = 1.0$ resulting in $\Delta F_1 = 0.058\frac{El}{h}$ and $\Delta F_2 = 0.133\frac{El}{h}$ which compare to $\Delta F_x - 0.2\frac{El}{h}$ necessary to displace the top of the uncracked element horizontally a unit amount. The extra stiffness is large enough to prevent most of the sliding along such a crack.

Removal of the extra stiffness is possible by using the D_T^{cc} of equation (4.4). For the same sliding mode, the resulting stress and nodal force increments are

$$\begin{Bmatrix} \Delta\sigma_1 \\ \Delta\sigma_2 \\ \Delta\tau_{12} \end{Bmatrix} = \frac{\Delta r_2}{h} \begin{Bmatrix} 0 \\ 0 \\ G sin\theta \end{Bmatrix}$$

and

$$\Delta F_1 = \frac{l}{2h} G \Delta r_2 sin\theta cos\theta$$

$$\Delta F_2 = \frac{l}{2h} G \Delta r_2 sin^2\theta.$$

However, zero normal stiffness in the direction parallel to the crack results from this modification.

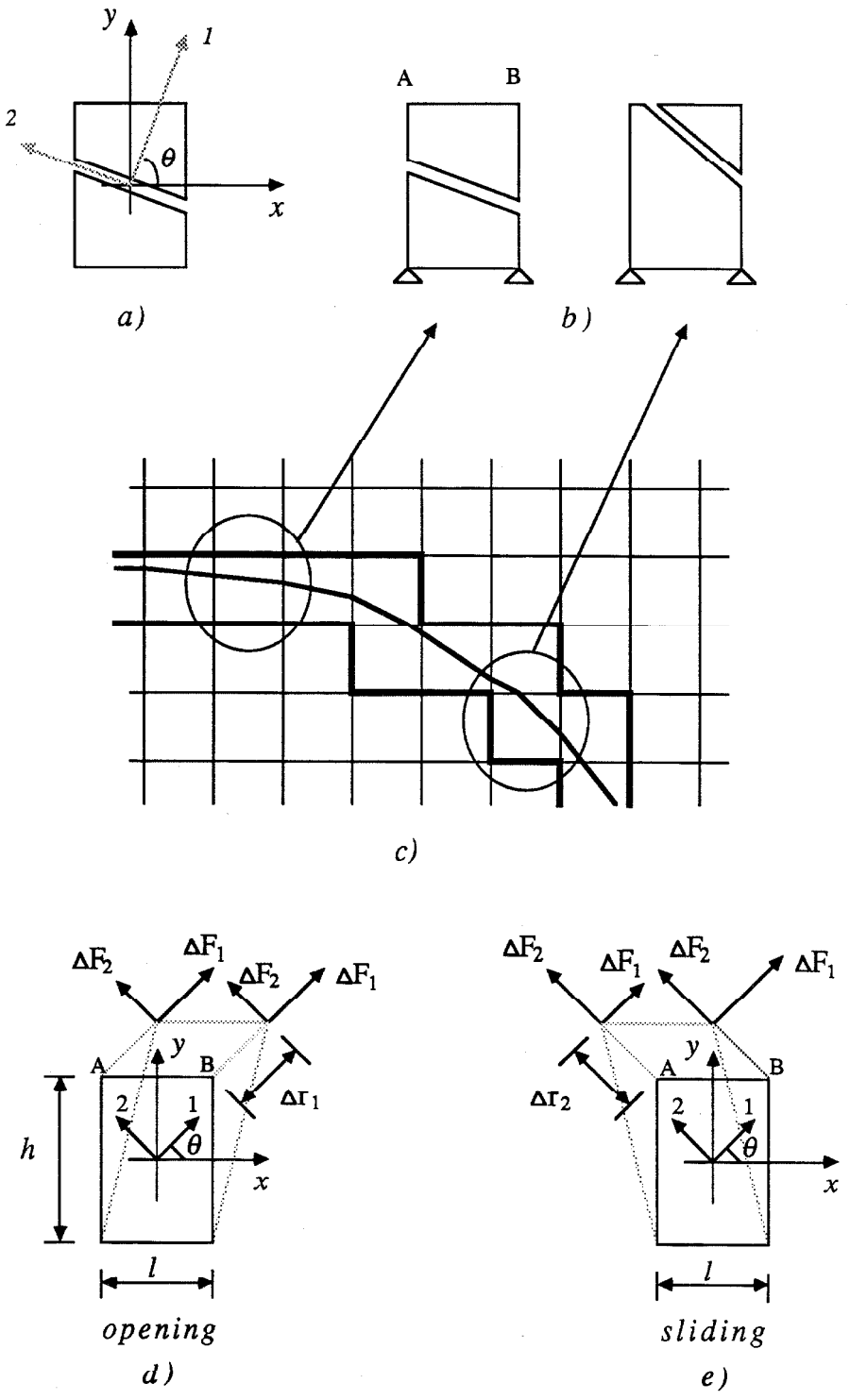

Figure 4.A.1. Coupling effects in a smeared crack element.

Chapter Five

SUMMARY AND CONCLUSIONS

5.1 Summary

The earthquake response of concrete gravity dam-water-foundation systems was investigated with emphasis on the nonlinear behavior associated with concrete cracking and water cavitation. For the sake of simplicity, the dam was idealized by considering only a separate monolith under plane stress conditions, and the two-dimensional assumption was extended to model the compressible infinite water domain. The dam-water system was treated as an integral system and the standard displacement-based finite element method was used to spatially discretize the field equations. Along the dam-water interface, stiff spring elements normal to the interface provided connection and allowed the proper slip condition. Viscous damping in the form of stiffness-proportional damping was used in the dam, but because of undesirable effects in cracked elements, the damping was omitted from an element as soon as it experienced cracking for the first time and for all times thereafter. Energy dissipation in the water reservoir through radiation in the infinite direction and absorption at the reservoir bottom was approximately accounted for based on one-dimensional wave propagation in the direction normal to these boundaries. Dam-foundation interaction was incorporated by assuming a rigid dam-base and using available influence

coefficients for a rigid plate on a three-dimensional viscoelastic half-space.

The time domain was discretized according to the Bossak 'α-method' and the choice of integration parameters provided a second order accurate, unconditionally stable (for linear response) numerical integration scheme with positive numerical damping.

Water cavitation was monitored at the center integration point of every water element at each iteration, and a bilinear material model accounted for the two-phase behavior; the inertial forces were calculated assuming a uniform distribution of mass throughout the reservoir. Several numerical studies demonstrated the cavitation model, and a full study of the effects of cavitation on the earthquake response of Pine Flat Dam was included.

Concrete cracks were included in the finite elements by adjusting their constitutive behavior, i.e., smeared crack representation. Two forms for the element tangent stiffness were considered. In one, an element with an open crack retains stiffness parallel to the crack, and the corresponding closed crack case is identical to the uncracked case. In the other, the open crack element loses its stiffness entirely, and the corresponding closed crack case retains stiffness in the direction normal to the crack but not in the parallel direction. Sliding along closed cracks followed the static friction theory, and since the elastic shear modulus was employed in both closed crack tangent matrices, iterations were required when sliding occurred. Water was not allowed into open cracks; they were subjected to absolutely zero normal stress.

Crack propagation employed an equivalent strength criterion which was defined for a regular arrangement of elements and a given stress intensity factor. Crack orientation coincided with the direction of principal tension, but other directions were also considered in the presence of weak planes. At the heel, the initiation strength was reduced to the propagation strength because of the singularity, and crack extension was confined only to the dam-foundation joint, i.e., a strong foundation was assumed. Detailed numerical studies were presented for the earthquake response of the Pine Flat Dam system under different cracking

conditions.

5.2 Discussion and Conclusions

1. The displacement-based finite element formulation for the water proved to be convenient regarding coupling with the dam and incorporation of smeared cavitation. Solution times were not excessive even though each node requires two degrees of freedom rather than the single degree of freedom for the alternative scalar wave equation.
2. Results from linear analysis indicate that cavitation is likely to occur under typical strong motion earthquake excitations.
3. Accurate modeling of water cavitation is difficult because of high frequency oscillations which occur upon closure of cavitated regions. These oscillations, which dominate the results of other numerical investigations, appear to be spurious from the dependence of their frequency on mesh fineness and from indications that they can be removed from finer and finer meshes with smaller and smaller amounts of damping. However, it is felt that, in many cases, good results can be achieved on moderately fine meshes by using amounts of damping that are small enough not to significantly affect the fundamental components of the system response. The analysis of Pine Flat Dam under twice the 1940 El Centro ground motions (linear dam, cavitation allowed in water) required an amount of stiffness-proportional damping in the water of 3% in the fundamental water mode to remove the oscillations, and the results generated are believed to be reasonably accurate. Here, the effect on the dam response was minor, including that from the tensile pressure cutoffs and the compression spikes following closure of cavitated regions. In the upper part of the reservoir where most cavitation occurred, these compression spikes at most doubled the total compressive pressure on the upstream face of the dam, still far below the level necessary to cause local impact damage. Unlike results from other investigations, the cavitated regions always retained contact with the dam face, probably a

consequence of suppressing the spurious oscillations.

4. Earthquake excitations sufficient to cause cavitation will also cause concrete cracking, so the assumption of a linear dam is not valid. Linear analysis identifies zones of high tensile stress near the base of the neck on both the upstream and downstream faces and at the heel of the dam.
5. The smeared approach to represent concrete cracking encounters a number of difficulties which are not well known. First, retention of certain terms in the tangent stress-strain relation when a crack is present leads to extraneous stiffness in the opening and sliding modes of an element. For example, the fiber stiffness in the direction parallel to the crack restrains sliding when the crack is not parallel to two opposite sides; on the other hand, removal of this stiffness eliminates the ability of the element to transmit axial loads in the direction parallel to the crack. The use of elements with discontinuous shape functions as a remedy to this difficulty should be further investigated. Second, the presence of stiffness-proportional damping in a cracked element significantly reduces the amount of opening and transmits large tensions to neighboring elements. Third, a propagating crack requires user input to force the trend of the crack to be consistent with the orientation of the cracks in the individual elements. Extension of the crack always to the neighboring element with the largest tensile stress may result in an unrealistic crack profile.
6. The crack propagation algorithm described in Chapter 4 produces narrow crack zones, not wide ones as is common in other investigations. Features of the algorithm responsible for narrow crack zones, believed to be more realistic, include
   - selection of the tangent stress-strain relation which avoids the extraneous stiffness in opening and sliding modes of a cracked element
   - removal of stiffness-proportional damping from an element once it cracks
   - a limit of one element per iteration into which a crack is initiated or

propagated

- the use of a propagation strength based on fracture mechanics criteria which is considerably below the initiation strength
- assignment of the propagation strength only to appropriate elements at the head of the crack tip.

7. As shown by four analyses of Pine Flat Dam with an initial, straight, through crack (three cases of a crack in the neck region, each at a different inclination, and one case of a crack at the base) subjected to 1.5 times El Centro with full reservoir, the presence of cracks does not necessarily imply failure. The most serious of these cases were the neck cracks, in particular the one inclined 18^o downstream which slid 3.4 ft away from the water. If used to assess the safety of an actual dam, results based on initial cracks should be treated with caution because of possible unconservatism about the choice of location of the crack or cracks. Previous investigations have produced few results regarding potential sliding displacements, so the present results are valuable in this regard.

8. Modeling of crack propagation is preferable to assuming initial cracks. The existence of weak planes (lift joints) influences the resulting crack pattern. In an analysis of Pine Flat Dam (1.5 El Centro, full reservoir) with horizontal weak planes (concrete tensile strength reduced by half) in every row of elements, only two cracks formed - a through crack in the neck and a partially through crack at the heel. However, the neck crack preferred to turn downward once it reached the interior, demonstrating that lift joints must be considerably weaker than the surrounding concrete to fully contain a crack. Without weak planes, the neck crack initiates perpendicular to a face and turns down into the body of the dam. An analysis of Pine Flat Dam (1.5 El Centro, full reservoir) showed such a crack to propagate close enough and parallel to the opposite face that an extremely fine mesh would have been necessary to obtain reliable results. For example, for the near vertically oriented end of the crack, the analysis suffers from the omission

of the fiber stiffness parallel to the crack. Branch cracks due to cantilever bending in the narrow zone between the main crack and the adjacent face tend to occur, and their accurate representation requires a fine mesh also. Although no instability occurred in the analysis, a steeply sloping crack would represent a hazard regarding sliding of the top of the dam or the wedge shaped portion of it below the branch crack if the main crack breaks through to the opposite face (possibly involving localized compression or shear failure). It is thought that some additional difficulties may arise in modeling such sliding along a curved crack.

9. Since propagating cracks tend to turn sharply down in the interior of the dam creating a possibly hazardous situation if they propagate far enough, an accurate incorporation of fracture mechanics becomes a necessity in safety assessment.
10. All of the cracks showed occasional high shear stresses in the contact zone during maximum opening which were accompanied by tensile stresses large enough to cause branch cracking perpendicular to the main crack near a dam face. No such cracks were permitted to form due to a lack of mesh fineness; they deserve further investigation.
11. Cracking of the dam reduces the dynamic water pressures generated in the reservoir and, thus, the amount of cavitation. Cracking is clearly the more important of the two nonlinearities.
12. For all of the analyses performed, compressive stresses remained within the linear range of concrete although some stresses in zones requiring finer discretizations may have been poorly represented. Future work that concentrates on the cracking phenomenon will be most productive.
13. Water intrusion into open cracks, not permitted in any of the analyses performed, deserves attention as its omission is unconservative. An opening of 0.1 ft with a duration of 0.2 to 0.3 sec, as seen for the initial horizontal crack in the first analysis, may or may not be sufficient to allow significant water intrusion. The sloping crack which initiated from the downstream

face in the last analysis underwent a much larger and longer opening there, a similar event occurring on the upstream face (not unlikely) would be of concern.